Title

Study of internal magnetic field via polarimetry in fusion plasmas

Author

Zhang, Jie

Publication Date

2013

University of California
Los Angeles

Study of internal magnetic field via polarimetry in fusion plasmas

A dissertation submitted in partial satisfaction
of the requirements for the degree
Doctor of Philosophy in Physics

by

Jie Zhang

2013

Abstract of the Dissertation

Study of internal magnetic field via polarimetry in fusion plasmas

by

Jie Zhang

Doctor of Philosophy in Physics

University of California, Los Angeles, 2013

Professor Troy A. Carter, Chair

The internal equilibrium magnetic field and magnetic fluctuations in tokamaks were studied via polarimetry in this project. This study was performed mainly using a recently developed millimeter-wave polarimeter system, which probes the plasma along a major radial chord using a retro-reflection geometry. The system launches a rotating linearly polarized beam and detects a phase shift directly related to the polarization change caused by the plasma. The magnetic field component along major radius (B_{R}) can be estimated from the measured phase shift. A phase resolution of $< 2°$ for $f < 500\ Hz$ and $0.3°$ ($\tilde{B}_R \sim 2\ Gauss$) for $500\ Hz < f < 500\ kHz$ has been achieved.

An interaction between Faraday rotation (FR) and Cotton-Mouton (CM) effects was first identified in polarimetry modeling for NSTX using a synthetic diagnostic code based on Mueller-Stokes calculus. The interaction, especially the influence of the CM effect on polarimetry measurements, was further investigated in a systematic theory-experiment comparison on DIII-D. The synthetic diagnostic code

was validated by accurately reproducing the measurements over a broad range of plasma conditions, and was intensively employed in the investigation. When the CM effect is predicted to be weak, the FR effect can well approximate the measurements. As the CM effect increases, it can compete with the FR effect in rotating the polarization of the EM-wave. This results in an apparent reduced polarimeter response to the FR effect. If sufficiently large, the CM effect can even reverse the handedness of a wave launched with circular polarization. This helps to understand the surprising experimental observations that the sensitivity to the FR effect can apparently be nearly eliminated at $B_T = 2.0\ T$.

The potential of mm-wave polarimetry to measure magnetic fluctuations is explored via both modeling and experiment. Simulations suggest that microtearing modes in NSTX-U will induce $\gtrsim 2^\circ$ ($f \sim 10\ kHz$) variations in polarimeter phase, which is primarily due to the associated magnetic fluctuations. Therefore the polarimeter is predicted to have sufficient sensitivity to observe magnetic fluctuations associated with microtearing modes. In FR-dominant case, the magnitude of density-weighted $\tilde{B}_R$ can be estimated from polarimeter measurements. For example, ~ 2 *Gauss* $\tilde{B}_R$ ($\tilde{B}_R/B_0 \approx 2 \times 10^{-4}$) is estimated for a $\sim 65\ kHz$ Toroidicity-induced Alfvén Eigenmode in a low B_T ($0.75\ T$) discharge. However, in the presence of strong CM effect, support from other diagnostics and modeling is required to determine the magnetic fluctuations.

The dissertation of Jie Zhang is approved.

George J. Morales

Christoph Niemann

Yuanxun (Ethan) Wang

William A. Peebles

Neal A. Crocker

Troy A. Carter, Committee Chair

University of California, Los Angeles

2013

To my parents, and Yuhou.

Table of Contents

5 Experimental study of plasma equilibrium

List of Figures

LIST OF TABLES

ACKNOWLEDGMENTS

I am very lucky to have been working in UCLA Plasma Diagnostic Group for my PhD project. Both my professionalism and personality thrive in the enjoyable environment. First of all, I want to express the deepest appreciation to Dr. Tony Peebles, who is a mentor to me more than physics and microwave technology. Your wisdom, diligence, high-standard requirements, and patience, all help to shape me to who I am. I would like to thank my committee chair, Prof. Troy Carter, who sets a perfect role model. You are persistently encouraging, and always kindly clear the fog for me after each "TNT" (Tony-Neal-Troy) meeting. I also wish to thank Dr. Neal Crocker, who tutored me in UNIX, coding, digitization, data analysis, English writing, and much much more.

I would like to thank Dr. Edward Doyle, Dr. Terry Rhodes, Dr. Guiding Wang, Prof. Anne White, Dr. Lei Zeng, Prof. William Heidbrink, Dr. Al Hyatt, Dr. George McKee, Dr. Craig Petty, Dr. Zheng Yan, Dr. Mike Van Zeeland, and... (the list goes on including every one of the DIII-D team), without whom the experiment on DIII-D would not have been possible. I want to express my appreciation to Dr. Lothar Schmitz, Dr. David Brower, Dr. Weixing Ding, Dr. Liang Lin, Dr. William Bergerson, and Dr. Peng Xu, from whom I gathered so many advices and brilliant ideas. I wish to thank the NSTX team, and especially Dr. Walter Guttenfelder, Dr. Robert Kaita, Dr. Shige Kubota, and Dr. Jon Menard, from whom I first learned the team work in big science.

I want to thank Prof. George Morales, who educated me in basic plasma physics through the course and careful dissertation review. I also want to thank Prof. Chris Niemann and Prof. Ethan Wang, who brought up interesting discussions and kindly serve on my committee. I want to thank the whole plasma research group at STRB and Rehab, from whom I obtained so much help during the head-scratching days at UCLA. Thank you goes to Dr. David Auerbach, Mr. Erik Everson, Prof. Walter Gekelman, Dr. Jon Hillesheim, Dr. Nathan Kugland, Ms. Meg Murphy, Dr. Patrick Pribyl, Mr. Derek Schaeffer, Dr. David Schaffner, Dr. Steve Vincena, and Dr. Yuhou Wang. I also would like to thank Zoltan Lucky, Xuan Nguyen, and Craig Wannberg, who have been providing continuous technical support. I really appreciate the family-like atmosphere created by this integrated group.

Final thank you goes to my parents, Yuzhen Lin & Suoqiang Zhang, and my love, Yuhou. My gratitude for your love and companion along this path is beyond the word.

Vita

2001–2004	Senior high school Qingdao No. 17 high school, Qingdao, China
2004–2008	Bachelor of Science Department of Modern Physics (0404) University of Science and Technology of China (USTC), Hefei, China
2008–2010	Master of Science Department of Physics and Astronomy University of California, Los Angeles (UCLA), Los Angeles, CA
04/2009–present	Graduate Student Researcher UCLA-Plasma Diagnostic Group

PUBLICATIONS AND PRESENTATIONS

Experimental validation of Mueller-Stokes theory and investigation of the influence of the Cotton-Mouton effect on polarimetry in a magnetized fusion plasma
J. Zhang, W. A. Peebles, N. A. Crocker, T. A. Carter, E. J. Doyle, A. W. Hyatt, T. L. Rhodes, G. Wang, and L. Zeng
Phys. Plasmas **20** (2013) 102519

A sensitivity assessment of millimeter-wave polarimetry for measurement of magnetic fluctuations associated with microtearing modes in NSTX-U
J. Zhang, N. A. Crocker, W. A. Peebles, T. A. Carter, and W. Guttenfelder
Plasma Phys. Control. Fusion **55** (2013) 045011

Design of a millimeter-wave polarimeter for NSTX-Upgrade and initial test on DIII-D
J. Zhang, W. A. Peebles, T. A. Carter, N. A. Crocker, E. J. Doyle, S. Kubota, X. Nguyen, T. L. Rhodes, C. Wannberg, and L. Zeng
Rev. Sci. Instrum. **83** (2012) 10E321

Simulation of microtearing turbulence in NSTX
W. Guttenfelder, J. Candy, S.M. Kaye, W.M. Nevins, E. Wang, **J. Zhang**, R.E. Bell, N.A. Crocker, G.W. Hammett, B.P. LeBlanc, D.R. Mikkelsen, Y. Ren, and H. Yuh
Phys. Plasmas **19** (2012) 056119

High spatial sampling global mode structure measurements via multichannel reflectometry in NSTX

N. A. Crocker, W. A. Peebles, S. Kubota, **J. Zhang**, R. E. Bell, E. D. Fredrickson, N. N. Gorelenkov, B. P. LeBlanc, J. E. Menard, M. Podestà, S. A. Sabbagh, K. Tritz, and H. Yuh

Plasma Phys. Control. Fusion **53** (2011) 105001

Interaction between Faraday rotation and Cotton-Mouton effects in polarimetry modeling for NSTX

J. Zhang, N. A. Crocker, T. A. Carter, S. Kubota, and W. A. Peebles

Rev. Sci. Instrum. **81** (2010), 10D519

Initial tests of NSTX-U millimeter-wave polarimeter on DIII-D

J. Zhang et al., 54th Annual Meeting of the APS Division of Plasma Physics, October 29–November 2, 2012, Providence, RI

Design of a millimeter-wave polarimeter for NSTX-Upgrade and initial test on DIII-D

J. Zhang et al., 19th Topical Conference of High-Temperature Plasma Diagnostics, May 6–10, 2012, Monterey, CA

Initial results of millimeter-wave polarimeter/interferometer prototype test

J. Zhang et al., 53rd Annual Meeting of the APS Division of Plasma Physics, November 14–18, 2011, Salt Lake City, UT

Millimeter wave polarimetry modeling on NSTX

J. Zhang et al., Joint US-EU Transport Taskforce Workshop,
April 6–9, 2011, San Diego, CA

Investigation of NTM via reflectometry and polarimetry on NSTX
J. Zhang et al., 52nd Annual Meeting of the APS Division of Plasma Physics,
November 8–12, 2010, Chicago, IL

Modeling the polarization properties of propagating electromagnetic waves in NSTX
J. Zhang et al., 18th Topical Conference of High-Temperature Plasma Diagnostics,
May 16–20, 2010, Wildwood, NJ

Modeling polarization of propagating electromagnetic waves in NSTX
J. Zhang et al., 51st Annual Meeting of the APS Division of Plasma Physics,
November 2–6, 2009, Atlanta, GA

CHAPTER 1

Introduction

This opening chapter presents the motivation for the project, and overviews the topics and major results of the dissertation.

1.1 Motivation

Controlled thermonuclear fusion is a promising energy source that can ultimately solve the worldwide energy crisis—the conflict between ever-growing energy consumption and depleting energy resources, especially nonrenewable fossil fuels [Freidberg, 2007]. Controlled thermonuclear fusion is based on the physical process that powers the stars: the fusion of atomic nuclei which releases the energy difference between the nuclei binding states before and after fusion. The most feasible process to exploit in a fusion reactor on earth is the fusion of the hydrogen isotopes deuterium ($_{1}^{2}\mathrm{D}$) and tritium ($_{1}^{3}\mathrm{T}$), resulting in the production of an α-particle (helium nucleus $_{2}^{4}\mathrm{He}$), a neutron ($_{0}^{1}\mathrm{n}$) and the release of 17.6 MeV of kinetic energy distributed amongst the fusion products according to their masses:

$$_{1}^{2}\mathrm{D} + _{1}^{3}\mathrm{T} \rightarrow _{2}^{4}\mathrm{He}\ (3.5\ MeV) + _{0}^{1}\mathrm{n}\ (14.1\ MeV) \tag{1.1}$$

To utilize this process in a fusion reactor for power generation requires the D-T fuel to be heated to high temperature, i.e., around 10 keV, to achieve a sufficiently large cross-section. At such temperature, the fuel is fully ionized, i.e., in plasma state. This hot plasma needs to be sufficiently dense and confined for sufficiently long time to achieve net power generation. To quantify the level of confinement, the fusion triple product is introduced:

$$n \cdot T \cdot \tau_E > 5 \times 10^{21} \ m^{-3} \cdot keV \cdot s \tag{1.2}$$

where n and T are the peak ion density and temperature in the plasma, respectively; and τ_E is the energy confinement time. When the above criteria (aka Lawson criteria) is satisfied, the D-T fuel enters a state where the plasma burning process becomes self-sustaining without the need for further externally applied heating. This state is usually referred to as "ignition", a metaphor derived from fossil fuels [Wesson, 2011].

In a star the confinement of the fusion plasma is achieved by its gravitational force, whereas in the laboratory the confinement has to be created artificially by other means. Inertial Confinement Fusion (ICF) and Magnetic Confinement Fusion (MCF) are the two methods presently under intensive research. ICF uses high-energy laser beams to heat and compress a pellet that contains a D-T mixture to achieve fusion reaction in the pellet core. MCF uses magnetic fields to achieve plasma confinement, and the tokamak has been the most successful concept [Wesson, 2011]. A fusion triple product of $1.5 \times 10^{21} \ m^{-3} \cdot keV \cdot s$ has been achieved in a tokamak, which is the highest value of any device to date [Kamada et al., 2002]. A schematic of the tokamak concept and its basic plasma operation are presented in Fig. 1.1. The toroidal field coils generate toroidal B-field prior to plasma breakdown. The inner poloidal field coils, also called Ohmic coils, act as a transformer with the toroidal plasma as the secondary coil, inducing large toroidal E-field that results in breakdown. The plasma current generates a poloidal B-field, which together with the toroidal field creates the helical B-field essential for plasma confinement. The outer poloidal field coils are for plasma positioning and shaping.

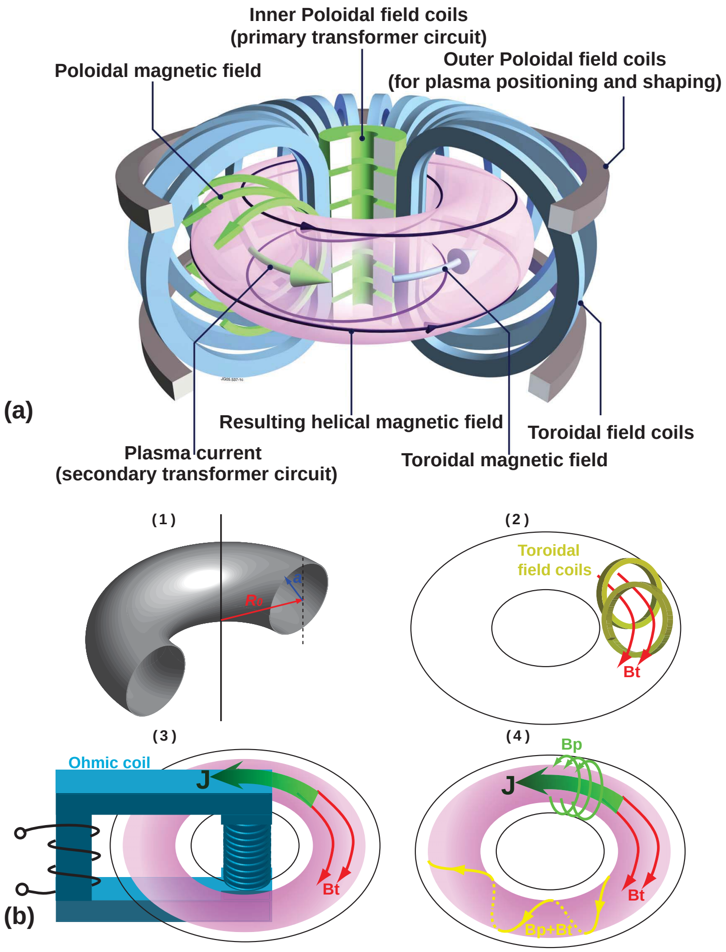

Figure 1.1: *(a) Schematic of a tokamak. (b) Basic plasma operation procedures: b1–gas into vacuum chamber; b2–toroidal field established; b3–Ohmic coil energized and breakdown occurs; b4–plasma confined by helical B-field* ($B_{poloidal} + B_{toroidal}$).

Knowledge of internal magnetic field and its fluctuations in tokamak plasmas is essential to MCF research. The equilibrium B-field has a direct impact on plasma confinement. For example, the B-field strength directly connects to the plasma-β, i.e., the ratio of plasma pressure (p_{plasma}) to magnetic pressure (p_{magnetic}):

$$\beta \equiv \frac{p_{\text{plasma}}}{p_{\text{magnetic}}} = \frac{n k_{\text{B}} T}{B^2/(2\mu_0)} \tag{1.3}$$

where k_{B} is Boltzmann constant, and μ_0 is vacuum permeability. Since the cost of the fusion reactor increases with the confining B-field strength, β can be considered as an economic indicator of reactor efficiency. The detailed B-field structure determines the plasma shape (e.g., the elongation and triangularity of the cross-section), safety factor ($q = rB_{\text{toroidal}}/(RB_{\text{poloidal}})$) profile and current density profile, which all can impact the plasma-β [Taylor et al., 1994]. Plasma modes also affect the confinement and transport of the plasma particle, energy and momentum in tokamaks. For example, the Neoclassical Tearing Mode (NTM) [La Haye, 2006] is large scale magnetohydrodynamic (MHD) instability driven by current or pressure gradients. It can degrade the plasma confinement and often leads to disruption. The disruption results in enormous particle and energy flux striking the vacuum chamber, which is disastrous for reactor scale devices, e.g., ITER [Aymar et al., 2002]. Magnetic measurements of the NTM can assist physical understanding of the mode. Such measurements can also be used to monitor the growth of the mode and provide information to the mode suppression control.

However, the measurements of internal B-field in tokamaks are very challenging. Traditionally these measurements are performed using two diagnostics techniques: B-dot probes (i.e., Mirnov coils) and Motional Stark Effect (MSE) [Levinton et al., 1990; Wroblewski and Lao, 1992]. The B-dot probe diagnostic measures the electric potential induced by a time-varying B-field. This diagnostic uses physical probes, so measurements are limited to the edge or outer cool region of fusion plasmas. Therefore it is incapable of measuring the detailed spatial mode structure and internal magnetic fluctuation level. The MSE diagnostic measures the polarization of excited neutral beam D_α emission, which directly relates to the local B-field pitch angle at the emission region. It has been used as a workhorse for internal equilibrium B-field measurement. The main drawback is that its operation requires Neutral Beam Injection (NBI) and therefore it is categorized as an intrusive diagnostic.

Polarimetry [Segre, 1999; Soltwisch, 1992] enables direct, non-intrusive measurements with high temporal resolution of internal magnetic field equilibria [Braithwaite et al., 1989; Brower et al., 2002] and fluctuations [Ding et al., 2003], as well as plasma density [Fuchs and Hartfuss, 1998] and current density profiles [Soltwisch, 1986] in magnetically confined plasmas. This diagnostic utilizes the fact that the polarization of an electromagnetic (EM) wave ($\omega \gg \omega_p, \omega_c$) changes as it propagates through a magnetized plasma due to plasma birefringence and optical activity [Segre and Nowak, 1993; Segre, 1999]. By measuring the polarization properties before and after the propagation, the internal quantities can be determined (see Fig. 1.2).

The polarimetry diagnostic has been routinely used on conventional high aspect ratio tokamaks, e.g., Joint European Torus (JET) [Boboc et al., 2006], Alcator C-Mod [Bergerson et al., 2012], and reversed field pinches (RFPs), e.g., Madison Symmetric Torus (MST) [Brower et al., 2003]. However, no detailed study of polarimetry has been performed for propagation in the major radial direction in spherical tori. (A spherical torus holds the plasma in a B-field with lower aspect ratio (R_0/a), shaping it more like a “cored apple” than a “donut”, e.g., National Spherical Torus eXperiment (NSTX) [Ono et al., 2000] shown in Fig. 1.3. Compared

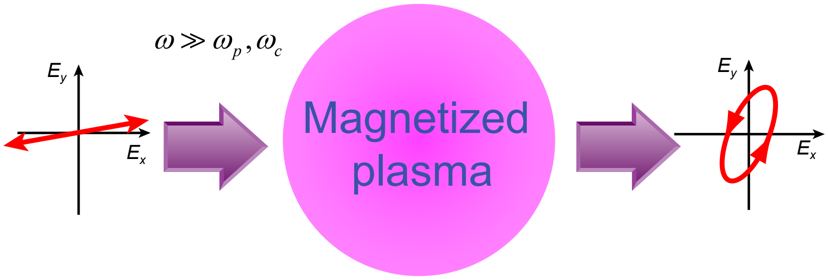

Figure 1.2: *Polarimetry diagnostic measures the polarizations of an EM-wave before and after it propagates through a magnetized plasma.* ω, ω_p, ω_c *are the probe EM-wave frequency, plasma frequency and cyclotron frequency, respectively.*

to conventional tokamaks, spherical tori can achieve higher plasma pressure for a given B-field, i.e., higher plasma-β; the field strength and shear also vary more strongly in the major radial direction.) Therefore, a 288 *GHz* polarimeter system was designed and fabricated at UCLA for installation on NSTX [Zhang et al., 2012], where it would have probed the plasma along a major radial chord using a retro-reflection geometry. However, an unexpected magnetic coil failure in 2011 resulted in the NSTX being shut down prematurely and work initiated on the NSTX-Upgrade device. In response to this failure, the polarimeter was transferred to the DIII-D tokamak [Luxon, 2002]. This allowed testing of the polarimeter system in preparation for future implementation on NSTX-Upgrade [Menard et al., 2012].

1.2 Major concepts–Faraday rotation & Cotton-Mouton effects

Magnetized plasmas modify polarization properties of EM-wave via two physical mechanisms: Faraday Rotation (FR) and Cotton-Mouton (CM, also known as

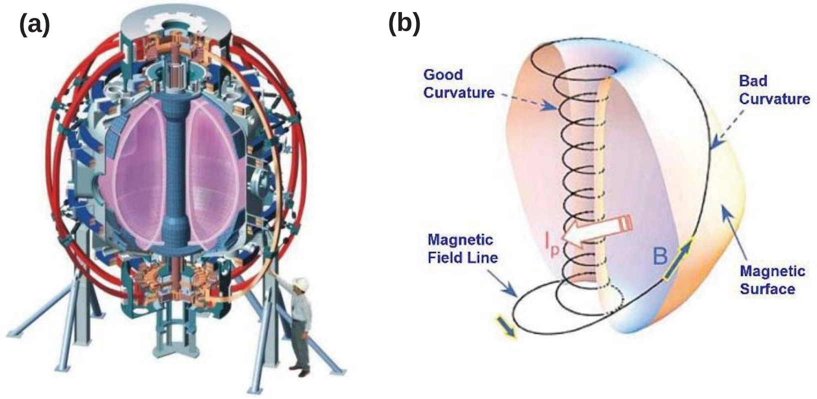

Figure 1.3: *Compared to conventional tokamaks: (a) NSTX holds the plasma in a tighter B-field, shaping it more like a "cored apple". (b) B-field strength and shear also vary more strongly in the major radial direction.*

Faraday conversion in Astronomy [Huang and Shcherbakov, 2011]) effects. The FR effect is the phenomenon where a linearly polarized wave rotates as it propagates along a B-field, i.e., $\vec{k} \parallel \vec{B}$ (see Fig. 1.4a). In this scenario, Left-hand Circular Polarization (LCP) & Right-hand Circular Polarization (RCP) waves are a pair of characteristic modes, which propagate at different phase velocities with their individual polarizations unchanged. The linearly polarized wave can be decomposed into equal power LCP & RCP components and the phase difference between them accumulates as the wave propagates. Since the LCP & RCP components have a modified relative phase, the resultant linear polarization presents a rotation in comparison to the initial polarization. The CM effect is the phenomenon where a linearly polarized wave can become elliptized as it propagates perpendicular to the B-field, i.e., $\vec{k} \perp \vec{B}$ (see Fig. 1.4b). In this case, linearly polarized X-mode & O-mode waves are the characteristic modes, with the X-mode having a slightly higher phase velocity. The phase difference accumulated between them along the propagation path causes elliptization of the initial linear polarization.

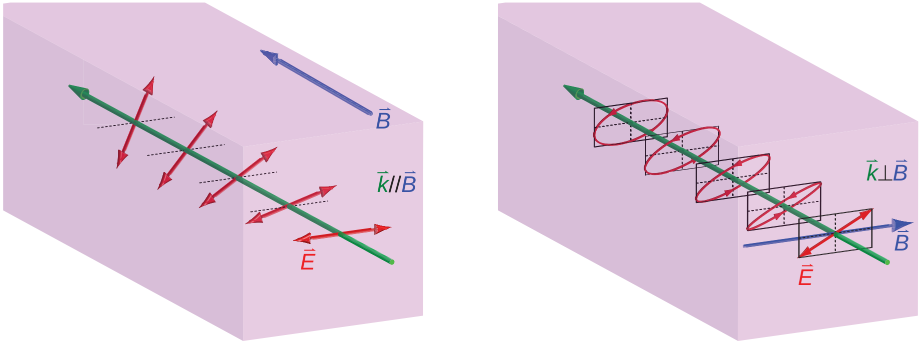

(a) ***(b)***

Figure 1.4: *Polarimetry effects in a magnetized plasma. (a) Faraday rotation effect causes a rotation of linearly polarized wave when* $\vec{k} \parallel \vec{B}$*. (b) Cotton-Mouton effect can cause a linearly polarized wave to become elliptized when* $\vec{k} \perp \vec{B}$*.*

In general cases where the wave propagates neither parallel nor perpendicular to the B-field, the plasma still has a pair of fast and slow characteristic modes at any position along the wave path. Their polarizations and phase velocities are determined by the local plasma parameters. The two modes are generally elliptically polarized with orthogonal polarization directions and opposite handedness. To be specific, the E-field ellipse of the fast characteristic mode has a major axis perpendicular to $\vec{B}_\perp$ and right-handedness with respect to $\vec{B}_\parallel$; the slow mode has a major axis parallel to $\vec{B}_\perp$ and left-handedness with respect to $\vec{B}_\parallel$. ('$\perp$' and '$\parallel$' are defined with respect to the propagation direction $\vec{k}$.) (see Fig. 1.5) An EM-wave of any polarization may be represented as some combination of this pair of characteristic modes. The recombined polarization is sensitive to the relative phase of its two components, so the phase difference accumulated along the wave propagation causes the combined polarization to change.

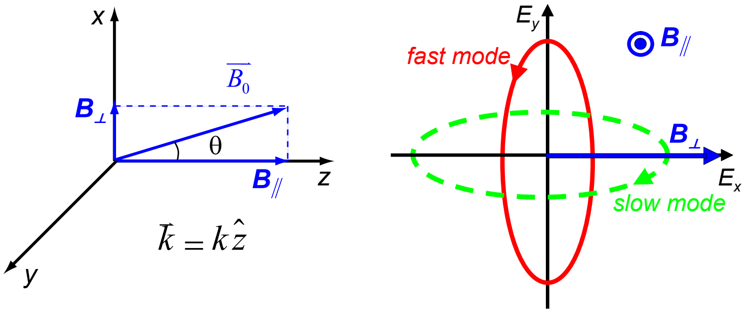

Figure 1.5: *Characteristic modes in a magnetized plasma. The fast mode (red solid ellipse) has a major axis perpendicular to $\vec{B}_\perp$ and right-handedness with respect to $\vec{B}_\parallel$; the slow mode (green dashed ellipse) has a major axis parallel to $\vec{B}_\perp$ and left-handedness with respect to $\vec{B}_\parallel$. ('$\perp$' and '$\parallel$' are defined with respect to the propagation direction $\vec{k}$.)*

As mentioned earlier, the tokamak B-field has a helical structure (see Fig. 1.1), and therefore for a probe beam propagating in a straight line both the FR and CM effects can occur since both $\vec{B}_\parallel$ and $\vec{B}_\perp$ components may be present. As will be discussed later, these two effects also interact with each other [Zhang et al., 2010]. The interaction can cause difficulties in interpretation of polarimetry measurements, especially in situations where neither effect is dominant. The line-integral nature of the diagnostic further increases the complication, since the FR and CM effects cannot be individually separated from the measurement which is made after propagation through the plasma. Therefore, numerical calculations are critical in assisting the design of polarimetry systems, as well as data interpretation.

1.3 Overview of the dissertation

1.3.1 Outline of the dissertation

The dissertation is organized as follows:

Chapter 1 presents motivation of the project and summarizes the topics and major results of the dissertation.

Chapter 2 briefly derives the polarimetry theory in a cold magnetized plasma. The Jones calculus and Mueller-Stokes calculus are reviewed.

Chapter 3 presents hardware design and initial tests of the 288 GHz polarimeter.

Chapter 4 describes a new synthetic diagnostic code and initial identification of the interaction between the FR and CM effects in a polarimetry modeling for NSTX.

Chapter 5 investigates the influence of the CM effect on polarimetry measurements via a dedicated equilibrium experiment on DIII-D. The possibility of polarimetry providing constrains to an equilibrium fitting code (EFIT) is also discussed.

Chapter 6 discusses the potential of measuring magnetic fluctuations via polarimetry. A sensitivity assessment of mm-wave polarimetry measuring the magnetic fluctuations associated with microtearing modes on NSTX-U is presented. The methodology of extracting magnetic fluctuation information from polarimetry measurements is discussed.

Chapter 7 presents conclusions of the dissertation. Future work of this project is also discussed.

1.3.2 Highlights of the dissertation

The 288 *GHz* polarimeter system launches a rotating linearly polarized beam and detects phase shifts directly related to the polarization changes caused by the plasma. Figure 1.6 presents the schematic of polarimeter layout, which can be conceptually divided into three sections: the source, quasi-optical, and receiver sections. As can be seen, a retro-reflection geometry along a major radius near midplane is used. The source employs a Single-Side-Band (SSB) modulation technique to generate a pair of orthogonally linearly polarized beams with a stable difference frequency. This pair of beams are then combined and converted to be counter-rotating, which creates the rotating linear launch. An essential quasi-optical isolation technique was developed to improve phase resolution by suppressing multi-reflections, which were identified as the major source of phase noise. Preliminary tests in the laboratory and on DIII-D indicated $< 2^\circ$ phase resolution in the frequency range of $f < 500$ *Hz*, and 0.3° in 500 *Hz* $< f < 500$ *kHz* were achieved. Detailed description of polarimeter hardware and initial tests are presented in Chapter 3.

A new synthetic diagnostic code based on Mueller-Stokes calculus (polarimetry theory in magnetized plasma is derived in Chapter 2) was developed to simulate the polarimeter response. It is a forward calculation code, taking inputs of density and B-field profiles along the diagnostic chord, and calculating the Mueller matrices along propagation path to evaluate the resultant detector output. This code has proven to be of great use in guiding the design of a polarimetry experiment where the plasma position is vertically scanned after its current reaches a flattop (see Section 4.4) and assisting in interpreting measurements. Interaction between the FR and CM effects was identified in a polarimetry modeling using a realistic NSTX equilibrium. This discovery directly motivated the design of a polarimetry experiment to study plasma equilibrium on the DIII-D tokamak. Detailed description of this synthetic diagnostic code is provided in Chapter 4.

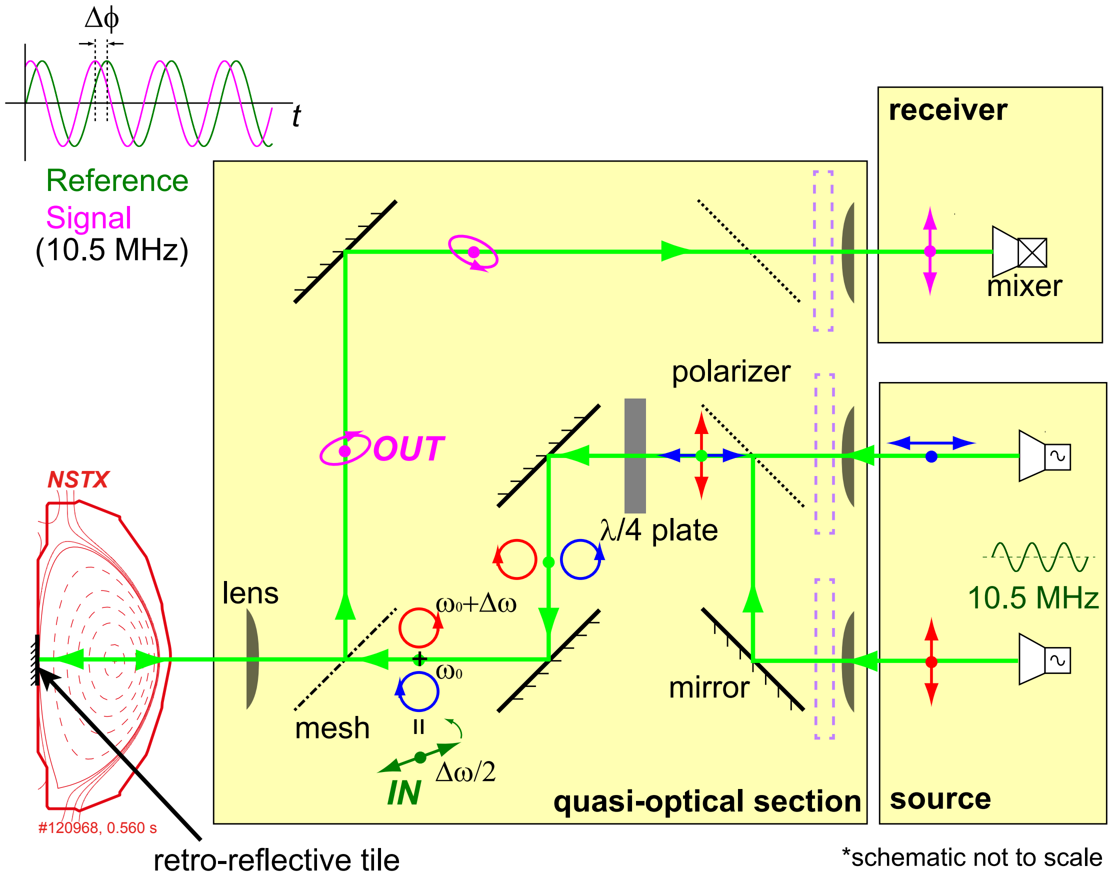

*schematic not to scale

Figure 1.6: *Schematic of quasi-optical design of 288 GHz polarimeter on NSTX. The green lines with arrows indicate beam propagation. Double-arrows, circles, and ellipses represent the polarization of mm-wave beam (in wave frame of reference, i.e., looking in the direction of wave source) at the corresponding positions.*

Prior to future implementation on NSTX-U, the polarimeter was prototyped on

DIII-D, where the CM effect is expected to be much stronger (typical $B_T \sim 2.0\ T$ versus $B_T \sim 0.5\ T$ on NSTX), and therefore the interaction between the FR and CM effects is expected to be significant. This offered a useful opportunity to investigate the influence of the CM effect on polarimetry measurements. Figure 1.7 shows time traces of experimental polarimetry phase measurements together with Mueller-Stokes theory predictions for two shots in the specially designed plasma equilibrium experiment. Both shots have the same vertical scan starting at 1000 *ms*. The theory (black curve)–experiment (green curve) comparison achieved very good agreement over a broad range of plasma conditions. (More plasma conditions are presented later.) This agreement validates Mueller-Stokes theory and builds confidence in use of the synthetic diagnostic code in data interpretation. In Fig. 1.7(a), the measurements (green curve) are well approximated by the FR-only calculations (red curve) when the CM effect is predicted to be weak. However, as the CM effect increases at stronger B_T, it can compete with the FR effect in rotating the polarization of the EM-wave. This results in an apparent reduction in polarimeter response to the FR effect, just as observed in the experiment. It is also found that if sufficiently large, the CM effect can even reverse the handedness of a wave launched with circular polarization. This helps to understand the experimental observations that the sensitivity to the FR effect can be nearly eliminated at $B_T = 2.0\ T$ (see Fig. 1.7b). The results also suggest that the CM effect on the plasma mid-plane can be potentially exploited to measure magnetic shear in tokamak plasmas. Detailed discussion of polarimetry contributions to plasma equilibrium study is presented in Chapter 5.

The potential of this 288 *GHz* polarimeter to measure the magnetic fluctuations is explored via both modeling and experiment. For example, simulations suggest that the microtearing modes in NSTX-U will induce $\gtrsim 2°$ ($f \sim 10\ kHz$) variations

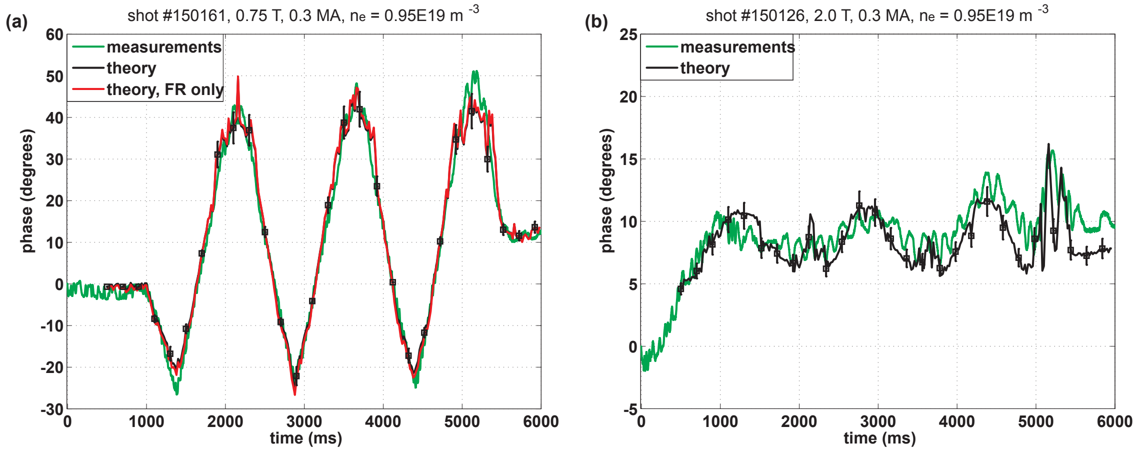

Figure 1.7: *Time traces of polarimetry phase of experimental measurements and Mueller-Stokes theory predictions for two shots. The shots have the same vertical scan starting at* 1000 *ms. The green curve is the measured phase below* 500 *Hz (phase resolution* $< 2°$*). The black curve is the calculated phase (every* 20 *ms) from the synthetic diagnostic code based on the theory.* $\sim 10\%$ *error bars are also indicated. The red curve is the calculated phase including only the FR effect. (a) Low* B_T *(*0.75 *T) case; (Note that the green, black, and red curves almost overlie each other.) (b) high* B_T *(*2.0 *T) case.*

in polarimeter phase (see Fig. 1.8) [Zhang et al., 2013a]. In a similar situation where the FR effect is dominant, it is relatively straightforward to estimate the magnitude of the density-weighted magnetic fluctuations (line-averaged and weighted by equilibrium density). Figure 1.9 presents the power spectral density of the normalized magnetic fluctuation ($\tilde{B}_R/B_0 \approx 1 \times 10^{-4}$) in a low density shot developed in the runaway electron experiment on DIII-D. However, in situations where the interaction between the FR and CM effects plays an important role, information from other diagnostics (especially density fluctuation measurements, e.g., beam emission spectroscopy, reflectometry) and theoretical modeling are required to extract the magnetic fluctuation information. Detailed discussion is presented in Chapter 6.

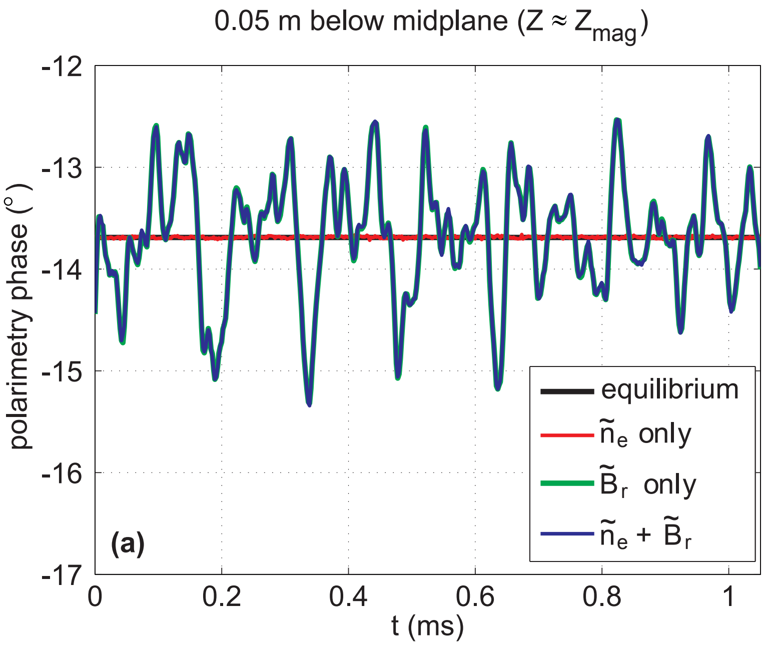

Figure 1.8: *Simulated polarimetry phase response to microtearing modes for a beam horizontally propagating across the plasma magnetic axis. Black horizontal line shows the equilibrium phase; red curve shows the fluctuating phase with only density fluctuations ($\tilde{n}_e$) included; green curve includes only radial magnetic fluctuations ($\tilde{B}_r$); blue curve includes both density and magnetic fluctuations ($\tilde{n}_e + \tilde{B}_r$). Note the blue curve almost overlies the green curve and the red curve only shows very weak variations around the black horizontal line.*

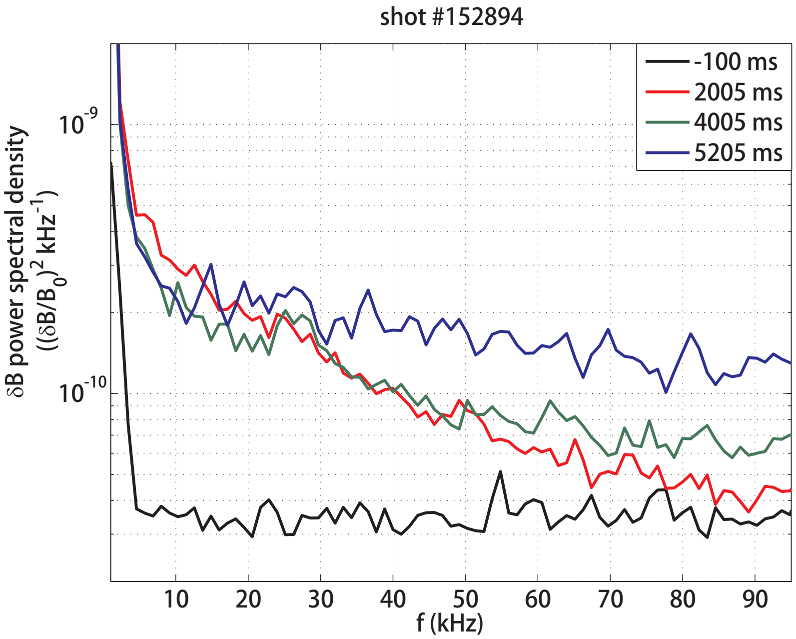

Figure 1.9: *Density-weighted magnetic fluctuation data measured by 288 GHz polarimeter for a DIII-D shot (#152894) in quiescent runaway electron experiment. The fluctuation measurement (−100 ms) prior to plasma breakdown is also included as an instrumental noise floor.*

CHAPTER 2

Polarimetry in magnetized plasmas

The polarimetry theory based on a cold plasma model captures the essential polarimetry effects in magnetized plasmas, which characterizes how the polarization of an EM-wave evolves during propagation. Jones calculus [Henry Hurwitz and Jones, 1941; Jones, 1941a,b, 1942, 1947a,b, 1948] and Mueller-Stokes calculus [McMaster, 1954] have been used to represent the polarization and its evolution. This chapter first reviews the general dispersion relation of EM-wave in plasmas. Appleton-Hartree equation is derived for high-frequency EM-wave propagation in a magnetized plasma. Then the two calculuses are reviewed and their relationship is presented.

2.1 General derivation of dispersion relation in plasmas

Consider an EM-wave propagating in a plasma. The wave E-field and B-field satisfy Maxwell's equations:

$$\begin{cases} \vec{\nabla} \times \vec{E} = -\dfrac{\partial \vec{B}}{\partial t} \\ \\ \vec{\nabla} \times \vec{B} = \mu_0 \varepsilon_0 \dfrac{\partial \vec{E}}{\partial t} + \mu_0 \vec{J} \end{cases} \tag{2.1}$$

The current $\vec{J}$ is the plasma response to the wave E-field. It follows Ohm's law:

$$\vec{J} = \overleftrightarrow{\sigma}_{3\times 3} \cdot \vec{E} \tag{2.2}$$

where $\overleftrightarrow{\sigma}_{3\times3}$ is the conductivity tensor, since the plasma is normally anisotropic, especially in the presence of a B-field.

The following is resulted by combining the above equations:

$$\vec{\nabla} \times (\vec{\nabla} \times \vec{E}) = (-\mu_0\varepsilon_0\frac{\partial^2}{\partial t^2} - \mu_0\overleftrightarrow{\sigma} \cdot \frac{\partial}{\partial t})\vec{E} \tag{2.3}$$

For the EM-wave with temporal dependence as $\vec{E} \propto e^{-i\omega t}$, thereby $\dfrac{\partial}{\partial t} \rightarrow -i\omega$, the above equation becomes:

$$\vec{\nabla} \times (\vec{\nabla} \times \vec{E}) = k_0^2\overleftrightarrow{\varepsilon} \cdot \vec{E} \tag{2.4}$$

where $k_0 \equiv \omega/c$; and the dielectric tensor is defined as:

$$\overleftrightarrow{\varepsilon}_{3\times3} \equiv \overleftrightarrow{I}_{3\times3} + \frac{i}{\omega\varepsilon_0}\overleftrightarrow{\sigma}_{3\times3} \tag{2.5}$$

If the plasma is considered to be uniform within the spatial scale of a few wavelengths (i.e., WKB approximation [Swanson, 2003]), a spatial dependence as $\vec{E} \propto e^{i\vec{k}\cdot\vec{r}}$ can be assumed, and correspondingly $\vec{\nabla} \rightarrow i\vec{k}$, then Eqn. 2.4 can be rewritten as:

$$\left(k^2\overleftrightarrow{I} - \vec{k}\vec{k} - k_0^2\overleftrightarrow{\varepsilon}\right) \cdot \vec{E} = 0 \tag{2.6}$$

The requirement for non-zero solutions of the wave E-field gives the dispersion relation:

$$\det\left(k^2\overleftrightarrow{I} - \vec{k}\vec{k} - k_0^2\overleftrightarrow{\varepsilon}\right) = 0 \tag{2.7}$$

and the eigenvectors of the matrix in Eqn. 2.6 correspond to the characteristic modes that maintain their polarizations during propagation.

2.2 Appleton-Hartree equation for high-frequency EM-wave propagation in a magnetized plasma

In the case of high-frequency EM-wave propagation ($\omega \gg \omega_{pe}, \omega_{ce} \gg \omega_{pi}, \omega_{ci}$, where the plasma frequency $\omega_p = \sqrt{nq^2/m\varepsilon_0}$, the cyclotron frequency $\omega_c = |q|B/m$, and subscripts 'i' and 'e' represent ions and electrons respectively), the plasma can be considered as an electron gas with the ions treated as a smooth continuous background charge distribution, i.e., a Lorentz plasma. With these assumptions, the dispersion relation of the EM-wave is expressed by Appleton-Hartree equation [Appleton, 1924; Hartree, 1931; Heald, 1978; Hutchinson, 2005; Stix, 1962]. The derivation is briefly reviewed below.

In a Cartesian coordinate system where $\hat{z} \parallel \vec{k}$ and $\vec{B}_0$ is in xz-plane (see Fig. 2.1a), the EM-wave E-field is $\vec{E} = \vec{E}_0 \operatorname{Re}\{\exp[i(kz - \omega t)]\}$. Equation 2.6 can be expressed as:

$$\begin{pmatrix} N^2 - \varepsilon_{xx} & -\varepsilon_{xy} & -\varepsilon_{xz} \\ -\varepsilon_{yx} & N^2 - \varepsilon_{yy} & -\varepsilon_{yz} \\ -\varepsilon_{zx} & -\varepsilon_{zy} & -\varepsilon_{zz} \end{pmatrix} \begin{pmatrix} E_x \\ E_y \\ E_z \end{pmatrix} = 0 \tag{2.8}$$

where $N \equiv |k|/|k_0|$ is the refractive index.

Express E_z in terms of E_x and E_y from the z component and then substitute into the x and y components. This reduces Eqn. 2.8 to 2-D:

$$\begin{gathered} \begin{pmatrix} N^2 - \eta_{xx} & -\eta_{xy} \\ -\eta_{yx} & N^2 - \eta_{yy} \end{pmatrix} \begin{pmatrix} E_x \\ E_y \end{pmatrix} = 0 \\ \eta_{ij} = \varepsilon_{ij} - \frac{\varepsilon_{iz}\varepsilon_{zj}}{\varepsilon_{zz}}, \quad i, j \in \{1, 2\}; 1 \sim `x', 2 \sim `y' \end{gathered} \tag{2.9}$$

Both ε_{ij} and η_{ij} are Hermitian matrices, with real diagonal elements and purely imaginary off-diagonal elements .

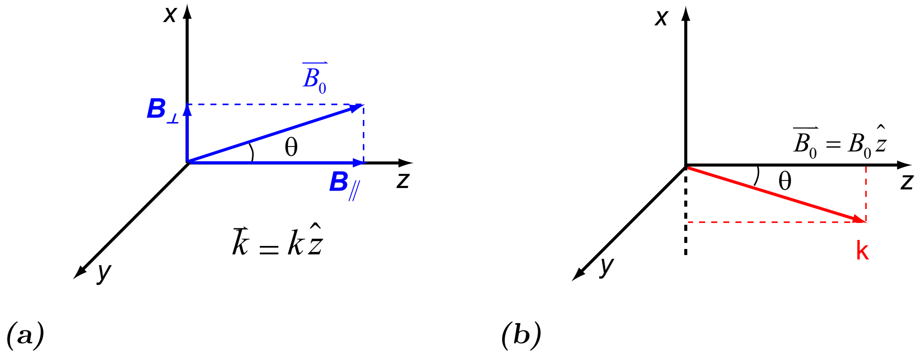

Figure 2.1: *Two definitions of Cartesian coordinate system. (a) $\hat{z} \parallel \vec{k}$; $\vec{B}_0$ in xz-plane. (b) $\hat{z} \parallel \vec{B}_0$; $\vec{k}$ in xz-plane.*

The refractive indices of the pair of characteristic modes discussed in Chapter 1 (“slow”∼‘1’,‘+’; “fast”∼‘2’,‘−’) can then be determined:

$$\begin{aligned} &\begin{vmatrix} N^2 - \eta_{xx} & -\eta_{xy} \\ -\eta_{yx} & N^2 - \eta_{yy} \end{vmatrix} = 0 \\ \Rightarrow \quad & N^4 - (\eta_{xx} + \eta_{yy})N^2 + \eta_{xx}\eta_{yy} - |\eta_{xy}|^2 = 0 \\ \Rightarrow \quad & N^2_{1,2} = \frac{1}{2}\left[(\eta_{xx} + \eta_{yy}) \pm \sqrt{(\eta_{xx} - \eta_{yy})^2 + 4|\eta_{xy}|^2}\right] \end{aligned} \tag{2.10}$$

The elements of dielectric tensor $\overleftrightarrow{\varepsilon}$ can be derived in a straightforward manner by first considering its form in a coordinate system where $\hat{z} \parallel \vec{B}_0$ and $\vec{k}$ is in xz-plane (see Fig. 2.1b). In this coordinate system:

$$\begin{aligned}\overleftrightarrow{\varepsilon}' &= \begin{pmatrix} 1-\dfrac{X}{1-Y^2} & i\dfrac{XY}{1-Y^2} & 0 \\ -i\dfrac{XY}{1-Y^2} & 1-\dfrac{X}{1-Y^2} & 0 \\ 0 & 0 & 1-X \end{pmatrix} \\ &= \overleftrightarrow{I} - \frac{X}{1-Y^2}\begin{pmatrix} 1 & -iY & 0 \\ iY & 1 & 0 \\ 0 & 0 & 1-Y^2 \end{pmatrix}\end{aligned} \tag{2.11}$$

where $X \equiv {\omega_{pe}}^2/\omega^2$, $Y \equiv \omega_{ce}/\omega$ [Hutchinson, 2005].

To convert the expression to the coordinate system where $\hat{z} \parallel \vec{k}$ and $\vec{B}_0$ is in xz-plane (see Fig. 2.1a), a rotation operation around $\hat{y}$-axis is applied:

$$\begin{aligned}\overleftrightarrow{\varepsilon} &= \overleftrightarrow{R}_y(\theta)\overleftrightarrow{\varepsilon}'\overleftrightarrow{R}_y^{-1}(\theta) \\ &= \overleftrightarrow{I} - \frac{X}{1-Y^2}\begin{pmatrix} 1-Y^2\sin^2\theta & -iY\cos\theta & Y^2\sin\theta\cos\theta \\ iY\cos\theta & 1 & iY\sin\theta \\ Y^2\sin\theta\cos\theta & -iY\sin\theta & 1-Y^2\cos^2\theta \end{pmatrix}\end{aligned} \tag{2.12}$$

where $\overleftrightarrow{R}_y(\theta)$ is the matrix that can rotate a vector around $\hat{y}$-axis counterclockwise by an angle of θ, which is the angle between $\vec{k}$ and $\vec{B}_0$.

$$\overleftrightarrow{R}_y(\theta) = \begin{pmatrix} \cos\theta & 0 & -\sin\theta \\ 0 & 1 & 0 \\ \sin\theta & 0 & \cos\theta \end{pmatrix} \tag{2.13}$$

Substitute the elements of $\overleftrightarrow{\varepsilon}$ into Eqn. 2.10. The Appleton-Hartree equation can be written as ($N_1 > N_2$):

$$N_{1,2}^2 = 1 - \frac{2X(1-X)}{2(1-X) - Y^2\sin^2\theta \pm \sqrt{Y^4\sin^4\theta + 4Y^2(1-X)^2\cos^2\theta}} \tag{2.14}$$

In the limit of $\theta \to \pi/2$, Eqn. 2.14 gives the dispersion relation for the familiar O- & X- modes; in the limit of $\theta \to 0$, Eqn. 2.14 becomes the dispersion relation for the LCP & RCP modes. The 2×1 transverse E-field vectors (components perpendicular to $\vec{k}$) corresponding to the two indices give the polarization of characteristic modes.

2.3 Jones calculus

In Jones calculus [Henry Hurwitz and Jones, 1941; Jones, 1941a,b, 1942, 1947a,b, 1948], the polarization of an EM-wave is expressed by the transverse E-field in the coordinate system in Fig. 2.1a:

$$\vec{E} = \begin{pmatrix} E_x \\ E_y \end{pmatrix} = \begin{pmatrix} a_x e^{i\delta_x} \\ a_y e^{i\delta_y} \end{pmatrix} = \sqrt{a_x^2 + a_y^2} e^{i\delta_x} \begin{pmatrix} \cos\alpha \\ \sin\alpha e^{i\delta} \end{pmatrix} , \quad \begin{cases} \tan\alpha \equiv a_y/a_x, & \alpha \in [0, \pi/2] \\ \delta \equiv \delta_y - \delta_x, & \delta \in (-\pi, \pi] \end{cases} \tag{2.15}$$

The wave E-field during propagation evolves according to the relation:

$$\vec{E}(z) = \overleftrightarrow{\mathbf{J}}(z) \cdot \vec{E}(0) \tag{2.16}$$

The 2×2 matrix $\overleftrightarrow{\mathbf{J}}(z)$ is called Jones matrix. Its expression will be derived below.

The pair of characteristic modes define the base vectors ("slow"∼'s',"fast"∼'f'):

$$\hat{E}_s = \begin{pmatrix} \cos\alpha_s \\ \sin\alpha_s e^{i\delta_s} \end{pmatrix} , \quad \hat{E}_f = \begin{pmatrix} \cos\alpha_f \\ \sin\alpha_f e^{i\delta_f} \end{pmatrix} \tag{2.17}$$

which are normalized and orthogonal to each other:

$$\begin{cases} \hat{E}_{s,f}^\dagger \cdot \hat{E}_{s,f} & = 1 \\ \hat{E}_{s,f}^\dagger \cdot \hat{E}_{f,s} & = 0 \end{cases} \tag{2.18}$$

Any E-field can be decomposed into this pair of base vectors:

$$\begin{aligned} \vec{E} &= A_s\hat{E}_s + A_f\hat{E}_f \ , \\ A_{s,f} &= \hat{E}^{\dagger}_{s,f} \cdot \vec{E} \end{aligned} \tag{2.19}$$

In the WKB limit, the magnetized plasma can be considered as a birefringent medium. Within an infinitesimal plasma slab, which is thick compared to the wavelength but thin compared to equilibrium gradients, the characteristic modes propagate with unchanged polarization and evolving phase:

$$\begin{cases} \hat{E}_{s,f}(z+\mathrm{d}z) = \hat{E}_{s,f}(z) \\ A_{s,f}(z+\mathrm{d}z) = e^{i\mathrm{d}\delta_{\mathrm{xs,xf}}} A_{s,f}(z) \end{cases} \tag{2.20}$$

Note that $\mathrm{d}\delta_{\mathrm{xs}}$ means the change in the absolute phase of the slow characteristic mode, i.e., the common phase of E_x and E_y in Eqn. 2.15; and correspondingly $\mathrm{d}\delta_{\mathrm{xf}}$ is the change in the fast mode absolute phase. Also note that "snapshot" approach is adopted here, i.e., partial derivative is taken with respect to z:

$$\begin{aligned} \delta_{\mathrm{xs,xf}}(z,t) &= \int_0^z k_{\mathrm{s,f}}(z')\mathrm{d}z' - \omega t \\ \frac{\partial \delta_{\mathrm{xs,xf}}}{\partial z} &= k_{\mathrm{s,f}}(z) = N_{\mathrm{s,f}}(z)\frac{\omega}{c} \end{aligned} \tag{2.21}$$

Evolution of the polarization within the plasma slab can be expressed as:

$$\begin{aligned} \vec{E}(z+\mathrm{d}z) &= A_s(z+\mathrm{d}z)\hat{E}_s(z+\mathrm{d}z) + A_f(z+\mathrm{d}z)\hat{E}_f(z+\mathrm{d}z) \\ &= e^{i\mathrm{d}\delta_{\mathrm{xs}}} A_s(z)\hat{E}_s(z) + e^{i\mathrm{d}\delta_{\mathrm{xf}}} A_f(z)\hat{E}_f(z) \\ &= e^{i\mathrm{d}\delta_{\mathrm{xs}}} \hat{E}_s\hat{E}^{\dagger}_s \cdot \vec{E} + e^{i\mathrm{d}\delta_{\mathrm{xf}}} \hat{E}_f\hat{E}^{\dagger}_f \cdot \vec{E} \\ &= \overleftrightarrow{P}\,\overleftrightarrow{K}\,\overleftrightarrow{P}^{\dagger} \cdot \vec{E} \\ &= \overleftrightarrow{\mathcal{J}}(z) \cdot \vec{E}(z) \end{aligned} \tag{2.22}$$

$$
\begin{aligned}
\overleftrightarrow{P} &\equiv \left(\hat{E}_s, \hat{E}_f\right) = \begin{pmatrix} \cos\alpha_s & \cos\alpha_f \\ \sin\alpha_s e^{i\delta_s} & \sin\alpha_f e^{i\delta_f} \end{pmatrix} \\
\overleftrightarrow{K} &\equiv \begin{pmatrix} e^{i\mathrm{d}\delta_{\mathrm{xs}}} & 0 \\ 0 & e^{i\mathrm{d}\delta_{\mathrm{xf}}} \end{pmatrix} = e^{i\mathrm{d}\delta_{\mathrm{comm}}} \begin{pmatrix} e^{i\mathrm{d}\delta_{\mathrm{diff}}/2} & 0 \\ 0 & e^{-i\mathrm{d}\delta_{\mathrm{diff}}/2} \end{pmatrix}
\end{aligned}
\tag{2.23}
$$

where

$$
\begin{cases} \mathrm{d}\delta_{\mathrm{comm}} = \left(\mathrm{d}\delta_{\mathrm{xs}} + \mathrm{d}\delta_{\mathrm{xf}}\right)/2 \\ \mathrm{d}\delta_{\mathrm{diff}} = \mathrm{d}\delta_{\mathrm{xs}} - \mathrm{d}\delta_{\mathrm{xf}} \end{cases}
\tag{2.24}
$$

and the Jones matrix for this slab is:

$$
\overleftrightarrow{\mathcal{J}}(z) = \overleftrightarrow{P}\,\overleftrightarrow{K}\,\overleftrightarrow{P}^{\dagger}
\tag{2.25}
$$

The plasma from 0 to z along wave path can be viewed as a stack of multiple plasma slabs of thickness $\mathrm{d}z_0, \mathrm{d}z_1, \ldots, \mathrm{d}z_{N-1}, \mathrm{d}z_N$ at position $z_0 = 0, z_1, \ldots, z_{N-1}$, $z_N = z$, respectively [Soltwisch, 1993], i.e.,

$$
\begin{cases} z_0 = 0 \\ z_j = \sum_{i=0}^{j-1} \mathrm{d}z_i, \quad j \in \{2, 3, \ldots, N\} \\ z_N = z \end{cases}
\tag{2.26}
$$

The plasma parameters are assumed to be slow varying (i.e., WKB approximation) between slabs, so reflections at the interface between slabs can be ignored. Therefore the total Jones matrix for the plasma from 0 to z can be derived from the slab model:

$$
\begin{aligned}
\overleftrightarrow{\mathbf{J}}(z) &= \prod_{j=0}^{N-1} \overleftrightarrow{\mathcal{J}}(z_j) \\
&= \overleftrightarrow{\mathcal{J}}(z_{N-1})\,\overleftrightarrow{\mathcal{J}}(z_{N-2}) \ldots \overleftrightarrow{\mathcal{J}}(z_1)\,\overleftrightarrow{\mathcal{J}}(z_0)
\end{aligned}
\tag{2.27}
$$

2.4 Mueller-Stokes calculus

Mueller-Stokes calculus [McMaster, 1954; Segre, 1999] can also be utilized to calculate the polarization of an EM-wave as it propagates through a magnetized plasma. It uses the Stokes vector, $\vec{s}$, in an abstract 4-D vector space, to represent the polarization.

$$\begin{aligned}\vec{s} &= \begin{pmatrix} s_0 \\ s_1 \\ s_2 \\ s_3 \end{pmatrix} = \begin{pmatrix} I_{\text{total}} \\ I_{0^\circ} - I_{90^\circ} \\ I_{+45^\circ} - I_{-45^\circ} \\ I_{\text{RCP}} - I_{\text{LCP}} \end{pmatrix} = s_0 \begin{pmatrix} 1 \\ \cos 2\chi \cos 2\psi \\ \cos 2\chi \sin 2\psi \\ \sin 2\chi \end{pmatrix} \\ &= \begin{pmatrix} a_x^2 + a_y^2 \\ a_x^2 - a_y^2 \\ 2a_x a_y \cos\delta \\ 2a_x a_y \sin\delta \end{pmatrix} = \left(a_x^2 + a_y^2\right) \begin{pmatrix} 1 \\ \cos 2\alpha \\ \sin 2\alpha \cos\delta \\ \sin 2\alpha \sin\delta \end{pmatrix}\end{aligned} \tag{2.28}$$

where $I_{\text{total}} = s_0 = \sqrt{s_1^2 + s_2^2 + s_3^2} = a_x^2 + a_y^2$; I means intensity; the notation 'I_θ' means the power of a detector would measure if it is setup to detect the linear polarization along θ direction; the notation 'I_{LCP}' & 'I_{RCP}' means the measured power for LCP & RCP detection, respectively. (Detailed detection setups are presented in Appendix A.5.) The polarization ellipse is depicted in Fig. 2.2. ψ and χ are the angles corresponding to the polarization direction and elliptization, respectively. $\{\psi,\chi\}$ is another pair of characterizing parameters, and one-to-one maps to the parameter pair $\{\alpha,\delta\}$, which is described in Section 2.3. The definition domains of these parameters are:

$$\begin{cases} \psi \in (-\frac{\pi}{2}, \frac{\pi}{2}] \\ \chi \in [-\frac{\pi}{4}, \frac{\pi}{4}] \end{cases}, \quad \begin{cases} \alpha \in [0, \frac{\pi}{2}] \\ \delta \in (-\pi, \pi] \end{cases} \tag{2.29}$$

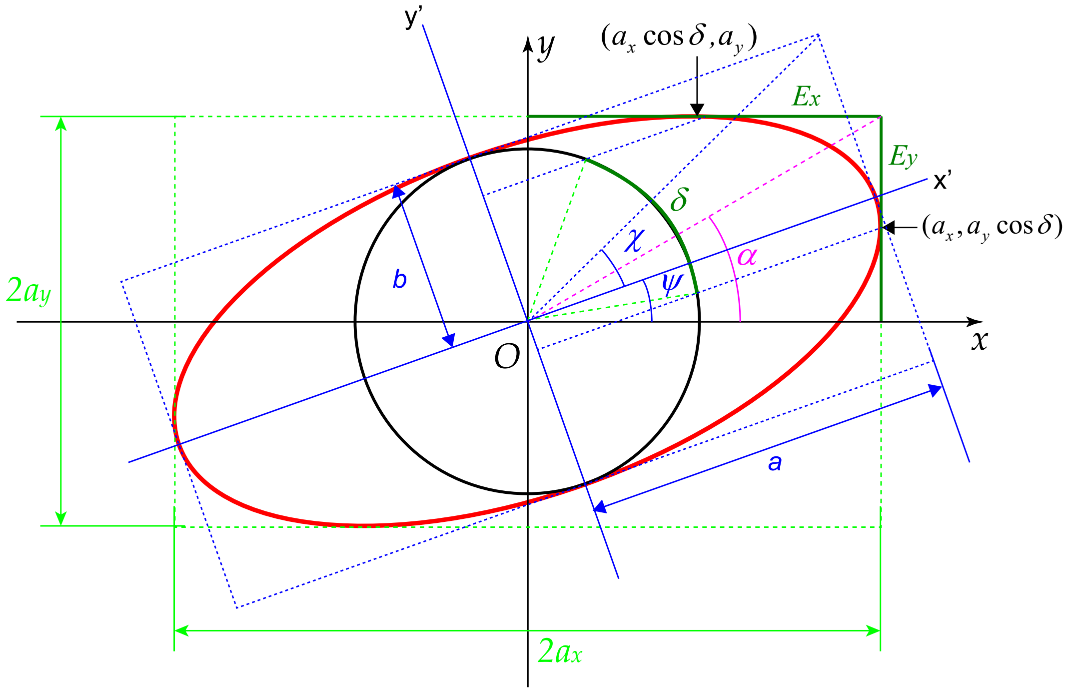

Figure 2.2: *Polarization ellipse and definition of angles.* $a^2 + b^2 = a_x^2 + a_y^2$

The polarization evolution follows:

$$\vec{s}(z)_{4\times1} = \overleftrightarrow{\mathbf{M}}(z)_{4\times4} \cdot \vec{s}(0)_{4\times1} \tag{2.30}$$

where z is the path parameter along propagation and $\overleftrightarrow{\mathbf{M}}$ is Mueller matrix. With knowledge of Mueller matrices along the path, the polarization evolution of the EM-wave can be fully characterized.

The analysis can be further simplified using additional assumptions. The high-frequency EM-wave is assumed to experience no dissipation due to collision, and absorption at cyclotron resonances is neglected, i.e., $s_0 \equiv 1$. The corrections from finite temperature effects are also excluded: the dispersive nonrelativistic corrections caused by the Doppler effect can be ignored by the fact that the phase velocity of the high-frequency EM-wave is close to the speed of light, much higher than the electron thermal velocity; the relativistic nondispersive contributions caused by relativistic mass dependence on the velocity is also ignored [Mirnov et al., 2007; Segre and Zanza, 2002]. With these assumptions, Eqn. 2.30 is reduced to 3-D:

$$\vec{s}(z)_{3\times 1} = \overleftrightarrow{\mathbf{M}}(z)_{3\times 3} \cdot \vec{s}(0)_{3\times 1} \tag{2.31}$$

where the 3×1 Stokes vector is:

$$\vec{s}_{3\times 1} = \begin{pmatrix} s_1 \\ s_2 \\ s_3 \end{pmatrix} = \begin{pmatrix} \cos 2\chi \cos 2\psi \\ \cos 2\chi \sin 2\psi \\ \sin 2\chi \end{pmatrix} = \begin{pmatrix} \cos 2\alpha \\ \sin 2\alpha \cos \delta \\ \sin 2\alpha \sin \delta \end{pmatrix} \tag{2.32}$$

This definition maps the polarization to a point on the Poincaré sphere, which is a unit sphere in an abstract 3-D space (see Fig. 2.3a). Orthogonal polarizations are mapped to opposing poles on the sphere, e.g., horizontal & vertical linear polarizations are the s_1 poles, and LCP & RCP are the s_3 poles.

The 3×3 Mueller matrix is:

$$\overleftrightarrow{\mathbf{M}}_{3\times 3} = \begin{pmatrix} M_{11} & M_{12} & M_{13} \\ M_{21} & M_{22} & M_{23} \\ M_{31} & M_{32} & M_{33} \end{pmatrix} \tag{2.33}$$

Note that this Mueller matrix is an orthogonal matrix. A short proof is as follows:

$$\begin{aligned} & s_j = M_{jm} s_m \\ \Rightarrow\ & s_j s_j = M_{jm} s_m M_{jn} s_n = M_{jm} M_{jn} s_m s_n = \delta_{mn} s_m s_n \\ \Rightarrow\ & M_{jm} M_{jn} = \delta_{mn} \\ \Rightarrow\ & \overleftrightarrow{\mathbf{M}}^T = \overleftrightarrow{\mathbf{M}}^{-1} \end{aligned} \tag{2.34}$$

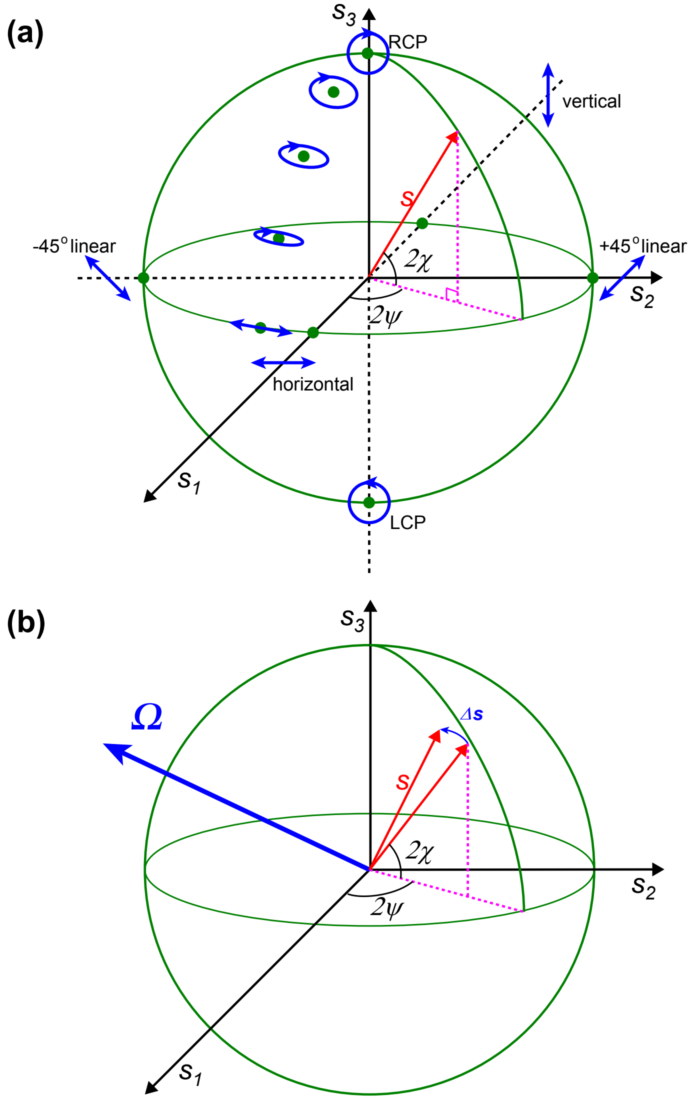

Figure 2.3: *(a) Stokes vector maps a polarization to a point on Poincaré sphere. (b) In Mueller-Stokes calculus, a step of polarization evolution ($\Delta\vec{s}$) is described as a small rotation of the Stokes vector $\vec{s}$ aound the axial vector $\vec{\Omega}$.*

Einstein summation convention is adopted here, i.e., when an index variable appears twice in a single term it implies summation of that term over all the values of the index. Therefore a Mueller matrix has only 3 independent elements (9 elements with 6 constraints). If the elements $\{M_{11}, M_{21}, M_{12}\}$ are known, the complete 3×3 matrix can be determined (see Appendix A.5).

Relationships between the two pairs of characterizing parameters $\{\psi,\chi\}$ and $\{\alpha, \delta\}$ can also be easily derived from Eqn. 2.32. For example, the ratio of s_3/s_2 from the two expressions using the two parameter pairs results in the following relation:

$$\tan 2\chi = \sin 2\psi \tan \delta \tag{2.35}$$

2.4.1 Differential form of Stokes vector evolution

In differential form the evolution of a Stokes vector also follows the ODE equation [Segre, 1999; Zienkiewicz et al., 1998]:

$$\frac{\mathrm{d}\vec{s}(z)}{\mathrm{d}z} = \vec{\Omega}(z) \times \vec{s}(z) \tag{2.36}$$

where $\vec{\Omega}(z)$ is related to local plasma parameters in the coordinate system in Fig. 2.4:

$$\vec{\Omega} = \frac{\omega_{pe}^2}{(N_1+N_2)c\omega^3\left[1-\left(\dfrac{e}{\omega m_e}\right)^2\left(\dfrac{B_x^2+B_y^2}{1-X}+B_z^2\right)\right]}\begin{pmatrix}\left(\dfrac{e}{m_e}\right)^2\left(\dfrac{B_x^2-B_y^2}{1-X}\right)\\ \left(\dfrac{e}{m_e}\right)^2\left(\dfrac{2B_xB_y}{1-X}\right)\\ 2\omega\dfrac{e}{m_e}B_z\end{pmatrix} \tag{2.37}$$

A step in polarization evolution corresponds to a small rotation of the Stokes vector with respect to the axial vector $\vec{\Omega}$ on Poincaré sphere (see Fig. 2.3b).

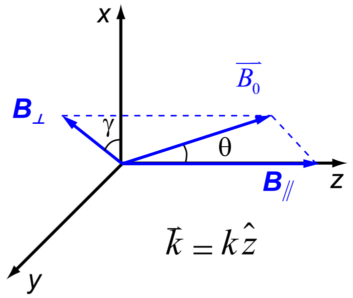

Figure 2.4: *Cartesian coordinate system where $\hat{z} \parallel \vec{k}$, and $\vec{B}_\perp$ forms an angle $\gamma \in (-\pi, \pi]$ with respect to $\hat{x}$.*

The individual FR and CM effect strength is defined as the integral of the expression [Guenther, 2004]:

$$\begin{cases} \dfrac{\mathrm{d}_{\mathrm{FR}}\psi}{\mathrm{d}z} = \dfrac{1}{2}\Omega_3 \xrightarrow{\omega_{pe}/\omega\to 0,\omega_{ce}/\omega\to 0} -C_{\mathrm{FR}}\lambda^2 n_e B_\parallel \\ \dfrac{\mathrm{d}_{\mathrm{CM}}\delta}{\mathrm{d}z} = \sqrt{\Omega_1^2+\Omega_2^2} \xrightarrow{\omega_{pe}/\omega\to 0,\omega_{ce}/\omega\to 0} C_{\mathrm{CM}}\lambda^3 n_e B_\perp^2 \end{cases} \tag{2.38}$$

and the integral forms are:

$$\begin{cases} \Delta_{\mathrm{FR}}\psi = \displaystyle\int \frac{\mathrm{d}_{\mathrm{FR}}\psi}{\mathrm{d}z}\mathrm{d}z \\ \Delta_{\mathrm{CM}}\delta = \displaystyle\int \frac{\mathrm{d}_{\mathrm{CM}}\delta}{\mathrm{d}z}\mathrm{d}z \end{cases} \tag{2.39}$$

where C_{FR} and C_{CM} are the coefficient constants historically used to characterize the pure FR and pure CM effect, respectively:

$$\begin{cases} C_{\mathrm{FR}} = \dfrac{e^3}{8\pi^2\varepsilon_0 m_e^2 c^3} \approx 2.6312 \times 10^{-13} \\ C_{\mathrm{CM}} = \dfrac{e^4}{16\pi^3\varepsilon_0 m_e^3 c^4} \approx 2.4568 \times 10^{-11} \end{cases} \tag{2.40}$$

Therefore a non-vanishing Ω_3 gives rise to the FR effect, while $\Omega_{1,2}$ correspond to the CM effect. The interaction between the FR and CM effects [Orsitto et al., 2010; Zhang et al., 2010], which will be discussed in more detail in Chapter 4 and Chapter 5, can be visualized with the geometric description of the polarization evolution: a 3-D rotation of the Stokes vector in the presence of both effects results in a Stokes vector different from the rotation due to either individual effect.

The interaction may also be seen from the differential expressions (Eqn. 16 in [Imazawa et al., 2012]) relating changes in χ and ψ to the FR and CM effects:

$$\frac{\mathrm{d}\chi}{\mathrm{d}z} = \frac{1}{2}\frac{\mathrm{d}_{\mathrm{CM}}\delta}{\mathrm{d}z}\sin(2\psi + 2\gamma) \tag{2.41a}$$

$$\frac{\mathrm{d}\psi}{\mathrm{d}z} = \frac{\mathrm{d}_{\mathrm{FR}}\psi}{\mathrm{d}z} - \frac{1}{2}\frac{\mathrm{d}_{\mathrm{CM}}\delta}{\mathrm{d}z}\tan 2\chi\cos(2\psi + 2\gamma) \tag{2.41b}$$

where γ is the transverse magnetic field pitch angle in the wave frame (see Fig. 2.4). Equation 2.41a shows the sensitivity of elliptization to ψ. FR modifies ψ, so it affects the elliptization. The second term on RHS of Eqn. 2.41b shows that the CM effect also intrinsically causes polarization rotation.

2.4.2 Mueller matrices for Faraday rotator plate and wave plate

An analogy can be made between the the polarimetry effects in a magnetized plasma and optical components: FR effect–Faraday rotator plate, CM effect–wave plate. The 3 × 3 Mueller matrix for:

(1) Faraday rotator plate which rotates a linear polarization by an angle of ψ:

$$\overleftrightarrow{\mathrm{M}}_{\mathrm{FR}} = \begin{pmatrix} \cos\psi & -\sin\psi & 0 \\ \sin\psi & \cos\psi & 0 \\ 0 & 0 & 1 \end{pmatrix} \tag{2.42}$$

(2) wave plate with its fast axis along $\hat{x}$ that introduces extra phase δ between E_y

and E_x:

$$\overleftrightarrow{\mathbf{M}}_{\mathrm{CM,x}} = \begin{pmatrix} 1 & 0 & 0 \\ 0 & \cos\delta & \sin\delta \\ 0 & -\sin\delta & \cos\delta \end{pmatrix} \tag{2.43}$$

For a wave plate with its fast axis oriented in another direction in xy-plane, the corresponding Mueller matrix is Eqn. 2.43 undergoing a rotation operation around $\hat{z}$.

Note that these two Mueller matrices are not commutative in general, i.e., for $\psi \neq \mathrm{m} \cdot \pi/2$, $\delta \neq \mathrm{n} \cdot \pi/2$ $(\mathrm{m}, \mathrm{n} \in \mathbb{Z})$:

$$\overleftrightarrow{\mathbf{M}}_{\mathrm{FR}} \overleftrightarrow{\mathbf{M}}_{\mathrm{CM}} \neq \overleftrightarrow{\mathbf{M}}_{\mathrm{CM}} \overleftrightarrow{\mathbf{M}}_{\mathrm{FR}} \tag{2.44}$$

If the magnetized plasma is divided into infinitesimal slabs, as described in Section 2.3, the polarimetry effects can be expressed as a product chain of the above Mueller matrices for each slab. In a case where both the FR and CM effects occur, the non-commutativity between the two forms of matrices prohibits to calculate the "total" FR effect by simply integrating $\overleftrightarrow{\mathbf{M}}_{\mathrm{FR}}$ over slabs, or the "total" CM effect by integrating $\overleftrightarrow{\mathbf{M}}_{\mathrm{CM}}$. This suggests that the the FR and CM effects cannot be easily separated in the final Mueller matrix, therefore the data interpretation is quite complicated in the presence of strong interaction between these two effects.

2.5 Relationship between Jones calculus & Mueller-Stokes calculus

Both calculuses are derived from the same set of assumptions: in the WKB limit, high-frequency EM-wave propagating in a cold magnetized plasma without dissipation and absorption. Jones calculus directly tracks the wave E-field in real space, while Mueller-Stokes calculus manipulates the Stokes vector in an abstract space. Their transforming matrices, Jones matrix and Mueller matrix, have a connection [Collett, 2003] that can be expressed by:

$$\overleftrightarrow{\mathbf{M}}_{4\times 4} = \overleftrightarrow{T}_{4\times 4}\left(\overleftrightarrow{\mathbf{J}}_{2\times 2} \otimes \overleftrightarrow{\mathbf{J}}^{*}_{2\times 2}\right)\overleftrightarrow{T}^{-1}_{4\times 4} \tag{2.45}$$

where

$$\overleftrightarrow{T} = \begin{pmatrix} 1 & 0 & 0 & 1 \\ 1 & 0 & 0 & -1 \\ 0 & 1 & 1 & 0 \\ 0 & -i & i & 0 \end{pmatrix} \tag{2.46}$$

and the direct product operation is defined as:

$$A \otimes B \equiv \begin{pmatrix} a_{11}B & a_{12}B \\ a_{21}B & a_{22}B \end{pmatrix} \tag{2.47}$$

From the above equation, it can be seen that the $e^{i\mathrm{d}\delta_{\mathrm{comm}}}$ factor in $\overleftrightarrow{K}$ (Eqn. 2.23) is eliminated during the direct product, i.e., the information of the common phase is lost. If the absolute phase of the E-field vector during propagation is desired, which is necessary to superpose two polarizations, Jones calculus has to be used. Except for this difference, these two calculus are equivalent, which is also verified by the calculations by synthetic diagnostic code in Section 4.2.1.

CHAPTER 3

Polarimeter hardware and initial tests on DIII-D

A 288 *GHz* ($\lambda = 1.04$ *mm*) polarimeter system is designed and fabricated at UCLA for NSTX. It was then installed on the DIII-D tokamak for plasma tests to prepare for future implementation on NSTX-Upgrade. This chapter presents the hardware development, implementation and initial tests of the polarimeter system.

3.1 NSTX polarimeter retro-reflects along a major radius

The polarimeter for NSTX is designed to operate along a major radial chord in retro-reflection geometry, which merely requires one midplane port window and a retro-reflector on the NSTX center stack for plasma access (see Fig. 3.1). To be specific, a rotating linearly polarized microwave beam is launched into the plasma from the outboard side. The beam retro-reflects at a flat reflective graphite tile on the inboard wall, and is finally detected by a receiver, which generates a sinusoidal voltage output. The phase shift between this output voltage and a reference sinusoidal wave directly relates to the plasma polarimetry effects. This geometry enables the diagnosis of B_{poloidal} around midplane, which is of great interest to the tokamak plasma research, since it directly relates to the plasma current profile. This retro-reflection design is also simpler to implement compared to the commonly used single pass vertical view, which normally requires a giant C-frame to isolate the polarimeter system from the tokamak vibrations [Braithwaite et al., 1989; Lanier et al., 1999; Rice, 1992; Soltwisch, 1986]. It is worth noting here that the retro-reflection by the flat tile does not cause any cancellation of the polarimetry effects, i.e., the FR and CM effects. It merely doubles the beam propagation path. (Detailed proof is presented in Appendix A.1.)

3.2 Choice of probe wavelength

The choice of probe wavelength is the most critical parameter for polarimetry design on NSTX. The chosen millimeter wavelength ($\lambda = 1.04\ mm$) is longer than common for polarimetry systems but is a good compromise between two competing constraints. On one hand, at longer wavelengths the plasma effects on wave polarization are much stronger (see Eqn. 2.38). This potentially allows for a more sensitive measurement of internal B-field, which is the primary motivation for the development of this polarimeter. On the other hand, at shorter wavelength refraction becomes less significant [Hutchinson, 2005]. This is critical for the detector to efficiently receive the returning beam in the previously described retro-reflection geometry. The corresponding $f = 288\ GHz$ frequency also allows the application of solid state microwave components, which are more robust and portable in comparison to the more delicate and bulky laser source.

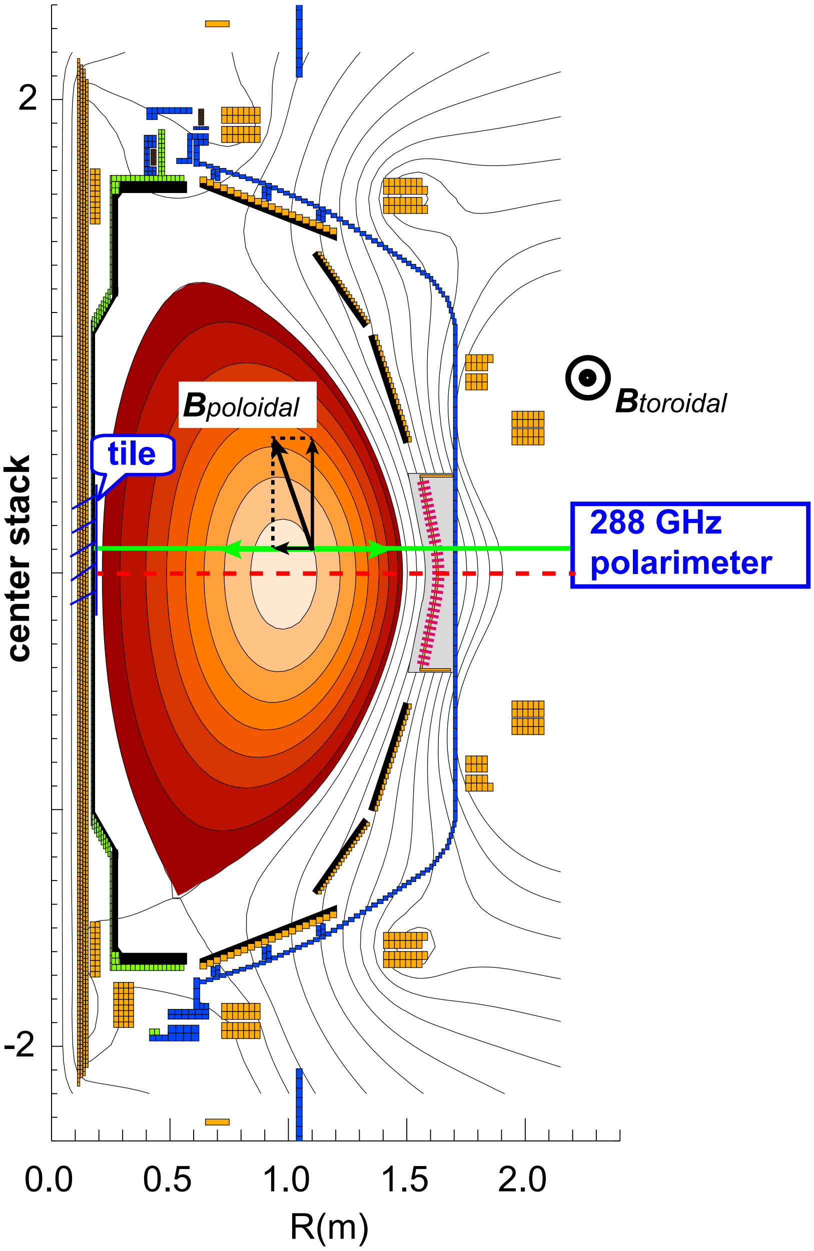

Figure 3.1: *The proposed 288 GHz polarimeter on NSTX uses retro-reflection geometry.*

3.3 Hardware design of 288 *GHz* polarimeter

The layout of the 288 *GHz* polarimeter is shown in Fig. 3.2. The system can be conceptually divided into the source, quasi-optical and receiver sections.

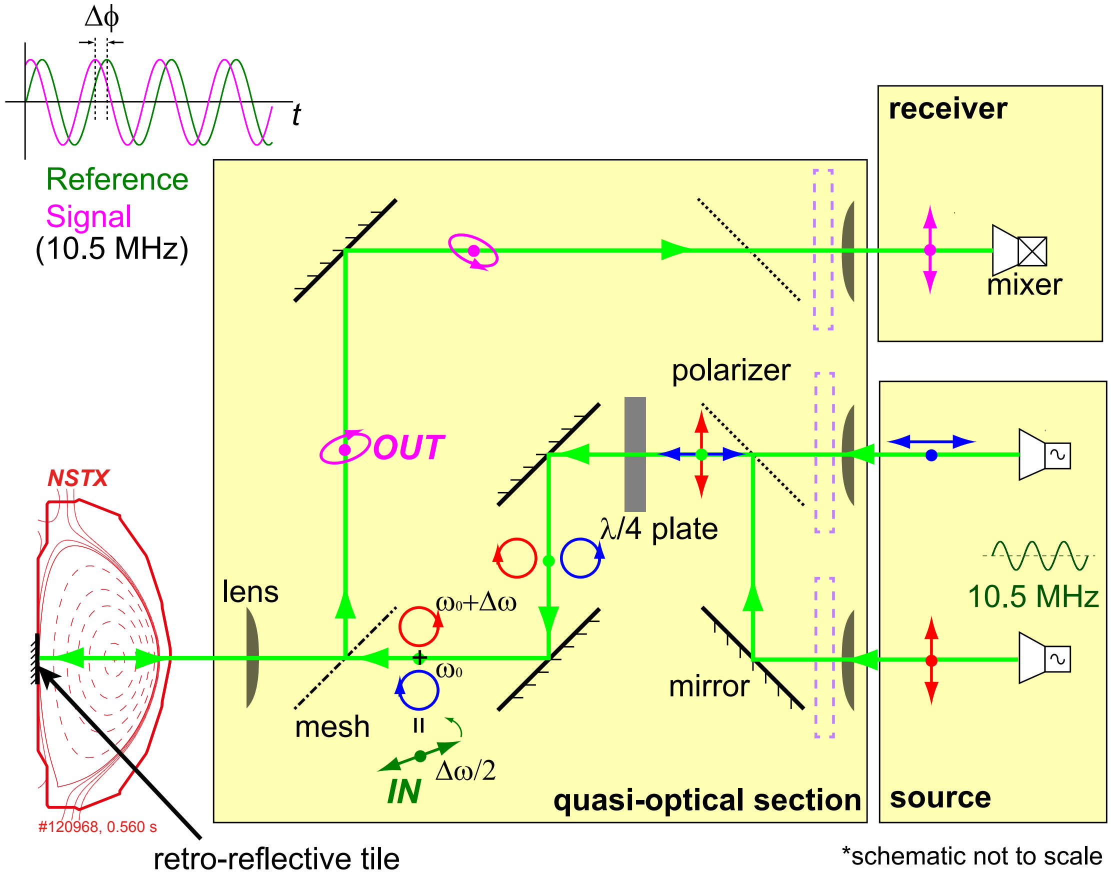

Figure 3.2: *Schematic of quasi-optical design of 288 GHz polarimeter on NSTX. The green lines with arrows indicate beam propagation. Double-arrows, circles, and ellipses represent the polarization of mm-wave beam (in wave frame of reference, i.e., looking in the direction of wave source) at the corresponding positions.*

3.3.1 Source section

The source section employs a Single-Side-Band (SSB) modulation technique to generate a pair of orthogonally linearly polarized beams with a stable difference frequency (see Fig. 3.3).

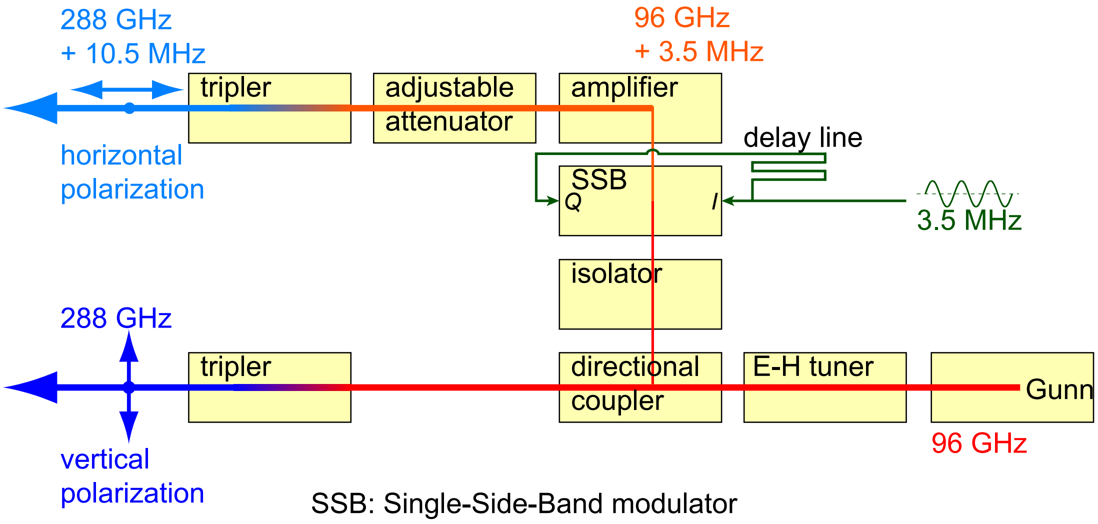

Figure 3.3: *Schematic of* 288 *GHz polarimeter source. Lines going through the microwave components indicate the microwave power flow.*

A 96 *GHz* Gunn diode oscillator generates ∼ 20 *dBm* of microwave radiation. A small fraction of the Gunn output power is coupled to the SSB modulator via a 10-*dB* directional coupler. In the SSB modulator, the 96 *GHz* frequency is upshifted using a stable 3.5 *MHz* crystal oscillator. The SSB modulator requires two separate 3.5 *MHz* I & Q inputs with 90° phase difference. This is achieved by splitting the crystal oscillator output and delaying one branch with a BNC cable of appropriate length. (Calculation of the cable length is presented in Appendix A.2.) The output of the SSB modulator is then amplified using a high gain W-band amplifier. The remainder of the original 96 GHz and the amplified 96 $GHz + 3.5$ MHz radiation are fed into separate frequency triplers and then coupled to free-space via dual-mode horns [Pickett et al., 1984] (see Appendix A.3). An E-H tuner is inserted between the Gunn and the input port of the directional coupler for impedance matching to achieve the optimum microwave power coupling. It was later replaced by a fixed length waveguide because it is unstable due to the mechanical vibrations and environmental temperature change. The latter cause is pretty severe at DIII-D, since the temperature in the machine hall can easily vary $> 10°$C during a day. A W-band isolator is used in the coupled port of the directional coupler to eliminate reflection from the SSB that can disturb the frequency stability of the original transmitted 96 GHz microwave radiation. The isolator is protected from the tokamak magnetic fields with a close-fitting, soft iron shield. An adjustable attenuator is inserted after the W-band amplifier to optimize the emerging power of the upshifted mm-wave radiation. (Detailed discussion about unbalanced power LCP + RCP launch is in Appendix A.4.) Necessary W-band waveguides are used to connect the above microwave components and also create the required orthogonal polarization between the two frequency offset beams. The emerging 288 GHz and 288 $GHz + 10.5$ MHz mm-wave radiations each have approximately 3 dBm power. A portion of the original 3.5 MHz crystal oscillator output is electronically tripled in frequency to provide a reference for the mm-wave phase shift measurements. A photo of the source before the magnetic shielding is shown in Fig. 3.4.

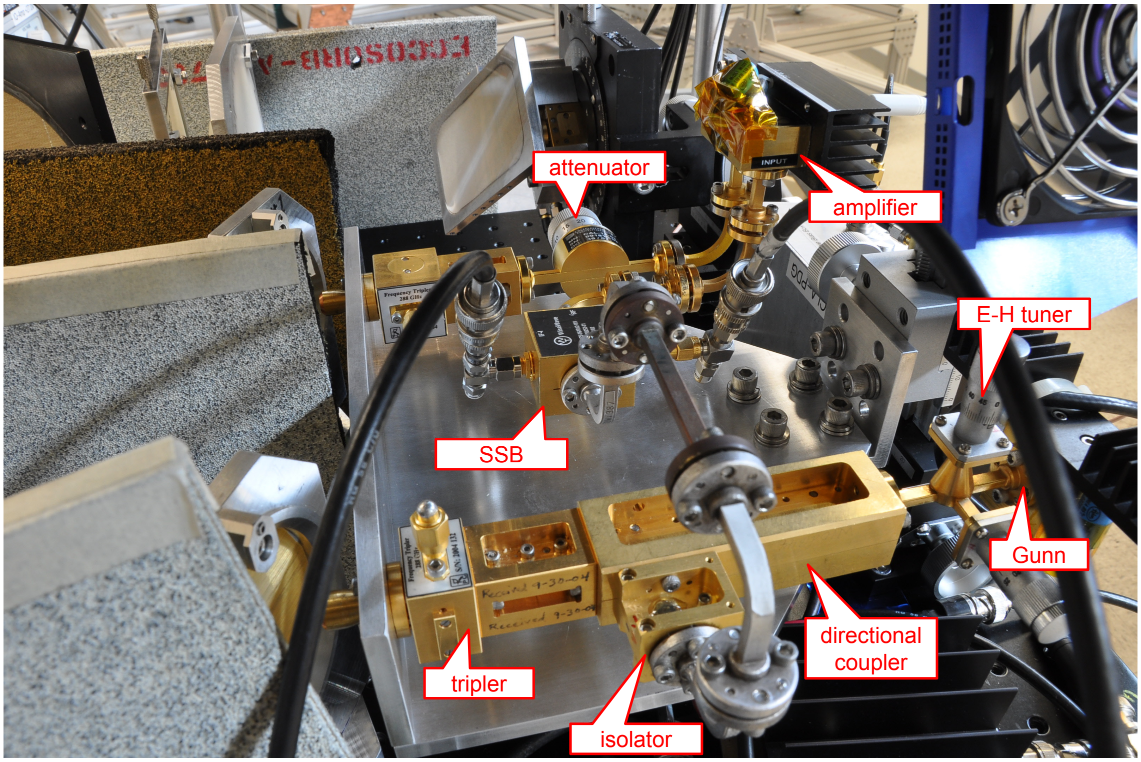

Figure 3.4: *A photo of the 288 GHz polarimeter source before magnetic shielding. Solid state microwave components are annotated.*

3.3.2 Quasi-optical and receiver sections

The aperture dimensions of the components used for beam manipulation are on the order of 10 *cm* (approximately 100 millimeter-wavelengths), which categorizes the design to the quasi-optical regime [Goldsmith, 1992]. The emerging mm-wave from the triplers is coupled to aspherical lenses made of high density polyethylene. These lenses convert the diverging mm-wave from the horns to collimated Gaussian beam propagation. A similar lens in front of the mixer focuses the returned beam into the dual-mode horn attached to the mixer. Another longer focal length lens is inserted between the beam splitting mesh and the plasma to control beam propagation and place a beam waist on the retro-reflective tile. The orthogonal linearly polarized beams launched from the two triplers are combined using a polarizer (the mm-wave from the SSB branch transmits and the wave from the Gunn branch reflects; see Appendix A.6.2) and converted to a pair of counter-rotating circularly polarized beams (LCP & RCP) via a birefringent crystal quartz $\lambda/4$ wave plate (see Appendix A.6.4). The combined LCP & RCP beams are equivalent to a linearly polarized beam whose polarization direction rotates at half of the difference frequency. Equation 3.1 proves that the resultant wave E-field is a linear polarization ($\delta = 0$) with its polarization rotating at half of the difference frequency ($\alpha = \omega_{\mathrm{df}} t/2$).

$$\begin{aligned}\vec{E} &= \vec{E}_{\mathrm{LCP}} + \vec{E}_{\mathrm{RCP}} \\ &= \frac{1}{\sqrt{2}} e^{i(\omega_{\mathrm{lo}}+\omega_{\mathrm{df}})t} \begin{pmatrix} 1 \\ -i \end{pmatrix} + \frac{1}{\sqrt{2}} e^{i\omega_{\mathrm{lo}} t} \begin{pmatrix} 1 \\ i \end{pmatrix} \\ &= \sqrt{2} e^{i(\omega_{\mathrm{lo}}+\omega_{\mathrm{df}}/2)t} \begin{pmatrix} \cos(\omega_{\mathrm{df}} t/2) \\ \sin(\omega_{\mathrm{df}} t/2) \end{pmatrix}\end{aligned} \tag{3.1}$$

As illustrated in Fig. 3.2, this combined beam transmits through a mesh (it maintains the polarization in transmission and reflection for beam incident at 45°; $\sim$ 90% reflection coefficient in E-field; see Appendix A.6.3), propagates through the plasma from the outboard side, retro-reflects at a flat reflective graphite tile ($>$ 99% reflective for mm-wave) on the inboard wall, which returns the beam through the plasma a second time. This returned beam then reflects from the mesh, and is directed towards the mm-wave receiver. During propagation through the magnetized plasma, the beam experiences polarization modifications related to the FR and CM effects. The vertical E-field component of the returned beam is selected by a polarizer and subsequently detected by a single-ended 288 *GHz* mixer. The mixer generates a sinusoidal voltage output at the original difference frequency after bandpass filtering (to suppress the undesired sidebands due to imperfect SSB modulation; see Appendix A.7), i.e., 10.5 *MHz*, corresponding to the rotating linearly polarized beam input. The phase shifts between the previously mentioned sinusoidal 10.5 *MHz* reference and mixer output voltage directly relate to the polarization changes caused by the plasma. For example, pure FR effect would advance the linear polarization rotation, resulting in a measured phase shift between the two sinusoidal waveforms. Later, to further improve the phase resolution, a mm-wave reference is created by a tracking receiver [Doane, 1980] detecting a fraction of the reflected beam from the beam splitter, which was dumped in the early design (dashed green line in Fig. 3.11). This helps to suppress the noise before the combination of the mm-wave beam pair. These noise include the jitter in the SSB modulation and the beam path length variation introduced by mechanical vibrations.

3.3.3 Multi-reflection feedback effect and quasi-optical isolation

The primary source of phase error is found to be a result of multi-reflection feedback effects. These effects are created due to the cavities formed in the system by reflections at the triplers and also the 288 *GHz* mixer. The highly reflective mesh (illustrated in Fig. 3.2) helps to isolate the effects of reflection from the triplers. The cavity formed between the tile and the mixer was therefore found to be dominant. As illustrated in Fig. 3.5, a beam can propagate multiple times in such a high-Q cavity before its power is attenuated to a negligible level. At the mixer, the E-field of this feedback beam (e.g., beam #2 in Fig. 3.5) interferes with the E-field of desired main return beam (beam #1 in Fig. 3.5), generating another sinusoidal power variation at the difference frequency.

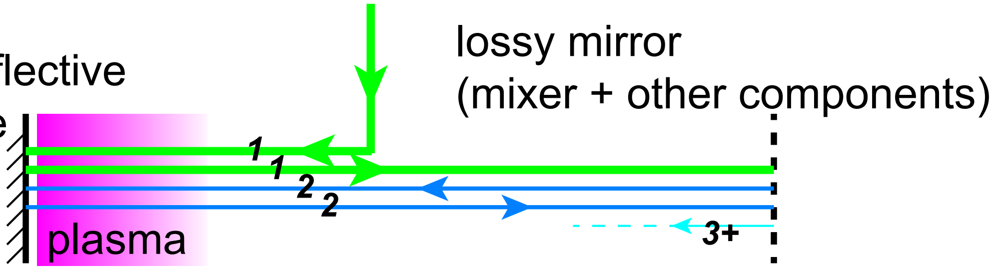

Figure 3.5: *A cavity formed between the tile and the mixer. The mixer and other quasi-optical components in between together are equivalent to a lossy mirror.*

Figure 3.6 clearly shows that the total power variation ($\tilde{P}_{1,1}+\tilde{P}_{1,2}$), which would be the measured sinusoidal waveform, presents a phase error ($\Delta\phi|_{\text{error}}$) compared with the desired clean waveform ($\tilde{P}_{1,1}$). As a result, the amplitude and phase of the 10.5 *MHz* waveform detected at the mixer become functions of the path length (L)

and the polarimetry phase shift ($\Delta\phi$) caused by the plasma.

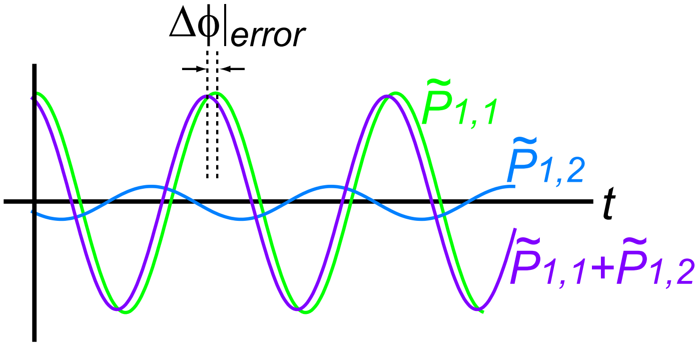

Figure 3.6: *The total power variation ($\tilde{P}_{1,1} + \tilde{P}_{1,2}$), which would be the measured sinusoidal waveform, presents a phase error ($\Delta\phi|_{\mathrm{error}}$) compared with the desired clean waveform ($\tilde{P}_{1,1}$).*

The quantitive phase error dependence on L and $\Delta\phi$ using realistic parameters is calculated and displayed in Fig. 3.7. The effective E-field reflection coefficient at the cavity ends (r) is estimated to be 0.15. (Detailed derivation is in Appendix A.9.) During a typical plasma operation cycle, L can vary a few tens of wavelengths due to plasma interferometry effects, and $\Delta\phi$ can vary tens of degrees due to plasma polarimetry effects. Mechanical vibration can also cause changes in L on the order of a few hundred microns. Due to these variations, as shown in Fig. 3.7, the resultant phase error can easily be at the level of 10°, if the feedback effect is left unsuppressed. Figure 3.7 also shows that the phase error can be decreased to $< 1°$ by reducing $r < 0.01$.

One approach to achieve this is introducing quasi-optical isolation to degrade the cavity Q. Inserting a +45° polarizer, a +45° Faraday rotator plate (see Appendix A.6.1) and a vertical polarizer in series creates a one-way passage for

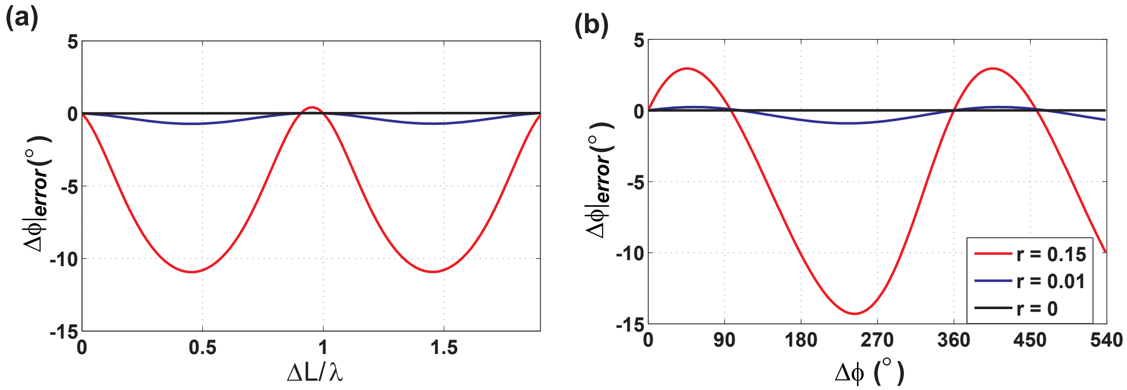

Figure 3.7: *Calculated error in polarimetry phase measurements caused by the feedback effects. (a) dependence on path length (L); (b) dependence on polarimetry phase* ($\Delta\phi$) *caused by a magnetized plasma. Red and blue curves show the phase error with effective E-field reflection coefficients at the cavity ends* $r = 0.15$ *and* $r = 0.01$*, respectively. The black horizontal curve shows zero phase error if there is no feedback effect, i.e.,* $r = 0$.

the main beam (see Fig. 3.8). The different components of the feedback beam are selectively isolated at the polarizers. Such isolators are inserted in the receiver path and also in both source branches, where linearly polarized beams are propagating.

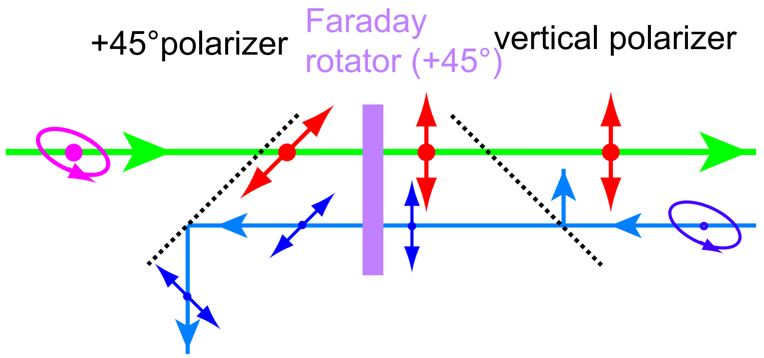

Figure 3.8: *Schematic of quasi-optical isolation. Green line indicates the desired main beam. Cyan line indicates the feedback beam. Polarizations in the frame of reference of the beam are depicted along the propagation.*

A photo of the 288 *GHz* polarimeter setup for NSTX in laboratory at UCLA-Plasma Diagnostic Group is shown in Fig. 3.9.

3.4 Implementation and initial tests on DIII-D

Due to the technical failure on NSTX in 2011, the polarimeter system was installed on the DIII-D tokamak for experimental demonstration prior to future implementation on NSTX-Upgrade. Minimal modifications were involved since the installation on both devices share the same radial retro-reflection geometry (see Fig. 3.10).

Figure 3.11 shows the schematic of the polarimeter implementation on DIII-D

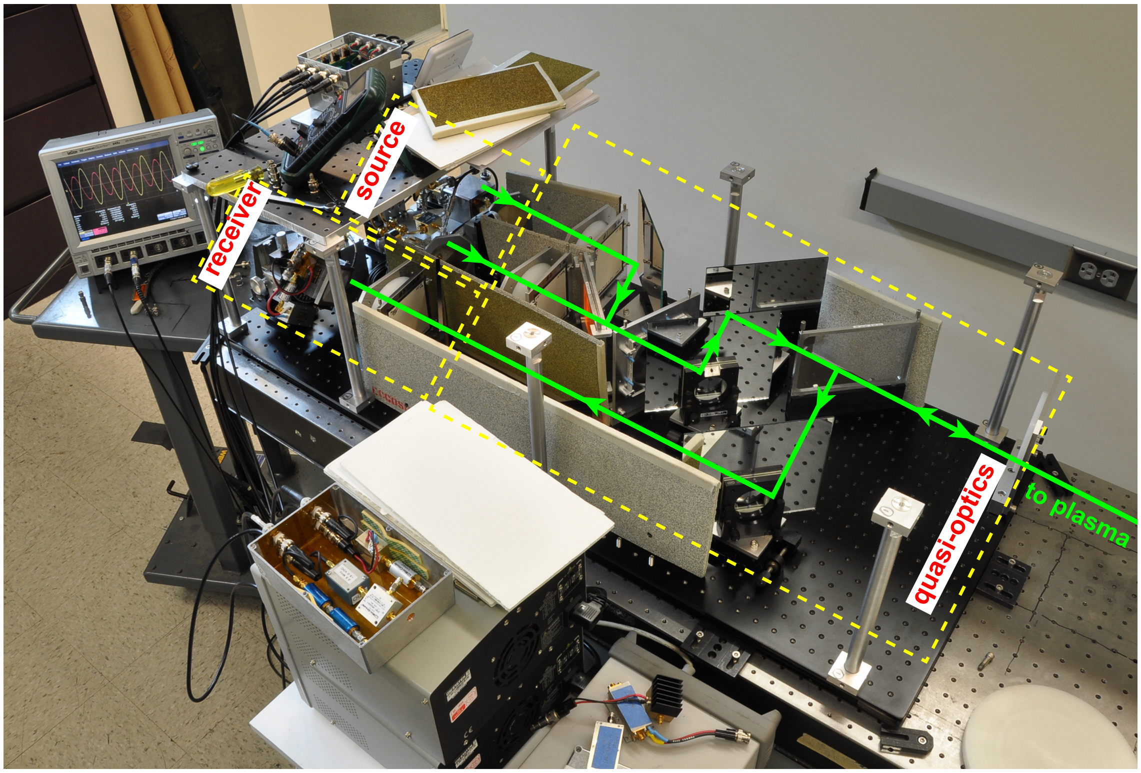

Figure 3.9: *A photo of the 288 GHz polarimeter setup for NSTX in laboratory at UCLA-Plasma Diagnostic Group. The polarimeter can be conceptually divided into the source, quasi-optical and receiver sections. The beam propagation path is illustrated with the green lines with arrows.*

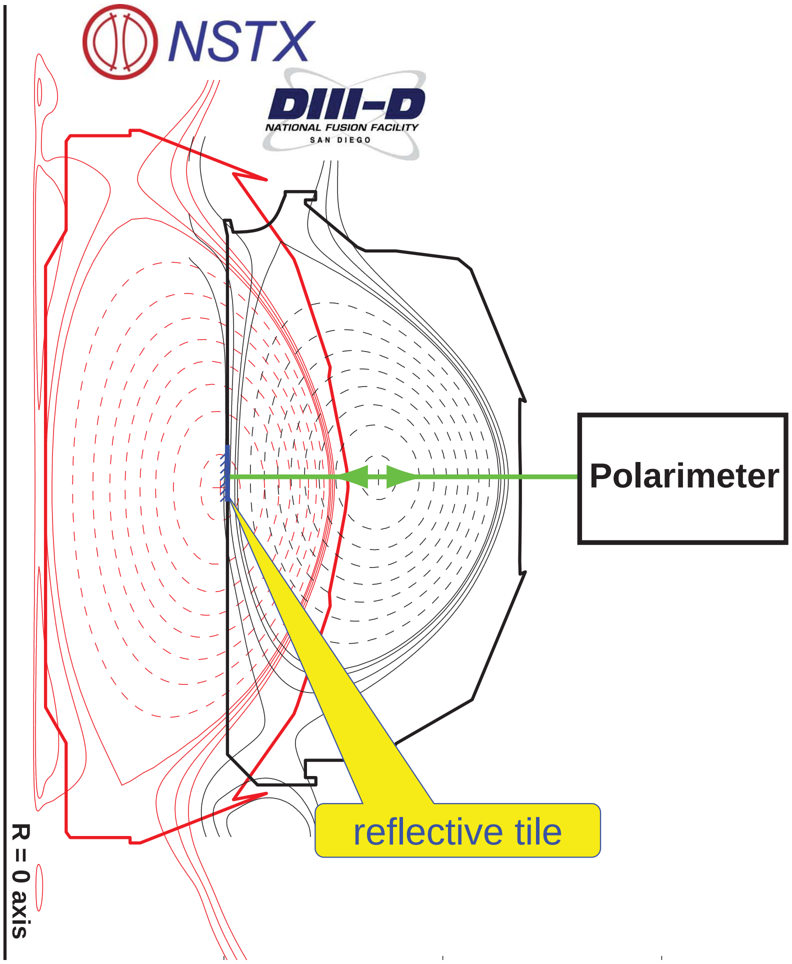

Figure 3.10: *Polarimeter on DIII-D has the same radial retro-reflection geometry as NSTX.*

and Fig. 3.12 shows a photo. As can be seen, a lens pair replaces the previously described long focal length lens to better control the beam propagation alignment and waist position, since the beam path is much longer than that on NSTX.

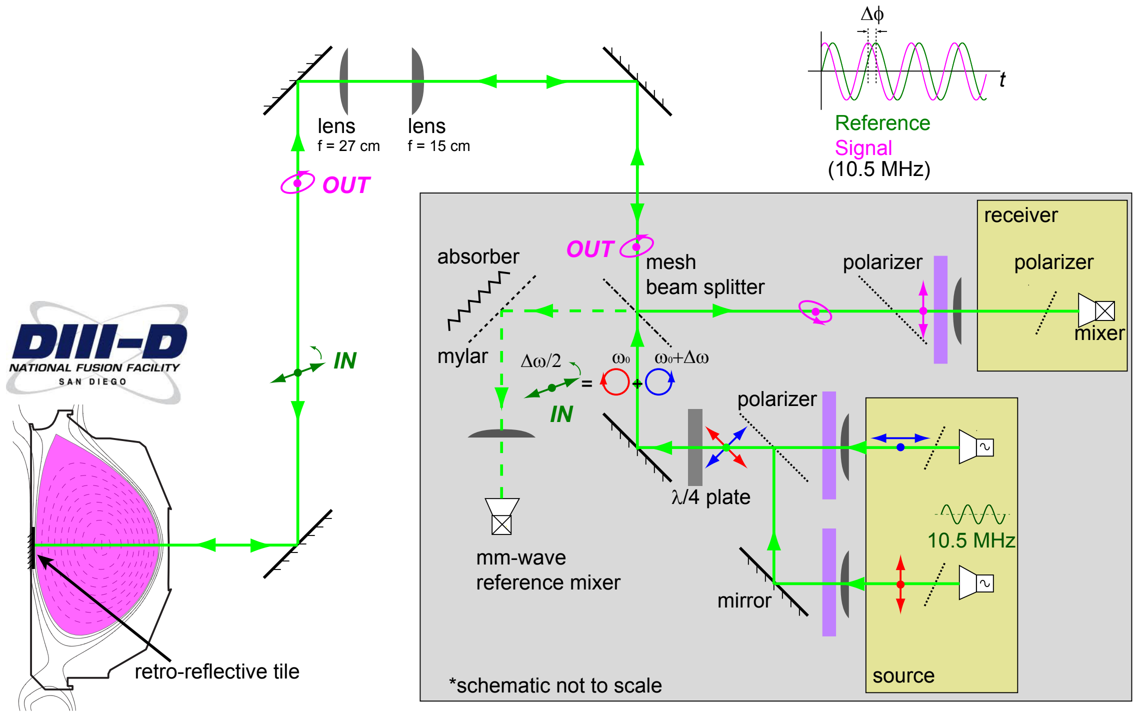

Figure 3.11: *Schematic of quasi-optical design of 288 GHz polarimeter on DIII-D. The green lines with arrows indicate beam propagation. Double-arrows, circles, and ellipses represent the polarization of mm-wave beam at the corresponding positions. A mm-wave reference is achieved by adding a tracking mixer to detect a fraction of reflected beam from the mesh beam splitter (dashed green line).*

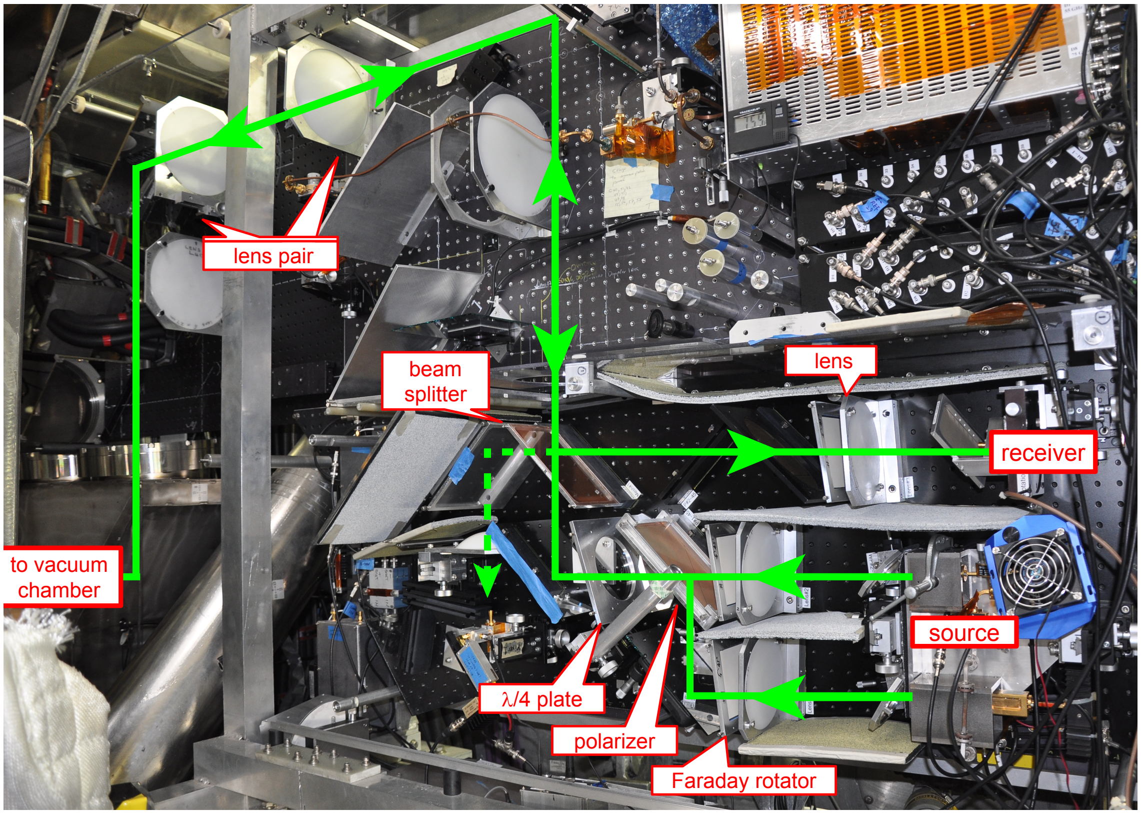

Figure 3.12: *A photo of the* 288 *GHz polarimeter implementation on DIII-D. The solid green lines indicate the beam propagation. The dashed green lines indicate the beam of mm-wave reference.*

3.4.1 Digitization, electronics and MDSplus tree design

Since a typical DIII-D discharge lasts ~ 10 seconds, it is impractical to digitize the signal and reference waveforms with full bandwidth ($f_{\text{sampling}} > 21\ MHz$), which would generate enormous amount of data. Initially, the design was to digitize the I & Q output of an analog quadrature demodulator. But the demodulator introduces phase distortion, and the low frequency I & Q output was expected to be susceptible to pickups during the propagation along the $\sim 100\ m$ BNC cables between the machine hall and the digitizer. The frequency aliasing technique is used in digitization. The sampling rate of 11.7 *MHz* aliases the 10.5 *MHz* difference frequency to 1.2 *MHz* (see Fig. 3.13). 1.2 *MHz* is wider than the filter pass band and spectra of most plasma MHD modes, which avoids the interference between folding frequencies.

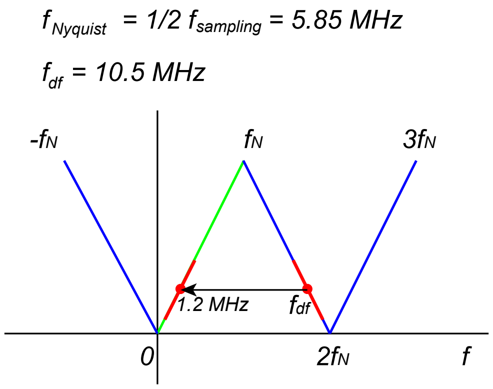

Figure 3.13: *Schematic of the frequency aliasing technique.* 11.7 *MHz sampling rate aliases the* 10.5 *MHz difference frequency down to* 1.2 *MHz (red dots).*

Schematic of the polarimeter electronic design is presented in Fig. 3.14.

Digitized data is stored in a MDSplus tree ‘PI’. Its design is presented in

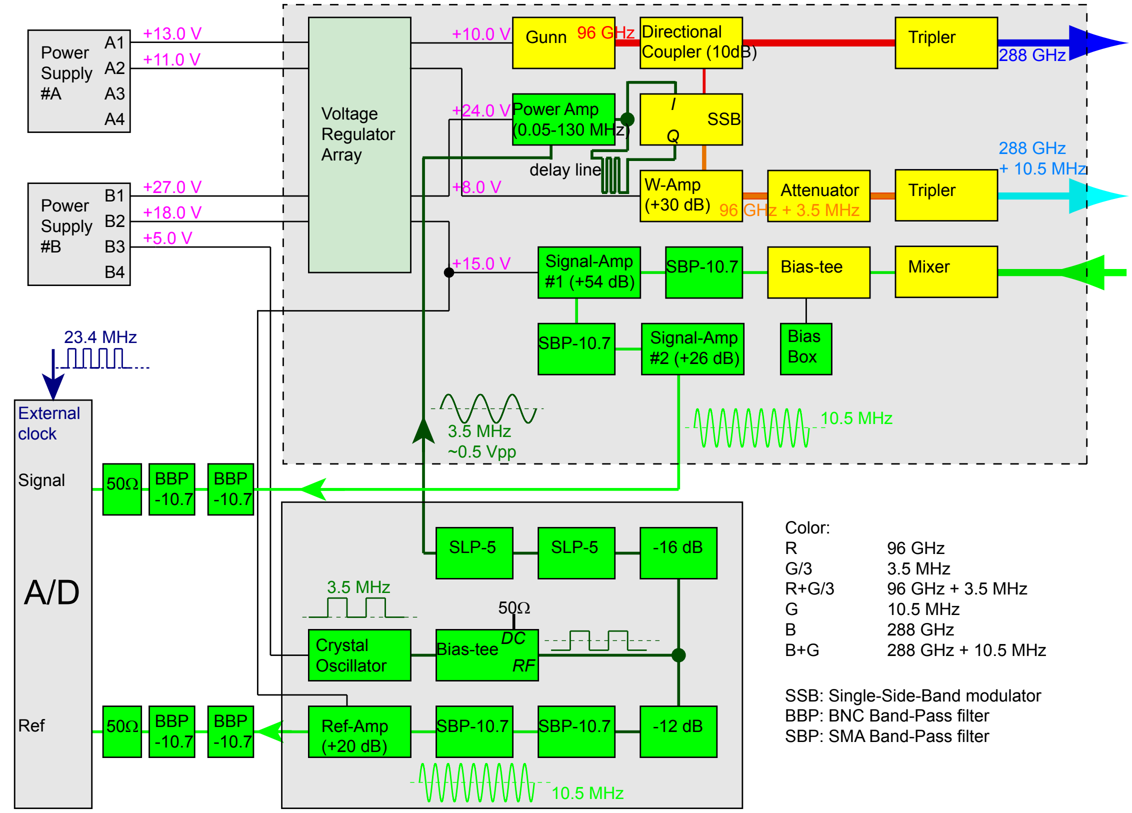

Figure 3.14: *Schematic of polarimeter electronic design.*

Fig. 3.15. (MDSplus is a set of software tools for data acquisition and storage and a methodology for management of complex scientific data. It allows all data from an experiment or simulation code to be stored into a single, self-descriptive, hierarchical structure. It is also the most widely used system for data management in the MCF program [Fredian and Stillerman, 2002].)

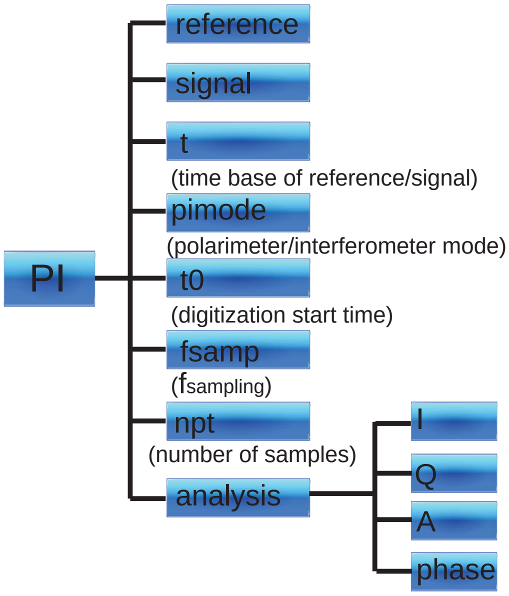

Figure 3.15: *MDSplus tree 'PI' design for Polarimeter/Interferometer data storage and management. Descriptions for the nodes are in parentheses.*

3.4.2 Phase calculation uses complex demodulation technique

The complex demodulation technique [Choi et al., 1986] is used to calculate the polarimetry/interferometry phase shift from the pair of measured sinusoidal waveforms. The two sinusoidal waveforms are converted to complex numbers by firstly Fourier transforming (FFT) and then inverse Fourier transforming (iFFT) on the positive frequencies. Then a digital quadrature demodulator is applied to calculate I & Q, from which the phase and amplitude can be extracted.

The complex demodulation algorithm is as follows:

$$
\begin{aligned}
&\begin{cases}
\text{ref: } x(t) = A_0 \cos(\omega_0 t + \phi_0) \xrightarrow{\text{FFT}} X(f) \xrightarrow{\text{iFFT}(X(f_+))} x'(t) = {}^1\!/_2 A_0 e^{i(\omega_0 t + \phi_0)} \\[1em]
\text{sig: } y(t) = A_1(t) \cos[\omega_0 t + \phi_1(t)] \xrightarrow{\text{FFT}} Y(f) \xrightarrow{\text{iFFT}(Y(f_+))} y'(t) = {}^1\!/_2 A_1(t) e^{i[\omega_0 t + \phi_1(t)]}
\end{cases} \\
&\Rightarrow 4y'(t) \cdot x'^*(t) = A_1(t) A_0 e^{i[\phi_1(t) - \phi_0]} = I(t) + iQ(t) \\
&\Rightarrow \begin{cases}
I(t) = A_1(t) A_0 \cos[\phi_1(t) - \phi_0] \\
Q(t) = A_1(t) A_0 \sin[\phi_1(t) - \phi_0]
\end{cases} \\
&\Rightarrow \begin{cases}
A_1(t) = \sqrt{I^2(t) + Q^2(t)} / A_0 \\
\Delta\phi(t) \equiv \phi_1(t) - \phi_0 = \tan^{-1}[Q(t)/I(t)]
\end{cases}
\end{aligned}
\tag{3.2}
$$

3.4.3 Interferometer setup verifies basic hardware operation

The system was initially setup as an interferometer after installation on DIII-D to verify the basic hardware operation in the harsh environment. In this configuration, the Gunn-branch beam is directly sent to the mixer as a local oscillator, instead of being launched into the plasma (see Fig. 3.16).

A typical plasma discharge on DIII-D (shot #147054) is presented in Fig. 3.17. As shown in the trace of D_α emission (see Fig. 3.17c), the plasma transitions from low performance mode (L-mode) to high performance mode (H-mode) at $\sim$ 1900 *ms*. Figure 3.17(a) illustrates that the 288 *GHz* interferometer can measure the line integrated density ($n_e L$) beyond the current ramp (Fig. 3.17b) and up to H-mode.

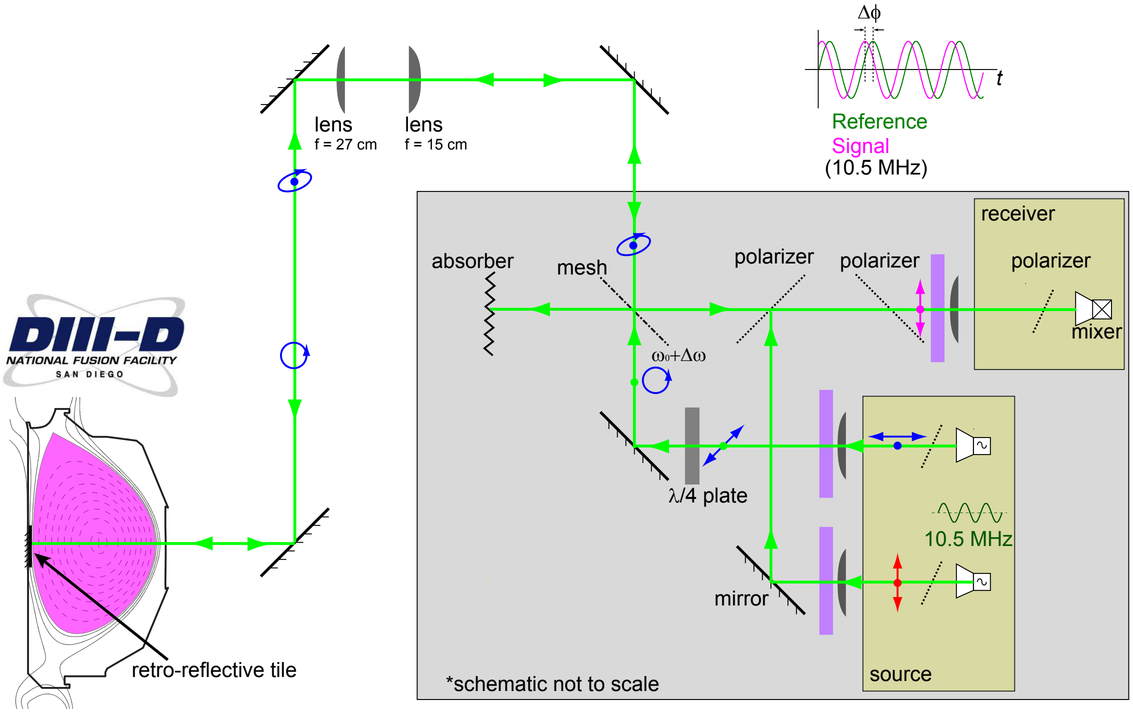

Figure 3.16: *The interferometer setup was initially used to verify the basic hardware operation.*

The line integrated density measured by CO_2 R0 interferometer [Zeeland et al., 2006a], which uses two wavelengths ($\lambda = 10.59\ \mu m, 0.632\ \mu m$) to compensate vibration, is also plotted for comparison. The interferometer failed to track the density at high plasma density region as a result of the fringe jumps due to temporary loss of signal. The beam can be severely refracted to miss the receiver at a density with sufficiently large transverse gradient.

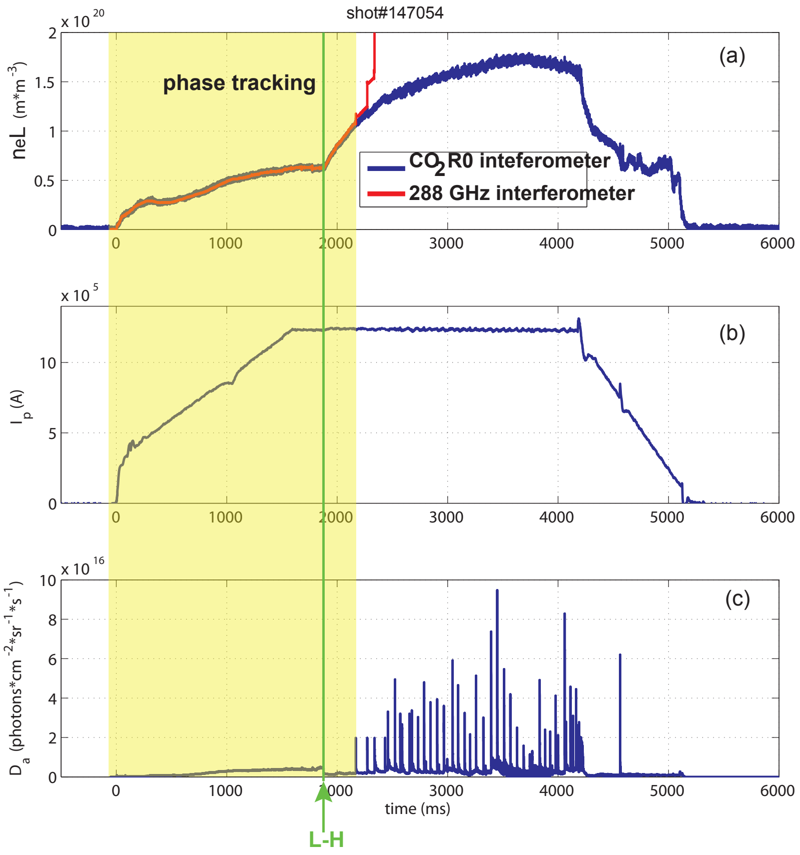

Figure 3.17: *Time traces of line integrated density (n_eL in panel a), plasma current (I_p in panel b) and D_α emission (D_α in panel c) of a typical DIII-D shot. (shot #147054)*

Figure 3.18 zooms in on the phase tracking during the plasma starting stage, i.e., when the plasma current (I_p) is ramping up during 0–1600 *ms* in Fig. 3.17(b). Two diagnostics simultaneously measure the line integrated density and the temporal traces are plotted at their full sampling rate: 288 *GHz* interferometer at 11.7 *MHz* in red and CO_2 R0 interferometer at 1.67 *MHz* in blue. The red curve closely follows the blue curve but it is contrastingly thin. This suggests that the 288 *GHz* interferometer features much higher S/N ratio and better sensitivity for low density measurements. This also demonstrates its possible use for density control during plasma start-up, where the DIII-D CO_2 interferometer system often suffers significant uncertainty.

3.5 In-situ mirror translation tests suppression of feedback effect

As discussed in Section 3.3.3, the quasi-optical isolation introduced is essential to achieve high phase resolution in polarimeter measurements. Its effectiveness in suppressing the multi-reflection feedback effect was quantitatively verified. The verification was performed by varying the cavity length (L) over a range of a few wavelengths. This is accomplished by manually translating the mirror, which simulates the plasma interferometry effect during plasma operations, as shown in Fig. 3.19.

The polarimeter response was recorded with data acquisition shots and the measured phase and amplitude variations without & with quasi-optical isolation are presented in Fig. 3.20. As can be seen, the phase variation is $\sim 12^\circ$ without isolation (see Fig. 3.20a), which agrees with the predicted phase error level shown in Fig. 3.7(a). The phase variation is $< 1^\circ$ with isolation (see Fig. 3.20b), demonstrating

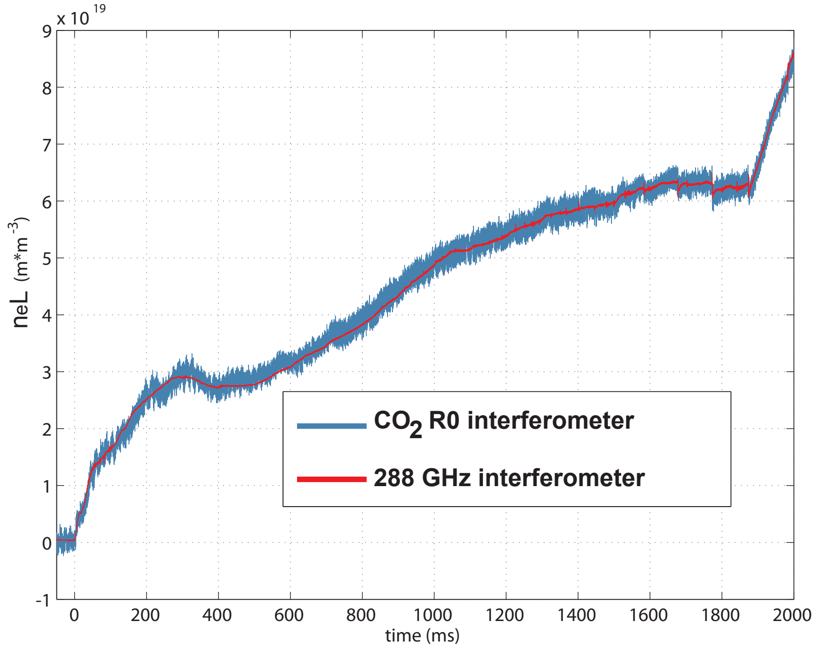

Figure 3.18: *Time trace of line integrated density ($n_e L$) during the starting stage of DIII-D shot #147054. Measurements from both interferometers are plotted with full sampling rate: 288 GHz interferometer at 11.7 MHz in red and CO_2 R0 interferometer at 1.67 MHz in blue.*

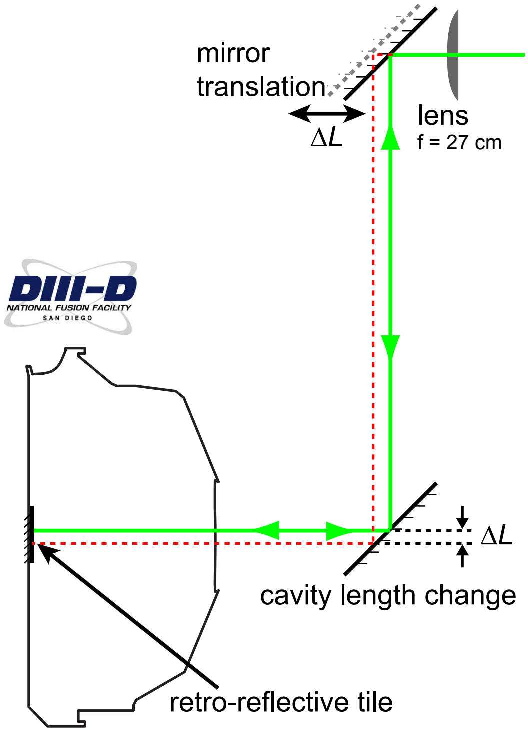

Figure 3.19: *The mirror is manually translated to vary the tile-mixer cavity length. The original cavity (in green) and varied cavity (in red) have a length difference of the mirror translation distance (ΔL).*

that the feedback effect is suppressed.

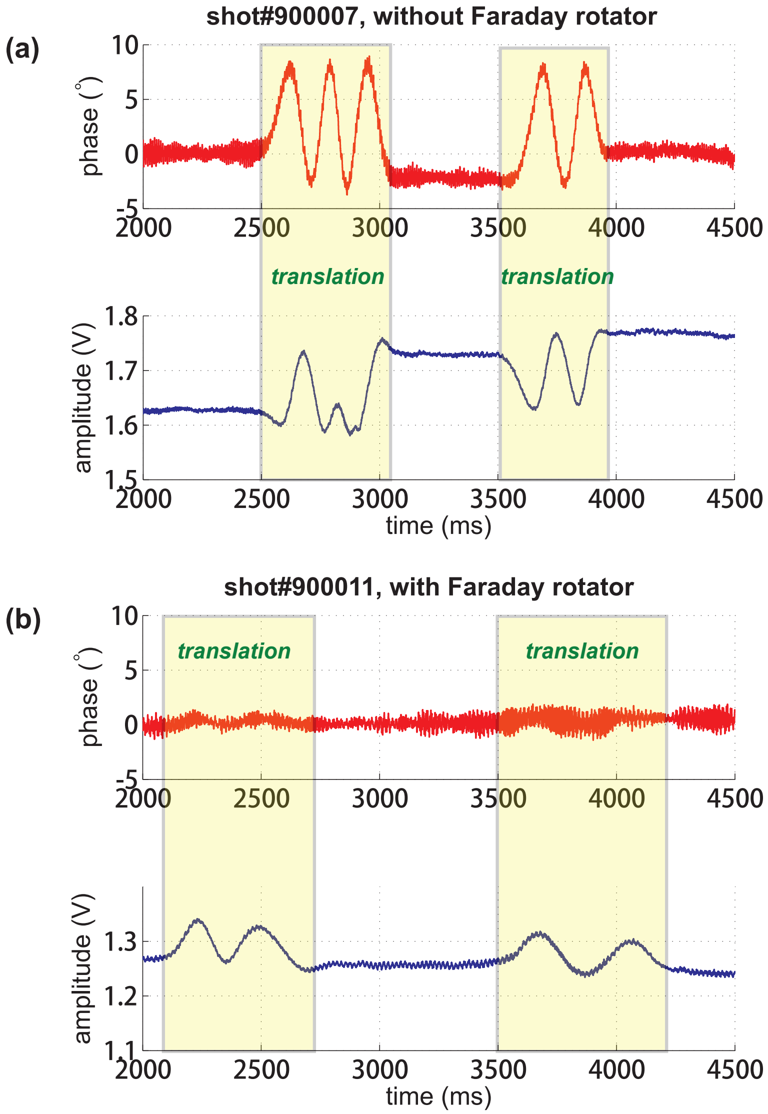

Figure 3.20: *Polarimeter phase and amplitude variation during mirror translation (shaded area): (a) without quasi-optical isolation; (b) with isolation.*

The residual variation in the signal amplitude in Fig. 3.20(b) is due to the coupling among multiple cavities. For example, two extra cavities are created by the slightly reflective lens surface between the tile and mixer (see Fig. 3.21). Careful tuning the lens position (on the order of 100 μm) can achieve a "sweet spot", where translating the mirror has minimal effect on the signal. As shown in Fig. 3.21, lens translation changes length of cavity #3, and this length is not affected by the plasma operation. Therefore if the lens is positioned at a spot where cavity #3 length is a multiple of wavelength, a node of a standing wave is positioned at the mixer, thereby minimizing the impact on the signal from the feedback effects.

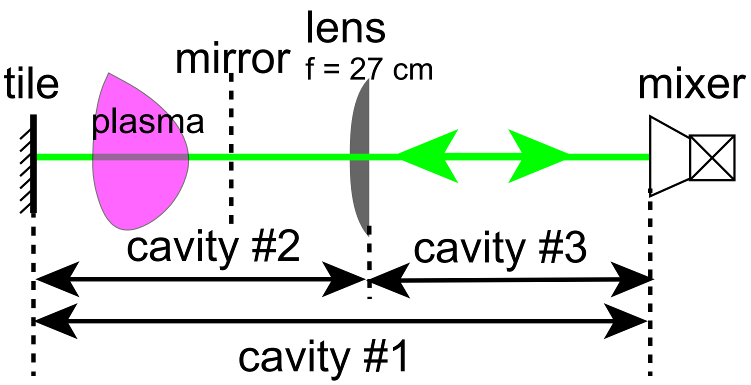

Figure 3.21: *3 cavities are created among the tile, lens, and mixer.*

3.6 Shielding of stray magnetic field essential to suppress phase noise

Immediately after the installation, a polarimeter phase noise of $\sim 4^\circ$ was measured before plasma breakdown. Similar level of noise was also observed to occur during power supply test shots (see Fig. 3.22), and during plasma operation when the probe beams are directly retro-reflected from a mirror outside the vacuum chamber, without propagating through the plasma (see Fig. 3.23a).

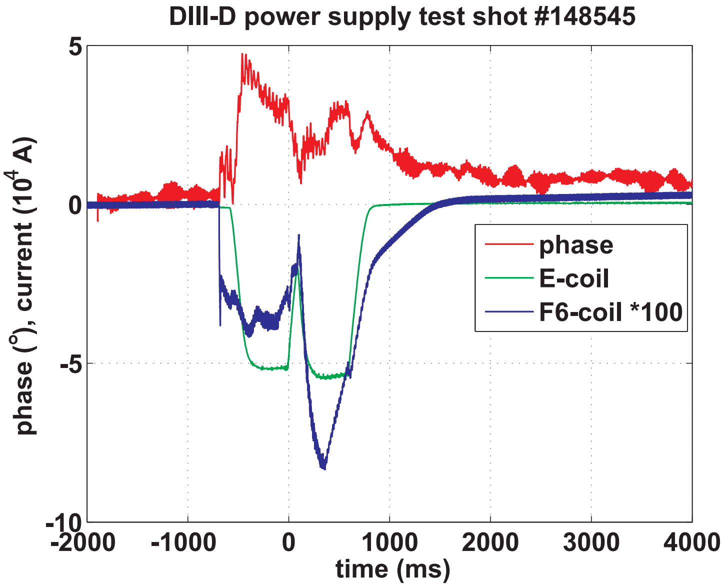

Figure 3.22: *~ 4° phase noise (in red) occurs during power supply test shot on DIII-D. The Ohmic coil (E-coil) current is in green; One of the plasma positioning and shaping coils, which is the closest to the polarimeter system, i.e., F6-coil current, is plotted in blue.*

Three hypotheses for the cause of this noise were tested. The first hypothesis is mechanical vibration. The polarimeter design is in principle immune to the vibrations after the two beams are combined but is susceptible to vibrations before the beam combination. It was found during the bench tests that the combining polarizer can vibrate as a drum in response to the air flow caused by acoustic noise during plasma operation. (This polarizer comprises a copper clad PET substrate mounted on an aluminum frame, as described in Apendix A.6.2.) However, covering up

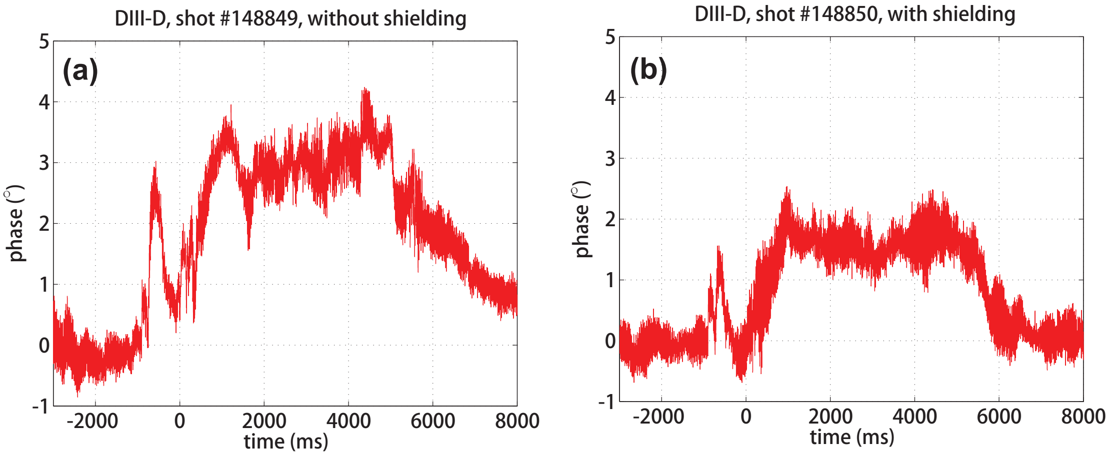

Figure 3.23: *Polarimeter phase noise measured with a retro-reflecting mirror outside the vacuum chamber during typical DIII-D plasma shots: (a) without shielding of stray B-field (#148849); (b) with shielding (#148850).*

the polarimeter system with Lexan sheets does not affect this noise. The second hypotheses is the electric noise. This kind of noise can result from the pickup along the $\sim 100\ m$ BNC cables between the receiver and digitizer. The possible ground loops in the complicated digitizer rack setup might also contribute to the electric noise. This hypothesis was tested by setting up the digitizer right beside the polarimeter to minimize the cable length and reduce the circuit complexity so that it is possible to ensure the elimination of any ground loops. A power supply test shot was digitized with this setup, showing the same noise in the measured phase thereby denying the electric noise hypothesis. The stray B-field was finally determined to be the primary cause, thereby verifying the third hypothesis. Figure 3.22 shows that the measured polarimeter phase waveform strongly correlates with the currents in the Ohmic coil (E-coil) and plasma positioning and shaping coil (e.g., F6-coil, which is the closed to the polarimeter). This stray B-field was also directly measured by a

Hall probe positioned at the polarimeter during a typical DIII-D shot (#149027), and is determined to be on the level of ~ 100 *Gauss* (see Fig. 3.24a). Then a permanent magnet (~ 2 *cm* cubical in size, surface B-field ~ 1 *Tesla*) was used to scan the components in the polarimeter system and identify components that are sensitive to B-field. It was found that the Mini-Circuit filters are sensitive to external B-field. A 10.5 *MHz* sinusoidal waveform was sent to propagate through a BBP-10.7 filter at the polarimeter location during a typical DIII-D shot (#148846). Figure 3.24(b) presents the phase shift between the returning and launched waveforms, which has a similar waveform as the measured stray B-field waveform, thereby again confirming the stray B-field hypothesis. The phase distortion possibly originates from the inductors used in the filters. A double layer iron shielding, which is capable of attenuating the stray B-field down to ~ 5 *Gauss*, was added to shield the electronic sections that contain filters. The polarimeter phase after this shielding is presented in Fig. 3.23(b), showing a phase resolution of $\lesssim 2°$ for $f < 500$ *Hz*. The cause of the residual $\lesssim 2°$ phase noise needs further investigation.

A DIII-D power supply test discharge, i.e., a vacuum shot (see Fig. 3.25), is analyzed to assess the phase resolution with the presence of decaying toroidal magnetic field. The phase resolution, i.e., the rms of the phase variations, over a wide frequency range of 500 *Hz*–1 *MHz* is approximately 0.3°. In order to assess the feedback effects induced by mechanical vibration, the extraneous noise, such as 60 *Hz* harmonics (electric noise from power line) were removed from the low frequency phase variations (< 500 *Hz*). The RMS of these low frequency variations is $\sim 0.2°$.

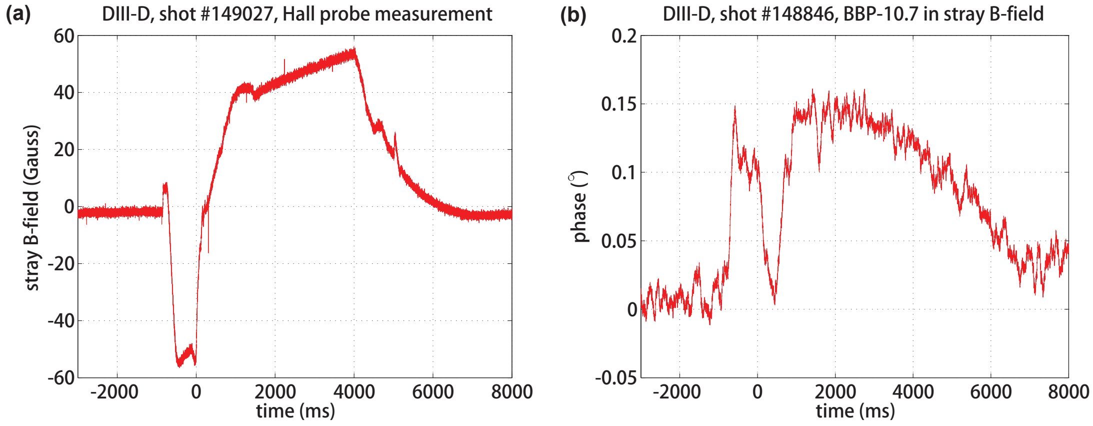

Figure 3.24: *(a) The stray B-field at the polarimeter system was measured by Hall probe in a typical DIII-D shot (#149027). (b) Phase distortion by a Mini-Circuits BBP-10.7 bandpass filter in stray B-field.*

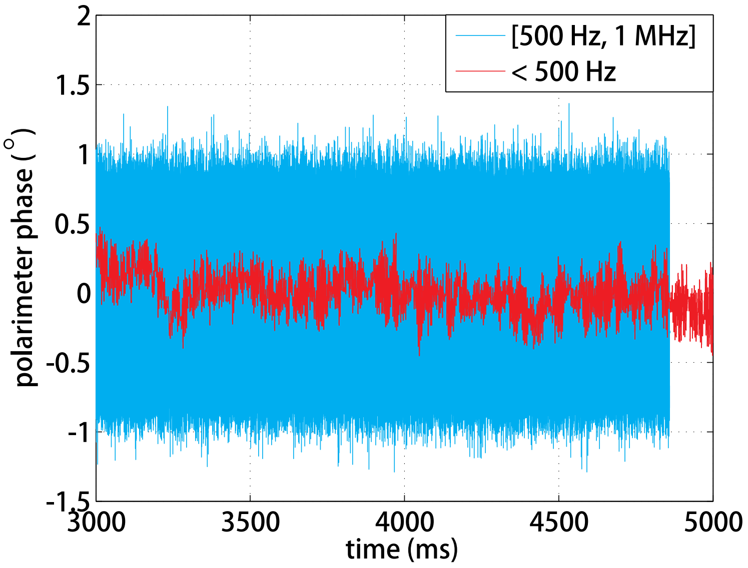

Figure 3.25: *Digitally filtered polarimetry phase variations within frequency range* 500 *Hz*–1 *MHz (cyan) and below* 500 *Hz (red, with* 60 *Hz harmonics removed) during a toroidal-field-only DIII-D shot (#147714,* $t = [3000\ ms, 5000\ ms]$*,* B_T *ramping down from* 0.7 *T to* 0.5 *T,* $I_p = 0$*).*

CHAPTER 4

Polarimetry calculations using synthetic diagnostic code

As discussed in Chapter 1, numerical calculations are critical to assist in the design of polarimetry experiments, as well as for the data interpretation. For this purpose, a synthetic diagnostic code based on Mueller-Stokes theory has been developed. This chapter firstly describes the inputs and outputs of the code. Then the code is preliminarily verified by achieving agreement in the comparison between code outputs and direct integral calculations. The first systematic application of this code is the polarimetry modeling for NSTX based on a realistic plasma equilibrium, in which the interaction between the FR and CM effects was identified. The code was also employed to provide guidance to the polarimetry experiment design on DIII-D.

4.1 Inputs and outputs of synthetic diagnostic code

The synthetic diagnostic code takes as inputs the electron density and B-field profiles along the diagnostic chord, and calculates the Mueller matrices along the wave path and evaluates the resultant detector output. The code traces the Stokes vector evolution using the ODE equation Eqn. 2.36, with three mutually orthogonal initial inputs:

$$\vec{s}(0) = \begin{pmatrix}1\\0\\0\end{pmatrix}, \quad \begin{pmatrix}0\\1\\0\end{pmatrix}, \quad \begin{pmatrix}0\\0\\1\end{pmatrix} \tag{4.1}$$

which correspond to horizontal linear, +45° linear, and RCP polarizations, respectively. The corresponding output Stokes vectors:

$$\vec{s}(z) = \begin{pmatrix}M_{11}(z)\\M_{21}(z)\\M_{31}(z)\end{pmatrix}, \quad \begin{pmatrix}M_{12}(z)\\M_{22}(z)\\M_{32}(z)\end{pmatrix}, \quad \begin{pmatrix}M_{13}(z)\\M_{23}(z)\\M_{33}(z)\end{pmatrix} \tag{4.2}$$

give the 3×3 Mueller matrices along the wave path.

With the launched linear polarization rotating at frequency $\omega_{\mathrm{df}}/2$, the initial condition is:

$$\vec{s}_{3\times1}(0) = \begin{pmatrix}\cos(\omega_{\mathrm{df}}t)\\\sin(\omega_{\mathrm{df}}t)\\0\end{pmatrix} \tag{4.3}$$

If the Mueller matrices along the beam path are known, the resultant Stokes vector can be determined:

$$\vec{s}_{3\times1}(z) = \begin{pmatrix}M_{11}\cos(\omega_{\mathrm{df}}t) + M_{12}\sin(\omega_{\mathrm{df}}t)\\M_{21}\cos(\omega_{\mathrm{df}}t) + M_{22}\sin(\omega_{\mathrm{df}}t)\\M_{31}\cos(\omega_{\mathrm{df}}t) + M_{32}\sin(\omega_{\mathrm{df}}t)\end{pmatrix} \tag{4.4}$$

This expression gives the wave polarization at any position along the propagation path. For the previously described detector, which is oriented to detect $|E_x|^2$ of the emerging wave ($z = 2L$), a sinusoidal voltage signal is generated with a polarimetry phase shift:

$$\phi = \tan^{-1}\left[\frac{M_{11}(2L)}{M_{12}(2L)}\right] \tag{4.5}$$

The temporal evolution of this phase shift can be calculated using time-evolving density and magnetic profiles determined from other diagnostics as inputs to the code.

4.2 Code verification

The preliminary verification of the code was performed by comparing the code outputs and results from direct theoretical calculations in simple scenarios. Specifically, artificial profiles were used as inputs to the code, e.g., a uniform density profile and a magnetic profile that causes the FR effect or the CM effect individually. The output Mueller matrices were then compared with the matrix forms presented in Section 2.4.2. The parameters that characterize the individual FR (ψ in Eqn. 2.42) or the CM effect (δ in Eqn. 2.43) were calculated by the line integrals of Eqn. 2.38. Agreement was achieved in these scenarios and therefore the code was preliminarily verified.

4.2.1 Rotating linear launch scenario

As described in Section 3.3.2, the rotating linear polarization launched by the 288 *GHz* polarimeter is achieved by combining a pair of mm-waves with LCP & RCP polarizations and with a slight difference frequency. This LCP + RCP launch scenario was simulated as a practice to further verify the code. A second module based on Jones calculus was added to the code. It takes the same inputs as the Mueller-Stokes module and calculates Jones matrices along the path, using Eqn. 2.25 and Eqn. 2.27. It was found that with the same input plasma equilibria, the output Jones matrices and Mueller matrices along the path satisfy the the relationship in

Eqn. 2.45. In addition, the polarimeter output with rotating linear launch was also calculated by both calculuses and then compared. As described in Section 3.3.2, the rotating linear polarization is the result of combining a pair of LCP & RCP with equal power but slightly different frequencies. The E-field for LCP & RCP launch was separately tracked by Jones calculus module and then superposed to determine the detector output. The Mueller-Stokes calculus module directly tracks the polarization of the linear launch and predicts the emerging polarization as well as the detector signal. These two calculated signals agree precisely (up to the numerical tolerance applied in calculations) and thereby build confidence in the use of this code to simulate the polarimeter response. It was also found that Mueller-Stokes code requires significantly less intensive computation, which is a big advantage in large scale calculations. The synthetic diagnostic calculations discussed later are referred to the Mueller-Stokes code.

4.3 Interaction between FR & CM effects in polarimetry modeling for NSTX

The first systematic application of the synthetic diagnostic code involved modeling the evolution of EM-wave polarization during propagation in NSTX using a realistic plasma equilibrium. The EM-wave propagates in the major radial direction in NSTX with retro-reflection from the center stack of the vacuum vessel, as shown in Fig. 3.1. (Major radial chords are horizontal chords radiating from the center stack of vacuum vessel.) This modeling illustrates that the CM effect is shown to be strongly weighted to the high-field region of the plasma. An interaction between the FR and CM effects is also clearly identified. The interaction is present when the magnetic field has both parallel and perpendicular components with respect to the wave propagation direction. Elliptization occurs when the wave polarization direction is neither parallel nor perpendicular to the local transverse B-field. Since the FR effect modifies the polarization direction during propagation, it must also affect the resultant elliptization. The CM effect also intrinsically results in rotation of the polarization direction, but this effect is less significant in the plasma conditions modeled. The interaction increases at longer wavelength and complicates interpretation of polarimetry measurements.

4.3.1 Plasma equilibrium used in modeling

The modeling results discussed here are obtained in a typical neutral-beam-heated L-mode plasma (shot #124764, 0.325 s, $B_T = 0.37\ T$) (see Fig. 4.1), which has a major radius of $R_0 = 0.85\ m$ and a minor radius $a = 0.67\ m$. The density profile is centrally peaked with a maximum of $n_0 = 4.7 \times 10^{19}\ m^{-3}$ at $R_{\text{axis}} = 1.0\ m$. The electron plasma and cyclotron frequencies are $f_{pe} = 61.4\ GHz$ and $f_{ce} = 10.5\ GHz$ on axis, respectively.

4.3.2 Modeling results and discussion

For the modeling performed based on the plasma equilibrium, where the radial views studied are well above the plasma midplane (i.e., $\geq 0.1\ m$), the polarization rotation caused by the CM effect is small in comparison with the total rotation ($< 15\%$). This is because throughout the majority of the wave path, either the absolute elliptization angle is small (i.e., $|\chi| \ll 45°$) or the CM effect is much weaker than the FR effect (i.e., $|\mathrm{d}_{\mathrm{CM}}\delta| \ll |\mathrm{d}_{\mathrm{FR}}\psi|$) (see Eqn. 2.41b). The following discussion in this section will

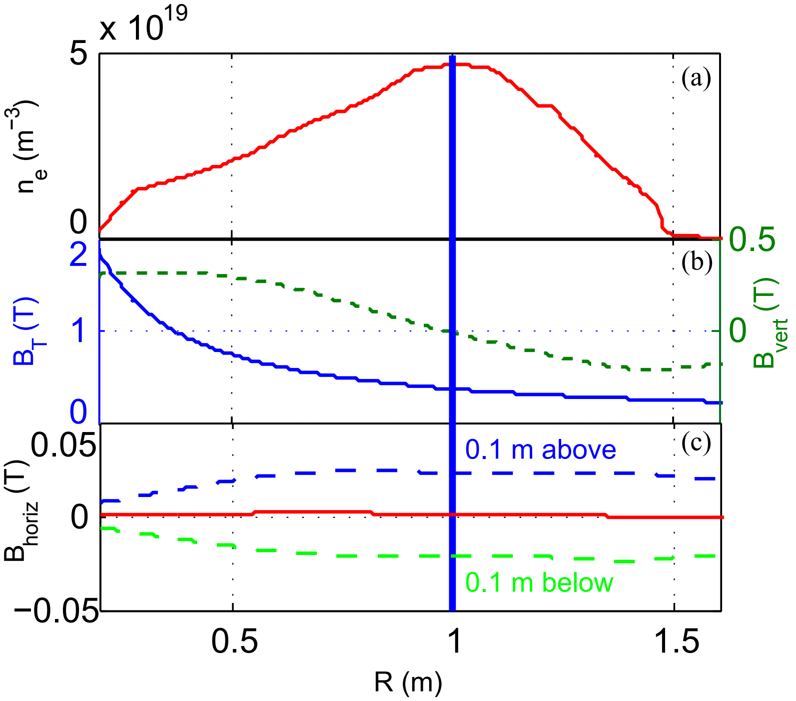

Figure 4.1: *(a) Density profile of a typical neutral-beam-heated L-mode plasma for modeling. (shot #124764, 0.325 s). (b) Toroidal (blue solid line) and vertical (green dashed line) magnetic field along major radius in the midplane (they vary little with height near the midplane). (c) Horizontal (i.e., radial) magnetic field along major radius 0.1 m above (blue dashed line), below (green dashed line), and in (red solid line) the midplane .*

focus on the impact of the FR effect on elliptization. It should be noted that along the chords close to the midplane, where the FR effect is weak, the rotation caused by the CM effect, although small, can be dominant.

The modeling shows that the magnitude of the elliptization angle increases most rapidly when the wave is in the high-field region ($R < R_{\text{axis}}$) (see Fig. 4.2). This stands in contrast with conventional tokamaks. Elliptization is sensitive to the strength of the perpendicular magnetic field (see Eqn. 2.38), of which the toroidal magnetic field B_T is a significant component. B_T varies approximately inversely with major radius in both conventional tokamaks and spherical tori, but in spherical tori, the variation is much stronger because of their relatively low aspect ratio. For instance, in NSTX ($R_0/a \simeq 1.27$) B_T varies from 0.2 T at the outer edge ($R = 1.6$ m) to 2 T close to the center stack ($R = 0.2$ m) (see Fig. 4.1c).

Modeling shows that the evolution of the elliptization depends strongly on the polarization direction in the high-field region. Figure 4.3 shows the dramatically different elliptization evolution for two waves launched in the midplane with launch angles of 0° and +45°. This dependence is expected since elliptization is strongly weighted to the high-field region and sensitive to ψ (see Eqn. 2.41a). For a chord in the midplane, the polarization direction in the high-field region is determined by the launch angle since the FR effect is very weak there ($\vec{B}_{\|}$ is very weak in the midplane).

Of particular interest, the modeling shows that the FR effect can play a significant role in elliptization. Chords away from the midplane can have significant $\vec{B}_{\|}$, so the FR effect can substantially change the polarization direction of the wave before it enters the high-field region. Figure 4.4 compares the elliptization evolution of a wave launched with horizontal linear polarization both with and without the influence of

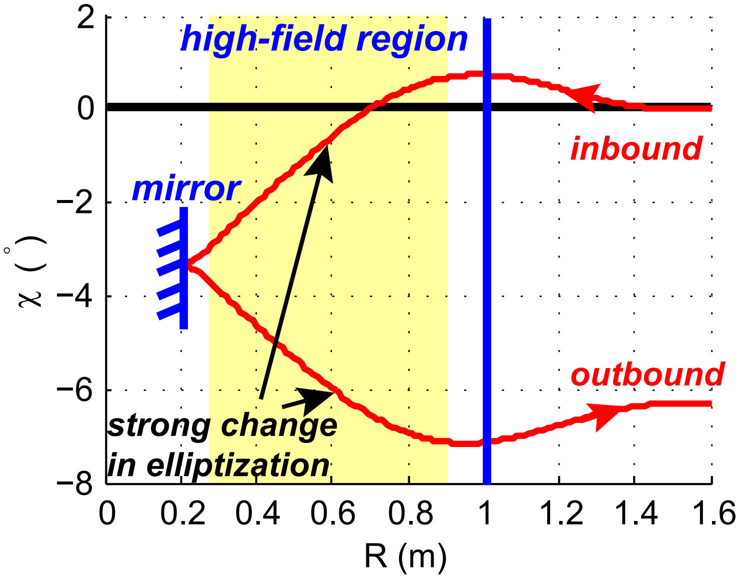

Figure 4.2: *Evolution of elliptization angle (χ) along chord in midplane for waves with horizontal linear polarization at launch (i.e., in toroidal direction). Vertical solid line indicates plasma center (i.e., peak density). The mirror is mounted on the center stack. ($f = 288$ GHz, $\lambda = 1.04$ mm)*

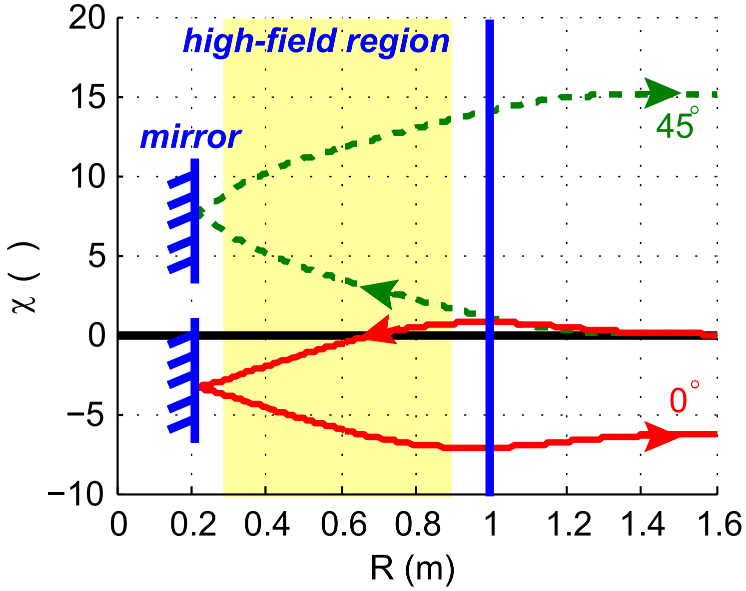

Figure 4.3: *Evolution of elliptization angle (χ) along chord in midplane for waves with horizontal (red solid line) and +45° (green dashed line) linear polarization at launch. Zero elliptization (i.e., linearly polarized) is highlighted on the grid. (f = 288 GHz, $\lambda = 1.04$ mm)*

the FR effect. The final elliptization of the wave is very different for the two cases. The modeled chord is 0.1 m above the midplane, where $|\vec{B}_{\parallel}|$ reaches a maximum of 0.024 T along the chord. For the case without FR effect, $\vec{B}_{\parallel}$ is simply set uniformly to zero along the chord. The impact of the FR effect on elliptization identified here is a primary element of the interaction between the two effects in this modeling.

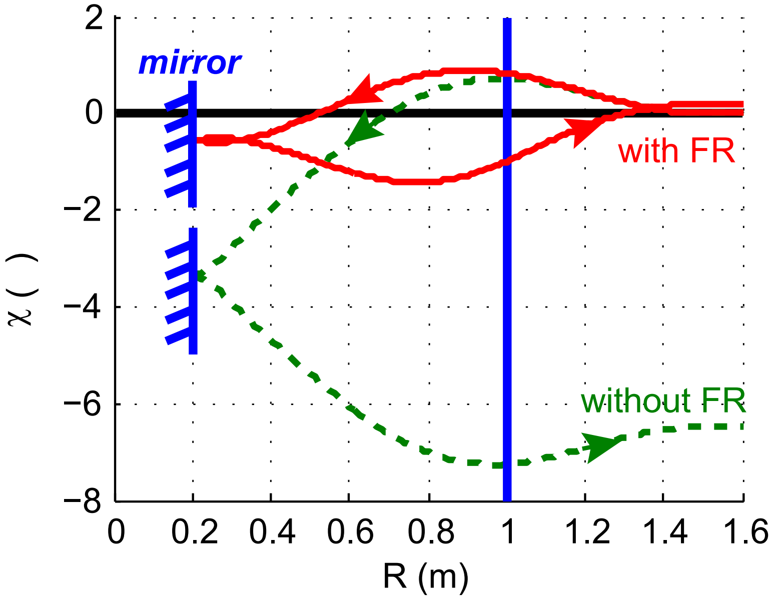

Figure 4.4: *Evolution of elliptization angle (χ) for waves with horizontal linear polarization at launch along a chord* 0.1 *m above midplane with (red solid line) and without (green dashed line) the FR effect. The FR effect is eliminated by setting* $\vec{B}_{\parallel} = 0$ *along chord). ($f = 288$ GHz, $\lambda = 1.04$ mm)*

Modeling shows a significant wavelength dependence in the strength of the impact of the FR effect on elliptization. Both the FR and CM effects are expected to become stronger with increasing wavelength (i.e., lower frequency) (see Eqn. 2.38). However, it is not obvious whether the impact of the FR effect on elliptization should become more or less significant as the wavelength increases. To assess this, the change in the final value of χ caused by including the FR effect is calculated (see Fig. 4.5). The change $\Delta\chi$ is normalized by the difference between the maximum and minimum final values of χ without the FR effect. This normalization factor serves as a measure of the strength of the elliptization effect. Figure 4.5 shows that the relative impact of the FR effect on elliptization increases with wavelength.

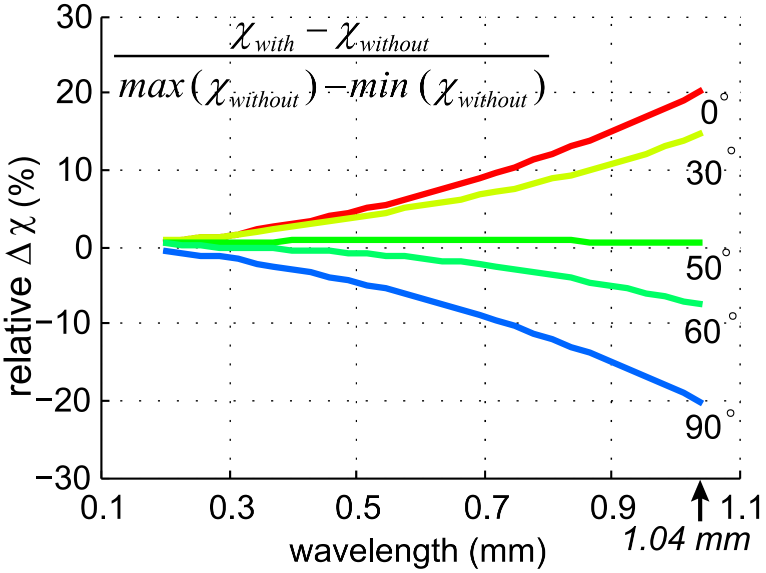

Figure 4.5: *Difference between the final elliptizations with and without the FR effect ($\Delta\chi$) versus wavelength for different launch angles. $\Delta\chi$ is normalized by the difference between the maximum and minimum final values of χ without the FR effect.*

4.3.3 Interaction complicates polarimetry data interpretation

The interaction complicates the interpretation of polarimetry measurements if both the FR and CM effects are large ($\Delta_{\mathrm{FR}}\psi > 45°$, $\Delta_{\mathrm{CM}}\delta > 90°$). For instance, this is the case for the planned "$48, 57\ \mu m$ poloidal polarimeter" in ITER [Pavlichenko et al., 2007] if the CM effect is large enough to be used as an alternative plasma density measurement. Under these conditions, the common practice of simply integrating Eqn. 2.38 to obtain the approximate total polarization rotation or elliptization [Boboc et al., 2006], is no longer valid.

Also, the interpretation of an array of chord measurements used to characterize the equilibrium [Brower et al., 2002; Rommers and Howard, 1996] becomes more complicated. The profile of rotation of polarization direction versus chord impact parameter is affected by the interaction, leading to a change in both the zero crossing and slope. Figure 4.6 shows an example of the impact of including the CM effect in calculating the predicted polarimetry phase response for another NSTX plasma equilibrium (shot #120968). The predicted polarimeter phase with rotating linear polarization launch is calculated and presented. The calculated phase versus chord height is compared using two different sets of assumptions for the calculation. The solid curve shows the full calculation, i.e., all components of the magnetic field are included; this includes both the FR and CM effects as well as any interaction. In contrast, the dashed curve shows a calculation for the same plasma that only includes the horizontal component of the B-field, thereby including only the FR effect in isolation and suppressing the CM effect. The calculated phase is distinctly different for the two cases, indicating that experimental measurements would be misinterpreted if the measured phase were incorrectly assumed to be only caused by the FR effect. For instance, the zero phase point in the solid curve which would be observed at the height of plasma magnetic axis (-5 *cm*) in the absence of the CM effect, is actually observed at -7 *cm* since the CM effect is significant ($\Delta_{\mathrm{CM}}\delta \approx 52°$).

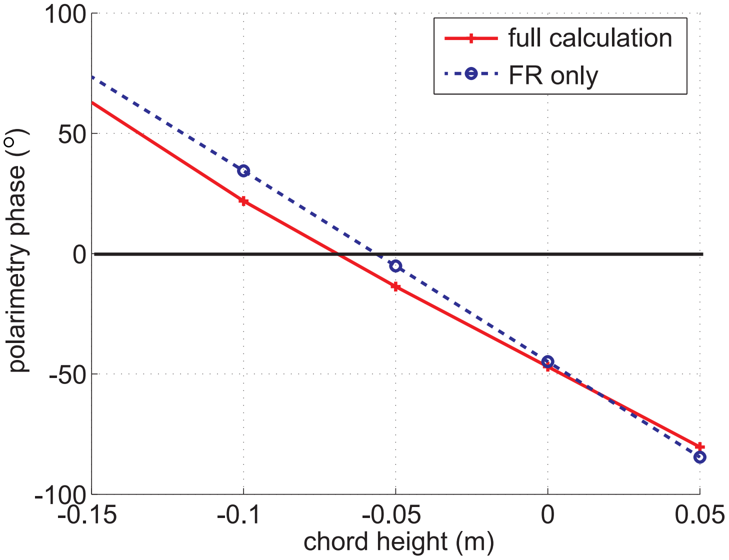

Figure 4.6: *Synthetic height scan of the polarimeter viewing chord referenced to NSTX machine midplane. (shot #120968,* 0.560 s*, magnetic axis at* -5 *cm) Polarimetry phase with a series of chord height is calculated by synthetic diagnostic code. The solid curve shows the predicted phase with both the FR and CM effects included. The dashed curve shows the predicted phase if only the FR effect is included. A solid horizontal line highlights the zero phase.*

4.4 Polarimetry simulations for equilibrium experiment on DIII-D

As will be discussed in Chapter 5, a series of plasma equilibria on DIII-D are used in the equilibrium study experiment. The design of the discharge parameters, especially the B_T strength, which is the most effective parameter that controls the CM effect, is guided by calculations based on a realistic DIII-D discharge (shot #148605). This discharge is an oval shaped "bouncing ball" plasma, whose vertical position starts to be scanned after the current reaches flattop, while the plasma shape, density and current are maintained (see detail in Section 5.1.2.2). The predicted polarimeter phase response versus chord height is presented in Fig. 4.7. As can be seen, at low B_T ($0.75\ T$), the phase is approximately proportional to the height, while at $B_T = 2.0\ T$, the phase is nearly insensitive to the height. This leads to the design of a series of shots utilized in the final equilibrium polarimetry experiment. These shots have the same plasma current ($I_p = 0.3\ MA$) and electron density ($n_e = 1 \times 10^{19}\ m^{-3}$), but different B_T strength, which is stepped up between shots from $0.75\ T$ to $2.0\ T$.

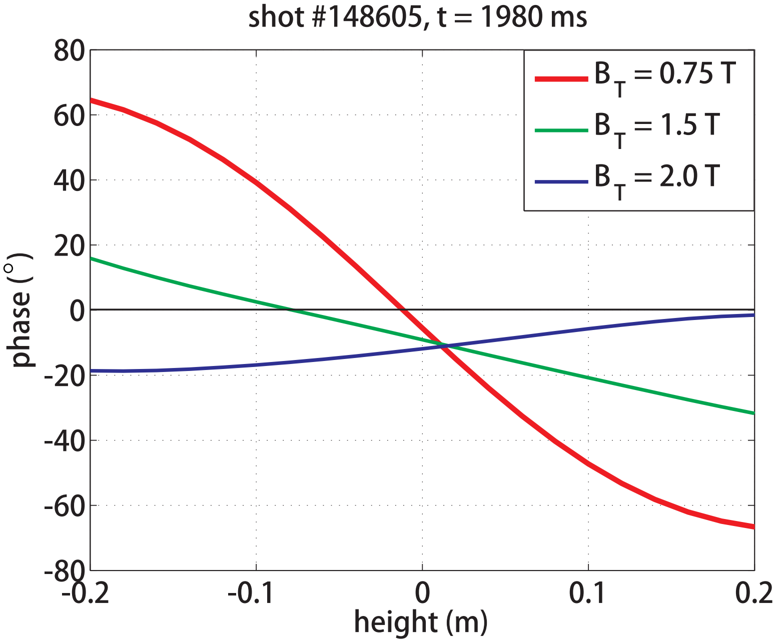

Figure 4.7: *The polarimeter phase versus chord height is calculated based on a realistic discharge on DIII-D (shot #148605).* B_T *is artificially scaled with three different factors.*

CHAPTER 5

Experimental study of plasma equilibrium via polarimetry

As previously discussed, the interaction between the FR and CM effects is expected to play an important role in mm-wave polarimetry in tokamak plasmas. This chapter presents the first experimental study of plasma equilibrium at DIII-D with the 288 *GHz* polarimeter system [Zhang et al., 2013b]. Through the experiment, the Mueller-Stokes theory is validated by the high level agreement achieved in the theory-experiment comparison. This comparison was performed over a broad range of plasma conditions where the relative contributions from the FR and CM effects are varied significantly. In particular, the influence of the CM effect on polarimetry in magnetized fusion plasmas is investigated in detail. The possibility of constraining EFIT by polarimetry measurements is also discussed.

5.1 Experimental validation of Mueller-Stokes theory and investigation of the influence of the CM effect on polarimetry in a magnetized fusion plasma

As discussed in Section 2.4, Mueller-Stokes theory can be used to calculate the polarization evolution of an EM-wave as it propagates through a magnetized plasma. Historically, the theory has been used to interpret polarimeter signals from systems operating on fusion plasmas. These interpretations have mostly employed approximations of Mueller-Stokes theory in regimes where either the Faraday rotation (FR) or the Cotton-Mouton (CM) effect is dominant. The current work presents the first systematic comparison of polarimeter measurements with the predictions of full Mueller-Stokes theory where conditions transition smoothly from a FR-dominant (i.e., weak CM effect) plasma to one where the CM effect plays a significant role. A synthetic diagnostic code, based on Mueller-Stokes theory accurately reproduces the trends evident in the experimentally measured polarimeter phase over this entire operating range, thereby validating Mueller-Stokes theory. The synthetic diagnostic code is then used to investigate the influence of the CM effect on polarimetry measurements. As expected, the measurements are well approximated by the FR effect when the CM effect is predicted to be weak. However, the code shows that as the CM effect increases, it can compete with the FR effect in rotating the polarization of the EM-wave. This results in a reduced polarimeter response to the FR effect, just as observed in the experiment. The code also shows, if sufficiently large, the CM effect can even reverse the handedness of a wave launched with circular polarization. This helps to understand the surprising experimental observations that the sensitivity to the FR effect can be nearly eliminated at $B_T = 2.0\ T$. The results also suggest that the CM effect on the plasma midplane can be exploited to potentially measure magnetic shear in tokamaks. These results establish increased confidence in the use of such a synthetic diagnostic code to guide future polarimetry design and interpret the resultant experimental data.

5.1.1 Introduction

In polarimetry diagnostic, normally either a high frequency microwave or far-infrared beam with known polarization propagates through a magnetized plasma and the transmitted polarization properties are measured. From the measured polarization change, information on plasma internal quantities such as density, current and magnetic field can be determined. This diagnostic has been adopted in various toroidal devices, primarily utilizing either the FR effect (rotation of a linearly polarized EM-wave due to a magnetic field component parallel to the beam propagation) [Bergerson et al., 2012; Riva et al., 2003; Zeeland et al., 2008a] or the CM effect (elliptization of a wave due to magnetic field components perpendicular to the beam propagation; also known as Faraday conversion in Astronomy) [Akiyama et al., 2006; Boboc et al., 2006; Fuchs and Hartfuss, 1998; Huang and Shcherbakov, 2011]. To interpret experimental results, Mueller-Stokes theory, which is also referred to as Poincaré sphere formalism [Segre, 1999] or the Stokes equation [Orsitto et al., 2011], has often been used to calculate the polarization properties of EM-waves after propagation through a plasma. Historically, such analysis has primarily utilized the approximations of Mueller-Stokes theory [Guenther, 2004] with assumptions that either the FR or CM effect dominates the other. However, the theory has not been experimentally validated over a wide range of plasma conditions, where the relative contributions from the FR and CM effects vary significantly. This work presents the first detailed investigation of the influence of the CM effect on polarimetry over this wide range of plasma conditions. In the reported experiment, a recently installed 288 *GHz* polarimeter, originally planned for NSTX [Menard et al., 2012; Ono et al., 2000; Zhang et al., 2012], was installed on DIII-D to probe a series of specially designed plasmas where the toroidal magnetic field is stepped up from 0.75 T to 2.0 T, thereby varying the CM effect from weak to strong (see Section 4.4). A synthetic diagnostic code based on Mueller-Stokes theory has also been used to compare with the polarimetry data over this entire operating range. The code agrees well with polarimeter measurements in all cases investigated, thereby establishing confidence in routine application for data interpretation, even when the CM effect has a significant influence on polarimetry measurements. In the limit of vanishing CM effect, the FR effect represents the accumulated optical path length difference between the launched LCP & RCP during the wave propagation, thereby causing polarization rotation. In this situation, the measurements are well approximated by the FR effect. However, as the CM effect strength increases, it can compete with the FR effect in rotating the wave polarization, resulting in a reduced polarimeter response to the FR effect. The code also shows that sufficiently large CM effect can even reverse the handedness of the waves launched with circular polarizations. In certain plasma conditions, the polarization rotation can be completely cancelled due to this reversal, eliminating the polarimetry sensitivity to the FR effect. Moreover, the results suggest that the CM effect on the plasma midplane can be exploited to measure magnetic shear.

5.1.2 Experimental arrangement

5.1.2.1 Polarimeter diagnostic

The experiment was performed using a recently installed 288 *GHz* polarimeter on DIII-D. Detailed hardware information regarding this system can be found in Chapter 3. A linearly polarized beam whose polarization rotates is produced by combining a pair of counter-rotating circularly polarized waves (LCP & RCP) with equal power but slight frequency difference ω_{df}. The beam is launched along a major radius into the plasma from the outboard side. It retro-reflects from a flat reflective graphite tile on the inside wall, propagates through the plasma a second time, and returns to a polarization sensitive detector. The detector is aligned to detect the beam E-field component in the toroidal direction, and outputs a sinusoidal waveform of frequency ω_{df}. The delay between the horizontal (i.e., toroidal direction) launch and the detection of the maximum signal can be used to assess the polarization changes caused by the magnetized plasma. The phase shift between the signal and a reference sinusoidal waveform, which is synchronized with the launched polarization rotation, is measured to determine the delay. For example, the FR effect would advance the launched horizontal linear polarization rotation, resulting in a phase shift of the maximum measured at the horizontal detector. With the geometry shown in Fig. 3.11, the CM effect is approximately proportional to B_T^2, while the FR effect is insensitive to B_T. Also note that the single-mirror retro-reflection geometry does not cause any cancellation of the polarimetry effects, but merely doubles the beam propagation path.

5.1.2.2 Development of plasmas

A series of oval shape, inside-wall-limited, low density ($n_e < 3 \times 10^{19}\ m^{-3}$), low temperature ($T_e < 1\ keV$), simple L-mode shots were developed for the theory validation experiment. Relatively low-density plasmas were selected to avoid severe beam refraction with temperatures sufficiently low to avoid any relativistic corrections. The L-mode plasmas possessed peaked density profiles that are typically much simpler than observed in H-mode, which normally involve more complicated profiles. These choices helped to achieve a clear comparison between measurements and theory predictions. After the plasma current reached a flattop, the target plasma was vertically scanned while maintaining the shape, density and current, i.e., a so-called "bouncing ball" scenario (see Fig. 5.1a). Figure 5.1(b) shows the magnetic flux contours at different times in shot #150161. The black horizontal line indicates the location of the polarimeter probe beam. The vertical scan allows theory-experiment comparison to be performed as the diagnostic chordal view was moved away from the plasma midplane, so that the FR effect is varied in time. Between shots the toroidal magnetic field strength was increased in discrete steps, while the plasma density and current were kept constant. The basic discharge parameters and estimated FR, CM effects are summarized in Table 5.1. The strength of the FR and CM effects are given by the line integrals of Eqn. 2.38 along a chord 5 cm above the plasma midplane.

For shots #150161, #150159, #150126, as B_T is increased from 0.75 T to 2.0 T, the FR effect is approximately constant while the CM effect increases from weak to strong. Critical diagnostic data were also acquired for offline plasma profile reconstruction analysis, e.g., CO_2 interferometers [Zeeland et al., 2006a], multi-points Thomson scattering [Carlstrom et al., 1992], Mirnov coils, etc.

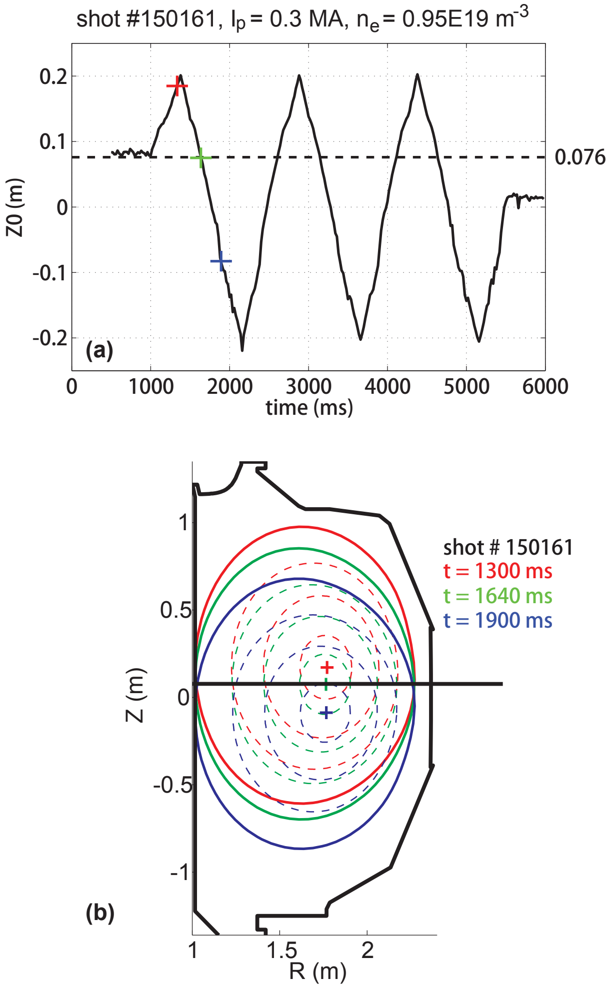

Figure 5.1: *In plasma shot #150161, the plasma position is vertically scanned after reaching the current flattop, while maintaining the plasma shape, density and current. (a) Time trace of vertical position of plasma center ($Z0$); the dashed horizontal line represents the polarimeter probe chord height. (b) Magnetic flux contours of three time slices corresponding to the red, green and blue marks in (a). The black horizontal line indicates the polarimeter probe beam.*

Table 5.1: *Basic discharge parameters and estimated Faraday rotation (FR, $\Delta_{\mathrm{FR}}\psi$) and Cotton-Mouton (CM, $\Delta_{\mathrm{CM}}\delta$) effects. Electron density (n_e) is line averaged along a vertical chord.*

Shot No.	B_T (T)	I_p (MA)	n_e ($10^{19}\ m^{-3}$)	$\Delta_{\mathrm{FR}}\psi$ (degrees)	$\Delta_{\mathrm{CM}}\delta$ (degrees)	Comments
150161	0.75	0.3	0.95	5.6	28.0	FR-dominant
150126	2.0	0.3	0.95	5.6	187.4	Strong CM
150159	1.5	0.3	0.95	5.6	101.6	Intermediate CM
150123	2.0	1.0	1.7	32.6	381.0	Strong FR & CM

5.1.3 Results

Figure 5.2 shows the temporal evolution of the measured polarimeter phase ($\Delta f < 500\ Hz$, phase resolution $< 2°$) of three different toroidal field strength shots while maintaining the plasma shape, density and current. (The red, blue and green curves correspond to the cases in the 1st through the 3rd row in Table 5.1, respectively.) The red curve is the 0.75 T case, showing that the phase is approximately proportional to the vertical distance between the probe chord and plasma midplane (see Fig. 5.1a), with the sign reversing as the chord vertically sweeps across the plasma center. The blue curve is the 2.0 T case, showing a surprisingly weak response to the same vertical scan with no sign reversal across plasma center. The green curve is the 1.5 T case, which lies in-between these two extremes. As will be presented later, the dramatically different responses are all consistent with the synthetic diagnostic code predictions using Mueller-Stokes theory. The following will focus on comparison between the measurements (illustrated in Fig. 5.2) and polarimeter phase calculated using the synthetic diagnostic code. The magnetic field profiles required as inputs to the code are determined using an equilibrium fitting code (EFIT) [Lao et al., 1985], with the fitting mode optimized for L-mode plasmas (i.e., with no edge gradient and current, and magnetic coil data only). The density profile is reconstructed from Thomson scattering, constrained by line-integrated density measurements from the CO_2 laser interferometers, and spatial mapping information from EFIT.

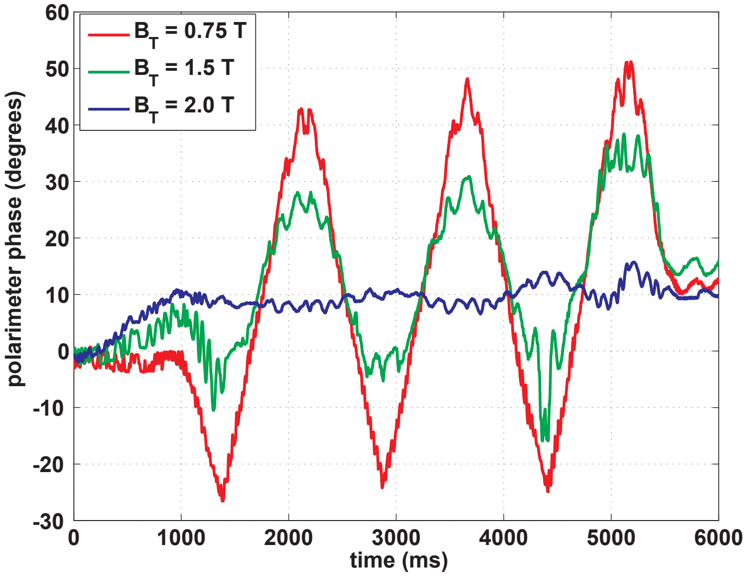

Figure 5.2: *Time traces of measured polarimetry phase of three shots, #150161 ($B_T = 0.75$ T, in red), #150159 ($B_T = 1.5$ T, in green) and #150126 ($B_T = 2.0$ T, in blue). These shots have the same plasma shape, density and current.*

Figure 5.3 separately compares phase measurements with predictions from the Mueller-Stokes theory for the cases where the relative contributions from the FR and CM effects vary significantly. (Panels a-d correspond to the 1st through the 4th row in Table 5.1, respectively.) The measured phase is plotted in green. The theory predictions are shown every 20 ms. The black curve is the full calculation including both FR and CM effects, as well as their interactions; ±10% error is estimated as an upper limit of the uncertainty from density and EFIT profile input, except for the unphysical spikes in the profiles. Also plotted is the FR-only calculation in red, where the transverse B-field components are artificially turned off, i.e., only B_R is included in the calculation. Figure 5.3(a) presents the low B_T case (shot #150161, $B_T = 0.75\ T$, $I_p = 0.3\ MA$, $n_e = 0.95 \times 10^{19}\ m^{-3}$). As can be seen, the three time traces illustrating the measurements (green), the full calculation (black), and the FR-only calculation (red) almost overlie each other showing that the synthetic diagnostic using Mueller-Stokes theory accurately predicts the experimental measurements. As can also be seen, in this plasma the measurement is dominated by the FR effect with very small contributions from the CM effect ($\Delta_{\mathrm{CM}}\delta < 30°$). Figure 5.3(b) shows the high B_T case where a similar FR effect to Fig. 5.3(a) is expected, but accompanied by a much stronger CM effect (shot #150126, $B_T = 2.0\ T$, $I_p = 0.3\ MA$, $n_e = 0.95 \times 10^{19}\ m^{-3}$, $\Delta_{\mathrm{CM}}\delta > 180°$). The FR effect is approximately the same as in shot #150161 (red curve in Fig. 5.3a), due to the similar density and current profiles in both shots. The similarity of the green and black curves again demonstrates good agreement between the code prediction and the measurement. Figure 5.3(c) illustrates the case with intermediate B_T and therefore an intermediate CM effect (shot #150159, $B_T = 1.5\ T$, $I_p = 0.3\ MA$, $n_e = 0.95 \times 10^{19}\ m^{-3}$). Again agreement is achieved between the measurement (green curve) and the full theory prediction (black curve). Note again, in this case, that the full calculation is quite distinct from FR-only calculation, which is similar to the red curve in Fig. 5.3(a). Figure 5.3(d) shows the time traces for shot #150123 ($B_T = 2.0\ T$, $I_p = 1.0\ MA$, $n_e = 1.7 \times 10^{19}\ m^{-3}$) which has both stronger FR and CM effects as well as stronger interactions in comparison to the previous three shots. The full theory prediction (black curve) yet again reproduces the measured phase (green curve). The FR-only calculation is plotted in red for comparison.

5.1.4 Discussion

As can be seen in Fig. 5.3, the synthetic diagnostic code based on Mueller-Stokes theory accurately predicts the measured polarimeter phase over a broad range of plasma conditions where the relative contributions from the FR and CM effects are varied significantly. This high level of agreement builds confidence in the use of this code to investigate the influence of the CM effect on polarimetry measurements. The code naturally includes both the FR and CM effects as well as their interactions, and enables the visualization of polarization evolution along the beam propagation path inside the plasma. The characterizing angle pair $\{\psi,\chi\}$ of the E-field ellipse can be determined from the local Stokes vector, which is the calculated Mueller matrices multiplied by the initial Stokes vector (Eqn. 3.1 in [Segre, 1999]). For the probe chords near plasma midplane ($|d| \leq 0.2\ m$), the FR effect, resulting from the horizontal magnetic field component B_R, is approximately proportional to d, the vertical distance between the chord and plasma midplane [Brower et al., 2002]. In contrast, the CM effect is almost constant over the vertical scan because of the invariant B_T contribution and weak density variation. Due to the height invariance of the CM effect, in the absence of the FR effect, approximately no phase variation is expected in the vertical scan.

Figure 5.4 shows a series of calculated polarization states at several positions along the propagation path for a chord 25 cm above the plasma midplane in the FR-

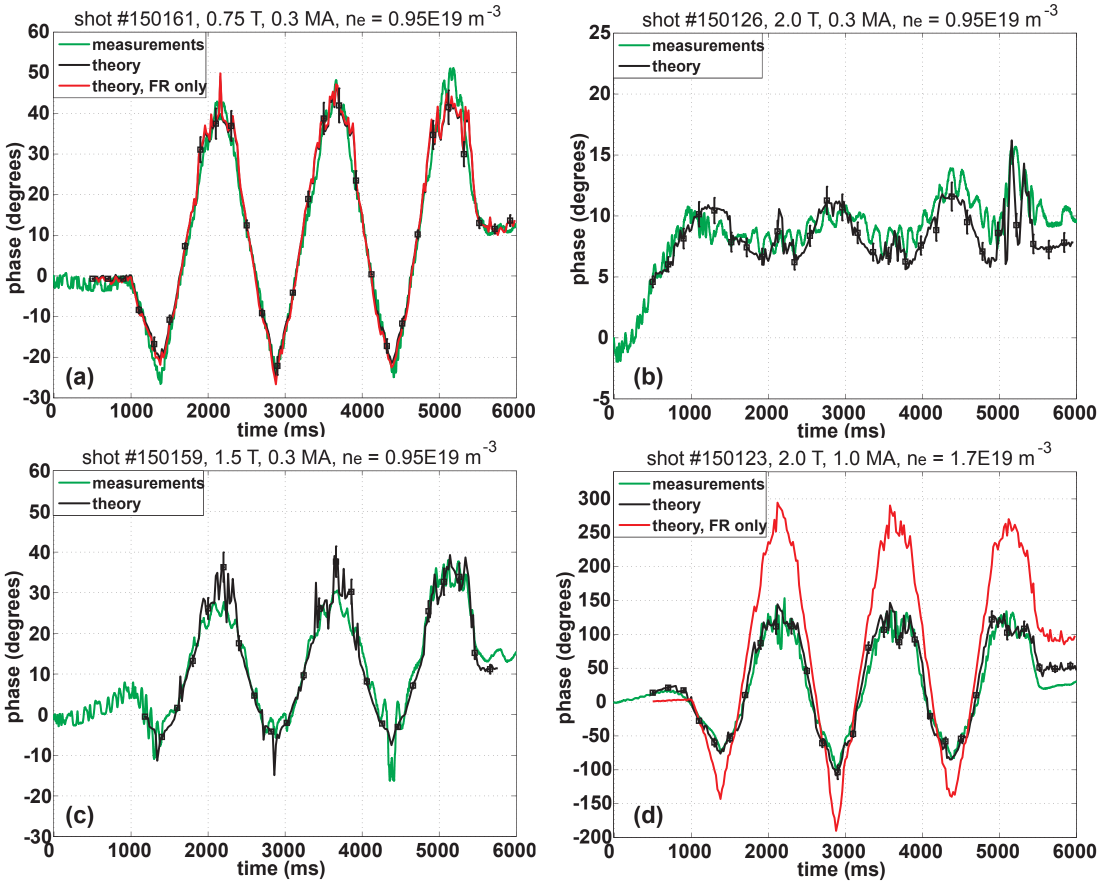

Figure 5.3: *Time traces of polarimetry phase of experimental measurements and Mueller-Stokes theory predictions for four different shots. The shots have the same vertical scan starting at 1000 ms. The green curve is the measured phase below 500 Hz (phase resolution < 2°). The black curve is the calculated phase from the synthetic diagnostic code based on the theory, using the EFIT magnetic profile and Thomson scattering density profile. The red curve is the calculated phase including only the FR effect. (a) Low B_T (0.75 T) case; (b) high B_T (2.0 T) case; (c) intermediate B_T (1.5 T) case; (d) is another high B_T (2.0 T) case with different I_p and n_e from (a–c).*

dominant case ($B_T = 0.75\ T$). All the polarization ellipses are depicted as observed in the laboratory frame, looking in the direction of increasing major radius. The figure shows a wave launched with +45° linear polarization because the polarization is most strongly impacted by the CM effect for this rotation angle at launch. Since the magnetic field perpendicular to the propagation path is approximately in the toroidal direction, a +45° launch is naturally divided into almost equal O- & X-mode components thereby maximizing the elliptization. As can be seen from the black ellipses, which show the full calculation including both the FR and CM effects, linear polarization is slowly elliptized exiting the plasma with a small final elliptization $\chi(2L) \approx 14^\circ$. The results of a calculation including only the FR effect are also plotted in red for comparison, showing that the linear polarization continuously rotates clockwise. The red line closely tracks the major axis of the black ellipse, consistent with the expected dominance of the FR effect in this case. Both calculations yield similar predictions for the microwave power that would be measured by the horizontally oriented detector. Also, of course, a wave launched with horizontal linear polarization would be much less impacted by the CM effect (not shown). Thus the modulation of power that would be measured by a horizontal detector for a rotating linear launch is predicted to be very similar for the combination of CM and FR effects to that for just the FR effect. This is evident in the close overlying of the experimental detector phase data with both the black (full calculation) and the red (FR-only) curves in Fig. 5.3(a).

The rotating linear polarization that is launched results from a superposition of two waves with counter-rotating circular polarizations, LCP & RCP, and slightly different frequencies. The two EM-waves have different wavelengths in the magnetized plasma primarily because of their different polarizations. (The

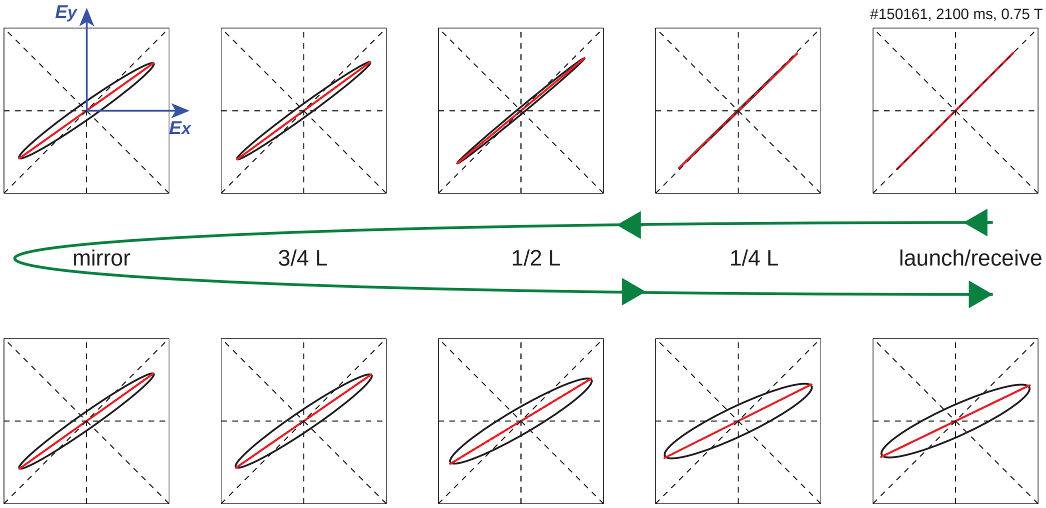

Figure 5.4: *Snapshots of inbound (upper row) and outbound (lower row) E-field ellipse of a +45° linear polarization launched along a chord 25 cm above the plasma midplane in FR-dominant case ($B_T = 0.75$ T). The black ellipses are the results from full calculation, and red lines are from the FR-only calculation. Please note that all the polarizations are observed in the laboratory frame, which is looking in the direction of increasing major radius.*

phase difference caused by the frequency difference is negligible in comparison with that caused by the different polarizations associated with their propagation.) The measured detector phase shift directly relates to this accumulated difference. For example, in the FR-dominant case, the LCP & RCP waves are approximately the characteristic polarizations, and both waves maintain their circularity. The LCP wave has a slightly shorter wavelength than the RCP, thereby creating an accumulation of phase difference. When the two waves are superimposed, a rotation in the resultant linear polarization is observed. Of course, in general the polarization of each wave evolves during propagation. For example, in a situation with a much larger CM effect (e.g., the $B_T \geq 1.5\ T$ cases) the polarization of each wave can evolve from circular to linear and then begin to elliptize again, but with a handedness reversed compared to the launch. In this situation, the accumulated phase difference actually begins to decrease after the handedness reversal. Figure 5.5 illustrates how this evolution can occur. The phase δ by which E_y leads E_x is a useful parameter to characterize the evolution, since it is changed by the strong B_T. A wave with LCP ($\delta = -90°$, $s_3 = -1$) can evolve to have linear polarization ($\delta = 0°$, $s_3 = 0$) and then become right-handed ($0° < \delta < 180°$, $s_3 > 0$) [Born et al., 2000]. During such evolution, the two waves, launched with orthogonal polarizations, maintain their orthogonality along the propagation path. Specifically, their polarization ellipses always have opposite handedness and orthogonally oriented major axes. The accumulation rate of the phase difference is a function of the polarization of the waves during propagation. In particular, the accumulation rate changes sign once the handedness of the waves reverses, so that any accumulated difference begins to diminish.

Figure 5.6 shows the evolution of a LCP wave in high $B_T = 2.0\ T$ (see

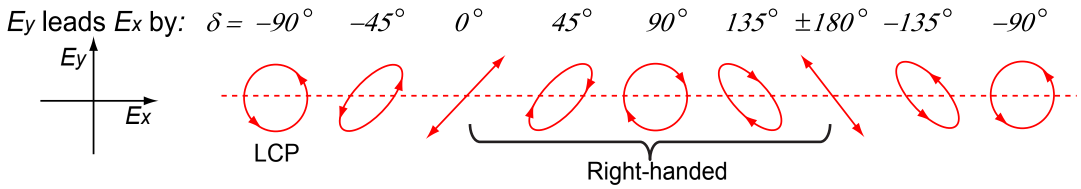

Figure 5.5: *Polarization evolution due to the CM effect. As the phase δ increases, the LCP ($\delta = -90^\circ$) can transition to linear polarization ($\delta = 0^\circ$) and then become right-handed ($0^\circ < \delta < 180^\circ$).*

Fig. 5.6a) and intermediate $B_T = 1.5\ T$ (see Fig. 5.6b) shots, with CM effect $\Delta_{\text{CM}}\delta \approx 187^\circ, 102^\circ$ respectively, along a probe chord $5\ cm$ above the plasma midplane. Figure 5.6(a) shows that the launched LCP gradually becomes linearly polarized as it approaches the reflective tile on the inside wall and then transitions to right-hand polarization. Similarly, the RCP launch, which is not shown, maintains its orthogonality and eventually converts to left-hand polarization. After the transition, because the handedness of the polarizations has been exchanged, the accumulated phase difference begins to diminish. In the case shown in Fig. 5.6(a), the transition point is close to half of the beam path, thus the accumulated phase difference during outbound almost exactly cancels the inbound accumulation. This cancellation is independent of the chord height due to the almost constant CM effect. Thus it results in a very weak phase response to the vertical scan (blue curve in Fig. 5.2), instead of a proportional FR-only response (red curve in Fig. 5.2). Figure 5.6(b) shows that in the intermediate B_T case the transition point occurs at approximately 3/4 of the way along the beam path, resulting in only a partial cancelation of the accumulated phase difference. This leads to a reduced phase response to the vertical scan (green curve in Fig. 5.2).

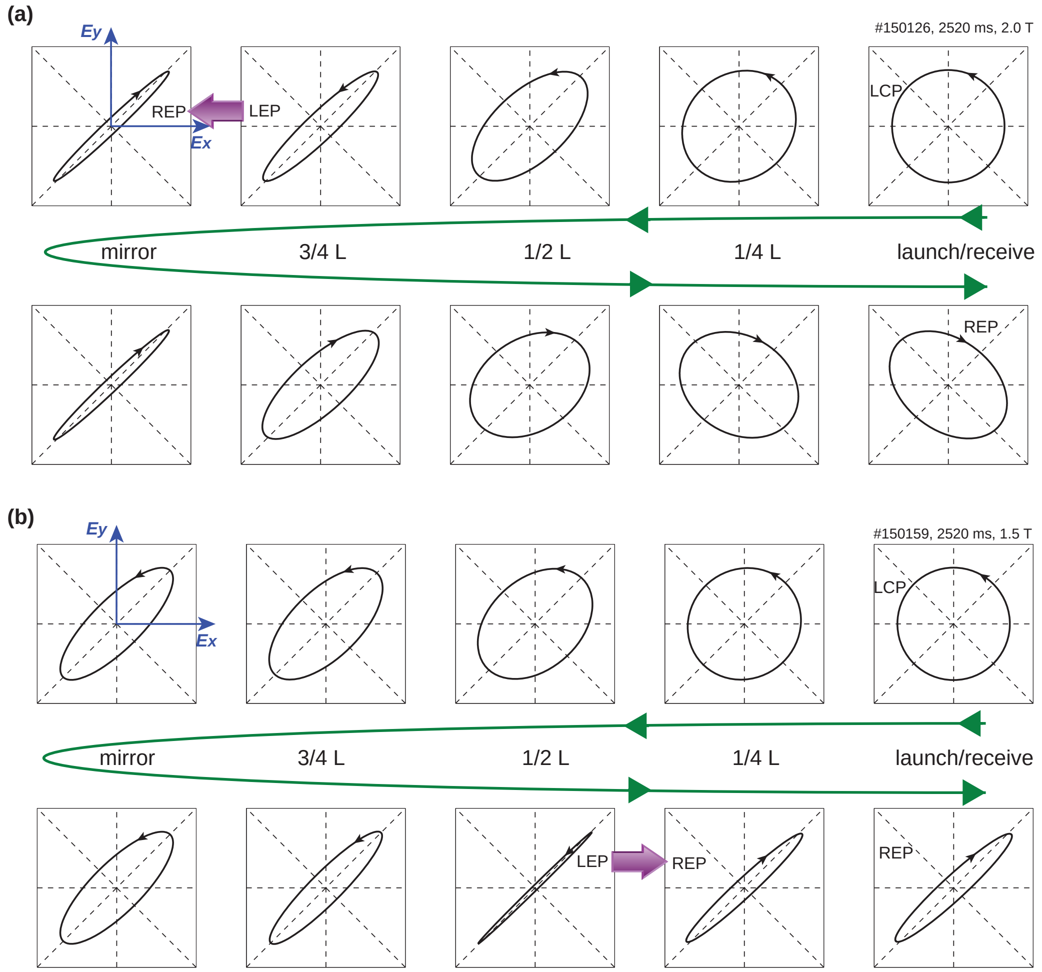

Figure 5.6: *Snapshots of polarization at different positions of a wave launched with LCP along a chord 5 cm above the plasma midplane. These two shots shown here have the same* $I_p = 0.3$ *MA,* $n_e = 0.95 \times 10^{19}$ m^{-3}*, but different* B_T*. (a)* $B_T =$ 2.0 *T, strong CM effect; (b)* $B_T = 1.5$ *T, intermediate CM effect. The transition points, where the handedness of the polarization reverses, from left-hand elliptical polarization (LEP) to right-hand elliptical polarization (REP), are marked with bold arrows.*

The plasma polarimetry effects are essentially a distributed response since both the FR and CM effects contribute along the entire beam path. Still it is helpful to consider a simple lumped optical component picture. As shown in Fig. 5.7, the CM and FR effect of the $B_T = 2.0\ T$ plasma (see Fig. 5.6a) are respectively equivalent to a $\lambda/4$ wave plate with its slow axis along toroidal direction, and a Faraday rotator. (A Faraday rotator is, as the name suggests, an optical component that can rotate the incoming polarization direction in the laboratory frame using the FR effect.) In this lumped component model, the $\lambda/4$ wave plate is arranged to be closer to the mirror because of the $1/R$ dependence of B_T while the FR effect is primarily from the plasma center. The combination of the mirror and $\lambda/4$ wave plate is equivalent to a reflective $\lambda/2$ wave plate. For a linear polarization launch, the polarization direction is rotated by the Faraday rotator, which is then flipped around the optical axis after passage through the equivalent $\lambda/2$ wave plate. Therefore the outbound rotation caused again by the return passage through the Faraday rotator cancels the inbound rotation.

To further investigate the influence of the CM effect on polarimetry measurements, an artificial B_T scan was simulated over an extended B_T range. The plasma equilibrium density and current profiles at $t = 3280\ ms$ of $B_T = 0.75\ T$ shot were used and kept constant through the simulation. The difference in polarimetry phase between probe chords 5 cm above and 5 cm below the plasma midplane is used to quantify the polarimeter sensitivity to the FR effect. Figure 5.8 shows the theoretically predicted sensitivity curve with $\pm 10\%$ error band and the previous experimental data points are over-plotted with $\pm 2^\circ$ error bar. The slight disagreement between the theory curve and experimental data point at $0.75\ T$ is because the equilibrium used in the simulation (when the plasma is centered on

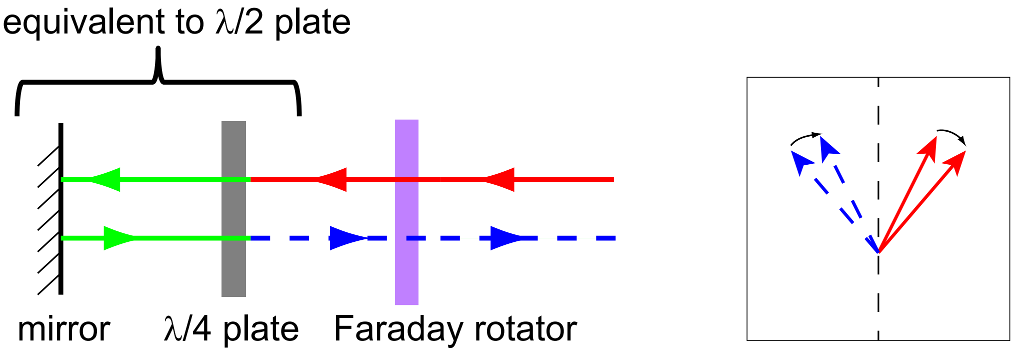

Figure 5.7: *Lumped optical component picture for high* $B_T = 2.0$ *T case. The combination of the mirror and* $\lambda/4$ *wave plate is equivalent to a reflective* $\lambda/2$ *wave plate. For a linear polarization launch, the polarization direction is rotated by the Faraday rotator, which is then flipped around the optical axis after passage through the equivalent* $\lambda/2$ *wave plate. Therefore the outbound rotation (blue vectors) caused again by the return passage through the Faraday rotator cancels the inbound rotation (red vectors).*

the machine midplane) is at different time from when the experimental data point is acquired (plasma centered at ± 5 *cm* with respect to the probe chord, which is 7.6 *cm* above the machine midplane). The slight disagreement with other B_T cases is also expected to be caused by the slight differences in the equilibria between shots. But nevertheless the clear trend in the data points is predicted by the theory simulation. The following discussion focuses on the simulation curve. The sensitivity is almost constant for the region $B_T < 0.9\ T$ (FR-dominant), and decreases as B_T approaches 1.9 T, where the plasma CM effect is equivalent to a $\lambda/2$ wave plate. As B_T increases beyond 1.9 T, the phase difference accumulates with opposite sign after the handedness reversal continues to grow beyond what was necessary to eliminate the accumulation prior to reversal. At this point in the B_T scan the sensitivity to the FR effect is negative because the handedness reversal causes the phase difference to accumulate with an opposite sign to that in the FR-dominant regime. As B_T continues to increase, a second handedness reversal develops along the path ($B_T \sim 2.1\ T$), leading to another change of the sign in the phase difference accumulation. This eventually leads to another full elimination of the accumulated phase difference and then another change in the sign of the sensitivity. This scenario indicates that there is a quasi-periodic oscillation in the sensitivity curve. However, the detailed curve structure depends on the density and magnetic profiles, which both are not uniform along the path. This will be investigated in future work.

The above discussion is clearly illustrated in Fig. 5.9, which shows cartoons of phase accumulation and de-accumulation regions of the beam path at four different B_T strengths. The handedness reversals are indicated by bold arrows. It is worth noting that the launched LCP requires at least $\Delta_{\mathrm{CM}}\delta = 90^\circ$ to transition to right-handed, while requires an extra $\Delta_{\mathrm{CM}}\delta = 180^\circ$ to transition back to left-handed (see

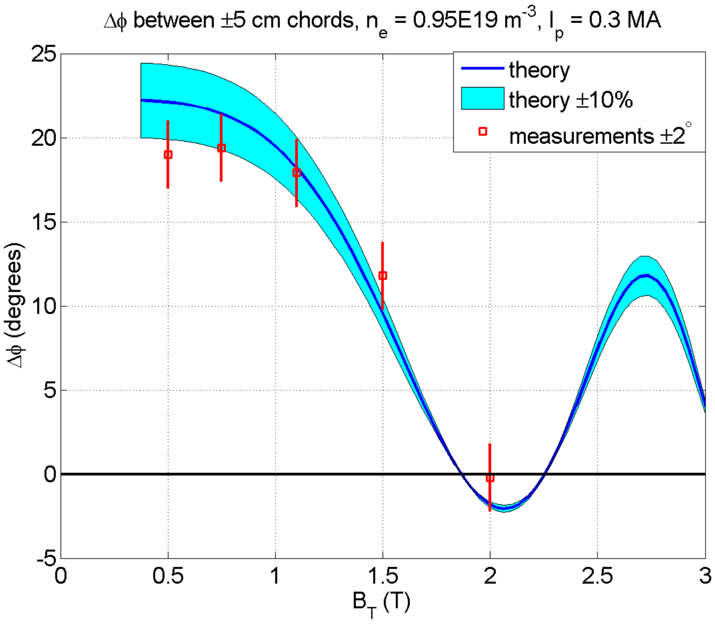

Figure 5.8: *Phase sensitivity for B_T scan simulations based on Mueller-Stokes theory (blue curve) with ±10% error band and experimental data overlay (square points) with ±2° error bar. The phase sensitivity ($\Delta\phi$) is the difference in polarimetry phase between chords 5 cm above and 5 cm below plasma midplane.*

Fig. 5.5). This explains why the phase de-accumulation region is longer than the accumulation region in $B_T = 2.1\ T$ case, where a negative sensitivity is predicted. At $B_T = 2.7\ T$, the phase de-accumulation region is significantly shorter than $B_T = 2.1\ T$ case because the high-field (i.e., inboard) region accounts for the majority of the CM effect. The FR effect, in contrast, is primarily from the plasma center. Those reasons can explain the nearly full sensitivity recovery at $B_T = 2.7\ T$.

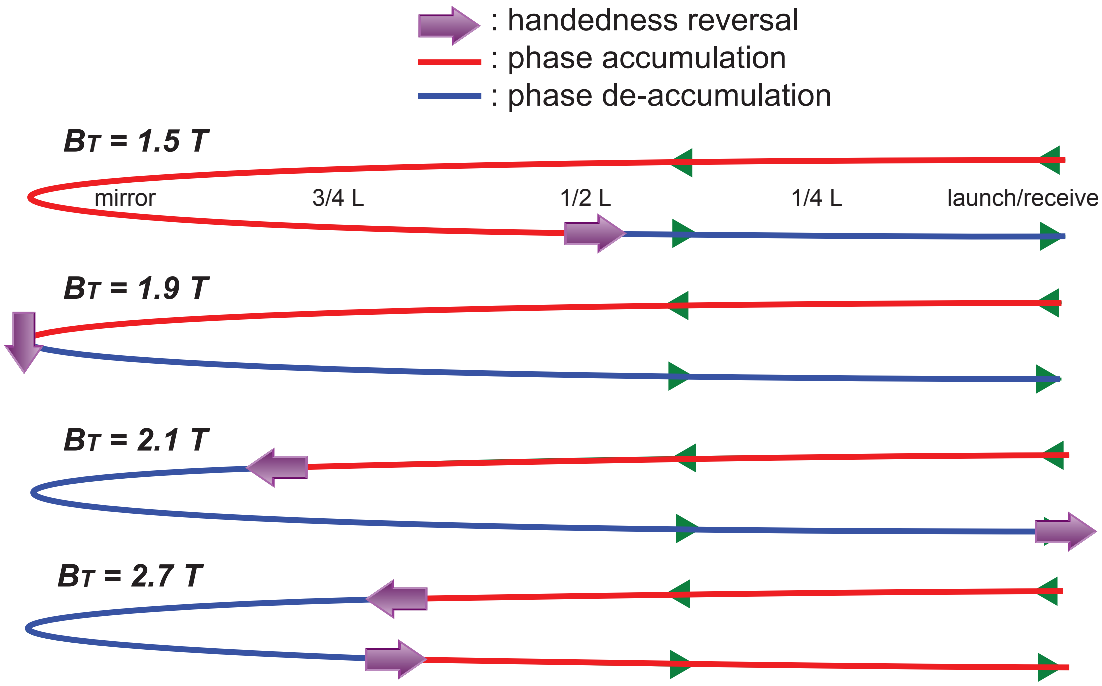

Figure 5.9: *Cartoons of phase accumulation (red) and phase de-accumulation (blue) regions of the beam path at four different B_T strengths. The bold arrows represent the handedness reversals.*

It is interesting to observe that in the range of $0.9\ T < B_T < 1.4\ T$, where the CM effect is moderate yet non-negligible ($30° \lesssim \Delta_{\rm CM}\delta < 90°$), the sensitivity also drops even without the handedness reversal, which requires $\Delta_{\mathrm{CM}}\delta > 90°$. This is because as the CM effect becomes significant, it can compete with the FR effect. As noted in Section 5.1.2.1, the delay between the horizontal (i.e., toroidal direction) launch and the detection of the maximum signal can be used to assess the polarization changes due to the magnetized plasma. The phase shift between the signal and a reference sinusoidal waveform, which is synchronized with the launched polarization rotation, is measured to determine the delay. The measured phase shift equals twice the launch angle that gives the maximal final horizontal E-field at $z = 2L$. In the cases being discussed, a horizontal linear polarization launch does not experience much rotation from the FR effect ($|\Delta_{\mathrm{FR}}\psi| \ll 45°$). It also remains near parallel with B_T during propagation, so the elliptization is weak. Figure 5.10(a) illustrates that in the simulated $B_T = 1.2\ T$ case, the final polarization ellipses are very thin, for such a horizontal launch along chords 5 cm above (black ellipse in solid line) and 5 cm below (black ellipse in dashed line) the plasma midplane. The horizontal launch experiences approximately the minimal elliptization compared to other launch angles, giving a final horizontal E-field close to maximal. Therefore a linear polarization launch angle of $-\psi(z = 2L)\big|_{\psi_0=0°}$ would approximately result in the maximal final horizontal E-field. So the phase shift measured by the horizontal detector approximately equals $-2\psi(z = 2L)\big|_{\psi_0=0°}$. In fact, the code shows that the launch angle that gives the maximal detector signal is approximate $-\psi(z = 2L)\big|_{\psi_0=0°}$. The FR-only calculations are also plotted in red for comparison, which show larger final angles thereby larger phase shifts than the full calculation.

An alternative approach to understanding the competition between the FR and the CM effects is provided by Eqn. 2.41b, which represents the polarization ellipse rotation rate inside the magnetized plasma. γ is the transverse magnetic field pitch angle in the wave frame, which is very small in the plasmas being discussed. In the limit of $\gamma \to 0$, (Eqn. 2.35 substituted into Eqn. 2.41b):

$$\frac{\mathrm{d}\psi}{\mathrm{d}z} \xrightarrow{\gamma\to 0} \frac{\mathrm{d}_{\mathrm{FR}}\psi}{\mathrm{d}z} - \frac{1}{4}\frac{\mathrm{d}_{\mathrm{CM}}\delta}{\mathrm{d}z}\sin 4\psi \tan\delta \tag{5.1}$$

The first term on the RHS is the FR-only term, and the second term represents the influence of the CM effect. For example, the horizontal launch along chord 5 *cm* below plasma midplane (dashed ellipses in Fig. 5.10a) maintains $0^\circ \leq \psi(z)\big|_{\psi_0=0^\circ} \ll 45^\circ$ and $0^\circ \leq \delta(z)\big|_{\psi_0=0^\circ} \ll 90^\circ$ throughout the propagation. Therefore the second term on the RHS always competes with the FR-only term in rotating the polarization ellipse, and as a result:

$$\left|\frac{\mathrm{d}\psi}{\mathrm{d}z}\right| < \left|\frac{\mathrm{d}_{\mathrm{FR}}\psi}{\mathrm{d}z}\right| \tag{5.2}$$

It is worth noting that in the cases where δ approaches 90°, e.g., Fig. 5.6(a) and 5.6(b), Eqn. 5.1 breaks down with the second term on the RHS going to infinity.

In Fig. 5.10(a) it is also clear to see that the black ellipses are asymmetric with respect to the horizontal line, although the chord locations are symmetric with respect to the plasma midplane. This asymmetry is caused by the presence of the magnetic field shear. In the absence of magnetic shear, i.e., the vertical magnetic field $B_Z = 0$, the emerging ellipses are mirror images (see Fig. 5.10b), with anti-symmetric rotation. On the plasma midplane, where there is no FR effect, the horizontal launch would result in the maximum of the horizontal detector signal and thereby zero phase shift. Therefore nonzero phase shift measured on the plasma midplane (e.g., Fig. 5.3b) is directly due to the existence of magnetic shear. This suggests a potential for exploiting the CM effect on the midplane to diagnose magnetic shear [Cano et al., 1971].

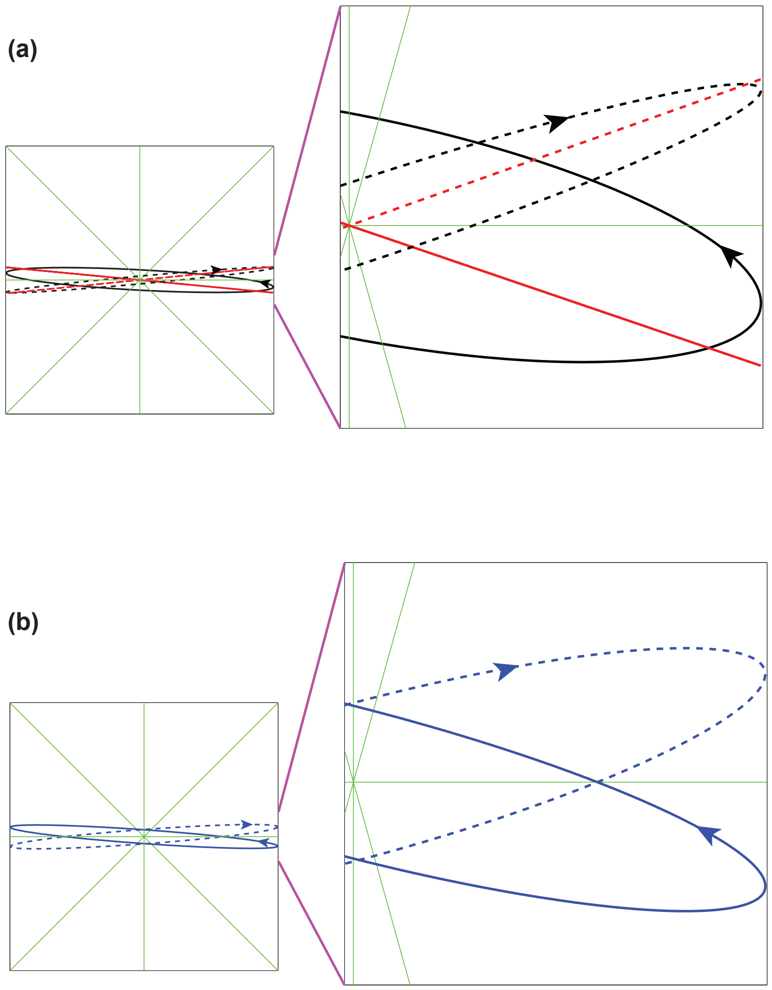

Figure 5.10: *Emerging polarization ellipses of horizontal launch along chord* 5 *cm above (solid lines) and* 5 *cm below (dashed lines) plasma midplane in the case of* $B_T = 1.2$ *T. A comparison of the full calculation (black), FR-only calculation (red) is plotted in (a) and the* $B_Z = 0$ *calculation (blue) is in (b). A cutout is shown on the right to assist visualizing the difference.*

The synthetic diagnostic code can also be used to guide future polarimetry design. For example, a simulation of a combined plasma density and B_T scan was performed and the results are presented in Fig. 5.11. As can be seen in this contour plot, at a certain density, the sensitivity goes through peaks and valleys as B_T increases, as illustrated in Fig. 5.8. Similar oscillations also occur for a density scan at fixed B_T, except in the very low B_T region, where both the FR and CM effects linearly increase with density (see Eqn. 2.38) but with the FR effect always dominant. The zeros of the sensitivity in the figure suggest that certain combinations of B_T and n_e, (e.g., $B_T \sim 1.9\ T$, $n_e \sim 1 \times 10^{19}\ m^{-3}$) should be avoided if a high sensitivity to B_R is desired.

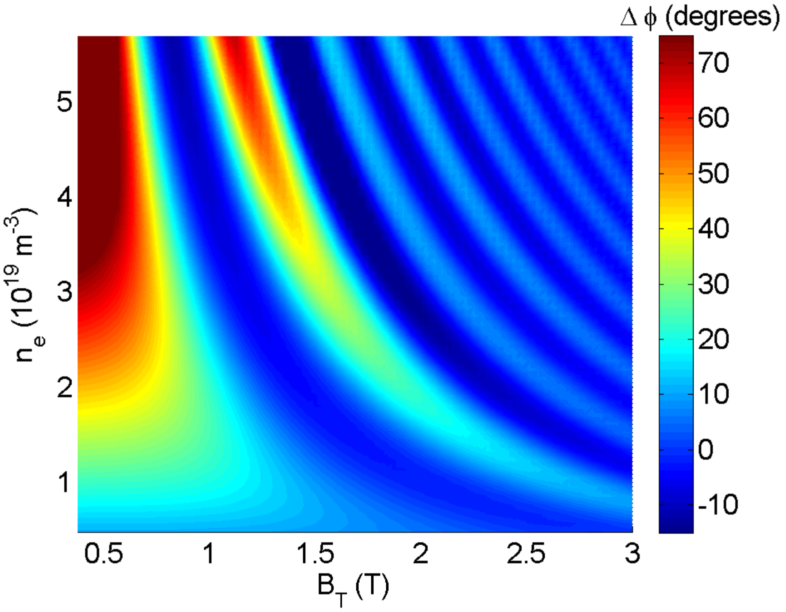

Figure 5.11: *Contour plot of phase sensitivity ($\Delta\phi$ in degrees, the difference in polarimetry phase between chords 5 cm above and 5 cm below plasma midplane) with n_e and B_T scan.*

5.1.5 Conclusions

Mueller-Stokes theory, which has been widely used to interpret polarimetry measurements in magnetized plasmas, has been systematically validated under a wide range of plasma conditions where the relative contributions from the FR and CM effects were varied significantly. Across this entire range of conditions, a synthetic diagnostic code based on Mueller-Stokes theory was found to always accurately predict the measured polarimeter phase. The high level of agreement provides strong validation of Mueller-Stokes theory. The influence of the CM effect on polarimetry measurements is investigated in detail with the aid of the synthetic diagnostic code. As expected, the measurements are well approximated by the FR effect when the CM effect is predicted to be weak. However, as the CM effect increases to a significant level, it can compete with the FR effect in rotating the polarization ellipse of the EM-wave, resulting in a reduced polarimeter response to the FR effect. The code also shows that sufficiently large CM effect can even reverse the handedness of the waves launched with circular polarizations. The results also suggest that the CM effect on the plasma midplane can be potentially exploited to measure magnetic shear. These results establish increased confidence in the use of such a synthetic diagnostic code to guide future polarimetry design and interpret the resultant experimental data.

5.2 Polarimetry can provide constraints to EFIT

EFIT is a computer code developed to translate measurements from plasma diagnostics into useful information like plasma geometry, stored energy, and current profiles. The measurements are obtained from diagnostics such as external magnetic probes, external poloidal flux loops, and the MSE. The Grad-Shafranov equilibrium equation [Wesson, 2011], which describes the force balance in a plasma, is solved using the available measurements as constraints on the toroidal current density J_T. Since the current also depends on the solution of the equation, the poloidal flux function Ψ, this is a nonlinear optimization problem. The equilibrium constraint allows the 2-D current density to be represented by two 1-D stream functions (i.e., the pressure function $P(\Psi)$ and current flux function $F(\Psi)$, which are functions only of flux Ψ) [Wesson, 2011]:

$$J_T = RP' + \frac{\mu_0}{R}FF' \tag{5.3}$$

This significantly reduces the complexity of the problem.

In the theory-experiment comparison discussed above, it was found that the comparison was sensitive to the input magnetic profiles generated by EFIT. Using improper assumptions in the EFIT calculations ("snap" files) can result in dramatic discrepancy in the comparison. As can be seen from Fig. 5.12(a), in the analysis of DIII-D shot #150161 (one of the "bouncing ball" L-mode shots presented in Section 5.1), the code calculations using EFIT01 ('JT' snap file: reasonable description of H-mode plasmas; edge current density is assumed to be finite yet remain small by constraining it to vanish only weakly; 3 parameters in FF' and 2 in P'; less robust) show a large discrepancy with the measurements. While using EFIT03 ('DEF' snap file: good description for Ohmic and L-mode plasmas; no edge current density is allowed; highly robust) reaches a high level of agreement. The improved agreement is a direct result of the differences between the two EFITs. The toroidal current density profiles generated by the two EFITs are illustrated in Fig. 5.12(b), presenting dramatically different features. The improper assumption used for EFIT01 results in negative current at the edge, which is unphysical.

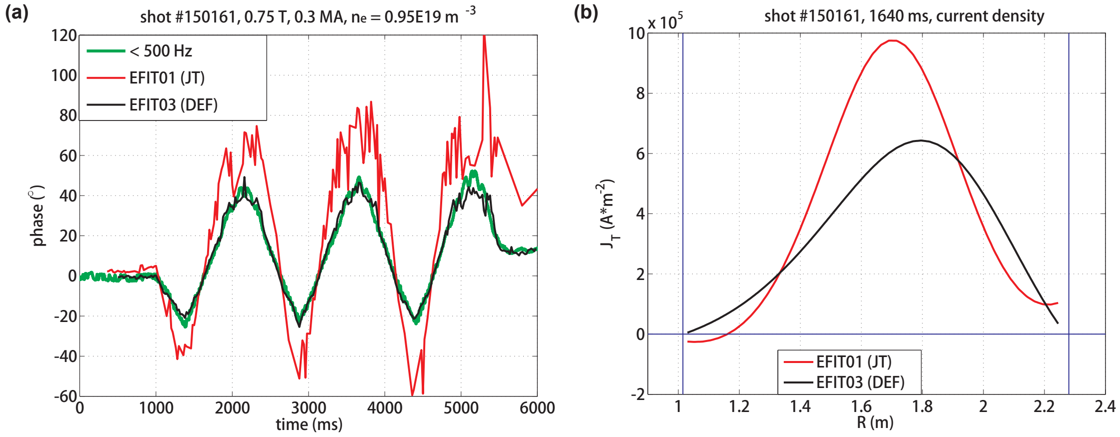

Figure 5.12: *(a) Comparison amongst the measurements (green curve), code calculations using EFIT01 ('JT' snap file; red curve) and EFIT03 ('DEF' snap file; black curve). (b) Toroidal density profiles (J_T) generated from EFIT01 (red curve) and EFIT03 (black curve).*

This result suggests that the polarimeter measurements can be potentially implemented and provide constraints to EFIT calculations. For example, the discrepancy in the theory-experiment comparison can be used as an indicator of whether the proper assumptions are used in the automated between-shots EFIT01 runs on DIII-D. Future work can potentially provide stronger constraints to EFIT. A possible algorithm is as follows: the polarimetry module takes the magnetic profile generated by the preliminary EFIT run and outputs the predicted polarimeter response. The response is then compared with the measurement, which feeds back to tune the parameters in the current density profile, and initiate another EFIT run. Such iteration continues until the predicted polarimeter response agrees with the measurement. This iteration loop can also enclose the fitting of electron density profile, if solely adjusting the magnetic profile fails to reach agreement.

CHAPTER 6

Study of magnetic fluctuations in tokamaks via polarimetry

The direct measurement of internal magnetic fluctuations in tokamaks via polarimetry opens a new path to study plasma modes that feature magnetic fluctuations. For example, the NTM [La Haye, 2006] is large scale MHD instability driven by current or pressure gradients. It can degrade the plasma confinement and often leads to disruption, particularly in high-β plasmas such as NSTX. Another example is the Alfvén Eigenmodes (AEs, including compressional AE—CAE, reversed shear AE—RSAE, toroidicity-induced AE—TAE) [Heidbrink, 2008; Wong, 1999], a kind of global modes induced by energetic particles. They cause fast-ion transport or loss, and therefore control the distribution of fusion α-particles and NBI heating. A third example is the microtearing modes [Drake and Lee, 1977], which are suspected as a source for anomalous electron heat transport. This chapter first presents a sensitivity assessment of mm-wave polarimetry for measurement of microtearing modes in NSTX-U. Then the methodology of extracting the magnetic fluctuation information from the polarimeter measurements is discussed. Specifically, the possibility of measuring (Neoclassical) Tearing Modes via polarimetry is explored.

6.1 A sensitivity assessment of mm-wave polarimetry for measurement of magnetic fluctuations associated with microtearing modes in NSTX-U

Recent nonlinear gyrokinetic calculations have indicated that microtearing modes are driven unstable in NSTX and may account for the observed anomalous electron thermal transport. In order to study magnetic fluctuations of both coherent and incoherent modes, a 288 GHz ($\lambda \approx 1$ mm) polarimeter is under development for NSTX-Upgrade. In order to assess whether the system will have sufficient sensitivity to observe microtearing modes in NSTX-U, a synthetic diagnostic code has been utilized to determine the expected phase fluctuation level. The fluctuating profiles for density and magnetic field generated by the non-linear gyrokinetic simulation are used as input to the code. Results indicate that the polarimeter phase fluctuation level due to the modeled microtearing modes is $\gtrsim 2°$. Utilizing the same model, it was also established that the calculated phase fluctuations are dominated by magnetic, not density fluctuations. This was especially true when the horizontal viewing chord was close (within ± 5 cm) to the plasma midplane. These results indicate that the polarimeter planned for NSTX-U should have sufficient sensitivity to observe magnetic fluctuations associated with microtearing modes [Zhang et al., 2013a].

6.1.1 Magnetic and density fluctuations of Microtearing modes

Microtearing modes are small scale tearing modes with large toroidal (n) and poloidal (m) mode numbers that have been predicted to be unstable in STs [Applegate et al., 2007; Levinton et al., 2007; Wong et al., 2007]. They are also predicted to be a significant contributor to anomalous electron thermal transport in some neutral beam heated ST plasmas. Theoretically they are driven unstable by having an electron-temperature gradient ∇T_e projected onto helically resonant radial perturbations of magnetic field lines, $\tilde{B}_{mn}$, with a rational value of the safety factor, $q = \mathrm{m/n}$. The parallel component of ∇T_e can drive a resonant parallel current, which reinforces $\tilde{B}_{mn}$ via Ampère's law [Guttenfelder et al., 2011]. The induced magnetic islands overlap adjacent rational surfaces, leading to stochasticity. Electrons can then free-stream along the perturbed field line trajectories, which occurs more easily in the presence of many high-n toroidal modes, thereby enhancing transport. The first successful non-linear gyrokinetic simulations have recently been reported for parameters based on an NSTX discharge (shot #120968, time $= 0.560\ s$, $B_T = 0.35\ T$, $I_p = 0.7\ MA$, $R/a = 0.82\ m/0.62\ m$, $P_{\mathrm{NBI}} = 4\ MW$, line-averaged electron density $n_e = 5.4 \times 10^{19}\ m^{-3}$) that is unstable to only microtearing modes [Guttenfelder et al., 2011, 2012]. Figure 6.1 shows a snapshot of the radial magnetic fluctuations ($\tilde{B}_r$, normal to flux surfaces), and normalized electron density fluctuations ($\tilde{n}_e/n_{e0}$) associated with the microtearing modes in an (R, Z) toroidal plane on NSTX. Figure 6.2 shows the radial profiles of $\tilde{B}_r$ standard deviation, equilibrium density and toroidal field along the chords across ($-0.05\ m$) and above ($+0.2\ m$) magnetic axis. As can be seen from Fig. 6.1, in the outboard region, the magnetic fluctuations are spatially broad and strong (amplitude $\sim 30\ Gauss$, $\sim 1\%$ of local equilibrium field), while in the inboard region, they are finer in structure and relatively weaker. In contrast, the density fluctuations in the outboard region are poloidally elongated ($k_\theta \rho_s \approx 0.2$, $\rho_s = c_s/\Omega_i$, $c_s = \sqrt{T_e/m_i}$, $\Omega_i = Z_i e B/m_i$) but radially narrow ($k_r \rho_s \gg 0$) with the fluctuation strength being roughly uniform (amplitude $\sim 2\%$ of local equilibrium density). The proposed 288 *GHz* polarimeter complements other diagnostics planned for NSTX-U that might also be applied to the investigation of microtearing modes. The Beam Emission Spectroscopy (BES) diagnostic planned for NSTX-U will probe density fluctuations, but the small radial scales that characterize microtearing mode density fluctuations pose a challenge for BES. The upgraded high-k scattering diagnostic planned for NSTX-U potentially has the required sensitivity to probe microtearing mode density fluctuations [Guttenfelder et al., 2012]. In contrast, the polarimeter can potentially be employed to directly probe microtearing mode magnetic fluctuations without being adversely affected by the small scale density fluctuations. In Fig. 6.1 the solid horizontal lines indicate the retro-reflecting diagnostic viewing chord of the polarimeter, which lies along a major radius near the plasma midplane. The sensitivity of the polarimeter to microtearing modes is investigated in detail using a recently developed synthetic diagnostic code [Zhang et al., 2010], which calculates the polarimeter response to given input density and magnetic profiles from the previously mentioned nonlinear gyrokinetic simulation [Guttenfelder et al., 2012].

6.1.2 Polarimetry code used in microtearing mode calculations

As previously described in Chapter 4, the synthetic diagnostic code is a forward calculation code, using Mueller-Stokes calculus to track the polarization evolution as the beam propagates. It calculates the Mueller matrices along the propagation and evaluates the resultant polarimetry phase shift at the detector. It takes electron density and magnetic field along the diagnostic chord as inputs, and calculates the polarimetry phase as the primary output. Using the time-varying density

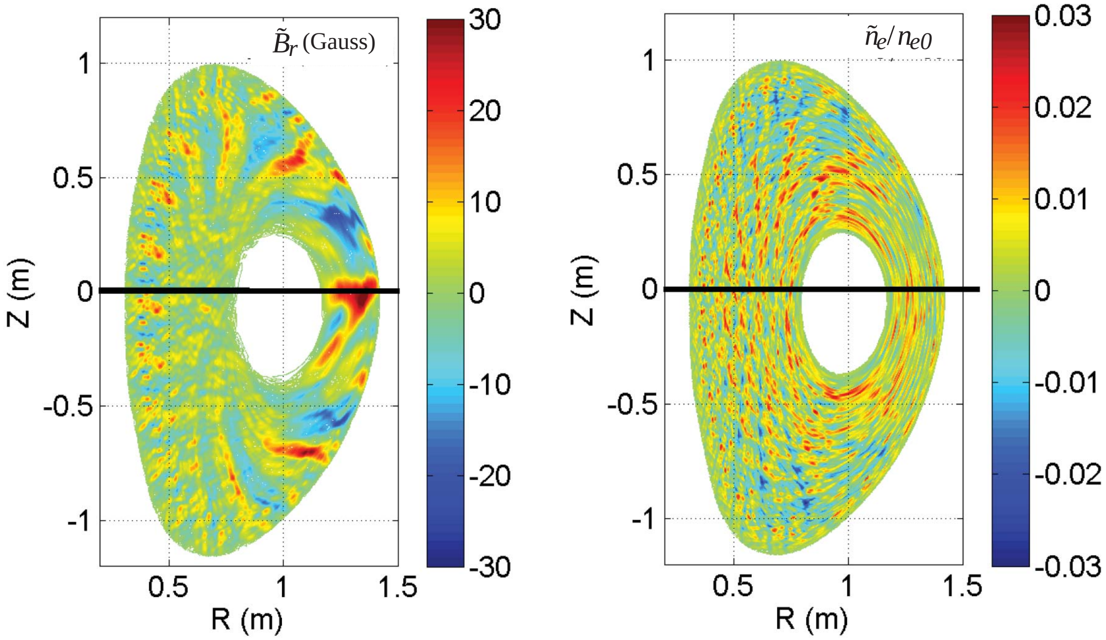

Figure 6.1: *A snapshot of radial magnetic fluctuations ($\tilde{B}_r$) and normalized density fluctuations ($\tilde{n}_e/n_{e0}$) associated with microtearing modes in an (R, Z) toroidal plane on NSTX generated by nonlinear gyrokinetic simulations. These islands rotate poloidally as time evolves. The horizontal lines indicate the horizontal beam path of the planned 288 GHz polarimeter.*

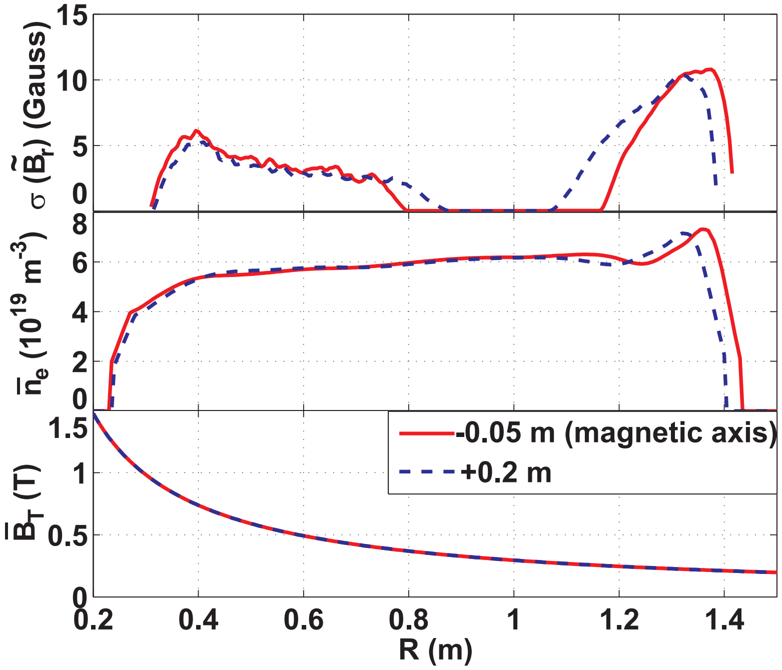

Figure 6.2: *Radial profiles of standard deviation of* $\tilde{B}_r$ *(*$\sigma(\tilde{B}_r)$ *), equilibrium electron density (*$\bar{n}_e$*) and toroidal field (*$\bar{B}_T$*) along the chords* 0.05 *m below (solid line) and* 0.2 *m above (dashed line) machine midplane, respectively. Note that the two curves almost overlie in the third panel.*

and magnetic profiles generated by the previously mentioned nonlinear gyrokinetic simulations, the code can calculate polarimetry phase at each instant of time, yielding a time-varying phase. It also provides an option to artificially suppress the FR and CM effects by suppressing individual components of the magnetic field, or density and magnetic fluctuations, to facilitate interpretation of calculated polarimetry phase. The code assumes beam propagation without refraction, which is a good assumption under most NSTX discharge conditions, where $\omega_{pe}, \omega_{ce} \ll 288\ GHz$. For the plasma equilibrium being discussed, beam refraction is estimated using a ray tracing code GENRAY [Smirnov and Harvey, 1995], which calculates the beam trajectory inside the plasma. The returning beam at the plasma outboard edge is predicted to vertically shift by only 2 *cm*, for a beam launched 0.2 *m* above the plasma midplane. (A few example beam trajectories are presented in Fig. 6.3.) This is the furthest away from the midplane that the polarimeter diagnostic can operate, by vertically jogging the plasma across the fixed viewing chord. This prediction validates the ray tracing assumption since the estimated beam deflection is $< 0.4°$. The propagating beam has an approximately constant beam diameter of 5 *cm*, implying that the system is capable of detecting magnetic structures with $k_\theta < 0.5\ cm^{-1}$ along the midplane [Jiang et al., 1999], which is satisfactory for the study of microtearing modes.

6.1.3 Results and discussion

The polarimetry phase response to microtearing modes calculated by the synthetic diagnostic code is shown for several cases in Fig. 6.4. Figure 6.4(a) shows the case when a beam horizontally propagates through the plasma magnetic axis, which is 5 *cm* below NSTX machine midplane for this plasma equilibrium; Fig. 6.4(b) shows

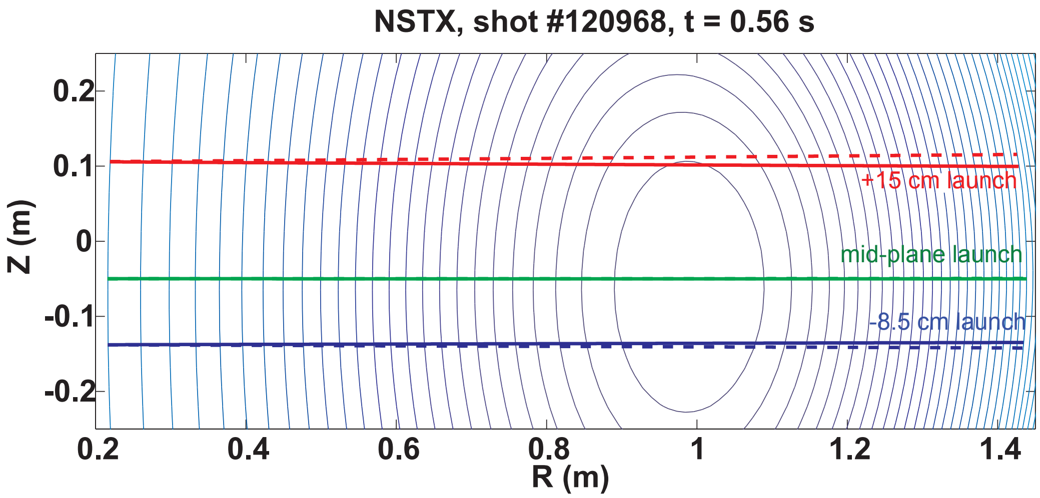

Figure 6.3: *The refraction of the 288 GHz polarimeter diagnosing beam in NSTX shot #120968. The solid lines are the inbound beam, and the dashed lines are the outbound beam after being reflected on the flat tile on the center stack. The green lines show that the launch on plasma midplane ($Z_0 = -5$ cm) does not experience much refraction. As the beam moves away from the midplane, the refraction becomes more significant. -8.5 cm launch beam (blue) has $\Delta Z = -7$ mm when it emerges; $+15$ cm launch beam (red) has $\Delta Z = +1.5$ cm.*

the case when the diagnostic chord is 0.2 m above the machine midplane (i.e., 0.25 m above the plasma midplane). The different curves in each panel correspond to cases where the radial magnetic and/or density fluctuations are artificially suppressed in the calculation. When all fluctuations are suppressed, only the plasma equilibrium information is utilized in the calculation. The black horizontal line (almost overlaid by the red in Fig. 6.4a) shows this situation in each panel, providing a reference phase with no fluctuations. The red curve, which shows only weak phase variation, corresponds to the case where the calculations include only the density fluctuations ($\tilde{n}_e$). The blue curve includes both density and radial magnetic fluctuations ($\tilde{n}_e + \tilde{B}_r$). The green curve, which is almost overlaid by the blue, includes only the radial magnetic fluctuations.

As can be seen when both magnetic and density fluctuations are included, the code predicts $\gtrsim 2°$ peak-to-peak semi-coherent phase variation ($f \sim 10\ kHz$). It is obvious from the similarity of the green and blue curves that the contribution to the blue curve is primarily from the magnetic fluctuations. The phase variations due to density fluctuations are negligible, when the beam propagates through the plasma magnetic axis, as illustrated in Fig. 6.4(a). This contribution becomes slightly more pronounced when the beam is farther away from the magnetic axis, as shown in Fig. 6.4(b), but is still relatively weak when compared to the phase variations induced by radial magnetic fluctuations alone. Other calculations for intermediate chord heights (not shown) are consistent with these conclusions. This is especially true for chord heights within $\pm 5\ cm$ of the magnetic axis. The contribution of perpendicular in-flux-surface, or binormal, magnetic fluctuations ($\tilde{B}_\theta$) is neglected. The maximum possible contribution from this component is assessed by a worst case calculation, which assumes a perturbation with a uniform profile and a magnitude equal to the maximum of the radial component, i.e., 30 *Gauss*. This is an upper-limit for the neglected component since $\tilde{B}_\theta \sim k_r\tilde{A}$, while $\tilde{B}_r \sim k_\theta\tilde{A}$, and it can be seen, by inspection of Fig. 2(b) in [Guttenfelder et al., 2011], that $|k_r\tilde{A}| < |k_\theta\tilde{A}|$, for the gyrokinetic simulation results considered. This calculation suggests the contribution is $< 10\%$ of the total phase fluctuations, so the following discussion of magnetic fluctuations refer only to the radial component. A more comprehensive consideration will be the subject of future work.

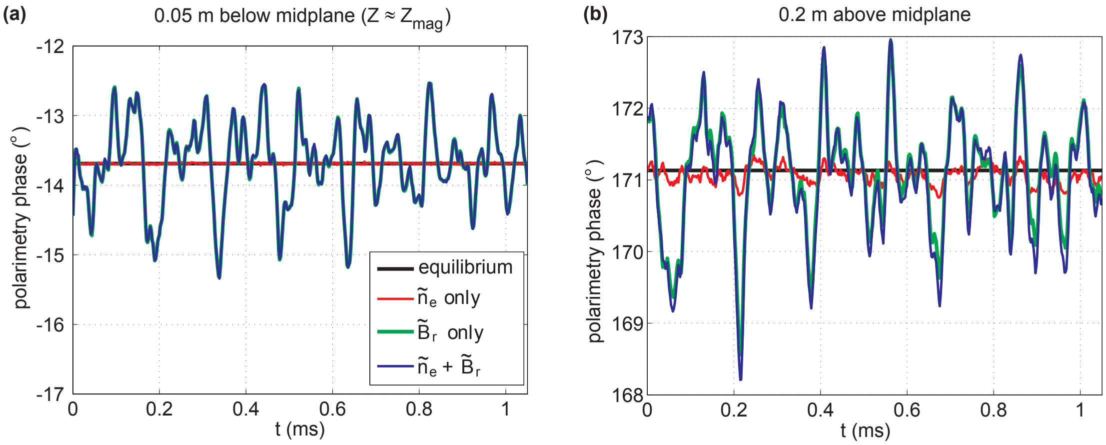

Figure 6.4: *Polarimetry phase calculated by the synthetic diagnostic code using fluctuation profiles generated by nonlinear gyrokinetic simulations for a beam horizontally propagating across the plasma magnetic axis (a), and 0.2 m above the machine midplane (b). Black horizontal line shows the equilibrium phase; red curve shows the fluctuating phase with only density fluctuations ($\tilde{n}_e$) included; green curve includes only radial magnetic fluctuations ($\tilde{B}_r$); blue curve includes both density and magnetic fluctuations ($\tilde{n}_e + \tilde{B}_r$). Also note the blue curve almost overlies the green curve and the red curve only shows very weak variations around the black horizontal line.*

The approximately 10 *kHz* phase fluctuations visible in the calculations shown in Fig. 6.4 are predicted to be detectable since their level is above the measured phase resolution of the polarimeter, which is $\sim 0.3°$ in a frequency range $1\ kHz < f < 100\ kHz$ (see Section 3.6). Note that the gyrokinetic simulation results considered here do not include plasma rotation ($\sim$ 10 *kHz* typical). Considering that the microtearing modes have large n numbers (n = 5 is shown in Fig. 6.1), the fluctuation frequency observed in an experiment will be substantially Doppler shifted but still in the range of sensitivity. The sensitivity of the polarimetry phase primarily to the FR effect caused by magnetic fluctuations results from two facts. First, of the various magnetic field effects that can contribute to the polarimeter phase fluctuation ($\tilde{\phi}$), the dominant contribution is from the FR effect ($\tilde{\psi}$). Figure 6.5 illustrates that including the CM effect from the equilibrium magnetic field makes little difference to the calculated phase fluctuations for the same chord heights shown in Fig. 6.5. Also, as noted above, the CM effect from $\tilde{B}_\theta$ is expected to be small. Second, the geometry of the diagnostic minimizes the contribution of density fluctuations to the FR effect. Due to the relatively minor contribution from the CM effect, the resultant fluctuating phase can then be represented to first order by:

$$\tilde{\phi} \approx 2\tilde{\psi} \xrightarrow{\text{to 1st order}} C\int \bar{n}_e \tilde{B}_\parallel \mathrm{d}l + \cancelto{0}{C\int \tilde{n}_e \bar{B}_\parallel \mathrm{d}l} \tag{6.1}$$

where C is a constant factor for a fixed wavelength, $B_\parallel$ is the magnetic field component parallel to the beam propagation, which is along the major radius in this case, and '$-$'and '$\sim$' represent equilibrium and fluctuation quantities, respectively [Ding et al., 2003]. Since propagation close to the plasma midplane means that the equilibrium $B_\parallel$ is always close to zero, the density fluctuation contribution to Eqn. 6.1 is much smaller than that due to magnetic fluctuations. However, as the chord moves away from the midplane, density fluctuations start to contribute (see Fig. 6.4) due to the increasing equilibrium $B_{\parallel}$. This trend is illustrated in Fig. 6.6.

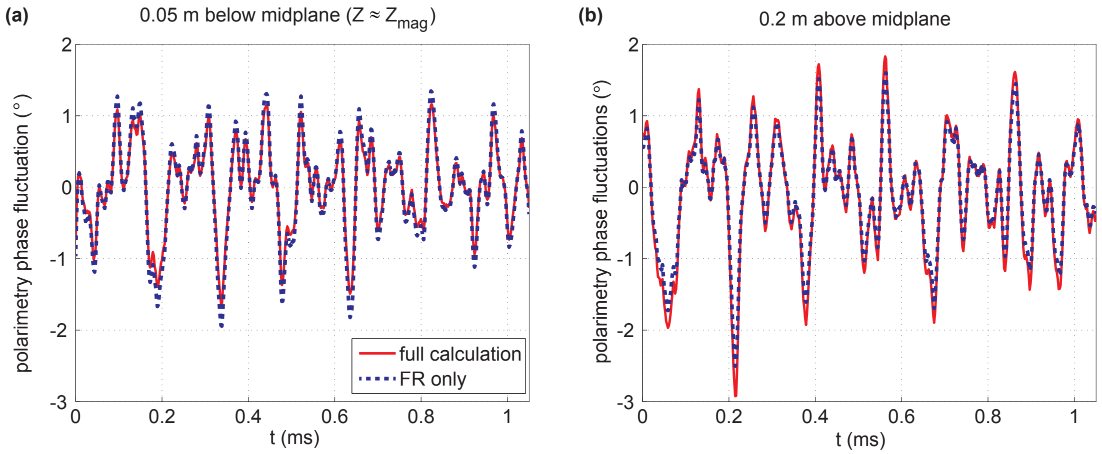

Figure 6.5: *Polarimetry phase fluctuations calculated by the synthetic diagnostic code for the chord across the plasma magnetic axis (a) and* 0.2 *m above the machine midplane (b). The solid curve shows the phase fluctuations with both FR and CM effects included. The dashed curve shows the results including only the FR effect.*

6.2 Methodology to extract magnetic fluctuations from polarimetry measurements

6.2.1 $\tilde{B}_R$ measurements in FR-dominant regime

Coherent modes in fusion plasmas usually feature both density fluctuations ($\tilde{n}$) and magnetic fluctuations ($\tilde{\vec{B}}$). Also, as discussed in Chapter 2, polarimetry is a line integrated diagnostic involving both n and $\vec{B}$. In general, it is challenging to extract the $\tilde{\vec{B}}$ information from polarimetry measurements. However, in special cases where

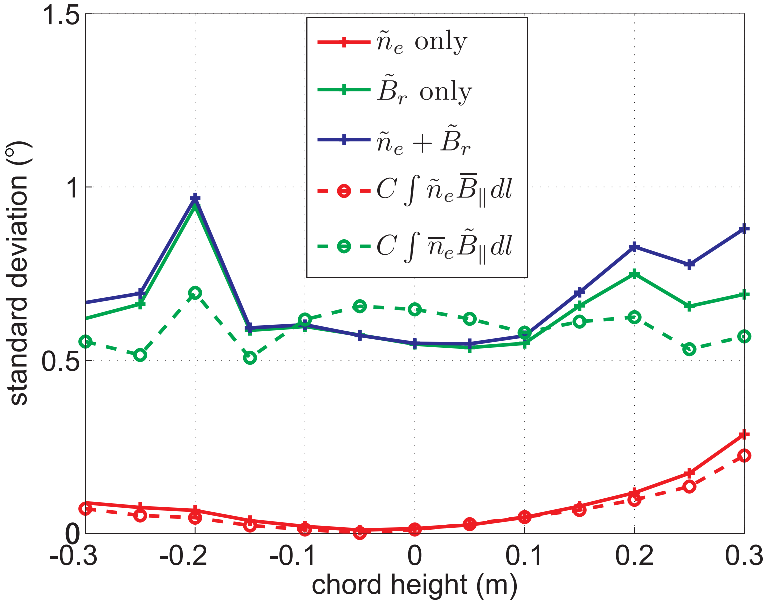

Figure 6.6: *Standard deviations (STD) of polarimetry phase fluctuations and line-integrated fluctuating quantities versus chord height. The solid red, green and blue curves correspond to the STD of the polarimetry phase fluctuations including only density fluctuations ($\tilde{n}_e$), only magnetic fluctuations ($\tilde{B}_r$), and both fluctuation quantities ($\tilde{n}_e+\tilde{B}_r$), respectively. The dashed red curve is the STD of estimated phase fluctuations from the line-integral of density fluctuations and equilibrium parallel magnetic field along the beam path. The dashed green curve is the STD of line-integral of equilibrium density and parallel magnetic field fluctuations.*

the argument made in Eqn. 6.1 is applicable, i.e., the FR effect is dominant and the probe chord is close to the plasma midplane, it is straightforward to estimate the $\tilde{B}_R$ directly from the measured polarimeter phase fluctuations $\tilde{\phi}$. It is worth noting here that the much finer radial structure of the $\tilde{n}$ than $\tilde{B}_r$ helps to suppress the $\tilde{n}$ contribution (the second term on the RHS of Eqn. 6.1) to the $\tilde{\phi}$ in the microtearing mode modeling, which might be different for other large-scale MHD modes. Also the phase relationship between the $\tilde{n}$ and $\tilde{\vec{B}}$ can introduce further complications. It is still expected that a reasonably accurate estimation of density-weight $\tilde{B}_R$ can be obtained on DIII-D using the 288 GHz polarimeter when the FR effect is dominant, as described above. Two examples of such $\tilde{B}_R$ measurements are provided below.

Figure 6.7 presents the spectrum of low-B_T shot #150161 ($B_T = 0.75\ T$), which is in FR-dominant regime (Fig. 5.3a). The $\sim 65\ kHz$ TAEs at time 800–1100 ms correspond to $\sim 0.2^\circ$ phase variation. With knowledge of the line-integrated equilibrium density $\int \bar{n} dl$, the density-weighted $\tilde{B}_R$ (line-averaged and weighted by equilibrium density) is estimated to be $\sim 2\ Gauss$. If the $\tilde{B}_R$ structure is also known, for example, from the NOVA-K modeling [Zeeland et al., 2006b], the local magnetic fluctuation level can be determined.

Extremely low density ($n_e \sim 10^{18}\ m^{-3}$) discharges on DIII-D have been used in experiments to study the growth and decay of runaway electrons. Since runaway electrons are largely collisionless, their orbit deviations (and thus eventual loss) must be dominantly induced by fluctuations of the magnetic field (as opposed to temperature or density). Although B_T is moderately high ($\sim 1.4\ T$), the low density helps to categorize the plasma condition to be in FR-dominant regime (see Fig. 5.11). The measured and calculated (four time slices) polarimeter phase are presented in Fig. 6.8. There is $\sim 5^\circ$ discrepancy between the measurements (green) and the

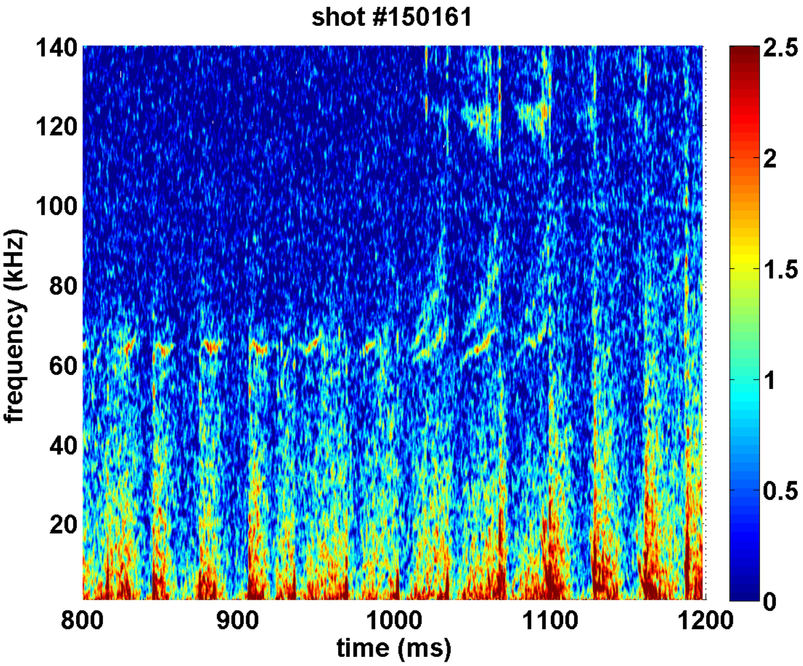

Figure 6.7: *Polarimeter phase spectrum of DIII-D shot #150161 ($B_T = 0.75$ T). ~ 65 kHz TAEs are at time 800–1100 ms.*

full calculation (black), which is possibly because of the inaccuracy in the input density profile or polarimeter system alignment issue. Even with this discrepancy, the FR-only calculation (red) accounts for the majority of the full calculation value. Therefore the measured polarimeter phase fluctuation ($\tilde{\phi}$) can be used to estimate the broad-band (turbulent) magnetic fluctuations $\tilde{B}_R$. Polarimetry $\tilde{B}_R$ measurements are presented in Fig. 6.9 for four time slices. (Polarimeter fluctuation signal after 5500 *ms* is severely contaminated by runaway electron emission, due to the development of a lock mode.) Fluctuation strength is normalized to the toroidal field at the magnetic axis ($B_0 = 1.4\ T$), and the fluctuation level prior to discharge initiation is included as a noise floor. Integrated over the frequency range 1–95 *kHz* the total fluctuation strength is measured to be $\tilde{B}_R/B_0 \approx 1 \times 10^{-4}$, which for this plasma ~ 1 *Gauss*. This magnetic fluctuations can potentially result in the runaway electron loss. Future work will focus on to reconcile these measurements with computational modeling varying the spatial structure of the measured $\tilde{B}_R$. It is also worth noting here that the power spectra exhibit an exponential frequency dependence over a broad range, e.g., the magenta line matches the red spectrum curve (2005 *ms*) pretty well in frequency range of 10–65 *kHz*. Further analysis can determine whether this phenomenon belongs to deterministic chaos [Maggs and Morales, 2011].

6.2.2 $\tilde{\vec{B}}$ estimation in the presence of large CM effect

It is more difficult to interpret the measurements in the presence of large CM effect, which is often the case for mm-wave polarimetry on DIII-D. The influence of the CM effect on polarimetry measuring the plasma equilibrium is discussed in detail in Section 5.1. The contour plot in Fig. 5.11 also offers guidelines for plasma

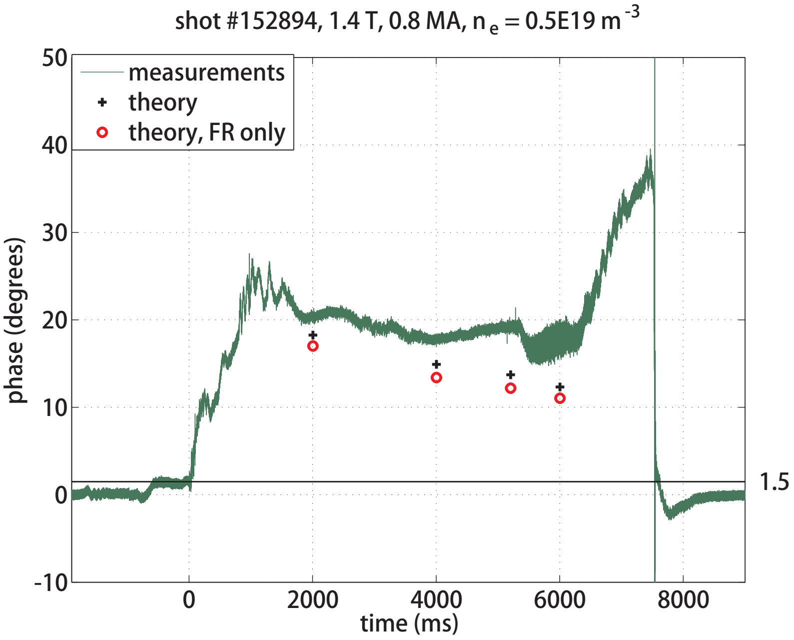

Figure 6.8: *Theory-experiment comparison for a DIII-D shot (#152894) in quiescent runaway electron experiment. The measured polarimeter phase is plotted in green, and the synthetic diagnostic calculation including both the FR and CM effects is in black, and the FR-only calculation is in red.*

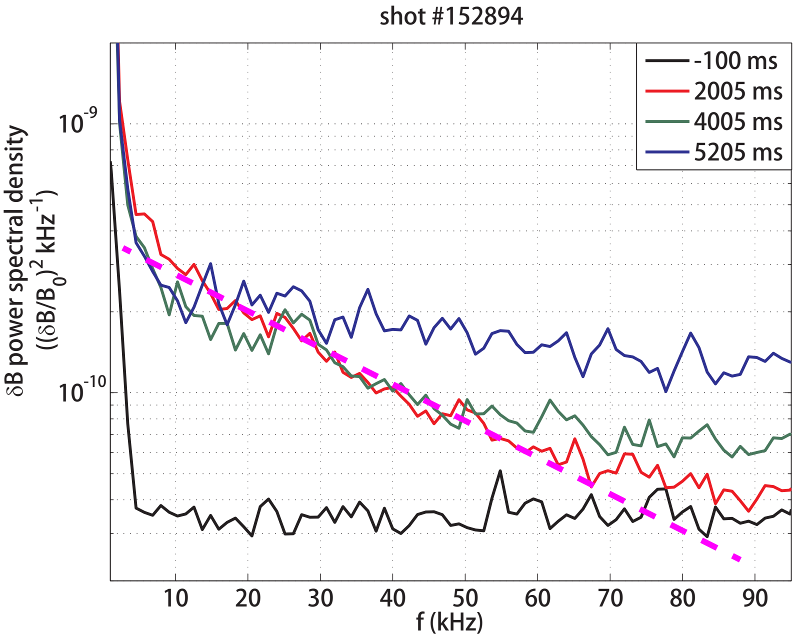

Figure 6.9: *Density-weighted magnetic fluctuation data measured by* 288 *GHz polarimeter for a DIII-D shot (#152894) in quiescent runaway electron experiment. The fluctuation measurement* (-100 *ms) prior to plasma breakdown is included as an instrumental noise floor. The magenta line is a linear fitting to the frequency spectrum of* 2005 *ms in frequency range of* 10–65 *kHz.*

design to achieve a sensitive $\tilde{B}_R$ (not only $\bar{B}_R$) measurement. It is worth noting that the contour plot varies with specific plasma parameters, e.g., plasma shape, current, detailed profile structure, etc. However, as long as the polarimeter phase measurements are acquired at plasma conditions well away from the zeros in the contour plot, where the sensitivity to the FR effect is inherently diminished, it is still possible to estimate the magnitude of $\tilde{\vec{B}}$. This requires the knowledge of $\tilde{n}$ profile from other diagnostics, and $\tilde{\vec{B}}$ structure and its phase relationship with $\tilde{n}$ derived from theories. The forward polarimetry code can then be used to predict the polarimeter response with the inputs of $\bar{n} + \tilde{n}$ and $\bar{\vec{B}} + \tilde{\vec{B}}$ profiles. The predicted polarimeter phase can be compared with the measurement and the difference can feed back to adjust the $\tilde{\vec{B}}$ magnitude until prediction agrees with measurement.

For example, tearing modes and *AEs have been observed via the 288 GHz polarimeter on DIII-D. The spectra of polarimeter phase are shown in Fig. 6.10 and Fig. 6.11, for two typical neutral-beam-heated DIII-D shots (#148997 and #149467), where tearing modes and AEs were present. Both shots have strong CM effect ($B_T = 2.0\ T$) and $\tilde{n}$ is expected to significantly contribute to the measured phase fluctuations. In principle, the BES system can provide the $\tilde{n}$ profile measurement. The NTMs can be modeled using the NIMROD [Gianakon et al., 2002] and PEST [Zeeland et al., 2008b] codes; the AEs can be modeled using the NOVA-K [Zeeland et al., 2006b] and M3D-K [Lang et al., 2010] codes. The procedures described above can then be performed to estimate the $\tilde{\vec{B}}$ level with incorporation of these information. This will be part of future work.

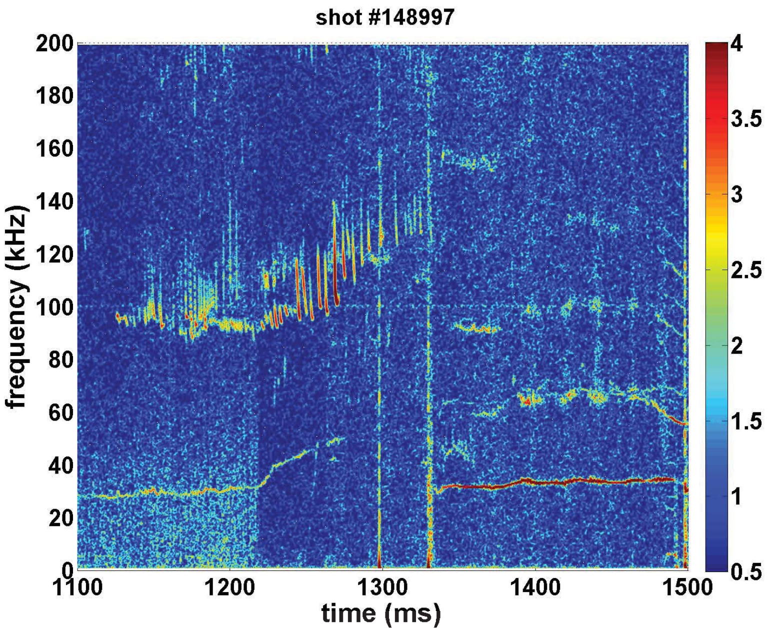

Figure 6.10: *Polarimeter phase spectrum with tearing modes and AEs. The* $\sim$ 100 *kHz modes at time* 1220–1300 *ms are RSAEs;* $\sim$ 30 *kHz mode at time* 1330–1500 *ms is tearing mode.*

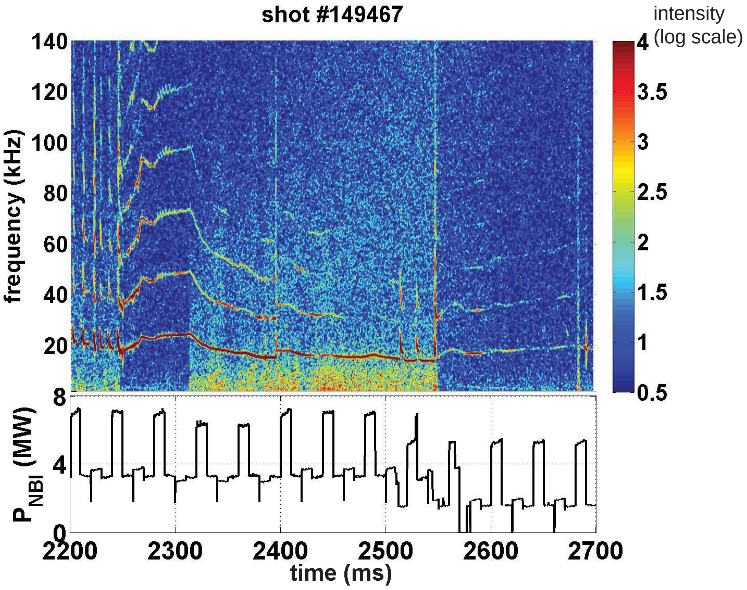

Figure 6.11: *Polarimeter phase spectrum shows tearing modes at* ~ 20 *kHz* ($\sim 2^\circ$ *phase fluctuation). NBI power is plotted in the lower panel.*

6.2.3 Modeling of NTMs on NSTX-U

Tearing modes are magnetic islands that break or tear the magnetic flux surfaces. A classical tearing mode is linearly unstable when the nonaxisymmetric state of the current density profile with the tearing mode island has lower magnetic energy than the original plasma. The NTM is a high-β phenomenon, which can occur even when the plasma current profile is classically stable. The NTMs are resistive tearing mode islands that are sustained by a helically perturbed bootstrap current. They can degrade both plasma energy and angular momentum and even lead to disruption in high-β plasma [La Haye, 2006]. NSTX is a high-β ($\beta_T \sim 18\%$) device and fully equipped with diagnostics, and therefore is an ideal platform to study the seeding, structure of NTMs [Breslau et al., 2011; Gerhardt et al., 2009, 2011; Menard et al., 2005, 2006]. Figure 6.12 shows a m=2/n=1 NTM in the frequency spectrum measured by B-dot probes.

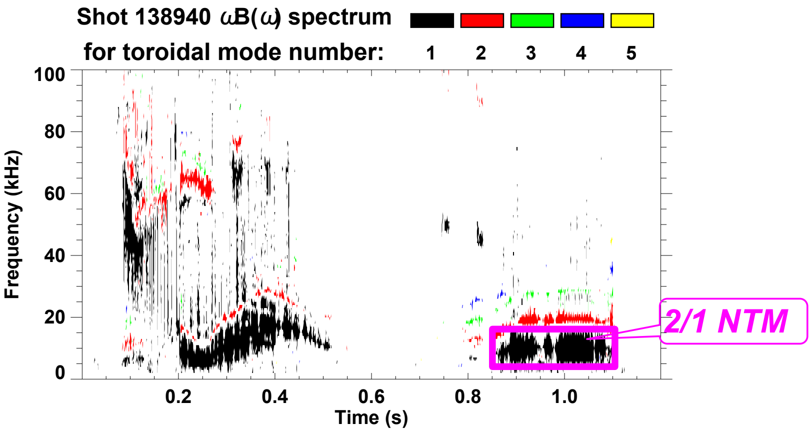

Figure 6.12: *2/1 NTM presents in the spectrum of magnetic probes in NSTX (#138940).*

The capability of the mm-wave polarimeter to measure the NTMs in fusion plasmas was preliminarily investigated via modeling. As can be seen in the diagnostic schematic (see Fig. 6.13), the magnetic islands associated with the NTMs (3/2 mode illustrated here) result in perturbations of B-field and density that are probed by the polarimeter retro-reflection beam. Therefore the polarimeter phase is expected to fluctuate in response to the rotating NTMs.

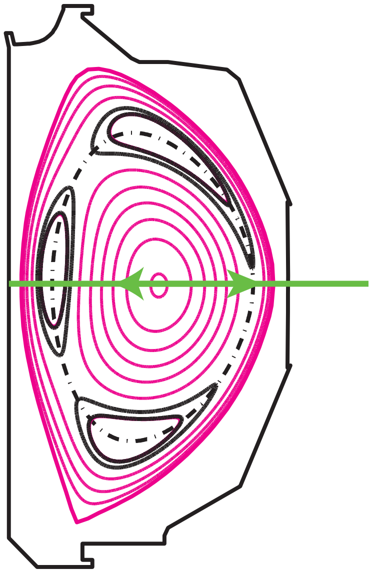

Figure 6.13: *The magnetic islands associate with the NTMs (3/2 mode illustrated here) result in perturbations of B-field and density that are probed by the polarimeter retro-reflection beam.*

The sensitivity of the polarimeter to magnetic fluctuations was first assessed by calculations based on a phenomenological model of NTMs. This model assumes a helically perturbed B-field around $q = \mathrm{m/n}$ rational surface:

$$\tilde{B}_\Psi = \tilde{B}_{\Psi 0} e^{-\frac{(\hat{\Psi} - \hat{\Psi}_{\mathrm{m,n}})^2}{(w/a)^2}} \cos(\mathrm{m}\theta - \mathrm{n}\phi) \tag{6.2}$$

where $\hat{\Psi}$ is the normalized poloidal flux, w is the island width, a is the minor radius, θ is the poloidal angle, ϕ is the toroidal angle. Although this model does not include $\tilde{n}_e$ associated with the NTMs, it still provides a useful assessment.

The typical 2/1 NTM on NSTX was modeled with realistic magnetic island structure determined using T_e profile and ultra-soft X-ray (USXR): island width $w \sim 0.1\ m$ at radial location $\hat{\Psi}_{2,1} \sim 0.15$ (see Fig. 6.14). Figure 6.15 presents the results of the polarimetry calculations, showing that $\sim 0.4°$ phase response is caused by 0.1% magnetic fluctuation ($\tilde{B}_{\Psi 0}/B_0$). This phase variation is dominated by the FR effect and its variation amplitude is approximately proportional to the fluctuation amplitude.

6.2.3.1 Reflectometer on NSTX-U can provide unique mode structure and density fluctuation measurements

Reflectometer measures plasma local density and has been routinely employed to provide $\tilde{n}$ measurements, which can be utilized in the methodology discussed in Section 6.2.2. O-mode has the dispersion relation: $\omega^2 = \omega_p^2 + c^2k^2$. The microwaves launched from the outboard side reflect at "cutoff" layer, where density is high enough ($\omega_p = \omega$, $k = 0$) (see Fig. 6.16a). The wave path length can be determined from the phase (ϕ) between reflected and launched waves. Based on the WKB approximations, this phase can be expressed as:

$$\phi(f) = 2k_0(f)\int_{R_{\mathrm{co}}(f)}^{R_{\mathrm{edge}}} \sqrt{1 - \frac{n(R)}{n_{\mathrm{co}}(f)}}\mathrm{d}R - \frac{\pi}{2} \tag{6.3}$$

where the subscripts "edge" and "co" correspond to the outboard edge and cutoff location, respectively.

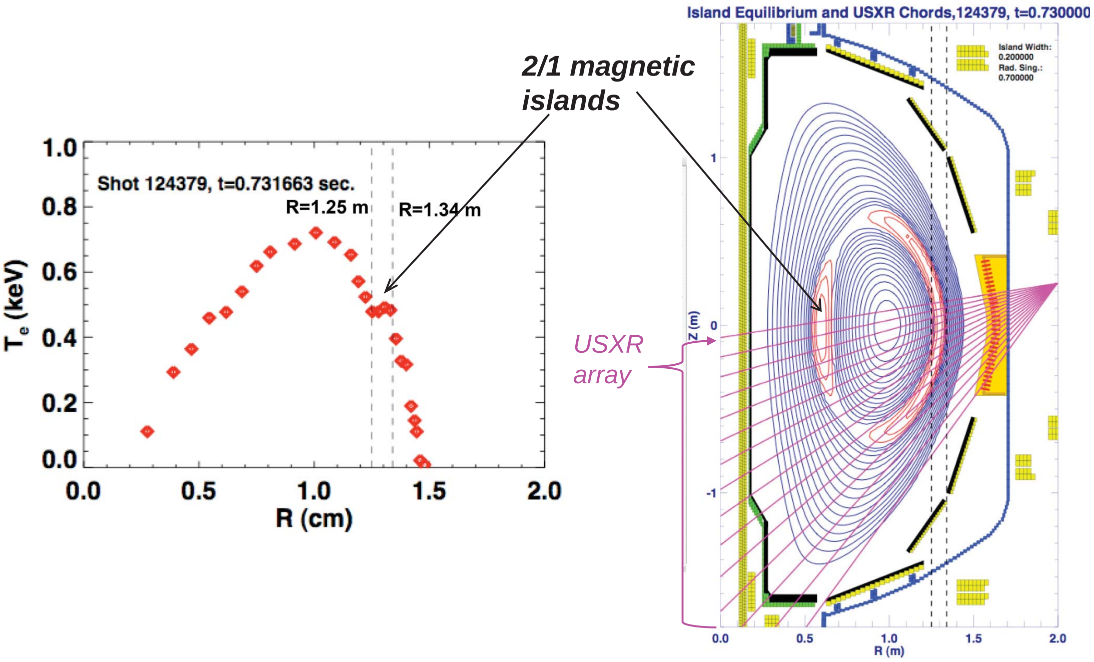

Figure 6.14: *Typical 2/1 NTM was modeled with the magnetic island structure determined using T_e profile and USXR: island width $w \sim 0.1$ m at radial location $\hat{\Psi}_{2,1} \sim 0.15$ (courtesy to S. P. Gerhardt).*

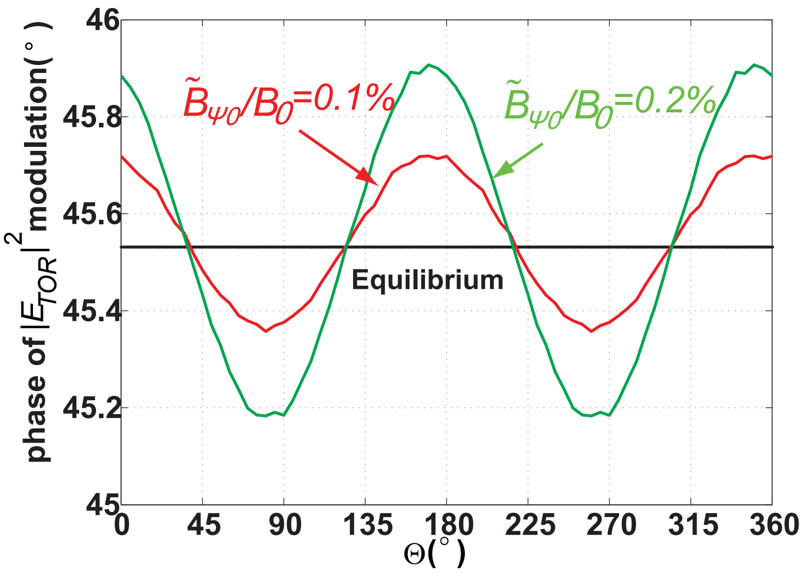

Figure 6.15: *Calculated polarimeter phase response to 2/1 NTM on NSTX. Two calculations with different fluctuation amplitude are shown ($\tilde{B}_{\Psi 0}/B_0 = 0.1\%, 0.2\%$). The equilibrium is based on shot #133959, $t = 0.882$ s, and the probe chord is 0.1 m below plasma midplane.*

A 16-channel fixed frequency reflectometer on NSTX (range $f = 30\text{–}75\ GHz$, corresponding to $n_{\rm co} = 1\text{–}7 \times 10^{19}\ m^{-3}$ for O-mode) (see Fig. 6.16b) was used to specifically estimate the displacement of the flux surfaces caused by the magnetic islands associated with the NTMs.

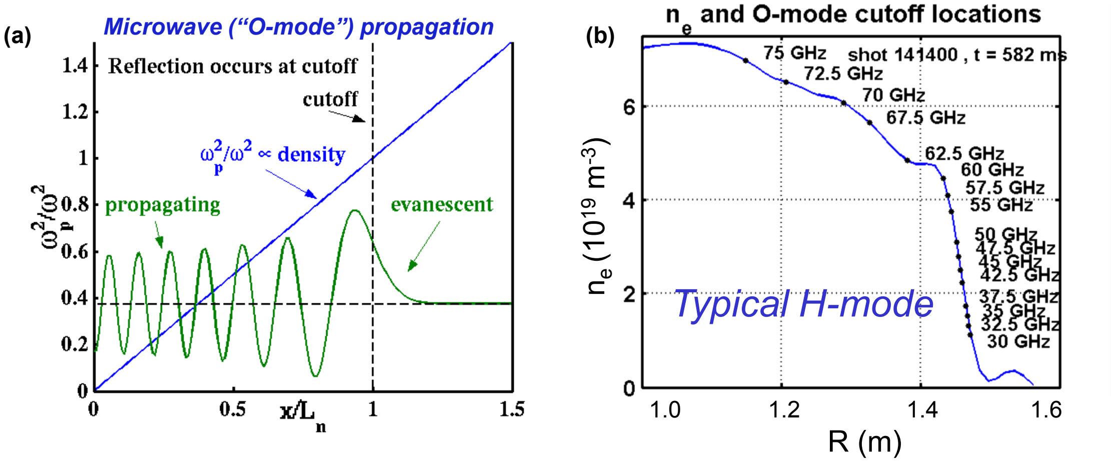

Figure 6.16: *(a) Principle of reflectometry diagnostic. (b) 16-channel fixed-frequency reflectometer array on NSTX. The density profile of a typical H-mode is presented here to illustrate the launched frequencies.*

NTM perturbs the density profile by flattening the density inside the magnetic islands. Figure 6.17(a) shows that the flattening causes displacement of the magnetic flux surfaces. (Density is equal on the same flux surface.) The displacement normally inverts around the island, but sometimes the NTM is coupled to a 1/1 kink, which only has positive displacement. If the kink is large compared to the NTM, the total displacement may not invert (see Fig. 6.17b).

The reflectometer response was modeled using a "mirror model", which assumes the reflectometer phase fluctuation is entirely due to the displacement of the cutoff

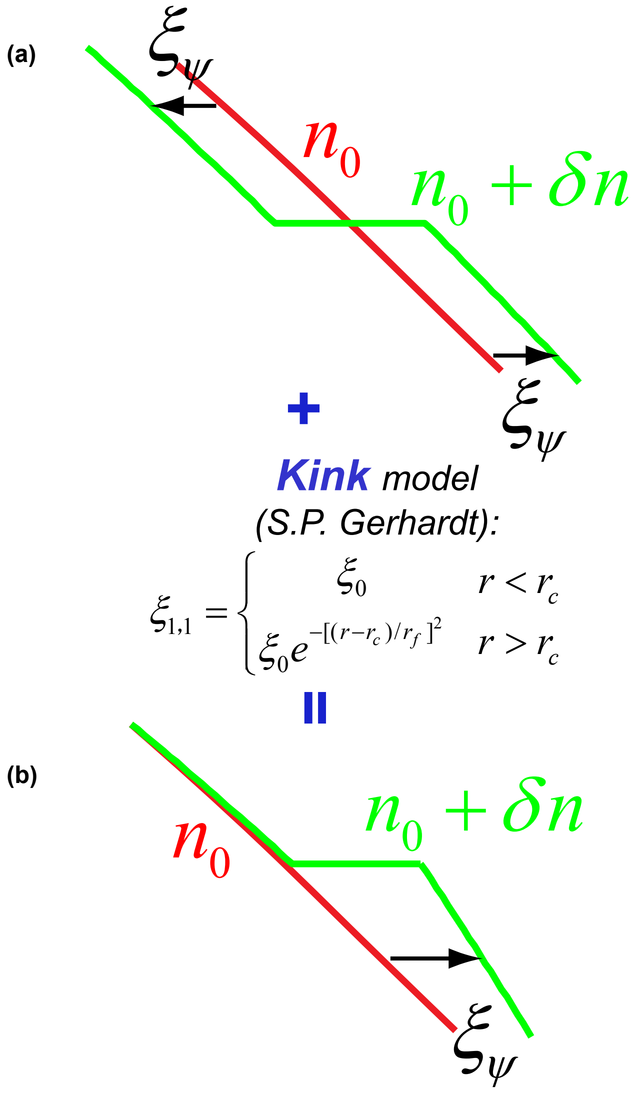

Figure 6.17: *(a) Displacement of magnetic flux surfaces inverts around the islands of NTM. (b) When coupled to a large 1/1 kink (based on the model of S. P. Gerhardt), the total displacement may not invert.*

layer, i.e., $\xi_{\Psi,\mathrm{mirror}} = \delta\phi/(2k_0)$. Figure 6.18(a) presents the perturbed density profiles due to NTM used in the calculations. In a plasma with a NTM, the reflectometer phase would be modulated as the island rotates by. The estimated displacement by the mirror model $\xi_{\Psi,\mathrm{mirror}}$ (black curve in Fig. 6.18b) roughly approximates the actual displacement ξ_Ψ (green curve in Fig. 6.18b).

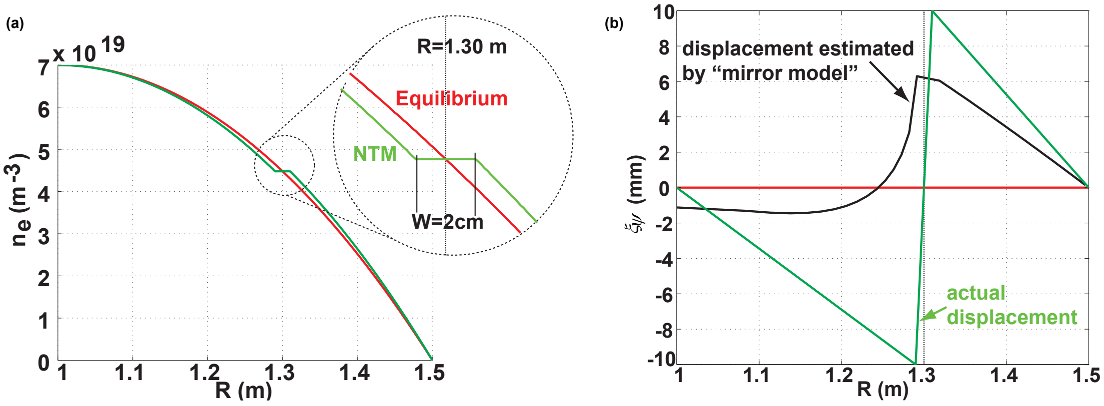

__Figure 6.18:__ (a) Perturbed density profile used in the reflectometer response calculations. (b) The displacement estimated using the "mirror model" (black curve) roughly approximates the actual displacement (green curve).

A similar modeling is performed on the scenario when the NTM is coupled to a 1/1 kink. As discussed above, the displacement becomes asymmetric in this case. The perturbed density profile and estimated reflectometer phase is presented in Fig. 6.19. The estimated reflectometer phase using the mirror model (blue curve in Fig. 6.19b) may not invert in the presence of asymmetric island.

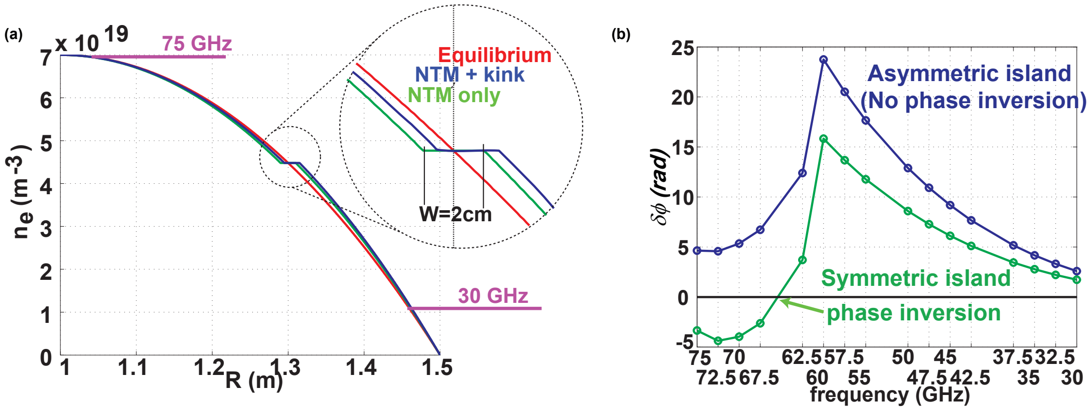

Figure 6.19: *(a) Displacement of the perturbed density profile is asymmetric when the NTM is coupled to an external kink. (b) The estimated reflectometer phase using the mirror model (blue curve) may not invert in the presence of asymmetric island.*

6.2.3.2 Kink-tearing modes observed by reflectometer on NSTX

Figure 6.20 shows the first measurements of tearing modes coupled with an external kink on NSTX [Crocker et al., 2011]. Figure 6.20(a) shows the fluctuation spectrum (shot #138940) from an edge reflectometer (30 *GHz*) in which a coherent mode and its 2nd and 3rd harmonics appear at ∼ 9, 18 and 27 *kHz*. Measurements from a toroidally distributed array of edge magnetic coils indicate that the 9 *kHz* mode has a toroidal mode number of n = 1 (propagating in the direction of the plasma toroidal rotation). Figure 6.20(b) shows the displacement amplitude of the mode at the four different times marked on the spectrum in Fig. 6.20(a), using the bandwidths and record lengths indicated in the figure for the analysis. The ranges of the cutoff densities and locations of the reflectometer array are indicated in Fig. 6.20(c), which shows density profiles from times early and late in the mode lifetime (see Fig. 6.20a). The $f = 9$ *kHz* mode is identified as a tearing mode using observations of the density and temperature profile evolution from multi-point Thomson scattering (MPTS). The density profiles shown in Fig. 6.20(c), as well as the electron temperature profiles from MPTS (not shown) exhibit a significant flat region near $R \sim 1.21$ m during the lifetime of the mode, indicating the presence of a magnetic island at that location. The flat region in both profiles is observed to develop during the onset of the mode between $t \sim 865$ ms and $t \sim 900$ ms, suggesting that the coherent mode is responsible for the flattening. The identification is further supported by the observation that charge exchange recombination spectroscopy (CHERS) measurements show a toroidal rotation of $f_{\mathrm{ROT}} \sim 9$ kHz in the flat region during the lifetime of the mode. The frequency of the coherent mode is consistent with the expectation for a magnetic island at rest in the plasma frame in the flat region.

An interesting feature of the mode structure measurement in Fig. 6.20(b) is that, in the region accessible to the reflectometer array, it differs significantly from the expectation for a tearing mode, resembling, instead, an external kink. The effective displacement gradually approaches zero from $R \sim 1.35$ m to $R \sim 1.25$ m, which is near the edge of the flat region in the density profile. However, the flat region caused by an island results from spreading of the density contours of the plasma away from the rational surface at the poloidal location of the island. This would cause the amplitude of the displacement oscillation observed by a reflectometer to peak at the edge of the island and fall off with distance [Menard et al., 2005]. Away from the flat region in the density profile, from $R \sim 1.35$ m to the outermost measurement close to the plasma edge, effective displacement is nearly constant with radius, giving little indication of vanishing at the plasma edge. This structure indicates that the $f = 9$ kHz tearing mode is coupled to an external kink. While coupling of tearing modes to kinks has been extensively investigated in NSTX [Breslau et al., 2011; Gerhardt et al., 2009, 2011; Menard et al., 2005] and other tokamaks [Brennan et al., 2007; Fredrickson, 2002; Gude et al., 1999; Nave et al., 2003], little attention has been given to the edge structure of the coupled kink-tearing modes. Notably, the peak-peak effective displacement from $R \sim 1.35\ m$ to the plasma edge ranges from $\sim 5\ mm$ to $\sim 7\ mm$ over time as the mode evolves. This is $\gtrsim 5\%$ of the $\sim 8\ cm$ width of the flat region in Fig. 6.20(c), which is not insignificant. These results indicate that fixed-boundary calculations, which force the edge displacement to be zero, are insufficient for understanding the evolution of coupled kink-tearing modes.

From the discussion above, it can be concluded that an experiment on NSTX-U jointly using the 16-channel reflectometer and 288 GHz polarimeter would be fruitful. It can promisingly contribute to the exploration of the kink-tearing mode coupling.

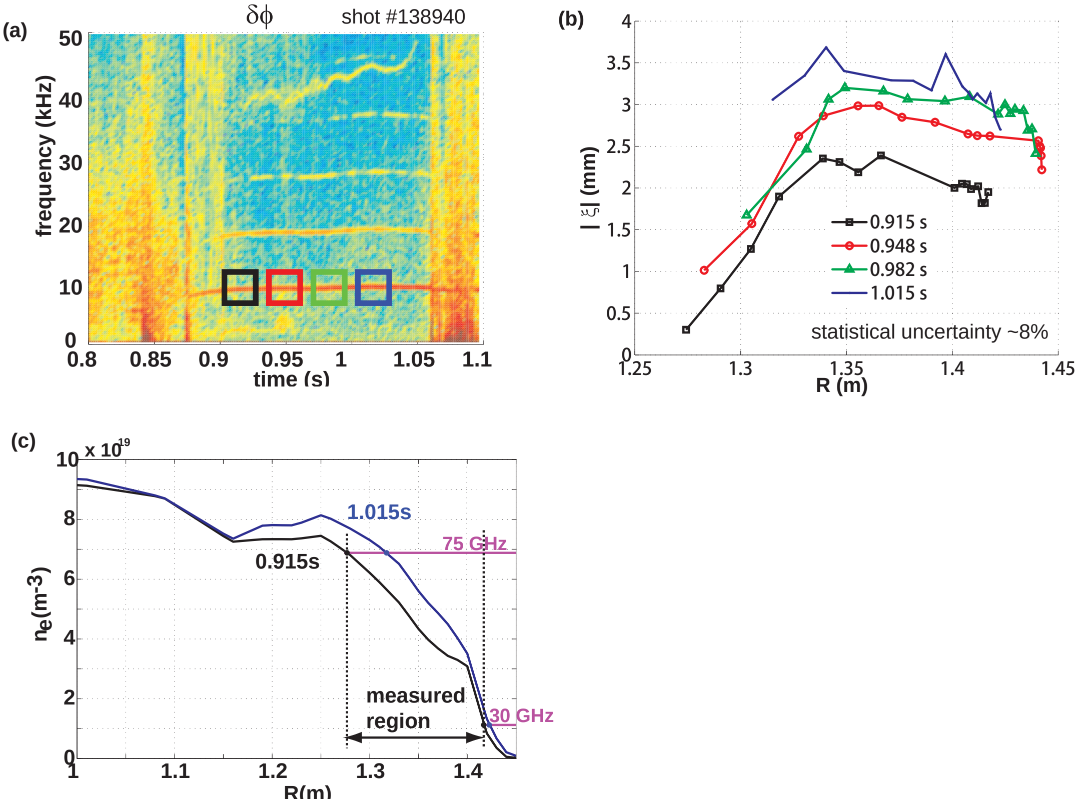

Figure 6.20: *(a) Edge reflectometer (30 GHz at $R \sim 1.42$ m) spectrum showing coherent mode and its harmonics ($f \sim 9, 18, 27$ kHz); (b) radial structure of effective displacement amplitude of coherent mode (analysis times and bandwidths indicated by rectangles in times in (a); (c) MPTS measurement of density profiles with radial range and density range indicated for reflectometer array cutoffs.*

CHAPTER 7

Conclusions and future work

This chapter summarizes the major conclusions of the dissertation and discusses future directions motivated by the results.

7.1 Conclusions

The internal equilibrium magnetic field and magnetic fluctuations in tokamaks are studied via polarimetry. This study is performed mainly using a recently developed mm-wave polarimeter system. This 288 *GHz* polarimeter was designed to probe the plasma along a major radial chord using a retro-reflection geometry on NSTX. It was put in plasma tests on the DIII-D tokamak. The system launches a rotating linearly polarized beam and detects a phase shift directly related to the polarization change caused by the plasma. The magnetic field component along major radius (B_{R}) can be estimated from the measured phase shift. The source employs a Single-Side-Band modulation technique to generate a pair of orthogonally linearly polarized beams with a stable difference frequency. This pair of beams are converted to counter-rotating circular polarizations, and combined to form a rotating linear polarization launch. An essential quasi-optical isolation technique was developed to improve phase resolution by suppressing multiple reflections, which were identified to be the major source of phase noise. Preliminary tests in the laboratory and later on DIII-D indicated an achievable phase resolution of $< 2^\circ$ in the frequency range of $f < 500$ Hz, and 0.3° ($\tilde{B}_R \sim 2$ $Gauss$) in 500 $Hz < f < 500$ kHz.

A systematic theory-experiment comparison was performed on DIII-D. In the experiment, the polarimeter measurements were compared with the predictions of Mueller-Stokes theory where plasma conditions transition smoothly from a FR-dominant (i.e., weak CM effect) plasma to one where the CM effect plays a significant role. A synthetic diagnostic code based on Mueller-Stokes theory accurately reproduced the trends evident in the experimentally measured polarimeter phase over this entire operating range, thereby validating Mueller-Stokes theory. The synthetic diagnostic code was then used to investigate the interaction between the FR and CM effects, which was identified in an earlier polarimetry modeling for NSTX. As a primary element of the interaction identified in the modeling, the FR effect affects elliptization. This is because the elliptization is sensitive to the relative angle between the polarization direction and transverse magnetic field, while the FR effect modifies the polarization direction thereby changing this angle. In the experiment on DIII-D, the investigation focuses on the influence of the CM effect on polarimetry measurements. As expected, the measurements are well approximated by the FR effect when the CM effect is predicted to be weak. However, the code shows that as the CM effect increases, it can compete with the FR effect in rotating the polarization of the EM-wave. This results in an apparent reduced polarimeter response to the FR effect, just as observed in the experiment. The code also shows, if sufficiently large, the CM effect can even reverse the handedness of a wave launched with circular polarization. This helps to understand the surprising experimental observations that the sensitivity to the FR effect can apparently be nearly eliminated at high enough

B_T (2.0 *T*). The results also suggest that the CM effect on the plasma midplane can be exploited to potentially measure magnetic shear in tokamaks. These results establish increased confidence in the use of such a synthetic diagnostic code to guide future polarimetry design and interpret the resultant experimental data. Moreover, the code can be integrated into EFIT in order to utilize the polarimeter measurements as constraints.

The potential of mm-wave polarimetry to measure magnetic fluctuations is explored via both modeling and experiment. Simulations suggest that microtearing modes in NSTX-U, which are a candidate for significant anomalous electron thermal transport, will induce $\gtrsim 2°$ ($f \sim 10$ *kHz*) variations in polarimeter phase. It was also established that this phase variation is primarily due to the magnetic fluctuations associated with the microtearing modes. These results predict that the polarimeter planned for NSTX-U should have sufficient sensitivity to observe magnetic fluctuations associated with microtearing modes. In similar situations where the FR effect is dominant, it is relatively straightforward to estimate the magnitude of the density-weighted magnetic fluctuations from polarimeter phase measurements. For example, ~ 2 *Gauss* $\tilde{B}_R$ ($\tilde{B}_R/B_0 \approx 2 \times 10^{-4}$) is estimated for a ~ 65 *kHz* TAE in a low B_T (0.75 *T*) discharge. Another measurement in a low density discharge in a runaway electron experiment suggests $\tilde{B}_R/B_0 \approx 1 \times 10^{-4}$ broad-band (integrated over 1 *kHz*–95 *kHz*) magnetic fluctuations. However, in the situation where the interaction between the FR and CM effects plays an important role, support from other diagnostics (especially density fluctuation measurements, e.g., reflectometry) and theoretical modeling is critical in extracting the magnetic fluctuation information.

7.2 Future work

As presented in Section 6.1, simulations predict that the polarimeter has sufficient sensitivity to observe the magnetic fluctuations associated with microtearing mode on NSTX-U. After the 288 *GHz* polarimeter being implemented on NSTX-U, an experiment focusing on the development and identification of microtearing modes is a natural extension of these simulations.

The synthetic diagnostic code can be applied to model polarimetry in any magnetized plasmas, including the proposed polarimeter systems for ITER [Donné et al., 2004; Kondoh et al., 2004]. In particular, the impact of the interaction on measurements can be assessed. Also, as described in Section 5.2, the polarimeter diagnostic can provide significant constraints to EFIT, especially on the current profile. This application, if successful, can also be implemented to the plasma control system, and will be especially useful in the NSTX-U solenoid-free current start-up and ramp-up experiments [Raman et al., 2013].

The capability of studying magnetic fluctuations via polarimetry can be further explored in experiment. As discussed in Section 6.2, the proposed joint experiment on NSTX-U using both the 16-channel reflectometer and 288 *GHz* polarimeter is expected to be fruitful, especially in exploring the coupling between the NTMs and kinks [Crocker et al., 2011]. A similar experimental approach can also be applied to study the relatively high frequency AEs, which exploits the advantage of high temporal resolution that both microwave diagnostics feature.

The synthetic diagnostic code can be refined. The code described in Chapter 4 assumes that an infinitesimal thin beam propagates along a straight line. The actual situation is that the mm-wave beam follows Gaussian propagation, i.e., the intensity distribution in transverse cross section is approximately a Gaussian function and the beam width is a function of the axial distance [Martin and Lesurf, 1978]. Therefore different parts of the mm-wave beam probe different portions of plasma, and they experience different polarimetry effects. For example, in plasma center, the lower part of the $\sim 7\ cm$ diameter beam would result in a sinusoidal signal with a different phase than that of the central part of the beam. Weighted by their relative intensities, both of them contribute to the final measured phase. The beam diameter also gradually reduces to $\sim 5\ cm$ when it reaches the retro-reflector. Moreover, from the GENRAY calculations, the beam is expected to experience refraction due to density gradient in the transverse direction, which changes the beam path as well as the probed magnetic components. Future development of the synthetic diagnostic code can incorporate these considerations to improve the precision of calculated polarimeter phase response.

APPENDIX A

Characterization of polarimeter components

A.1 Retro-reflection mirror

On the interface between the mirror surface and vacuum, the tangential components of E-field on either side of the boundary are related by [Jackson, 1998]:

$$\hat{n} \times (\vec{E}_2 - \vec{E}_1) = 0 \tag{A.1}$$

where $\hat{n}$ is the normal of the surface. Therefore an incoming transverse E-field induces an outgoing E-field with equal magnitude in the opposite direction, as shown in Fig. A.1.

$$\vec{E}_{\text{out}} = -\vec{E}_{\text{in}} \tag{A.2}$$

In the laboratory frame, the polarization of the wave does not change though. As inferred from the expression of the E-field in Jones calculus (see Eqn. 2.15), this sign reversal corresponds to a change of π in the common phase δ_x, but the polarization characterizing parameters $\{\alpha,\ \delta\}$ are unchanged and continue to evolve during the outbound propagation. Therefore the mirror does not cause any cancellation in the polarimetry effects.

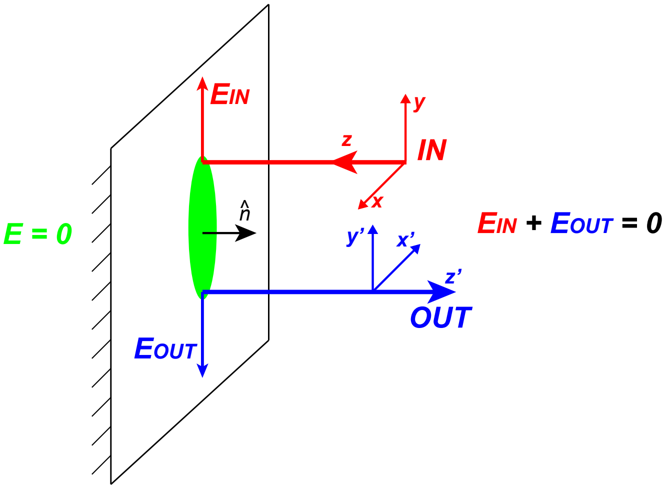

Figure A.1: *Retro-reflection mirror effect. The mirror flips the direction of incoming transverse E-field:* $\vec{E}_{\text{out}} = -\vec{E}_{\text{in}}$*. The definition of the Cartesian coordinate system in the wave frame is also changed.*

A.1.1 Mirror effect in synthetic diagnostic code

The synthetic diagnostic code tracks the wave polarization in the wave frame (i.e., $\hat{z} \parallel \vec{k}$, Fig. 2.4). And the Cartesian coordinate system experiences a transformation at the retro-reflection mirror, as shown in Fig. A.1:

$$\begin{cases} \hat{x}' = -\hat{x} \\ \hat{y}' = \hat{y} \\ \hat{z}' = -\hat{z} \end{cases} \tag{A.3}$$

where the xyz is for the incoming wave, while the $x'y'z'$ is for the outgoing wave.

Combine Eqn. A.2 and Eqn. A.3. The wave E-field satisfies:

$$\begin{aligned} &\begin{cases} E'_x = -E_x = E_{x'} \\ E'_y = -E_y = -E_{y'} \end{cases} \Rightarrow \begin{cases} E_{x'} = -E_x \\ E_{y'} = E_y \end{cases} \\ \Rightarrow &\begin{cases} \alpha' = \alpha \\ \delta' = \delta + \pi \end{cases} \Rightarrow \begin{cases} \psi' = -\psi \\ \chi' = -\chi \end{cases} \end{aligned} \tag{A.4}$$

And the magnetic field components are related by:

$$\begin{cases} B_{x'} = -B_x \\ B_{y'} = B_y \\ B_{z'} = -B_z \end{cases} \tag{A.5}$$

A.2 Use of BNC cable as delay line

The RG58 C/U BNC cable is used as delay line to create the 90° phase shifted I & Q input required by the SSB modulator. Impedance of the cable is 50 Ω and capacity is 105 pF/m; the dielectric material is polyethylene; designed for $f_{\mathrm{RF}} \leq 1\ GHz$.

The 3.5 *MHz* sinusoidal wave propagates through the BNC cable as an EM-wave, with its phase velocity:

$$v_p = \frac{c}{n} = \frac{c}{\sqrt{\varepsilon_r}} = \frac{c}{\sqrt{2.25}} = \frac{2}{3}c \tag{A.6}$$

And the phase delay caused by a BNC cable of length ΔL is:

$$\Delta\phi = 2\pi f \Delta t = 2\pi f \frac{\Delta L}{v_p} \tag{A.7}$$

Therefore to achieve 90° phase shift for the 3.5 *MHz* sinusoidal wave, the required length is:

$$\Delta L = \frac{1}{4}\frac{v_p}{f} = 14.276\ m \tag{A.8}$$

A.3 Dual-mode horn

The dual-mode conical horn has nearly equal beam shape in the E-/H-plane far-field patterns with a 3-*dB* half angle of 6°, as shown in Fig. A.2 [Pickett et al., 1984].

A.4 Unbalanced power launch

The combination of equal power LCP + RCP launch is a rotating linear polarization, which is proved in Eqn. 3.1. If the power of these two beams is unbalanced, the result is a rotating ellipse with fixed elliptization. This corresponds to a constant $s_3 = I_{\mathrm{RCP}} - I_{\mathrm{LCP}}$ component in Stokes vector (see Eqn. 2.28). The launched polarization on Poincaré sphere is shown as the blue circle of latitude in Fig. A.3(a).

The power imbalance in LCP + RCP launch does not effect the phase detection of the mixer though. For a mixer oriented at angle of θ with respect to $\hat{x}$, the measured

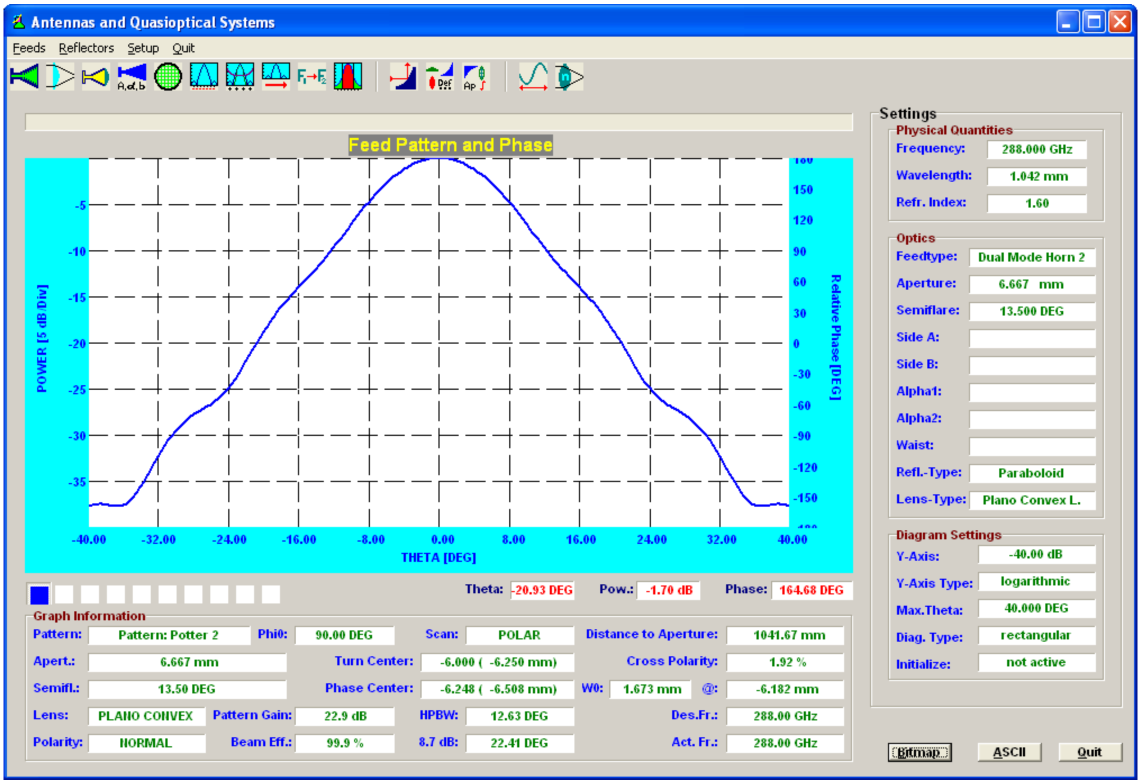

Theta: -20.93 DEG
Pow.: -1.70 dB
Phase: 164.68 DEG

Graph Information

Pattern: Pattern: Potter 2
Phi0: 90.00 DEG
Scan: POLAR
Distance to Aperture: 1041.67 mm
Apert.: 6.667 mm
Turn Center: -6.000 (-6.250 mm)
Cross Polarity: 1.92 %
Semifl.: 13.50 DEG
Phase Center: -6.248 (-6.508 mm)
W0: 1.673 mm
@: -6.182 mm
Lens: PLANO CONVEX
Pattern Gain: 22.9 dB
HPBW: 12.63 DEG
Des.Fr.: 288.00 GHz
Polarity: NORMAL
Beam Eff.: 99.9 %
8.7 dB: 22.41 DEG
Act. Fr.: 288.00 GHz

Settings

Physical Quantities

Frequency: 288.000 GHz
Wavelength: 1.042 mm
Refr. Index: 1.60

Optics

Feedtype: Dual Mode Horn 2
Aperture: 6.667 mm
Semiflare: 13.500 DEG
Side A:
Side B:
Alpha1:
Alpha2:
Waist:
Refl.-Type: Paraboloid
Lens-Type: Plano Convex L.

Diagram Settings

Y-Axis: -40.00 dB
Y-Axis Type: logarithmic
Max.Theta: 40.000 DEG
Diag. Type: rectangular
Initialize: not active

Figure A.2: *Far-field pattern of Pickett Potter dual-mode horn at 288 GHz (figure from manufacture).*

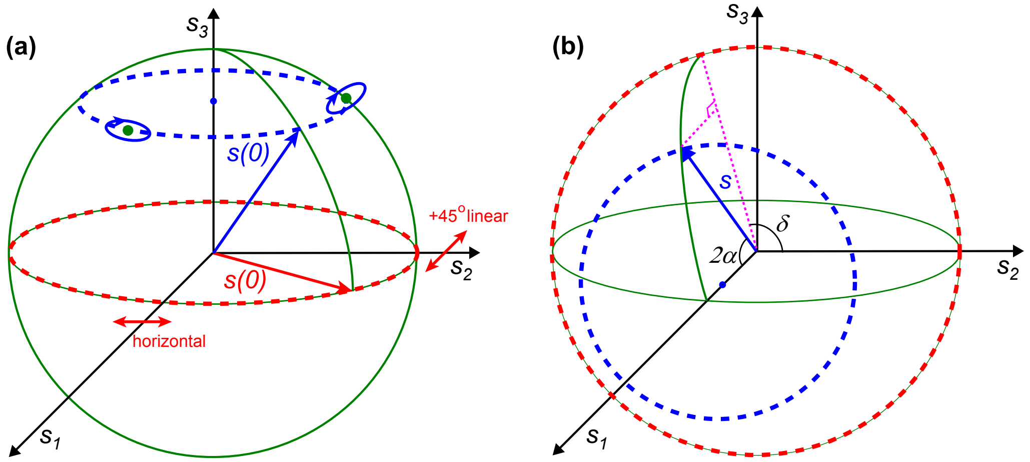

Figure A.3: *(a) The polarization $\vec{s}(0)$ for LCP + RCP launch maps to a dot progressing along a circle of latitude on Poincaré sphere. Equal power launch corresponds to the dashed red equator; unbalanced launch corresponds to the dashed blue circle. (b) Equal power O + X launch maps to a dot progressing along the dashed red circle. Unbalanced launch maps to the dashed blue circle, whose axis is $\hat{s}_1$.*

power is:

$$\begin{aligned} P_\theta = 1/4\{1 \quad &+ \quad \sin 2\chi \quad (M_{13} + M_{23}) \\ &+ \quad \cos 2\chi \quad [(M_{11}\cos 2\theta + M_{21}\sin 2\theta)\cos 2\psi \\ &\qquad\qquad + (M_{12}\cos 2\theta + M_{22}\sin 2\theta)\sin 2\psi]\} \end{aligned} \tag{A.9}$$

Therefore with an evolving ψ but constant χ at launch, the signal has a different amplitude but the same phase as equal power launch. This can be also be understood as that the excessive portion of either LCP or RCP only generates a DC offset and signal amplification at the mixer.

A.5 Polarimeter launch and detection

There are various combinations of launch and detection setups. For example, the polarimeter can launch:

(1) LCP + RCP, i.e., rotating linear polarization (red circle in Fig. A.3a, $s_0 \equiv 1$, $\psi(0) = \omega_{\rm df} t/2$, $\chi(0) = 0$)

$$\vec{s}_{3\times1}(0) = \begin{pmatrix} \cos(\omega_{\rm df} t) \\ \sin(\omega_{\rm df} t) \\ 0 \end{pmatrix} \longrightarrow \vec{s}_{3\times1}(z) = \begin{pmatrix} M_{11}\cos(\omega_{\rm df} t) + M_{12}\sin\omega_{\rm df} t \\ M_{21}\cos(\omega_{\rm df} t) + M_{22}\sin\omega_{\rm df} t \\ M_{31}\cos(\omega_{\rm df} t) + M_{32}\sin\omega_{\rm df} t \end{pmatrix} \tag{A.10}$$

(2) O + X, i.e., horizontal and vertical polarization (red circle in Fig. A.3b, $s_0 \equiv 1$, $\alpha(0) = \pi/4$, $\delta(0) = \omega_{\rm df} t$)

$$\vec{s}_{3\times1}(0) = \begin{pmatrix} 0 \\ \cos(\omega_{\rm df} t) \\ \sin(\omega_{\rm df} t) \end{pmatrix} \longrightarrow \vec{s}_{3\times1}(z) = \begin{pmatrix} M_{12}\cos(\omega_{\rm df} t) + M_{13}\sin(\omega_{\rm df} t) \\ M_{22}\cos(\omega_{\rm df} t) + M_{23}\sin(\omega_{\rm df} t) \\ M_{32}\cos(\omega_{\rm df} t) + M_{33}\sin(\omega_{\rm df} t) \end{pmatrix} \tag{A.11}$$

With the detection setup as shown in Fig. A.4, the power measured by the detector I_D is shown in Eqn. A.12.

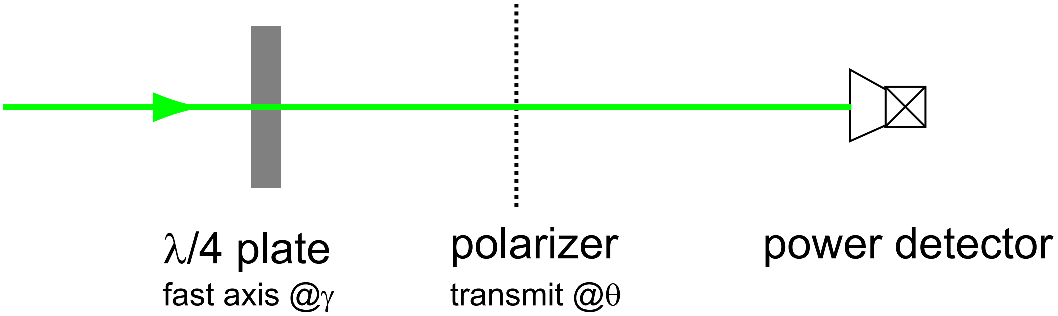

Figure A.4: *Layout of polarization detection. The $\lambda/4$ wave plate is oriented as its fast axis forms an angle γ with respect to $\hat{x}$ (horizontal direction). The following polarizer transmits the linear polarization at angle θ. A power detector then measured the transmitted beam power.*

$$I_D(\gamma,\theta) = \frac{1}{2}\left[1 + A(\gamma,\theta)s_1 + B(\gamma,\theta)s_2 + C(\gamma,\theta)s_3\right],$$

$$\begin{cases} A(\gamma,\theta) = \cos 2\gamma \cos(2\theta - 2\gamma) \\ B(\gamma,\theta) = \sin 2\gamma \cos(2\theta - 2\gamma) \\ C(\gamma,\theta) = \sin(2\theta - 2\gamma) \end{cases} \tag{A.12}$$

Equation A.13 demonstrates that with specific configurations, all three Stokes vector components can be directly measured.

$$I_D(\gamma,\theta) = \begin{cases} \dfrac{1+s_1}{2}, & \gamma=\theta=0, \text{ i.e., } 0^\circ \text{ polarization power} \\ \dfrac{1+s_2}{2}, & \gamma=\theta=\pi/4, \text{ i.e., } 45^\circ \text{ polarization power} \\ \dfrac{1+s_3}{2}, & \theta-\gamma=\pi/4 \end{cases} \tag{A.13}$$

The full 3×3 Mueller matrix can be determined with rotating linear polarization launch and simultaneous measurements (by beam splitting) from two detectors oriented at 0° and 45° respectively.

$$\begin{aligned} I_D(0,0) &= \frac{1}{2}[1+A_1\sin(\omega_{\mathrm{df}}t+\phi_1)], \\ I_D(\pi/4,\pi/4) &= \frac{1}{2}[1+A_2\sin(\omega_{\mathrm{df}}t+\phi_2)] \end{aligned} \tag{A.14}$$

$$\begin{cases} A_1 = C\sqrt{M_{11}^2+M_{12}^2} \\ \phi_1 = \tan^{-1}\left(\dfrac{M_{11}}{M_{12}}\right) \end{cases}, \quad \begin{cases} A_2 = C\sqrt{M_{21}^2+M_{22}^2} \\ \phi_2 = \tan^{-1}\left(\dfrac{M_{21}}{M_{22}}\right) \end{cases} \tag{A.15}$$

where C is a factor that accounts for the beam power loss due to refraction, dissipation during propagation, etc.

From the three equations: ϕ_1, ϕ_2 and A_1/A_2, the 3 independent elements of the orthogonal 3×3 Mueller matrix (see Section 2.4) can be determined.

A.6 Tests of polarimeter quasi-optical components

The polarimeter quasi-optical components were systematically characterized with the layout shown in Fig. A.5. The Gunn output is amplitude modulated by a PIN diode switch, which operates at 200 *kHz* square waveform. This chopped output is then tripled in frequency and coupled to free space by a dual-mode horn, and converted to a parallel propagating beam by an $f = 6$ *inch* lens. The beam is horizontally polarized, transmitting through the component being tested and eventually detected by another dual-mode horn attached to a single-ended mixer. The horn at the mixer is surrounded by absorber to prevent reflections. Three kinds of mounts are placed between the lens and mixer to enable the separate insertion of Faraday rotator, polarizers in the beam path.

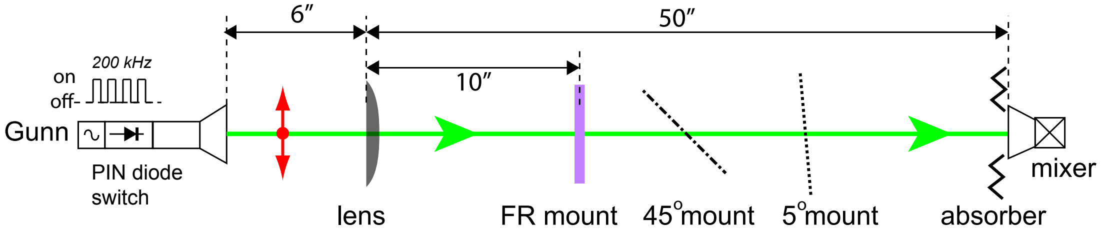

Figure A.5: *Layout for testing polarimeter quasi-optical components. The Gunn output is amplitude modulated with a PIN diode switch, which operates at* 200 *kHz square waveform.*

A.6.1 Faraday rotator

The black curve in Fig. A.6 is the Gunn output power versus mixer orientation. The minimum at 90° demonstrates that the output is horizontally polarized. The difference in the peak values at 0° and 180° probably results from the slight wobble during the mixer rotation. The other three curves show the power of this horizontal polarization propagates through Faraday rotator #1 in different configurations. The red curve is with the Faraday rotator mounted in a way so that its mark is facing the source, whereas the blue one is the Faraday rotator in the opposite direction. The green curve is a repeat of the red curve, with a different Gunn frequency. It can be concluded that the Faraday rotator can rotate the linearly polarized wave of 96.0 ± 0.1 GHz by $45^\circ \pm 1^\circ$, with an attenuation of ~ 3 dB. Figure A.7 demonstrates that two Faraday rotators are very close in performance.

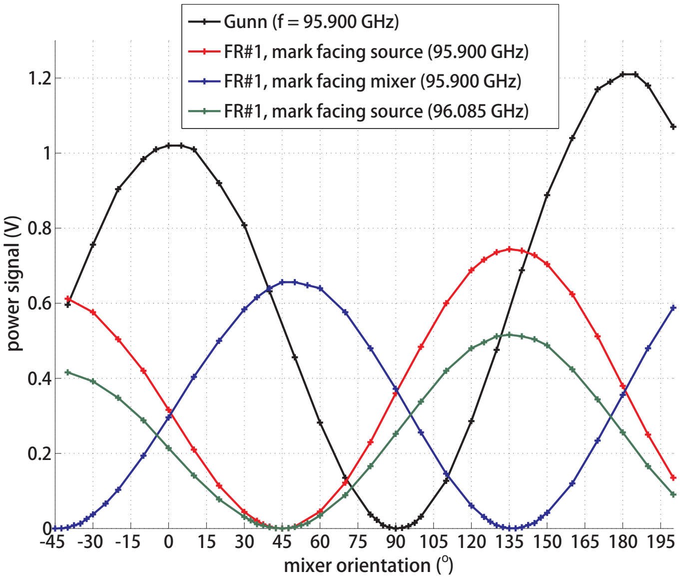

Figure A.6: *The mixer signal after a horizontal polarization propagating through the 45° Faraday rotator is plotted versus mixer orientation.*

A.6.2 Polarizer

There are two kinds of polarizers used in the polarimeter system, one kind uses free standing wire grid, and the other kind is copper clad PET substrate (a cross section schematic is shown in Fig. A.8). The leakage of these two kinds of polarizers is compared in Fig. A.9. It can be seen that the PET polarizer is $\sim 3\%$ versus the

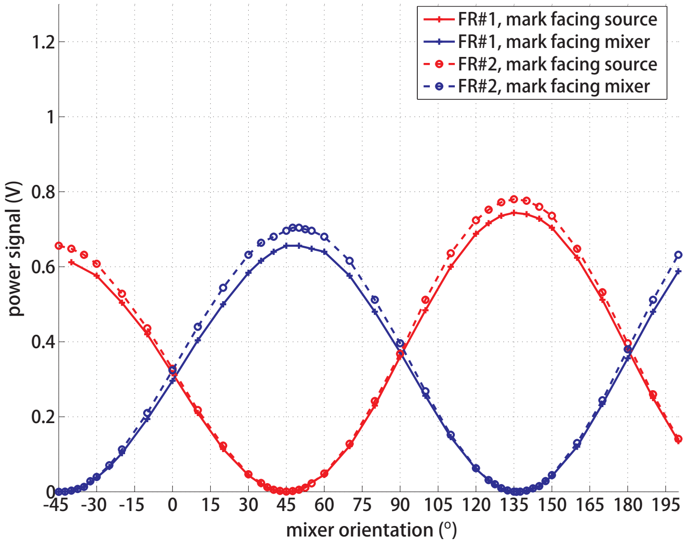

Figure A.7: *Comparison of Faraday rotator #1 and #2.*

free-standing wire grid polarizer ∼ 1.5% in leakage.

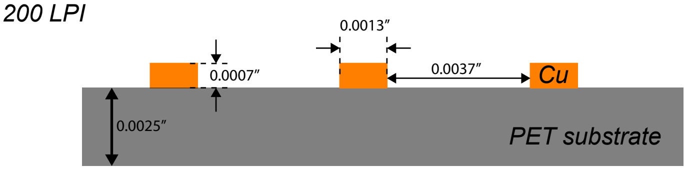

Figure A.8: *Schematic of the PET substrate polarizer cross section (200 LPI).*

Also worth noting here is the ‘45°’ polarizer, which combines the pair of mm-wave beams polarized at ±45° (see Fig. 3.11). This polarizer is oriented at 45° in the beam path, and its 35.3° wire angle appears to be 45° when projected to the beam transverse plane.

The beam polarization after it propagates through the ‘45°’ polarizer was

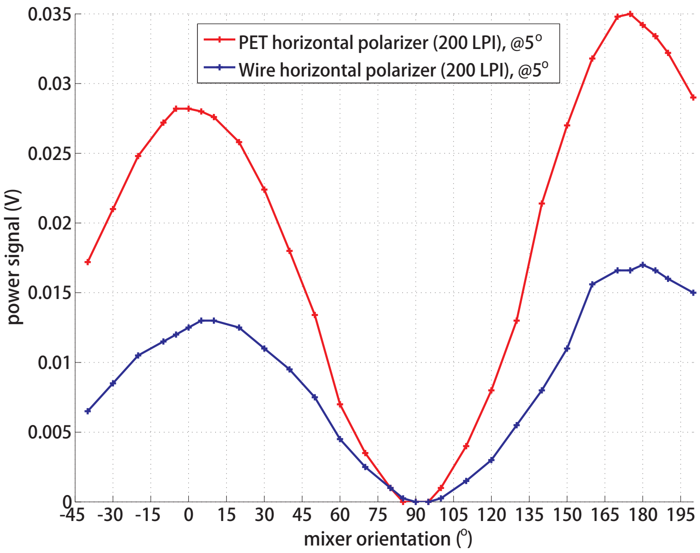

Figure A.9: *Transmitted horizontal polarization (leakage) when the polarizer is oriented at 5° in beam path. The leakage of the PET polarizer (200 LPI, copper strips facing source; red curve) and the free-standing wire grid polarizer (200 LPI, blue curve) is plotted.*

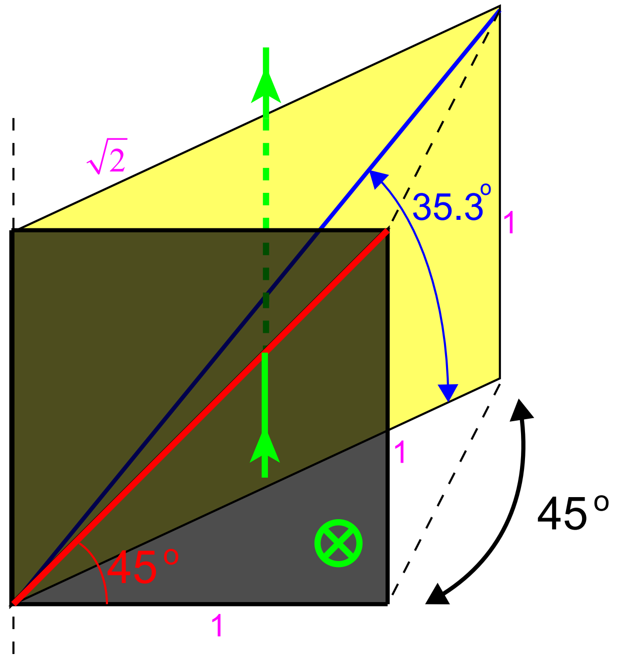

Figure A.10: *The polarizer is oriented at 45° in the beam path, and its 35.3° wire angle (blue line in the yellow plane) appears to be 45° when projected to the beam transverse plane (red line in the gray plane).*

measured with the mixer (see Fig. A.11). It can be seen that better angle accuracy is achieved when the PET side is facing the source (blue curve). In the final design, two such '45°' polarizers were clipped together to increase the Lines Per Inch (LPI).

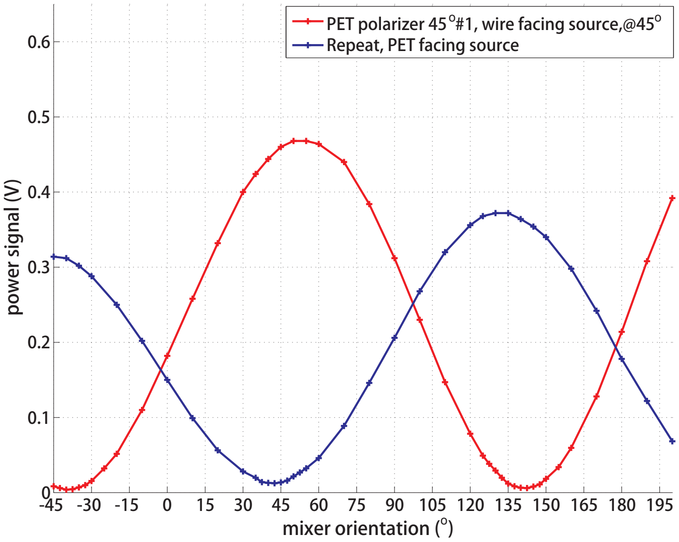

Figure A.11: *Beam polarization after it propagates through the '45°' PET substrate polarizer.*

A.6.3 Beam splitting mesh

It is critical that the mesh has equal transmission and reflection coefficients to all polarizations so that it is capable to maintain the circular polarization during beam splitting. This mesh has a rectangular pattern, which is 80(H) × 125(V) LPI (i.e., $\sim 1 : \sqrt{2}$), so it appears to be square when inserted at 45° in the beam path (same argument as in Section A.6.2).

The mesh was characterized with the layout as shown in Fig. A.12. The mesh was verified to be able to maintain the linearity of launched linear polarization oriented at horizontal, vertical, ±45° or ±35°. The transmission coefficient was $T_{\parallel} = [12.8\%, 14.6\%]$ for horizontal launch and $T_{\perp} = [13.5\%, 15.3\%]$ for vertical launch.

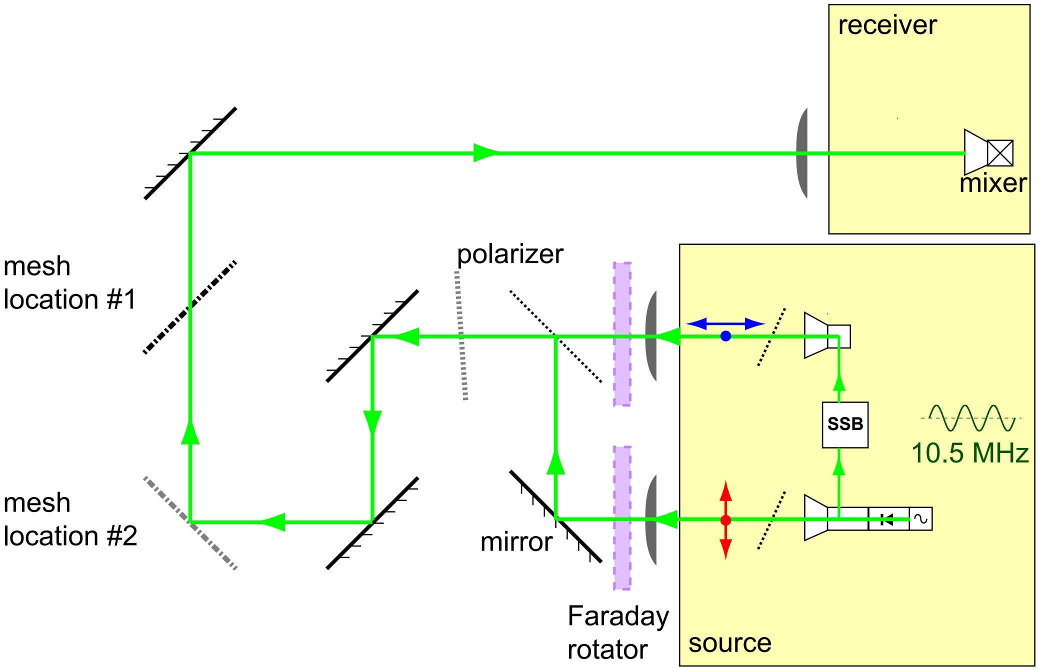

Figure A.12: *Layout for characterizing beam splitting mesh. The mesh is mounted at location #1 for transmission coefficient measurement, with a mirror mounted at location #2. The reflection coefficient is measured with the mesh mounted at location #1. The Gunn output is amplitude modulated. Linear polarization oriented at horizontal, vertical, ±45° or ±35° can be launched. Faraday rotators, polarizers are inserted as necessary to launch these polarizations.*

A roof-top reflector, which is composed of two mirrors (aluminum plates for mm-wave) attached perpendicular to each other, was used to characterize different meshes. The reflector is equivalent to a reflective $\lambda/2$ wave plate with its axis along the joint edge. Figure A.13 presents a top view of the roof-top reflector, showing that after two reflections (see Fig. A.1), the E-field perpendicular to the joint edge is flipped while the E-field parallel to the joint edge is unchanged.

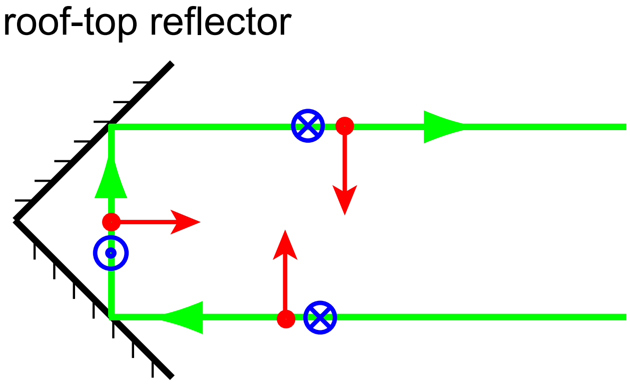

Figure A.13: *The roof-top reflector is equivalent to a reflective $\lambda/2$ wave plate with its axis along the joint edge. This is a top view of the roof-top reflector, showing that after two reflections, the E-field perpendicular to the joint edge (red) is flipped while the E-field parallel to the joint edge (blue) is unchanged.*

This roof-top reflector was inserted before the lens pair in the DIII-D polarimeter system (see Fig. 3.11) and aligned to retro-reflect the probe beam. The launched linear polarization flips around the reflector joint edge, and therefore a phase shift is resulted in the measured sinusoidal waveform. This phase shift varies as the joint edge is rotated. The beam splitting mesh has slightly different transmission coefficients (also reflection coefficients) to horizontal and vertical polarizations, and therefore can distort the linear dependence between the measured phase shift and reflector angle. As can be seen in Fig. A.14, the rectangular mesh (125×88 *LPI*) introduces less distortion than the square mesh (100 LPI).

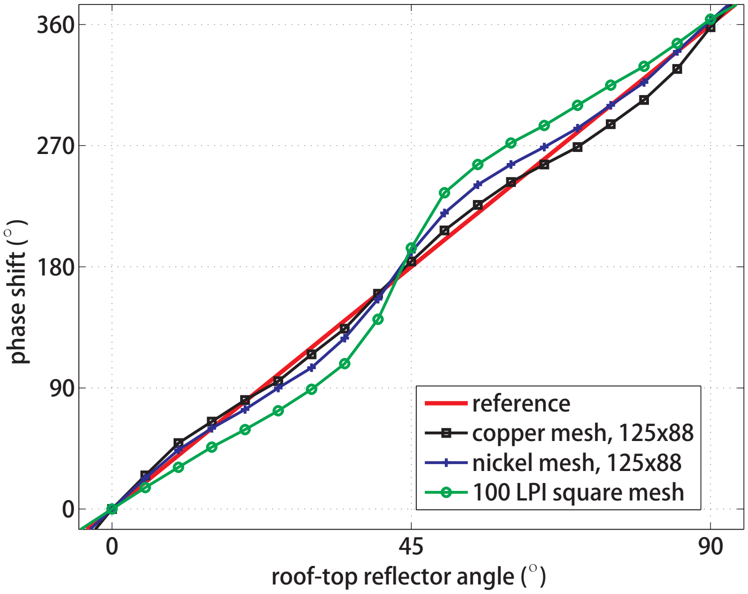

Figure A.14: *Different meshes are characterized by roof-top reflector. The mesh distorts the linear dependence between the measured phase shift and reflector angle. The red line shows the ideal linear dependence.*

This characterization curve can be potentially used to calibrate the phase measured in the plasma experiments where the FR effect is dominant, i.e., the elliptization is not significant.

A.6.4 Crystal quartz $\lambda/4$ wave plate

The crystal quartz $\lambda/4$ wave plates were tested for the phase shift and transmission coefficient with the layout in Fig. A.15. The system is setup as an interferometer and the amplitude and phase of the 10.5 *MHz* sinusoidal waveform are measured when varying the tilt angle of the wave plate. Two wave plates have slightly different thicknesses ($d_1 = 0.2134''$, $d_2 = 0.2146''$), to bracket the uncertainties of the differential refraction indices ($|n_X - n_O| \in [0.0474, 0.0480]$). The measured phase shift is shown in Fig. A.16.

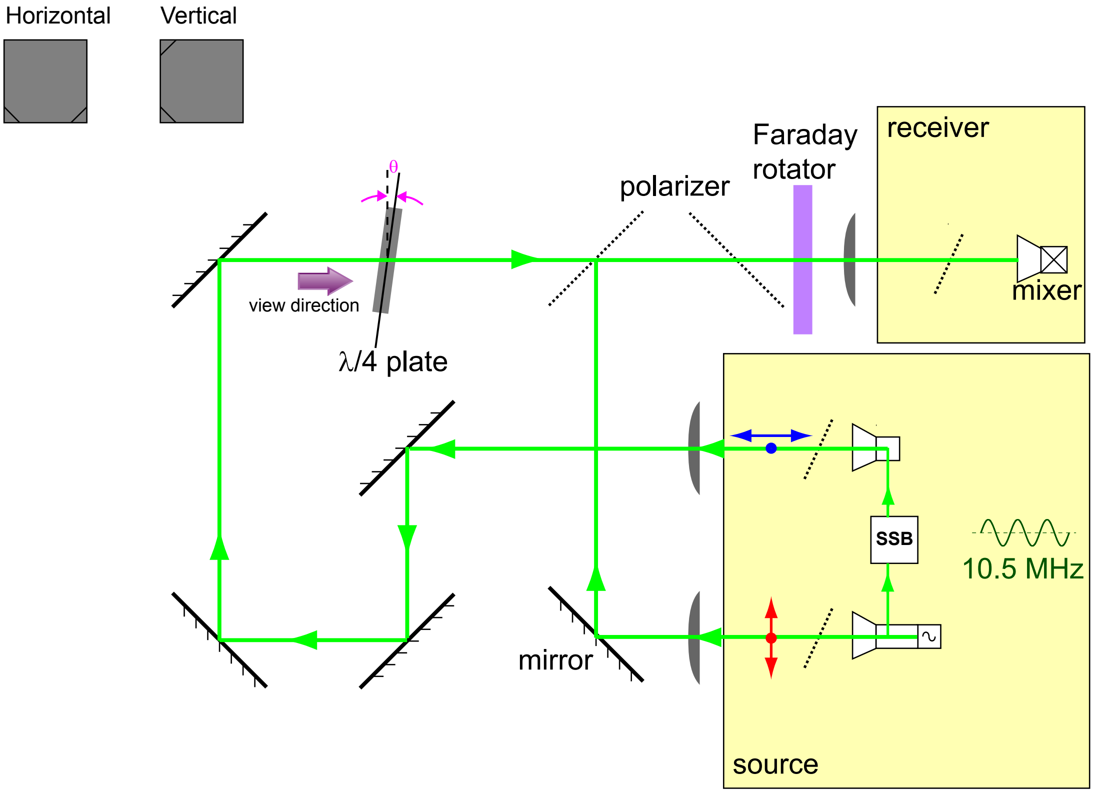

Figure A.15: *Layout for characterizing crystal quartz $\lambda/4$ wave plate. The wave plate orientation is defined as shown on the upper-left corner if viewed as the bold arrow indicates.*

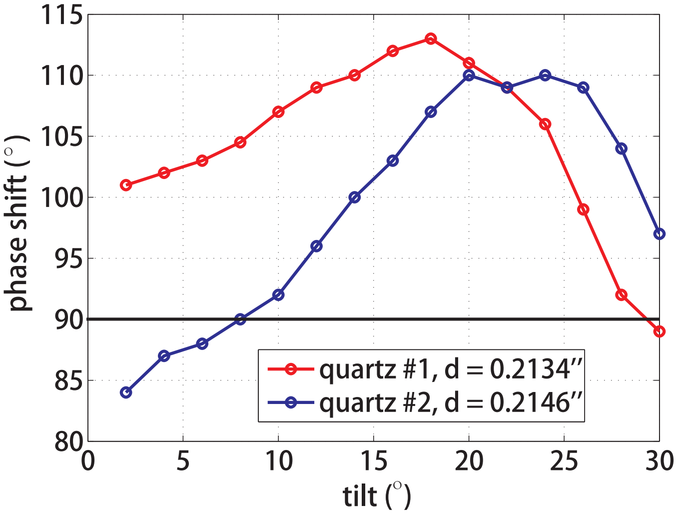

Figure A.16: *Measured phase shift of the $\lambda/4$ wave plate versus its tilting angle.*

A.6.4.1 Etalon effect

The two parallel surfaces of the $\lambda/4$ wave plate compose an etalon. Therefore the transmission coefficient T depends on the tile angle θ [Hecht, 2002].

$$\begin{aligned} T &= \frac{1}{1 + F\sin^2(\delta/2)}, \\ F &= \frac{4R}{(1-R)^2}, \quad \delta = \left(\frac{2\pi}{\lambda_0}\right) 2nd\cos\theta \\ R &= \left|\frac{n-1}{n+1}\right|^2, \text{ for normal incidence} \end{aligned} \tag{A.16}$$

where d is the thickness of the wave plate, n is the refractive index of quartz, λ_0 is the wavelength in vacuum.

Figure A.17 compares the theory predictions (solid and dashed curves) and measurements (scattered points) of the etalon effect. The theory predictions are based on Eqn. A.16 with the refractive indices as $n_{\mathrm{O}} = 2.1059$ for horizontally oriented wave plate and $n_{\mathrm{X}} = 2.1533$ for vertically oriented wave plate. The measurements qualitatively follow the trend of the curves.

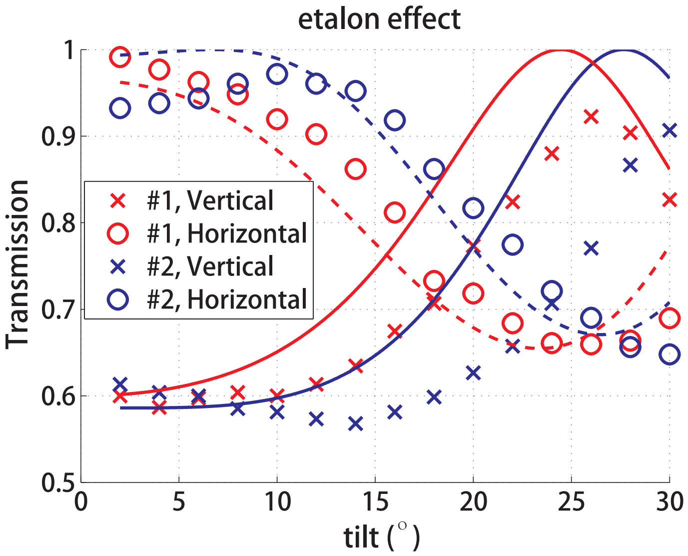

Figure A.17: *Transmission coefficient measurement and theory prediction of the $\lambda/4$ wave plate. The solid and dashed curves are the transmission coefficients predicted by the theory of etalon effect (see Eqn. A.16). The refractive indices are assumed as $n_O = 2.1059$ for horizontally oriented wave plate and $n_X = 2.1533$ for vertically oriented wave plate. The measured transmission coefficients are scattered points.*

The system was setup as a polarimeter and the quartz wave plate #2 was inserted at $\sim 8°$ in the beam path, as shown in Fig. A.18. The measured power signal versus mixer orientation is presented in a compass plot (see Fig. A.19).

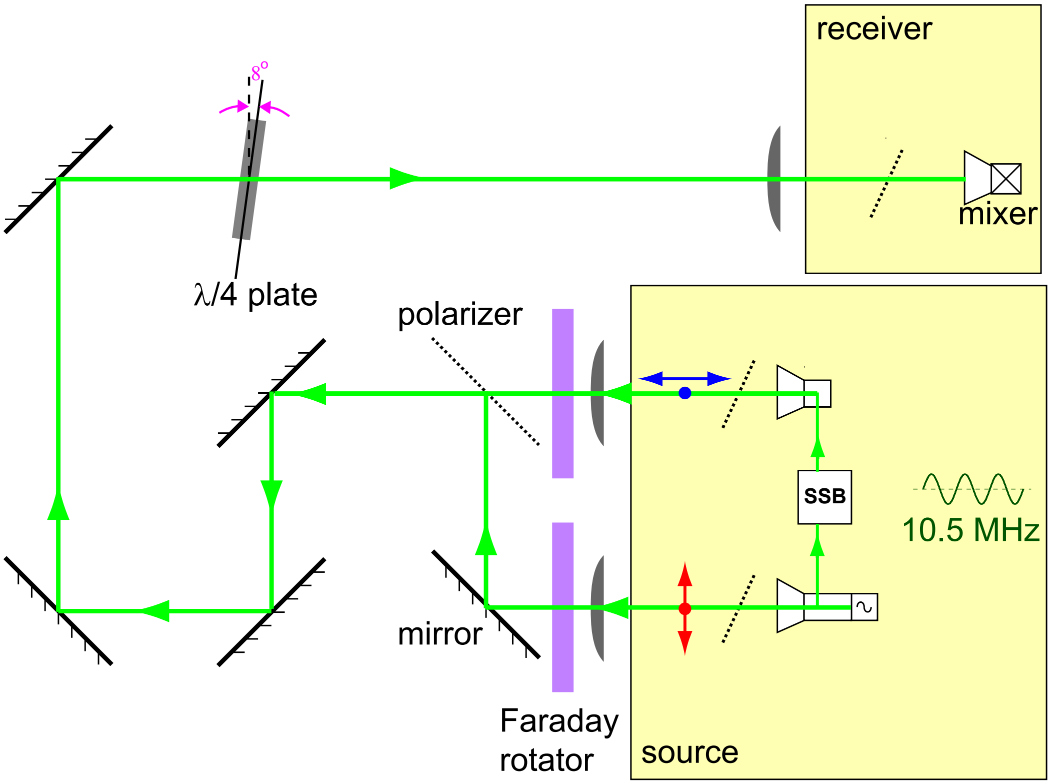

Figure A.18: *The system was setup as a polarimeter and the second* $\lambda/4$ *wave plate was inserted at* $\sim 8^\circ$ *in the beam path.*

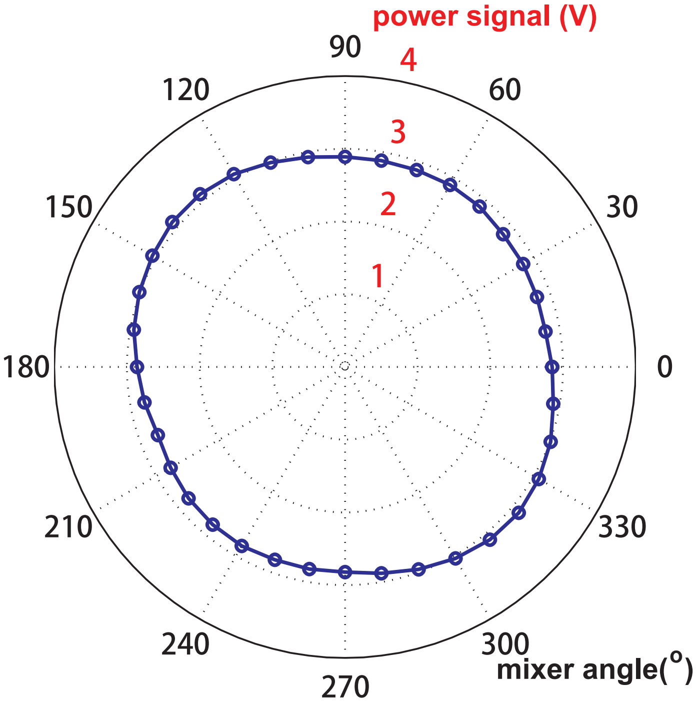

Figure A.19: *Polarization circularity is checked with the power signal measured by a rotating mixer. The voltage versus mixer angle is presented in a compass plot.*

A.7 Bandpass filtering

The bandpass filtering is essential to achieve high phase resolution. The phase noise primarily originates from the incomplete suppression of the carrier and other sidebands in the SSB modulator ($96\ GHz$ and $96\ GHz - 3.5\ MHz$ are $> 30\ dB$ lower in power than $96\ GHz + 3.5\ MHz$), and these frequencies are not only tripled but also nonlinearly mixed in the tripler, generating an array of frequencies with the separation of $3.5\ MHz$: $288\ GHz + m \cdot 3.5\ MHz,\ m \in \mathbb{Z}$. At the receiver these SSB branch frequencies mix with the Gunn branch frequency $288\ GHz$, and mix among generates harmonics of $3.5\ MHz$, whereas the desired mixing is: $288\ GHz \bigotimes 288\ GHz + 10.5\ MHz \rightarrow 10.5\ MHz$. Figure A.20 presents that the undesired frequencies are suppressed by $\sim 55\ dB$ down in comparison to the $10.5\ MHz$ with two bandpass filters.

A.8 Initial polarimeter design

The initial polarimeter concept is presented in Fig. A.21. Initially, the heterodyne source design utilized the frequency-sweeping technique, which creates a difference frequency by delaying a linearly scanned Gunn frequency, as shown in Fig. A.22. This technique suffers from two major problems. One problem is the difference frequency instability caused by the nonlinear Gunn frequency-bias response (see Fig. A.23) and the delay-line (W-band waveguide) length variation due to either thermal effect or mechanical vibrations. The other problem is the challenge in digitization and the associated data analysis. The abrupt change of difference frequency in the retracing region causes spikes in the signal, as illustrated in Fig. A.22, which distorts the

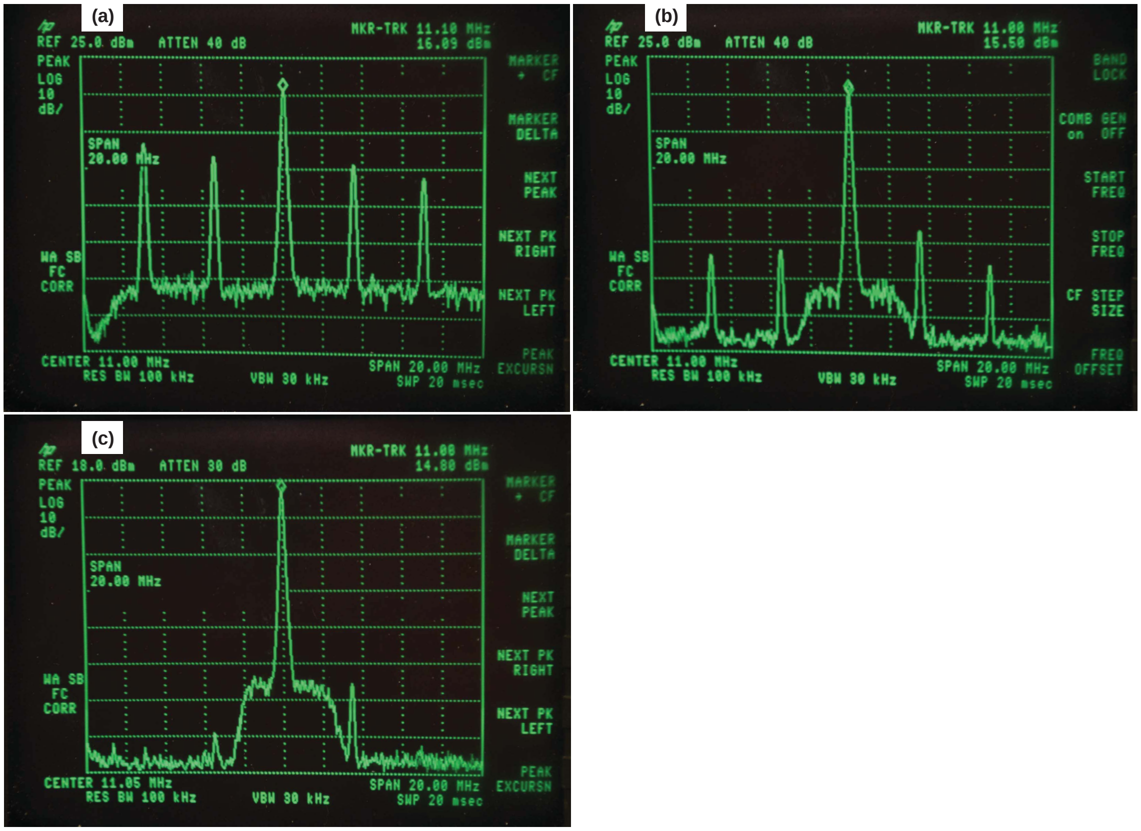

Figure A.20: *The polarimeter signal is heavily bandpass filtered to suppress undesired frequencies. (a) Raw signal frequency spectrum without any filtering; (b) with 1 SBP-10.7+ filter; (c) with 2 SBP-10.7+ filters. From the* 10.5 *MHz peak, the Gunn frequency noise is estimated about* 100 *kHz wide at 3-dB point.*

sinusoidal wave even after filtering. This also causes difficulties in developing the algorithm to extract phase.

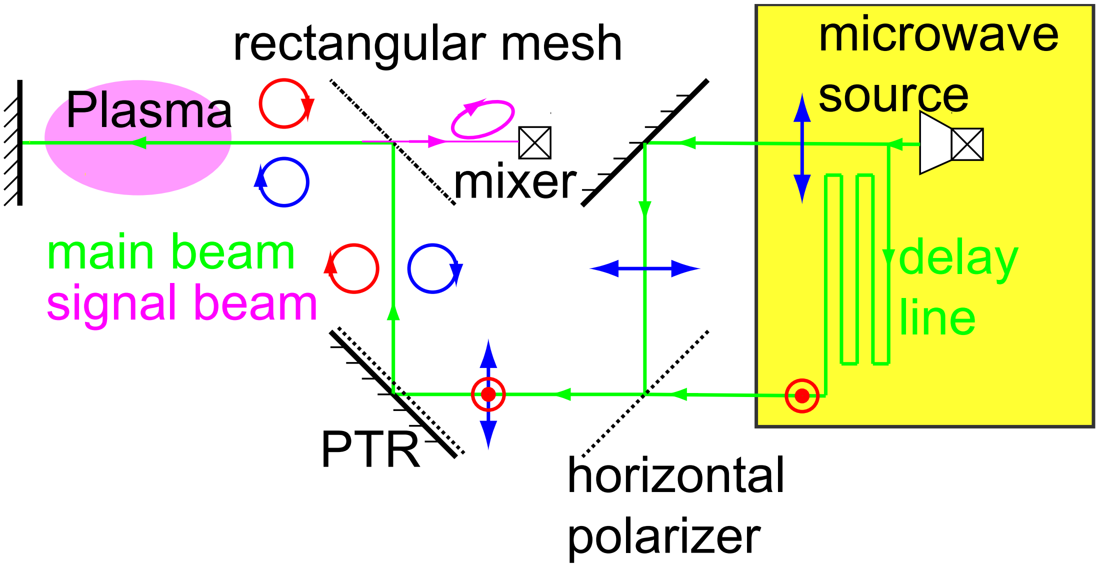

Figure A.21: *Initial design of 288 GHz polarimeter. Frequency-sweeping technique is used to create a heterodyne microwave source, and PTR (Polarization Transforming Reflector) is used to convert the wave polarization from linear to circular.*

Moreover, a so-called "PTR" (Polarization Transforming Reflector), as indicated in Fig. A.21, was used to convert the wave polarization from linear to circular. Figure A.24 shows that an incoming $+45°$ linear polarization can be decomposed into equal vertical and horizontal components, which reflect from the vertical polarizer and the mirror behind it, respectively. The $\lambda/4$ difference in their path length due to the polarizer-mirror separation can transform the combined polarization to be LCP. Similarly, an incoming $-45°$ linear polarization is converted to RCP. This PTR design is an innovative concept, and was proven to be functional in laboratory tests.

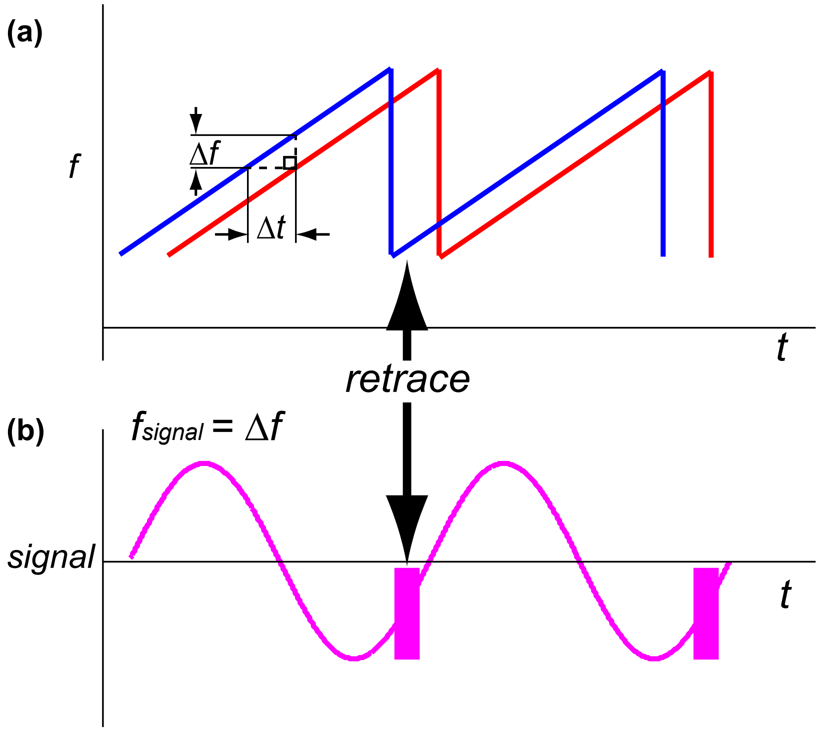

Figure A.22: *(a) Initial heterodyne source design utilized the frequency-sweeping technique, which creates a difference frequency by delaying a linearly scanned Gunn frequency. (b) Abrupt change in the difference frequency in retracing region causes spikes in the signal.*

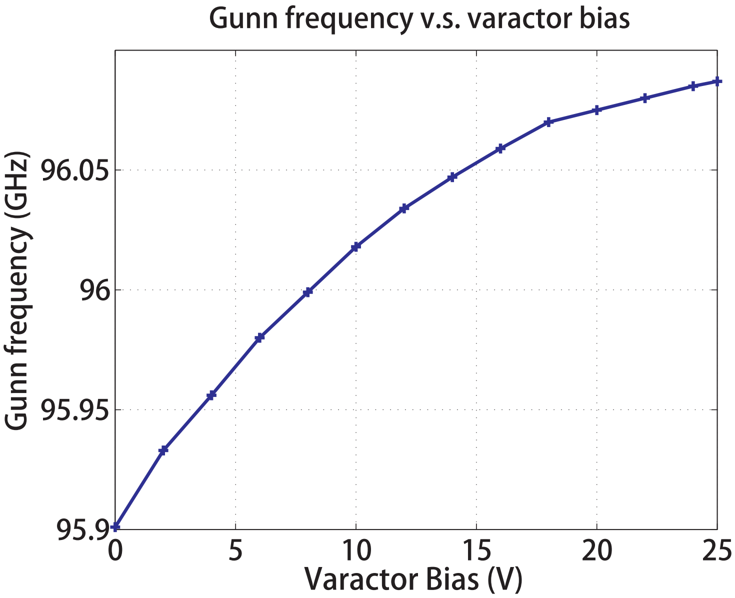

(Varactor Tuned Gunn Oscillator; Ducommun; OGV-10960217-01;
Diode bias +10.5 V, 0.23 A,17.5 dBm output)

Figure A.23: *The varactor tuned Gunn used in the initial polarimeter design has a nonlinear frequency-bias response.*

It is not adopted in the final design mainly due to its vulnerability to mechanical vibrations, which is a big concern for the systems operating near tokamaks.

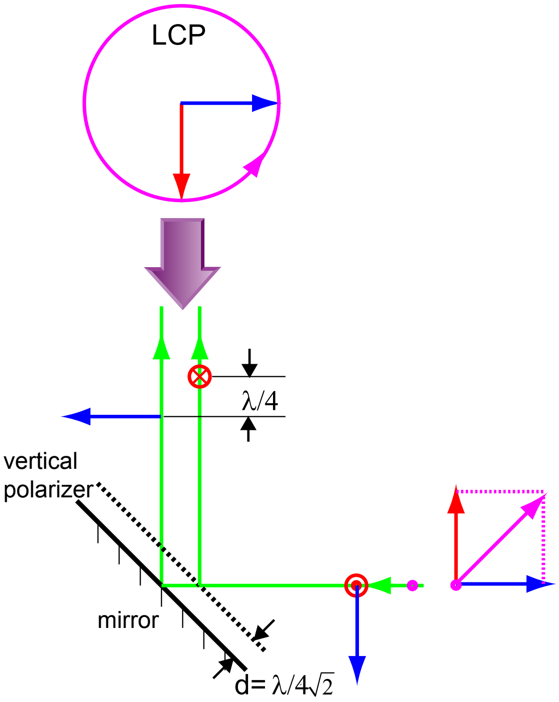

Figure A.24: *Schematic of "PTR" (Polarization Transforming Reflector). A +45° linear polarization can be decomposed into equal vertical and horizontal components, which reflects from the vertical polarizer and the mirror behind it, respectively. The $\lambda/4$ difference in their path length due to the polarizer-mirror separation can transform the combined polarization to be LCP. The bold arrow indicates the view direction in which the polarization is depicted.*

A.9 Derivation of multi-reflection feedback effect

As shown in Fig. 3.5, the cavity can be simplified as a following model: the graphite tile is a 100% reflective mirror for microwave; the mixer and other quasi-optical components in between together form a lossy mirror with a reflection coefficient in E-field:

$$\begin{aligned} r &= 0.9^2 \text{ (mesh, round trip)} \\ &\quad \times(\sqrt{2}/2)^2 \text{ (linear polarizer, round trip)} \\ &\quad \times 1/3 \ \text{ (mixer, } \mathit{VSWR} \approx \mathit{2{:}1}) \\ &\approx 0.15 \end{aligned} \tag{A.17}$$

Note that each beam composes of two frequencies: 288 $GHz \sim$ 'lo', 288 $GHz +$ 10.5 $MHz \sim$ 'lo+df'.

$$\begin{aligned} E &= E_1 + E_2 + \cdots \\ &= \left[A_{\text{lo}} e^{-i(\omega_{\text{lo}} t - k_{\text{lo}} L)} + A_{\text{lo+df}} e^{-i(\omega_{\text{lo+df}} t - k_{\text{lo+df}} L - \delta)}\right]_1 \\ &\quad + \left\{ r e^{i\theta} \left[A_{\text{lo}} e^{-i(\omega_{\text{lo}} t - 2k_{\text{lo}} L)} + A_{\text{lo+df}} e^{-i(\omega_{\text{lo+df}} t - 2k_{\text{lo+df}} L - 2\delta)}\right]\right\}_2 \\ &\quad + O(r^2) \end{aligned} \tag{A.18}$$

where the subscripts '1' and '2' indicate the E-field corresponding to the numbered beam; A is the E-field amplitude; L is the path length; δ is the phase difference due to plasma polarimetry effects; $re^{i\theta}$ represents the reflection coefficient and phase shift introduced at the lossy mirror; $O(r^2)$ includes the E-field of higher order feedback beams (beam #3, etc.). With the assumption $A_{\text{lo}} = A_{\text{lo+df}} = A$, $k_{\text{lo+df}} = k_{\text{lo}} + k_{\text{df}}$,

$\omega_{\mathrm{lo+df}} = \omega_{\mathrm{lo}} + \omega_{\mathrm{df}}$, the signal at the mixer can be expressed as:

$$
\begin{aligned}
P &= {}^1\!/\!_2 E \cdot E^* \\
&= {}^1\!/\!_2 \left[(E_1 \cdot E_1^*)_{1,1} + (E_1 \cdot E_2^* + E_2 \cdot E_1^*)_{1,2} + (E_2 \cdot E_2^*)_{2,2} + \cdots \right] \\
&= A^2 \left[1 + \cos(\omega_{\mathrm{df}} t - k_{\mathrm{df}} L - \delta) \right] \big|_{1,1} \\
&\quad + r A^2 \left\{ \cos(k_{\mathrm{lo}} L + \theta) + \cos\left[(k_{\mathrm{lo}} + k_{\mathrm{df}}) L + \delta + \theta \right] \right. \\
&\quad \left. + 2 \cos\left[(k_{\mathrm{lo}} + {}^1\!/\!_2 k_{\mathrm{df}}) L + {}^1\!/\!_2 \delta - \theta \right] \cos(\omega_{\mathrm{df}} t - {}^3\!/\!_2 k_{\mathrm{df}} L - {}^3\!/\!_2 \delta) \right\} \big|_{1,2} \\
&\quad + O(r^2) \\
&= P_{DC} + A_{\Sigma}(L, \delta) \cos\left[\omega_{\mathrm{df}} t - \Delta\phi|_{\Sigma}(L, \delta) \right] + O(r^2)
\end{aligned}
\tag{A.19}
$$

where subscript ‘Σ’ indicates the measured amplitude or phase at the mixer; P_{DC} means the time-independent part of the signal. It is obvious that both the measured amplitude and phase are functions of the beam path length (L) and polarimetry phase (δ).

APPENDIX B

List of polarimeter components

Table B.1: *Polarimeter component list*

Component	**Manufacturer**	**M/N**	**Specification**	**Quantity**
Solid-state components				
Bias tuned Gunn oscillator	WiseWave	GBT-10962520-0M	Bias +10.0 *V*, 0.35 *A*, 20 *dBm* output	1
E-H tuner	Dorado			1
Directional Coupler	Hughes	45326H-1210	10-dB directional coupler	1
96 *GHz* Isolator	WiseWave		96 *GHz* isolator	1
288 *GHz* Frequency Tripler	RPG		passive, input frequency 80–106.6 *GHz*, conversion efficiency 2-3%	2
96 *GHz* Power Amplifier	Ducommun	SBP-9639633018-1010-S1	Bias +8.0 *V*, 0.65 *A*, 30 *dB* gain, 20 *dBm* output	1
Attenuator	Ducommun	CAL-10-02		1
96 *GHz* SSB Modulator	WiseWave	FSS-961012-W1		1
288 *GHz* Mixer	RPG			2
PIN Diode Switch	Hughes	47976H-1800	Bias +2.0 *V* (block)–−15.0 *V* (transmit), 200 *kHz* square wave operation for AMing	1
Electronics				

Continued on next page

Table B.1 – continued from previous page

Component	Manufacturer	M/N	Specification	Quantity
Amplifier				
1st mixer Amplifier chain #1	Amplica	AVD706301	Bias +15.0 V, $G \sim 54$ dB, 10–150 MHz (3-dB), 1.4 dB NF, Saturate@3.2 Vpp	1
1st mixer Amplifier chain #2	Mini-Circuits	ZFL-1000VH	Bias +15.0 V, $G \sim 25$, 10–1000 MHz, 4.5 dB NF, Saturate@11 Vpp	1
2nd mixer Amplifier chain #1	Amplica	AVD706301	Bias +15.0 V, $G \sim 54$ dB, 10–130 MHz, 1.5 dB NF, Saturate@3.2 Vpp	1
2nd mixer Amplifier chain #2	Mini-Circuits	ZFL-500HLN	Bias +15.0 V, $G \sim 11.5$, 10–500 MHz, 3.8 dB NF	1
E-Reference Signal Amplifier	Mini-Circuits	ZFL-1000VH-8	Bias +15.0 V, $G \sim 20.6$, 10–1000 MHz, 4.5 dB NF	1
IQ Power Amplifier	Mini-Circuits	ZHL-32A BNC	Bias +24.0 V, 0.05–130 MHz, amplify IQ to ~ 8 Vpp	1
AMing Amplifier chain #1	Mini-Circuits	ZFL-500LN+	Bias +15.0 V, 0.1–500 MHz	1
AMing Amplifier chain #2	FEMTO	HVA-10M-60-B	Bias ±15.0 V, $G \sim 40/60$ dB, DC–10 MHz	1
Bias tee				

Continued on next page

Table B.1 – continued from previous page

Component	Manufacturer	M/N	Specification	Quantity
@1st mixer	Picosecond	5575A	10 *kHz*–12 *GHz*	1
@2nd mixer	Mini-Circuits	ZFBT-4R2GW+	0.1–4200 *MHz*	1
@Crystal Oscillator	Mini-Circuits	ZFBT-4R2GW+	0.1–4200 *MHz*	1
Crystal Oscillator & its circuit	ECS	ECS-P85-A-ND	Bias +5.0 *V*, 3.5 *MHz*, ±100 *ppm*	2
Filter				
SBP-10.7+	Mini-Circuits	SBP-10.7+	9.5–11.5 *MHz*	6
BBP-10.7+	Mini-Circuits	BBP-10.7+	9.5–11.5 *MHz*	6
SLP-5	Mini-Circuits	SLP-5	*DC*–5 *MHz*	2
BLP-5+	Mini-Circuits	BLP-5+	*DC*–5 *MHz*	2
BLP-10.7+	Mini-Circuits	BLP-10.7+	*DC*–11.5 *MHz*	2
50 Ω **Terminator/SMA**				3
Negative Bias Box for Mixer	UCLA-PDG		monitor mixer current by voltage over 100 Ω	1
Voltage Regulator Array	UCLA-PDG		4 positive channels (LM350, +1.2–+33.0 *V*, 3.0 *A*), 4 negative channels (LM337, −1.2–−37.0 *V*, 1.5 *A*)	1

Continued on next page

Table B.1 – continued from previous page

Component	Manufacturer	M/N	Specification	Quantity
BNC cable		RG58 C/U	$R = 50\ \Omega$, $C = 105\ pF/m$, PE insulation, $\varepsilon = 2.25$	
Optical table	ThorLabs	PBG11107	UltraLight Series I Breadboard–$4' \times 2' \times 0.98''$, trimmed to $48'' \times 20.5'' \times 0.98''$, honeycomb layer structure	1
Quasi-optical components				
Lens			High density polyethylene, $n = 1.53$ for $\lambda_0 = 1.04\ mm$	
$f = 8''$ lens	UCLA-PDG			2
$f = 15\ cm$ lens	UCLA-PDG			2
$f = 5''$ lens	UCLA-PDG			2
$f = 100\ cm, 84'', 94'', 104''$ lens	UCLA-PDG			4
$f = 3''$ lens	UCLA-PDG			2
& mount	UCLA-PDG		$5''$ outer diameter, $4.5''$ clear aperture	6
Rectangular Mesh	UCLA-PDG		$80 \times 125\ LPI$	2

Continued on next page

Table B.1 – continued from previous page

Component	Manufacturer	M/N	Specification	Quantity
Free Standing Wire Grid Polarizer				
3″ diameter rotatable	UCLA-PDG		400 *LPI*	2
Vertical polarizer	UCLA-PDG		200 *LPI*	1
PET Substrate, Copper Clad Polarizer	UCLA-PDG		200 *LPI* (Copper 0.0013″ wide), Substrate 0.0025″ thick, Copper 0.0007″ thick, mounted on a 7″ × 5″ frame, 6.5″ × 4″ aperture	
Vertical Polarizer				1
Horizontal Polarizer				1
45° Polarizer				4
Small Vertical Polarizer & mount			mounted on $4'' \times 2.75''$ frame, $3.5'' \times 2.25''$ aperture	2
Mount for polarizer/mesh	UCLA-PDG		length = 7″	10
Crystal Quartz Wave Plate	Boston Piezo-Optics		for $\lambda_0 = 1.04\ mm$, $n_O \approx 2.1059$, $n_X \approx 2.1533$	

Continued on next page

Table B.1 – continued from previous page

Component	**Manufacturer**	**M/N**	**Specification**	**Quantity**
$\lambda/4$ Wave Plate #1			X-cut quatz wave plates, Chemically polished both sides, $3.937'' \pm 0.008''$ square, Z axis marked by (2) corner notches at 45°, $0.2146'' \pm 0.0001''$ thick	1
$\lambda/4$ Wave Plate #2			X-cut quatz wave plates, Chemically polished both sides, $3.937'' \pm 0.008''$ square, Z axis marked by (2) corner notches at 45°, $0.2134'' \pm 0.0001''$ thick	1
& mount	UCLA-PDG		2 orientations (45° & H/V) for square wave plate	1
Faraday Rotator	Thomas Keating Ltd		45° for $f = 287.75$ *GHz*	3
& mount	UCLA-PDG		9 *cm* square clear aperture	3
Mirror with tilt capability	UCLA-PDG			4
& 1D translational mount	Newport	421, 423 series		4
Rotational Stage	Daedal			1
xyz-3D translational stage	OptoSigma			4

Continued on next page

Table B.1 – continued from previous page

Component	Manufacturer	M/N	Specification	Quantity
Power Supply	Instek	GPS-4303	4 channels	2
Absorber				

APPENDIX C

Synthetic diagnostic code in MATLAB

The flow chart of the synthetic diagnostic code is presented in Fig. C.1.

Core MATLAB code for polarimetry calculations:

```
% read EFIT tree or load GEQDSK file
% caculate B-field components B_T, B_Z, B_R
% read Thomson scattering data

% probe beam frequency
omega = 2.*pi.*f; % f = 288e9 Hz

% define calculation grid
z0 = (Rcoord(1)+Rcoord(end))./2;
zspan_in = [Rcoord(1):5e-3:Rcoord(end)]'-z0;
zspan_out = zspan_in;
dz = diff(zspan_in(1:2));

% map B-field & n_e to grid

%% prepare for inbound calculations
Bx_in = -B_T;
By_in = B_Z;
Bz_in = -B_R;
```

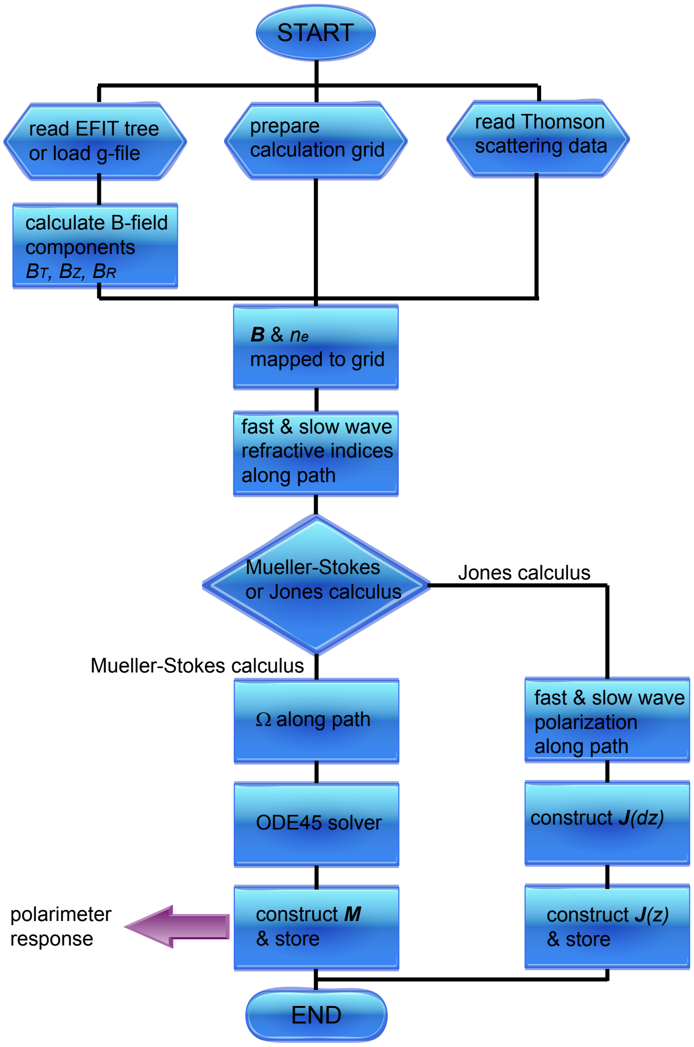

Figure C.1: *Flow chart of the synthetic diagnostic code.*

```

% cyclotron & plasma frequencies
omega_c_in = @(z) q_e.*B_0_in(z)./m_e;
omega_p_in = @(z) sqrt((n_e_in(z).*q_e.^2)./(epsilon_0.*m_e));

% refractive indices of fast & slow wave
% NOTE: special treatment needed for case theta_n_in = 0.
theta_n_in = @(z) acos(B_z_in(z)./B_0_in(z));
beta_n_in = @(z) atan2(B_y_in(z),B_x_in(z));
P_n_in = @(z) (omega_p_in(z)./omega).^2;
C_n_in = @(z) (omega_c_in(z)./omega).^2;
F_n_in = @(z) 2.*omega./omega_c_in(z).*(1-P_n_in(z)).*cos(theta_n_in(z))./(sin(theta_n_in(z))).^2;

n_slow_in = @(z) sqrt(1-P_n_in(z)./(1-C_n_in(z).*(sin(theta_n_in(z)).^2)./2./(1-P_n_in(z))+sqrt((C_n_in(z).^2).*(sin(theta_n_in(z)).^4)./4./((1-P_n_in(z)).^2)+C_n_in(z).*cos(theta_n_in(z)).^2)));
n_fast_in = @(z) sqrt(1-P_n_in(z)./(1-C_n_in(z).*(sin(theta_n_in(z)).^2)./2./(1-P_n_in(z))-sqrt((C_n_in(z).^2).*(sin(theta_n_in(z)).^4)./4./((1-P_n_in(z)).^2)+C_n_in(z).*cos(theta_n_in(z)).^2)));

% capital Omega
Omega_1_in = omega./c.*(n_slow_in(z)-n_fast_in(z)).*cos(2.*beta_n_in(z))./sqrt(1+(F_n_in(z).^2));
Omega_2_in = omega./c.*(n_slow_in(z)-n_fast_in(z)).*sin(2.*beta_n_in(z))./sqrt(1+(F_n_in(z).^2));
Omega_3_in = omega./c.*(n_slow_in(z)-n_fast_in(z)).*F_n_in(z)./sqrt(1+(F_n_in(z).^2));

%% similar preparation for outbound
```

```
Bx_out = B_T;
By_out = B_Z;
Bz_out = B_R;

omega_c_out = @(z) q_e.*B_0_out(z)./m_e;
omega_p_out = @ (z) sqrt((n_e_out(z).*q_e.^2)./(epsilon_0.*m_e));

theta_n_out = @(z) acos(B_z_out(z)./B_0_out(z));
beta_n_out = @(z) atan2(B_y_out(z),B_x_out(z));
P_n_out = @(z) (omega_p_out(z)./omega).^2;
C_n_out = @(z) (omega_c_out(z)./omega).^2;
F_n_out = @(z) 2.*omega./omega_c_out(z).*(1-P_n_out(z)).*cos(
    theta_n_out(z))./(sin(theta_n_out(z))).^2;

n_slow_out = @(z) sqrt(1-P_n_out(z)./(1-C_n_out(z).*(sin(theta_n_out(z)
    ).^2)./2./(1-P_n_out(z))+sqrt((C_n_out(z).^2).*(sin(theta_n_out(z))
    .^4)./4./(1-P_n_out(z)).^2+C_n_out(z).*cos(theta_n_out(z)).^2)));
n_fast_out = @(z) sqrt(1-P_n_out(z)./(1-C_n_out(z).*(sin(theta_n_out(z)
    ).^2)./2./(1-P_n_out(z))-sqrt((C_n_out(z).^2).*(sin(theta_n_out(z))
    .^4)./4./(1-P_n_out(z)).^2+C_n_out(z).*cos(theta_n_out(z)).^2)));

Omega_1_out = omega./c.*(n_slow_out(z)-n_fast_out(z)).*cos(2.*
    beta_n_out(z))./sqrt(1+(F_n_out(z).^2));
Omega_2_out = omega./c.*(n_slow_out(z)-n_fast_out(z)).*sin(2.*
    beta_n_out(z))./sqrt(1+(F_n_out(z).^2));
Omega_3_out = omega./c.*(n_slow_out(z)-n_fast_out(z)).*F_n_out(z)./sqrt
    (1+(F_n_out(z).^2));

%% calculate Jones matrices
% _f ~ ’fast’; _s ~ ’slow’; _c ~ ’common’; _d ~ ’difference’;
```

```
% inbound
J_in = zeros(2,2,length(zspan_in));
J_dz = zeros(2,2);
J_in(:,:,1) = eye(2);
for k = 2:length(zspan_in)
    z = zspan_in(k);
    delta_s_in = -n_slow_in(z).*omega./c.*dz;
    delta_f_in = -n_fast_in(z).*omega./c.*dz;

    % fast characteristic wave Stokes vector
    s_fast_in(1) = -1./sqrt(1+(F_n_in(z).^2)).*cos(2.*beta_n_in(z));
    s_fast_in(2) = -1./sqrt(1+(F_n_in(z).^2)).*sin(2.*beta_n_in(z));
    s_fast_in(3) = -F_n_in(z)./sqrt(1+(F_n_in(z).^2));
    [alpha_fast_in,delta_fast_in] = stokes2alphadelta_z(s_fast_in);

    sin_af = sin(alpha_fast_in);
    cos_af = cos(alpha_fast_in);
    exp_ds = exp(-1i*delta_s_in);
    exp_df = exp(-1i*delta_f_in);

    J_dz = [sin_af.^2.*exp_ds+cos_af.^2.*exp_df,...
        sin_af.*cos_af.*exp(1i*(delta_fast_in)).*(exp_df-exp_ds);
        sin_af.*cos_af.*exp(-1i*(delta_fast_in)).*(exp_df-exp_ds),...
        sin_af.^2.*exp_df+cos_af.^2.*exp_ds];

    J_in(:,:,k) = J_dz*J_in(:,:,k-1);
end

% outbound
% mirror reflection
```

```
J_out = zeros(2,2,length(zspan_out));
J_out(:,:,1) = [1,0;0,-1]*J_in(:,:,end);
for k = 2:length(zspan_out)
    z = zspan_out(k);
    delta_s_out = -n_slow_out(z).*omega./c.*dz;
    delta_f_out = -n_fast_out(z).*omega./c.*dz;

    s_fast_out(1) = -1./sqrt(1+(F_n_out(z).^2)).*cos(2.*beta_n_out(z));
    s_fast_out(2) = -1./sqrt(1+(F_n_out(z).^2)).*sin(2.*beta_n_out(z));
    s_fast_out(3) = -F_n_out(z)./sqrt(1+(F_n_out(z).^2));

    [alpha_fast_out,delta_fast_out] = stokes2alphadelta_z(s_fast_out);

    sin_af = sin(alpha_fast_out);
    cos_af = cos(alpha_fast_out);
    exp_ds = exp(-1i*delta_s_out);
    exp_df = exp(-1i*delta_f_out);

    J_dz = [sin_af.^2.*exp_ds+cos_af.^2.*exp_df,...
        sin_af.*cos_af.*exp(1i*(delta_fast_out)).*(exp_df-exp_ds);
        sin_af.*cos_af.*exp(-1i*(delta_fast_out)).*(exp_df-exp_ds),...
        sin_af.^2.*exp_df+cos_af.^2.*exp_ds];

    J_out(:,:,k) = J_dz*J_out(:,:,k-1);
end

%% calculate the three basis polarization stokes vector evolution
% inbound
s_in_0 = zeros(length(zspan_in),3); % horizontal linear
s_in_45 = zeros(length(zspan_in),3); % 45 linear
```

```
s_in_RC = zeros(length(zspan_in),3); % right circular

options = odeset('RelTol',1e-5);
sol_in_0 = ode45(@odes_in_z_A,zspan_in,[1;0;0],options);
sol_in_45 = ode45(@odes_in_z_A,zspan_in,[0;1;0],options);
sol_in_RC = ode45(@odes_in_z_A,zspan_in,[0;0;1],options);

s_in_0(:,1:3) = deval(sol_in_0,zspan_in)';
s_in_45(:,1:3) = deval(sol_in_45,zspan_in)';
s_in_RC(:,1:3) = deval(sol_in_RC,zspan_in)';

% outbound
s_out_0 = zeros(length(zspan_out),3); % horizontal linear
s_out_45 = zeros(length(zspan_out),3); % 45 linear
s_out_RC = zeros(length(zspan_out),3); % right circular

%% calculate Muller matrices
M_in = zeros(3,3,length(zspan_in));
for k = 1:length(zspan_in)
    M_in(1:3,1,k) = s_in_0(k,1:3)';
    M_in(1:3,2,k) = s_in_45(k,1:3)';
    M_in(1:3,3,k) = s_in_RC(k,1:3)';
end

% mirror reflection
s_out_0(1,1:3) = [s_in_0(end,1);-s_in_0(end,2);-s_in_0(end,3)];
s_out_45(1,1:3) = [s_in_45(end,1);-s_in_45(end,2);-s_in_45(end,3)];
s_out_RC(1,1:3) = [s_in_RC(end,1);-s_in_RC(end,2);-s_in_RC(end,3)];

sol_out_0 = ode45(@odes_out_z_A,zspan_out,s_out_0(1,:)',options);
```

```
sol_out_45 = ode45(@odes_out_z_A,zspan_out,s_out_45(1,:)',options);
sol_out_RC = ode45(@odes_out_z_A,zspan_out,s_out_RC(1,:)',options);

s_out_0(:,1:3) = deval(sol_out_0,zspan_out)';
s_out_45(:,1:3) = deval(sol_out_45,zspan_out)';
s_out_RC(:,1:3) = deval(sol_out_RC,zspan_out)';

M_out = zeros(3,3,length(zspan_out));
for k = 1:length(zspan_out)
    M_out(1:3,1,k) = s_out_0(k,1:3)';
    M_out(1:3,2,k) = s_out_45(k,1:3)';
    M_out(1:3,3,k) = s_out_RC(k,1:3)';
end

%% save calculation results
save(results_file,'shot','time','h','f','Rcoord','Zcoord','R_mesh','
    Z_mesh','B_R','B_Z','B_T','psi_RZ','rho_RZ','n_e','z0',...
     'zspan_in','J_in','M_in','ne_in','Bx_in','By_in','Bz_in',...
     'zspan_out','J_out','M_out','ne_out','Bx_out','By_out','Bz_out');

%% function odes_in_z_A
function s_in_prime=odes_in_z_A(z,s_in)
global Omega_1_in Omega_2_in Omega_3_in;
s_in_prime = [(Omega_2_in(z)).*s_in(3)-(Omega_3_in(z)).*s_in(2);...
    (Omega_3_in(z)).*s_in(1)-(Omega_1_in(z)).*s_in(3);...
    (Omega_1_in(z)).*s_in(2)-(Omega_2_in(z)).*s_in(1)];
end

%% function odes_out_z_A
function s_out_prime=odes_out_z_A(z,s_out)
```

```
global Omega_1_out Omega_2_out Omega_3_out;
s_out_prime = [(Omega_2_out(z)).*s_out(3)-(Omega_3_out(z)).*s_out(2);...
    (Omega_3_out(z)).*s_out(1)-(Omega_1_out(z)).*s_out(3);...
    (Omega_1_out(z)).*s_out(2)-(Omega_2_out(z)).*s_out(1)];
end
```

Input/code.m

BIBLIOGRAPHY

T. Akiyama, K. Kawahata, Y. Ito, S. Okajima, K. Nakayama, S. Okamura, K. Matsuoka, M. Isobe, S. Nishimura, C. Suzuki, Y. Yoshimura, K. Nagaoka, C. Takahashi, and CHS Experimental Group. Cotton-Mouton polarimeter with HCN laser on CHS. *Rev. Sci. Instrum.*, 77(10), 2006. doi:10.1063/1.2229275.

D. J. Applegate, C. M. Roach, J. W. Connor, S. C. Cowley, W. Dorland, R. J. Hastie, and N. Joiner. Micro-tearing modes in the mega ampere spherical tokamak. *Plasma Phys. Control. Fusion*, 49(8), 2007. doi:10.1088/0741-3335/49/8/001.

E. V. Appleton. Geophysical influences on the transmission of wireless waves. *Proceedings of the Physical Society of London*, 37(1), 1924. doi:10.1088/1478-7814/37/1/312.

R. Aymar, P. Barabaschi, and Y. Shimomura. The ITER design. *Plasma Phys. Control. Fusion*, 44(5), 2002. doi:10.1088/0741-3335/44/5/304.

W. F. Bergerson, P. Xu, J. H. Irby, D. L. Brower, W. X. Ding, and E. S. Marmar. Far-infrared polarimetry diagnostic for measurement of internal magnetic field dynamics and fluctuations in the C-MOD Tokamak (invited). *Rev. Sci. Instrum.*, 83(10), 2012. doi:10.1063/1.4731757.

A. Boboc, L. Zabeo, A. Murari, and JET EFDA Contributors. Simultaneous Cotton-Mouton and Faraday rotation angle measurements on JET. *Rev. Sci. Instrum.*, 77, 2006. doi:10.1063/1.2229169.

Max Born, Emil Wolf, and A. B. Bhatia. *Principles of Optics*. 2000. ISBN 0521784492, 9780521784498.

G. Braithwaite, N. Gottardi, G. Magyar, J. O'Rourke, J. Ryan, and D. Veron. JET polari-interferometer. *Rev. Sci. Instrum.*, 60(9), 1989. doi:10.1063/1.1140666.

D. P. Brennan, A. D. Turnbull, M. S. Chu, R. J. La Haye, L. L. Lao, T. H. Osborne, and S. A. Galkin. Resistive stability of 2/1 modes near 1/1 resonance. *Phys. Plasmas*, 14(5), 2007. doi:10.1063/1.2515224.

J.A. Breslau, M.S. Chance, J. Chen, G.Y. Fu, S. Gerhardt, N. Gorelenkov, S.C. Jardin, and J. Manickam. Onset and saturation of a non-resonant internal mode in NSTX and implications for AT modes in ITER. *Nucl. Fusion*, 51(6), 2011. doi:10.1088/0029-5515/51/6/063027.

D. L. Brower, W. X. Ding, S. D. Terry, J. K. Anderson, T. M. Biewer, B. E. Chapman, D. Craig, C. B. Forest, S. C. Prager, and J. S. Sarff. Measurement of the current-density profile and plasma dynamics in the reversed-field pinch. *Phys. Rev. Lett.*, 88, 2002. doi:10.1103/PhysRevLett.88.185005.

D. L. Brower, W. X. Ding, S. D. Terry, J. K. Anderson, T. M. Biewer, B. E. Chapman, D. Craig, C. B. Forest, S. C. Prager, and J. S. Sarff. Laser polarimetric measurement of equilibrium and fluctuating magnetic fields in a reversed field pinch (invited). *Rev. Sci. Instrum.*, 74, 2003. doi:10.1063/1.1526927.

R. Cano, I. Fidone, and M. J. Schwartz. Spatial determination of the direction of the magnetic field in a tokamak configuration. *Phys. Rev. Lett.*, 27, 1971. doi:10.1103/PhysRevLett.27.783.

T. N. Carlstrom, G. L. Campbell, J. C. DeBoo, R. Evanko, J. Evans, C. M. Greenfield, J. Haskovec, C. L. Hsieh, E. McKee, R. T. Snider, R. Stockdale, P. K. Trost, and M. P. Thomas. Design and operation of the multipulse Thomson scattering diagnostic on DIII-D (invited). *Rev. Sci. Instrum.*, 63(10), 1992. doi:10.1063/1.1143545.

D. W. Choi, E. J. Powers, Roger D. Bengtson, G. Joyce, D. L. Brower, N. C. Luhmann, and W. A. Peebles. Digital complex demodulation applied to interferometry. *Rev. Sci. Instrum.*, 57(8), 1986. doi:10.1063/1.1138762.

E. Collett. *Polarized Light in Fiber Optics.* Press Monographs Series. 2003. ISBN 9780819457615.

N. A. Crocker, W. A. Peebles, S. Kubota, J. Zhang, R. E. Bell, E. D. Fredrickson, N. N. Gorelenkov, B. P. LeBlanc, J. E. Menard, M. Podestà, S. A. Sabbagh, K. Tritz, and H. Yuh. High spatial sampling global mode structure measurements via multichannel reflectometry in NSTX. *Plasma Phys. Control. Fusion*, 53(10), 2011. doi:10.1088/0741-3335/53/10/105001.

W. X. Ding, D. L. Brower, S. D. Terry, D. Craig, S. C. Prager, J. S. Sarff, and J. C. Wright. Measurement of internal magnetic field fluctuations in a reversed-field pinch by Faraday rotation. *Phys. Rev. Lett.*, 90, 2003. doi:10.1103/PhysRevLett.90.035002.

J. L. Doane. Broadband superheterodyne tracking circuits for millimeter-wave measurements. *Rev. Sci. Instrum.*, 51(3), 1980. doi:10.1063/1.1136209.

A. J. H. Donné, M. F. Graswinckel, M. Cavinato, L. Giudicotti, E. Zilli, C. Gil, H. R. Koslowski, P. McCarthy, C. Nyhan, S. Prunty, M. Spillane, and C. Walker. Poloidal polarimeter for current density measurements in ITER. *Rev. Sci. Instrum.*, 75(11), 2004. doi:10.1063/1.1804372.

J. F. Drake and Y. C. Lee. Kinetic theory of tearing instabilities. *Phys. Fluids*, 20 (8), 1977. doi:10.1063/1.862017.

T. W. Fredian and J. A. Stillerman. MDSplus. Current developments and future directions. *Fusion Engineering and Design*, 60(3), 2002. doi:10.1016/S0920-3796(02)00013-3.

E. D. Fredrickson. Observation of spontaneous neoclassical tearing modes. *Phys. Plasmas*, 9(2), 2002. doi:10.1063/1.1435003.

Jeffrey P. Freidberg. *Plasma Physics and Fusion Energy*. 2007. doi:10.1017/CBO9780511755705.

Ch. Fuchs and H. J. Hartfuss. Cotton-Mouton effect measurement in a plasma at the W7-AS stellarator. *Phys. Rev. Lett.*, 81, 1998. doi:10.1103/PhysRevLett.81.1626.

S. P. Gerhardt, D. P. Brennan, R. Buttery, R. J. La Haye, S. Sabbagh, E. Strait, M. Bell, R. Bell, E. Fredrickson, D. Gates, B. LeBlanc, J. Menard, D. Stutman, K. Tritz, and H. Yuh. Relationship between onset thresholds, trigger types and rotation shear for the m/n = 2/1 neoclassical tearing mode in a high-β spherical torus. *Nucl. Fusion*, 49(3), 2009. doi:10.1088/0029-5515/49/3/032003.

S. P. Gerhardt, E. Fredrickson, D. Gates, S. Kaye, J. Menard, M. G. Bell, R. E. Bell, B. P. Le Blanc, H. Kugel, S. A. Sabbagh, and H. Yuh. Calculation of the non-inductive current profile in high-performance NSTX plasmas. *Nucl. Fusion*, 51(3), 2011. doi:10.1088/0029-5515/51/3/033004.

T. A. Gianakon, S. E. Kruger, and C. C. Hegna. Heuristic closures for numerical simulations of neoclassical tearing modes. *Phys. Plasmas*, 9(2), 2002. doi:10.1063/1.1424924.

P. F. Goldsmith. Quasi-optical techniques. *Proceedings of the IEEE*, 80(11), 1992. doi:10.1109/5.175252.

A. Gude, S. Günter, S. Sesnic, and ASDEX Upgrade Team. Seed island of neoclassical tearing modes at ASDEX Upgrade. *Nucl. Fusion*, 39(1), 1999. doi:10.1088/0029-5515/39/1/308.

K. Guenther. Approximate method to extract the pure Faraday and Cotton-Mouton effects from polarimetry measurements in a tokamak. *Plasma Phys. Control. Fusion*, 46(9), 2004. doi:10.1088/0741-3335/46/9/006.

W. Guttenfelder, J. Candy, S. M. Kaye, W. M. Nevins, E. Wang, R. E. Bell, G. W. Hammett, B. P. LeBlanc, D. R. Mikkelsen, and H. Yuh. Electromagnetic transport from microtearing mode turbulence. *Phys. Rev. Lett.*, 106, 2011. doi:10.1103/PhysRevLett.106.155004.

W. Guttenfelder, J. Candy, S. M. Kaye, W. M. Nevins, E. Wang, J. Zhang, R. E. Bell, N. A. Crocker, G. W. Hammett, B. P. LeBlanc, D. R. Mikkelsen, Y. Ren, and H. Yuh. Simulation of microtearing turbulence in national spherical torus experiment. *Phys. Plasmas*, 19(5), 2012. doi:doi:10.1063/1.3694104.

D. R. Hartree. The propagation of electromagnetic waves in a refracting medium in a magnetic field. *Mathematical Proceedings of the Cambridge Philosophical Society*, 27, 1931. doi:10.1017/S0305004100009440.

Mark A. Heald. *Plasma diagnostics with microwaves*. 1978. ISBN 77013781.

E. Hecht. *Optics*. 2002. ISBN 9780805385663.

W. W. Heidbrink. Basic physics of Alfvén instabilities driven by energetic particles in toroidally confined plasmas. *Phys. Plasmas*, 15(5), 2008. doi:10.1063/1.2838239.

Jr. Henry Hurwitz and R. Clark Jones. A new calculus for the treatment of optical systems. *J. Opt. Soc. Am.*, 31(7), 1941. doi:10.1364/JOSA.31.000493.

L. Huang and R. V. Shcherbakov. Faraday conversion and rotation in uniformly magnetized relativistic plasmas. *Monthly Notices of the Royal Astronomical Society*, 416(4), 2011. doi:10.1111/j.1365-2966.2011.19207.x.

I. H. Hutchinson. *Principles of Plasma Diagnostics*. 2005. ISBN 9780521675741.

R. Imazawa, Y. Kawano, and Y. Kusama. Highly accurate approximate solutions of the Stokes equation for high electron density and long laser wavelength. *Plasma Phys. Control. Fusion*, 54(5), 2012. doi:10.1088/0741-3335/54/5/055005.

J. D. Jackson. *Classical Electrodynamics*. 1998. ISBN 9780471309321.

Y. Jiang, D. L. Brower, and N. E. Lanier. Interferometric measurement of high-frequency density fluctuations in Madison symmetric torus. *Rev. Sci. Instrum.*, 70 (1), 1999. doi:10.1063/1.1149275.

R. Clark Jones. A new calculus for the treatment of optical systems. *J. Opt. Soc. Am.*, 31(7), 1941a. doi:10.1364/JOSA.31.000488.

R. Clark Jones. A new calculus for the treatment of optical systems. *J. Opt. Soc. Am.*, 31(7), 1941b. doi:10.1364/JOSA.31.000500.

R. Clark Jones. A new calculus for the treatment of optical systems. *J. Opt. Soc. Am.*, 32(8), 1942. doi:10.1364/JOSA.32.000486.

R. Clark Jones. A new calculus for the treatment of optical systems. *J. Opt. Soc. Am.*, 37(2), 1947a. doi:10.1364/JOSA.37.000107.

R. Clark Jones. A new calculus for the treatment of optical systems. *J. Opt. Soc. Am.*, 37(2), 1947b. doi:10.1364/JOSA.37.000110.

R. Clark Jones. A new calculus for the treatment of optical systems. *J. Opt. Soc. Am.*, 38(8), 1948. doi:10.1364/JOSA.38.000671.

Y Kamada, T Fujita, S Ishida, M Kikuchi, S Ide, T Takizuka, H Shirai, Y Koide, T Fukuda, N Hosogane, K Tsuchiya, T Hatae, H Takenaga, M Sato, H Nakamura, O Naito, N Asakura, H Kubo, S Higashijima, Y Miura, R Yoshino, K Shimizu, T Ozeki, T Hirayama, M Mori, Y Sakamoto, Y Kawano, A Isayama, K Ushigusa, Y Ikeda, H Kimura, T Fujii, T Imai, M Nagami, S Takeji, T Oikawa, T Suzuki, T Nakano, N Oyama, S Sakurai, S Konoshima, T Sugie, K Tobita, T Kondoh, H Tamai, Y Neyatani, A Sakasai, Y Kusama, K Itami, M Shimada, and H Ninomiya. Fusion plasma performance and confinement studies on JT-60 and JT-60U. *Fusion Sci. Technol.*, 42(2-3), 2002.

T. Kondoh, A. E. Costley, T. Sugie, Y. Kawano, A. Malaquias, and C. I. Walker. Toroidal interferometer/polarimeter density measurement system on ITER. *Rev. Sci. Instrum.*, 75(10), 2004. doi:10.1063/1.1786640.

R. J. La Haye. Neoclassical tearing modes and their control. *Phys. Plasmas*, 13(5), 2006. doi:10.1063/1.2180747.

Jianying Lang, Guo-Yong Fu, and Yang Chen. Nonlinear simulation of toroidal Alfvén eigenmode with source and sink. *Phys. Plasmas*, 17(4), 2010. doi:10.1063/1.3394702.

N. E. Lanier, J. K. Anderson, C. B. Forest, D. Holly, Y. Jiang, and D. L. Brower. First results from the far-infrared polarimeter system on the Madison Symmetric Torus reversed field pinch. *Rev. Sci. Instrum.*, 70, 1999. doi:10.1063/1.1149490.

L. L. Lao, H. S. John, R. D. Stambaugh, A. G. Kellman, and W. Pfeiffer. Reconstruction of current profile parameters and plasma shapes in tokamaks. *Nucl. Fusion*, 25(11), 1985. doi:10.1088/0029-5515/25/11/007.

F. M. Levinton, G. M. Gammel, R. Kaita, H. W. Kugel, and D. W. Roberts. Magnetic field pitch angle diagnostic using the motional Stark effect (invited). *Rev. Sci. Instrum.*, 61, 1990. doi:10.1063/1.1141776.

F. M. Levinton, H. Yuh, M. G. Bell, R. E. Bell, L. Delgado-Aparicio, M. Finkenthal, E. D. Fredrickson, D. A. Gates, S. M. Kaye, B. P. LeBlanc, R. Maingi, J. E. Menard, D. Mikkelsen, D. Mueller, R. Raman, G. Rewoldt, S. A. Sabbagh, D. Stutman, K. Tritz, and W. Wang. Transport with reversed shear in the National Spherical Torus Experiment. *Phys. Plasmas*, 14(5), 2007. doi:10.1063/1.2734124.

J. L. Luxon. A design retrospective of the DIII-D tokamak. *Nucl. Fusion*, 42(5), 2002. doi:10.1088/0029-5515/42/5/313.

J. E. Maggs and G. J. Morales. Generality of deterministic chaos, exponential spectra, and Lorentzian pulses in magnetically confined plasmas. *Phys. Rev. Lett.*, 107, 2011. doi:10.1103/PhysRevLett.107.185003.

D. H. Martin and J. Lesurf. Submillimetre-wave optics. *Infrared Physics*, 18, 1978. doi:10.1016/0020-0891(78)90048-9.

W. H. McMaster. Polarization and the Stokes parameters. *American Journal of Physics*, 22(6), 1954. doi:10.1119/1.1933744.

J. E. Menard, R. E. Bell, E. D. Fredrickson, D. A. Gates, S. M. Kaye, B. P. LeBlanc, R. Maingi, S. S. Medley, W. Park, S. A. Sabbagh, A. Sontag, D. Stutman, K. Tritz, W. Zhu, and the NSTX Research Team. Internal kink mode dynamics in high-β NSTX plasmas. *Nucl. Fusion*, 45(7), 2005. doi:10.1088/0029-5515/45/7/001.

J. E. Menard, R. E. Bell, D. A. Gates, S. M. Kaye, B. P. LeBlanc, F. M. Levinton, S. S. Medley, S. A. Sabbagh, D. Stutman, K. Tritz, and H. Yuh. Observation of instability-induced current redistribution in a spherical-torus plasma. *Phys. Rev. Lett.*, 97, 2006. doi:10.1103/PhysRevLett.97.095002.

J. E. Menard, S. Gerhardt, M. Bell, J. Bialek, A. Brooks, J. Canik, J. Chrzanowski, M. Denault, L. Dudek, D.A. Gates, N. Gorelenkov, W. Guttenfelder, R. Hatcher, J. Hosea, R. Kaita, S. Kaye, C. Kessel, E. Kolemen, H. Kugel, R. Maingi, M. Mardenfeld, D. Mueller, B. Nelson, C. Neumeyer, M. Ono, E. Perry, R. Ramakrishnan, R. Raman, Y. Ren, S. Sabbagh, M. Smith, V. Soukhanovskii, T. Stevenson, R. Strykowsky, D. Stutman, G. Taylor, P. Titus, K. Tresemer, K. Tritz, M. Viola, M. Williams, R. Woolley, H. Yuh, H. Zhang, Y. Zhai, A. Zolfaghari, and the NSTX Team. Overview of the physics and engineering design of NSTX upgrade. *Nucl. Fusion*, 52(8), 2012. doi:10.1088/0029-5515/52/8/083015.

V. V. Mirnov, W. X. Ding, D. L. Brower, M. A. Van Zeeland, and T. N. Carlstrom.

Finite electron temperature effects on interferometric and polarimetric measurements in fusion plasmas. *Phys. Plasmas*, 14(10), 2007. doi:10.1063/1.2790886.

M. F. F. Nave, E. Lazzaro, R. Coelho, P. Belo, D. Borba, R. J. Buttery, S. Nowak, F. Serra, and EFDA-JET Contributors. Triggering of neo-classical tearing modes by mode coupling. *Nucl. Fusion*, 43(3), 2003. doi:10.1088/0029-5515/43/3/303.

M. Ono, S. M. Kaye, Y.-K. M. Peng, G. Barnes, W. Blanchard, M. D. Carter, J. Chrzanowski, L. Dudek, R. Ewig, D. Gates, R. E. Hatcher, T. Jarboe, S. C. Jardin, D. Johnson, R. Kaita, M. Kalish, C. E. Kessel, H. W. Kugel, R. Maingi, R. Majeski, J. Manickam, B. McCormack, J. Menard, D. Mueller, B. A. Nelson, B. E. Nelson, C. Neumeyer, G. Oliaro, F. Paoletti, R. Parsells, E. Perry, N. Pomphrey, S. Ramakrishnan, R. Raman, G. Rewoldt, J. Robinson, A. L. Roquemore, P. Ryan, S. Sabbagh, D. Swain, E. J. Synakowski, M. Viola, M. Williams, J. R. Wilson, and NSTX Team. Exploration of spherical torus physics in the NSTX device. *Nucl. Fusion*, 40(3Y), 2000. doi:10.1088/0029-5515/40/3Y/316.

F. P. Orsitto, A. Boboc, P. Gaudio, M. Gelfusa, E. Giovannozzi, C. Mazzotta, and A. Murari. Mutual interaction of Faraday rotation and Cotton-Mouton phase shift in JET polarimetric measurements. *Rev. Sci. Instrum.*, 81(10), 2010. doi:10.1063/1.3502039.

F. P. Orsitto, A. Boboc, P. Gaudio, M. Gelfusa, E. Giovannozzi, C. Mazzotta, A. Murari, and JET EFDA Contributors. Analysis of Faraday rotation in JET polarimetric measurements. *Plasma Phys. Control. Fusion*, 53(3), 2011. doi:10.1088/0741-3335/53/3/035001.

R. Pavlichenko, K. Kawahata, and T. Donne. Design of the 48, 57 μm poloidal polarimeter for ITER. *Plasma and Fusion Research*, 2, 2007. doi:10.1585/pfr.2.S1040.

H. M. Pickett, J. C. Hardy, and Jam Farhoomand. Characterization of a dual-mode horn for submillimeter wavelengths (short papers). *Microwave Theory and Techniques, IEEE Transactions on*, 32(8), 1984. doi:10.1109/TMTT.1984.1132801.

R. Raman, D. Mueller, S. C. Jardin, T. R. Jarboe, B. A. Nelson, M. G. Bell, S. P. Gerhardt, E. B. Hooper, S. M. Kaye, C. E. Kessel, J. E. Menard, M. Ono, V. Soukhanovskii, and the NSTX Research Team. Non-inductive plasma start-up on NSTX and projections to NSTX-U using transient CHI. *Nucl. Fusion*, 53(7), 2013. doi:10.1088/0029-5515/53/7/073017.

B. W. Rice. Fifteen chord FIR polarimetry system on MTX. *Rev. Sci. Instrum.*, 63 (10), 1992. doi:10.1063/1.1143527.

M. Riva, L. Zabeo, E. Joffrin, D. Mazon, D. Moreau, A. Murari, R. Felton, K. Guenther, X. Litaudon, F. Sartori, C. Taliercio, and G. Tresset. Real time safety factor profile determination in JET. *Fusion Engineering and Design*, 66–68 (0), 2003. doi:10.1016/S0920-3796(03)00310-7.

J. H. Rommers and J. Howard. A new scheme for heterodyne polarimetry with high temporal resolution. *Plasma Phys. Control. Fusion*, 38, 1996. doi:10.1088/0741-3335/38/10/008.

S. Segre and S. Nowak. Analytic expression for the influence of plasma birefringence on Faraday-rotation measurements in a tokamak plasma. *Il Nuovo Cimento D*, 15 (6), 1993. doi:10.1007/BF02482466.

S. E. Segre. A review of plasma polarimetry - theory and methods. *Plasma Phys. Control. Fusion*, 41(2), 1999. doi:10.1088/0741-3335/41/2/001.

S. E. Segre and V. Zanza. Finite electron temperature effects in plasma polarimetry and interferometry. *Phys. Plasmas*, 9(7), 2002. doi:10.1063/1.1485075.

A. P. Smirnov and R. W. Harvey. Calculations of the current drive in DIII-D with the GENRAY ray tracing code. In *Bull. Am. Phys. Soc.*, volume 40, 1995.

H. Soltwisch. Current distribution measurement in a tokamak by FIR polarimetry (invited). *Rev. Sci. Instrum.*, 57(8), 1986. doi:10.1063/1.1138803.

H. Soltwisch. Current density measurements in tokamak devices. *Plasma Phys. Control. Fusion*, 34(12), 1992. doi:10.1088/0741-3335/34/12/001.

H. Soltwisch. Application of Jones matrices to the analysis of far-infrared wave propagation in tokamak plasmas. *Plasma Phys. Control. Fusion*, 35(12), 1993. doi:10.1088/0741-3335/35/12/010.

Thomas Howard Stix. *The theory of plasma waves.* 1962.

D. G. Swanson. *Plasma Waves.* Plasma Physics. 2003. ISBN 9780750309271.

T. S. Taylor, H. St John, A. D. Turnbull, V. R. Lin-Liu, K. H. Burrell, V. Chan, M. S. Chu, J. R. Ferron, L. L. Lao, R. J. La Haye, E. A. Lazarus, R. L. Miller, P. A. Politzer, D. P. Schissel, and E. J. Strait. Optimized profiles for improved confinement and stability in the DIII-D tokamak. *Plasma Phys. Control. Fusion*, 36(12B), 1994. doi:10.1088/0741-3335/36/12B/019.

J. Wesson. *Tokamaks.* International Series of Monographs on Physics. 2011. ISBN 9780199592234.

K. L. Wong, S. Kaye, D. R. Mikkelsen, J. A. Krommes, K. Hill, R. Bell, and B. LeBlanc. Microtearing instabilities and electron transport in the NSTX spherical tokamak. *Phys. Rev. Lett.*, 99, 2007. doi:10.1103/PhysRevLett.99.135003.

King-Lap Wong. A review of Alfvén eigenmode observations in toroidal plasmas. *Plasma Phys. Control. Fusion*, 41(1), 1999. doi:10.1088/0741-3335/41/1/001.

D. Wroblewski and L. L. Lao. Polarimetry of motional Stark effect and determination of current profiles in DIII-D (invited). *Rev. Sci. Instrum.*, 63, 1992. doi:10.1063/1.1143463.

M. A. Van Zeeland, R. L. Boivin, T. N. Carlstrom, T. Deterly, and D. K. Finkenthal. Fiber optic two-color vibration compensated interferometer for plasma density measurements. *Rev. Sci. Instrum.*, 77(10), 2006a. doi:10.1063/1.2336437.

M. A. Van Zeeland, G. J. Kramer, M. E. Austin, R. L. Boivin, W. W. Heidbrink, M. A. Makowski, G. R. McKee, R. Nazikian, W. M. Solomon, and G. Wang. Radial structure of Alfvén eigenmodes in the DIII-D tokamak through electron-cyclotron-emission measurements. *Phys. Rev. Lett.*, 97(13), 2006b. doi:10.1103/PhysRevLett.97.135001.

M. A. Van Zeeland, R. L. Boivin, T. N. Carlstrom, and T. M. Deterly. CO_2 laser polarimeter for Faraday rotation measurements in the DIII-D tokamak. *Rev. Sci. Instrum.*, 79, 2008a. doi:10.1063/1.2955859.

M. A. Van Zeeland, J. H. Yu, M. S. Chu, K. H. Burrell, R. J. La Haye, T. C. Luce, R. Nazikian, W. M. Solomon, and W. P. West. Tearing mode structure in the DIII-D tokamak through spectrally filtered fast visible bremsstrahlung imaging. *Nucl. Fusion*, 48(9), 2008b. doi:10.1088/0029-5515/48/9/092002.

J. Zhang, N. A. Crocker, T. A. Carter, S. Kubota, and W. A. Peebles. Interaction between Faraday rotation and Cotton-Mouton effects in polarimetry modeling for NSTX. *Rev. Sci. Instrum.*, 81(10), 2010. doi:10.1063/1.3479042.

J. Zhang, W. A. Peebles, T. A. Carter, N. A. Crocker, E. J. Doyle, S. Kubota, X. Nguyen, T. L. Rhodes, C. Wannberg, and L. Zeng. Design of a millimeter-wave polarimeter for NSTX-Upgrade and initial test on DIII-D. *Rev. Sci. Instrum.*, 83 (10), 2012. doi:10.1063/1.4733735.

J. Zhang, N. A. Crocker, W. A. Peebles, T. A. Carter, and W. Guttenfelder. A sensitivity assessment of millimeter-wave polarimetry for measurement of magnetic fluctuations associated with microtearing modes in NSTX-U. *Plasma Phys. Control. Fusion*, 55(4), 2013a. doi:10.1088/0741-3335/55/4/045011.

J. Zhang, W. A. Peebles, N. A. Crocker, T. A. Carter, E. J. Doyle, A. W. Hyatt, T. L. Rhodes, G. Wang, and L. Zeng. Experimental validation of Mueller-Stokes theory and investigation of the influence of the Cotton-Mouton effect on polarimetry in a magnetized fusion plasma. *Phys. Plasmas*, 20(10), 2013b. doi:http://dx.doi.org/10.1063/1.4826956.

O. C. Zienkiewicz, Y. P. Svirko, and N. I. Zheludev. *Polarization of Light in Nonlinear Optics*. 1998. ISBN 9780471976400.